Universidade do Minho
Escola de Engenharia

Mahsa Taheri

Structural Response and Cracking Behaviour of Fibre Reinforced Concrete Beams with Hybrid Flexural Reinforcement

February, 2021

Mahsa Taheri Structural Response and Cracking Behaviour of Fibre Reinforced Concrete Beams with Hybrid Flexural Reinforcement

UMinho | 2021

Universidade do Minho
Escola de Engenharia

Mahsa Taheri

Structural Response and Cracking Behaviour of Fibre Reinforced Concrete Beams with Hybrid Flexural Reinforcement

Dissertation Presented in Partial Fulfilment of the Requirement for the Degree of Doctor of Philosophy of Civil Engineering

Work unde the Supervision of the
Professor Joaquim António Oliveira de Barros

February, 2021

Acknowledgements

This dissertation presents the scientific research carried out at the Civil Engineering Department of the University of Minho, Guimarães, Portugal, as partial fulfilment of the requirement for the degree of doctor of philosophy of Civil Engineering.

I would like to express my sincere gratitude to my supervisor Prof. Joaquim Barros, for providing this research opportunity and for his obligingness and cordial support, encouragement and advice throughout the research.

My gratitude is due to the Professors and Staff of the Civil Engineering Department of the University of Minho and the Institute for Sustainability and Innovation in Structural Engineering (ISISE) for their consideration and kindness. My sincere appreciation also goes to the Director and, in particular, the Technicians of the structural laboratory (LEST). Their supports, loyalty and enthusiastic assistance were invaluable.

I would like to express my deepest sense of gratitude to the Director, Engineers, and Technicians of the Civitest Company for their valuable collaborations and supports in developing the materials.

Finally, I extend my profound gratitude to all my lovely family to whom this thesis is dedicated; my affectionate spouse “Hamidreza” for his genuine love, sacrifices, whose unconditional supports and patience made it possible for me to pursue this degree, my lovely son “Mehrsam” who is a tremendous blessing to my life and his passion is the source of motivation for me; and my compassionate mother, “Mrs Vajiheh”, who taught me the persistence and rectitude in my whole life and who dedicated her life to her children.

I would also like to perpetuate the memory of my father who left us very soon when I was a child. He is always in my heart. May God place his soul in peace!

Statement of Integrity

I hereby declare having conducted my thesis with integrity. I confirm that I have not used plagiarism or any form of falsification of results in the process of the thesis elaboration. I further declare that I have fully acknowledged the Code of Ethical Conduct of the University of Minho.

Abstract

In the present research, the structural response of concrete beams with an innovative hybrid flexural reinforcing (HFR) scheme is studied. The adopted HFR comprises an effective reinforcement solution in terms of durability, where noncorrodible fibre reinforced polymer (FRP) bars of significant tensile strength are positioned at near the outer surface of the tensile zone of the cross-section, while ductile steel bars located at an inner level with thicker concrete cover. Additionally, the reinforcing contribution of distinct fibres diffused in fibre reinforced concrete (FRC) is mobilised to suppress the necessity of using steel stirrups and to reduce the percentage of conventional flexural reinforcement.

The research includes experimental programs for assessing the post-cracking response of three series of steel fibre reinforced self-compacting concrete (SFRSCC) of different concrete strength class and volume fraction of fibres. This post-cracking behaviour is assessed in term of stress-crack width response, which is evaluated according to the recommendations of *fib* Model Code 2010 and from inverse analysis, both considering the results obtained in three-point notched beam bending tests and material nonlinear analysis with a finite element method. In the structural level, the flexural capacity and cracking behaviour of SFRSCC beams with HFR scheme were evaluated in the four-point bending test.

Additionally, the potentiality of the HFR scheme is evaluated by developing two closed-form models. The first one is developed based on the smeared crack approach, being capable of determining the moment-curvature response of a rectangular cross-section made of FRC with HFR scheme (HFR/FRC), where perfect bond is assumed between reinforcements and surrounding concrete. The second model includes an integrated approach developed for the prediction of crack width and crack spacing HFR/FRC beams supported by the discrete crack approach. This model is capable to take into consideration the post-cracking response of FRC in terms of stress-crack opening relationship and to mobilise the shear bond-sliding characteristics of steel- and FRP-to-concrete interaction. Predictive performance of the developed models is evaluated by the test results of present research and the ones represented in literature.

Resumo

No presente trabalho é investigada a resposta estrutural de vigas de betão reforçadas com um inovador sistema híbrido (HFR). Este sistema híbrido é composto por varões de polímero reforçado com fibras (FRP) e varões de aço, os quais podem ser aplicados sem ou com pré-tensão, de forma a ser maximizada a durabilidade dos elementos estruturais reforçados com este sistema, com comportamento dúctil em rotura. Os varões de FRP, apesar de terem comportamento linear-elástico com rotura frágil, são imunes a fenómenos de corrosão e têm elevada resistência à tração, pelo que são colocados próximo da extremidade mais tracionada da viga. Por seu lado, devido à sua suscetibilidade a fenómenos de corrosão, as armaduras de aço dispostas com maior recobrimento, mas o seu comportamento elasto-plástico assegura a ductilidade necessária aos elementos estruturais reforçados com este sistema híbrido. Tendo em conta que os estribos em aço são os reforços mais suscetíveis a fenómenos de corrosão, pois encontram mais próximos da superfície externa das vigas, são no presente trabalho substituídos por fibras discretas, através da utilização de betão reforçado com fibras (FRC). As fibras podem ainda reduzir a percentagem de armadura de flexão, bem como melhorar a aderência destas ao betão.

A investigação realizada inclui um programa experimental para determinar a lei constitutiva de modo I de fratura dos betões autocompactáveis reforçados com fibras de aço (SFRSCC) desenvolvidos, de diferente classe de resistência e com diferentes percentagens de fibras. Essa lei foi determinada quer recorrendo às recomendações do *fib* Model Code 2010, como por análise inversa, ambas considerando os resultados obtidos em ensaios de flexão sob três pontos de carga em vigas de SFRSCC com entalhe a meio vão. A investigação experimental inclui ainda um programa de ensaios com vigas esbeltas de SFRSCC sob quatro pontos de carga, de forma a analisar o seu comportamento em serviço (abertura e espaçamento de fissuras; flecha) e em estado último (capacidade de carga e modo de rotura).

Para simular o comportamento em serviço e para estados limites últimos, foram desenvolvidos dois modelos analíticos. O primeiro permite determinar a relação momento-curvatura de elementos de FRC com reforço híbrido de flexão, admitindo-se perfeita aderência entre os reforços e o betão envolvente.

O segundo modelo estende as potencialidade do anterior, através da simulação do deslizamento entre armaduras e betão envolvente, pelo que é capaz de estimar a abertura e espaçamento entre fissuras. A boa capacidade preditiva destes modelos é demonstrada através da comparação dos resultados previstos pelos modelos e os registados, quer nos ensaios experimentais realizados, como em resultados experimentais obtidos por outros investigadores.

Contents

List of abbreviations

Abbreviations	
ACI	American Concrete Institute
ASTM	American Society for Testing and Materials
CMOD	Crack mouth opening displacement
EBR	Externally bonded reinforcement
ECC	Engineered cement composite
EN	European Norm
FEM	Finite element method
FRC	Fibre reinforced concrete
FRSCC	Fibre reinforced self-compacting concrete
FRP	Fibre reinforced polymer
FRP/RC	FRP reinforced concrete
GFRP	Glass fibre reinforced polymer
HESF	Hooked end steel fibres
HFR	Hybrid flexural reinforcements
H/FRC	FRC element with hybrid flexural reinforcement
HFR/RC	Reinforced concrete with hybrid flexural reinforcement
HCP	Hydrated cement paste
HPFRC	High-performance fibre reinforced concrete
H/RC	Reinforced concrete element with hybrid flexural reinforcement
IP	Integration point
IFE	Interface finite elements
ITZ	Interface transition zone
JSCE	Japan Society of Civil Engineers
LVDT	Linear variable displacement transducer
NSM	Near-surface mounted technique
PBR	Pure bending region

Continued on next page

Abbreviations (*Continued from previous page*)

PP	Polypropylene
PVA	Polyvinyl alcohol
RC	Reinforced concrete
R/FRC	Reinforced fibre reinforced concrete
R/SFRSCC	Reinforced steel fibre reinforced self-compacting concrete
RILEM	International Union of Laboratories and Experts in Construction Materials
SCC	Self-compacting concrete
SFRC	Steel fibre reinforced concrete
SFRSCC	Steel fibre reinforced self-compacting concrete
SGR	Steel and GFRP reinforced element
SH-FRC	Strain-hardening fibre reinforced concrete
SIFCON	Slurry infiltrated fibre concrete
SLS	Serviceability limit state
SR	Steel reinforcement
steel/RC	Steel reinforced concrete
Stg	Strain gage
S/FRC	Steel reinforced fibre reinforced concrete
S/RC	Steel reinforced concrete
SS-FRC	Strain-softening fibre reinforced concrete
VMA	Viscosity modifying admixture
ULS	Ultimate limit state
UTT	Uniaxial tensile test

List of notations

Notations		
Greek letters		
α	Normalised transition strain	-
α_f	Fibre orientation factor	-
β	Normalised tensile strain of FRC at bottom fibre	-
β_{tu}	Normalised ultimate tensile strain	-
β_1, β_2	Constant parameter	-
γ	Ratio between modulus of elasticity of concrete in compression and tension	-
γ_F	Ratio between modulus of elasticity of FRP bars and concrete	-
γ_s	Ratio between modulus of elasticity of steel bar and concrete	-
δ	Vertical deflection	mm
δ^k	Vertical deflection in *k*th generic step of calculation	mm
δ_{SLS}	Vertical deflection corresponding to the serviceability limit states	mm
ε_c	Strain in concrete	-
ε_{cc}	Compressive strain of concrete	-
$\varepsilon_{cc,p}$	Strain corresponding to the concrete compressive strength	-
$\varepsilon_{cc,p}^{PC}$	Strain at the compressive strength of the plain concrete	-
$\varepsilon_{cc,p}^{SFRC}$	Strain corresponding to the concrete compressive strength in SFRC	-
$\varepsilon_{cc,top}$	Compressive strain of FRC at the top fibre of cross-section	-
ε_{ccy}	compressive yield strain of concrete (or FRC)	-
ε_{ccu}	Ultimate compressive strain of concrete	-
ε_{cm}	Mean strain in concrete (or FRC)	-
ε_{cr}	Cracking strain of concrete	-
ε_{ct}	Tensile strain of concrete	-
ε_{ct1}	Tensile strain of concrete at section 1	-
ε_{ctu}	Ultimate tensile strain of concrete	-

Continued on next page

Notations (*Continued from previous page*)

$\varepsilon_{ct,bot}$	Tensile strain of FRC at the bottom fibre of cross-section	-
$\varepsilon_{ct,p}$	Strain corresponding post-cracking strength of FRC in tension	-
$\varepsilon_{ef,i}$	Effective strain of the generic i^{th} layer	-
$\varepsilon_{ef,r}$	Effective strain of the reinforcement layer	-
ε^{f}	Fracturing strain of concrete	-
ε_{F}	Tensile strain of FRP (or GFRP) bar	-
ε_{F}^{pr}	pre-stressing strain of FRP bars	-
ε_{Fu}	Ultimate tensile strain of FRP (or GFRP) bar	-
ε_{G}^{*}	Strain of GFRP bar in hybrid reinforced concrete beam for which steel is yielded while concrete is crushed simultaneously in compression	-
ε_{Gu}	Ultimate strain of GFRP	-
ε_{r}	Strain of reinforcing bar	-
ε_{r2}	Strain of reinforcing bar at section 2	-
ε_{ry}	Strain at yielding of reinforcing bar	-
ε_{ru}	Ultimate strain in reinforcing bar	-
ε_{sh}	Shrinkage strain	-
ε_{sy}	Yielding strain of steel	-
ε_{su}	Ultimate strain of steel	-
ε_{s}^{pr}	pre-stressing strain of steel bars	-
ε_{sm}	Mean strain in steel reinforcement	-
ε_{trn}	Transition strain of FRC	-
ζ	Normalised yield strain of steel bars	-
η	Normalised post-cracking modulus of FRC	-
θ	Overall rotation of pure bending region	rad
κ_1, κ_2	Constant parameters	-
λ	Normalised compressive strain of FRC at the top fibre of cross-section	-
λ_1	Constant parameter	-

Continued on next page

Notations (*Continued from previous page*)

λ_{cu}	Normalised ultimate compressive strain of FRC	-
μ	Normalised post-cracking residual strength of FRC	-
ν	Normalised tensile strain of FRP bars	-
ν_{fu}	Normalised ultimate tensile strain of FRP bars	-
ξ	Distribution coefficient	-
ϑ	Coefficient related to concrete cover and bar spacing	-
ρ_b^{SR}	Balanced reinforcement ratio in steel reinforced concrete beams	-
ρ_F	Percentage of longitudinal FRP reinforcement	-
ρ_G	Percentage of longitudinal GFRP reinforcement	-
ρ_G^*	Reinforcing ratio of GFRP bar in hybrid reinforced concrete beam for which steel is yielded while concrete is crushed simultaneously in compression	-
ρ_s	Percentage of longitudinal steel reinforcement	-
$\rho_{s,eff}$	Effective percentage of longitudinal steel reinforcement	-
σ_c	Stress of concrete	N/mm^2
σ_{cc}	Compressive stress of concrete	N/mm^2
$\sigma_{cc}^{'}$	Normalised compressive stress of FRC	N/mm^2
σ_{ccy}	Compressive yield strength of concrete (or FRC)	N/mm^2
σ_{cr}	Cracking stress of concrete	N/mm^2
σ_{ct}	Tensile stress of FRC	N/mm^2
σ_{ct}'	Normalised tensile stress of FRC	-
$\sigma_{ct,p}$	Tensile strength of strain hardening fibre reinforced concrete	N/mm^2
σ_F	Tensile stress of FRP bar	N/mm^2
$\sigma_F^{'}$	Normalised tensile stress of FRP bar	-
σ_{Fu}	Ultimate stress of FRP bar	N/mm^2
σ_{Gu}	Ultimate stress of GFRP	N/mm^2
σ_G^*	The actual stress of GFRP bar when steel bar is yielding while concrete is crushed simultaneously in compression	N/mm^2

Continued on next page

Notations (*Continued from previous page*)

σ_r	Stress of reinforcement	N/mm^2
σ_{r2}	Stress of reinforcement at section 2	N/mm^2
σ_{ru}	Ultimate stress in reinforcement	N/mm^2
σ_{ry}	Yielding stress of reinforcement	N/mm^2
σ_R	Constant residual tensile strength	N/mm^2
$\sigma_s^{'}$	Normalised stress in steel reinforcement	-
σ_{sr}	Stress in steel reinforcement at crack initiation	N/mm^2
σ_{st}	Stress in steel reinforcement in cracked section	N/mm^2
σ_{sy}	Yielding stress of steel	N/mm^2
σ_{su}	Ultimate stress of steel	N/mm^2
$\sigma(w)$	Post-cracking tensile stress of FRC	N/mm^2
τ, $\tau(x)$	Shear bond stress	N/mm^2
τ_{bm}	Average shear bond strength	N/mm^2
τ_m	Maximum average bond stress	N/mm^2
τ_R	Residual bond stress	N/mm^2
τ_0	Bond stress at null sliding	N/mm^2
χ	Curvature	1/mm
$\chi_{cr,reg}$	Curvature of cracked region	1/mm
χ_{cr}	Cracking curvature	1/mm
χ_e	Effective curvature	1/mm
χ_i	curvature in the i^{th} generic stage	1/mm
χ_i'	Normalised curvature	-
$\chi_{uncr,reg}$	Curvature of uncracked section	1/mm
ψ	Normalised tensile strain of steel bars	-
ψ_{su}	Normalised ultimate tensile strain of steel bars	-
ω	Normalised compressive yield strain of FRC	-
$\Delta\theta$	Increment of overall rotation of the pure bending region	rad

Continued on next page

Notations (*Continued from previous page*)

Δ_F	Normalised cover thickness of FRP bars	-
ΔL	the extension of the pure bending region area	mm
Δ_s	Normalised cover thickness of steel bars	-

Latin Letter

α_i	Normalised tensile stress corresponding to crack width w_i	-
b	Width of section	mm
b_c	Breadth of concrete in layer with reinforcement	mm
b_i	Width of i^{th} layer	mm
b_{ri}	Equivalent width of reinforcement of i^{th} layer	mm
C	Concrete cover, central distance of the bar from tensile face of section	mm
c_o	Clear rib spacing of the steel bars	mm
C_{eff}	Effective cover	mm
c_F	Concrete cover of FRP bar	mm
c_G	Concrete cover of GFRP bar	mm
c_s	Concrete cover of steel bar	mm
d_b	Diameter of reinforcing bar	mm
d_{cr}	Depth of crack apex	mm
d_{cr}^*	Depth of cracked layer in the beam reinforced by steel and GFRP reinforcing ratio of ρ_G^*	mm
$d_{cr,b}^{SR}$	Depth of layer at which concrete cracking strain (ε_{cr}) is attained for the balanced condition for steel reinforced concrete elements	mm
d_f	Diameter of the fibre	mm
d_F	Depth of FRP layer from the top surface of the cross-section	mm
d_G	Depth of GFRP layer from the top surface of the cross-section	mm
d_i	Depth of i^{th} layer	mm
d_{NA}	Depth of neutral axes	mm

Continued on next page

Notations (*Continued from previous page*)

d_{NA}^{*}	Depth of neutral axes in the beam reinforced by steel and GFRP reinforcing ratio of ρ_G^*	mm
$d_{NA,b}^{SR}$	Depth of neutral axis in balanced condition in steel reinforced concrete elements	mm
$d_{r,i}$	Depth of i^{th} layer with longitudinal reinforcing bars	mm
d_s	Depth of steel layer from the top surface of the cross-section	mm
f_{cc}	Compressive strength of concrete	N/mm^2
f_{ck}	Characteristic values of compressive strength of concrete	N/mm^2
f_{cm}	Average compressive strength of concrete	N/mm^2
f_{cr}	Cracking stress of the concrete	N/mm^2
f_{ct}	Tensile strength of concrete	N/mm^2
f_{ctm}	Average tensile strength of concrete	N/mm^2
$f_{Fts,m}$	Average residual strength of FRC in the serviceability limit state	N/mm^2
$f_{Ftu,m}$	Average residual strength of FRC in the ultimate limit state	N/mm^2
f_{res}	Post-cracking residual strength of concrete	N/mm^2
$f_{Ri,k}$	Characteristic flexural residual strengths	N/mm^2
$f_{Ri,m}$	Average flexural residual strengths corresponding to $CMOD_i$	N/mm^2
f_y	yield strength of steel bar	N/mm^2
G_f	Fracture energy	N/mm
h	Height of cross-section	mm
h_{cc}	Height of concrete compression zone	mm
h_{ct}	Height of concrete tensile zone	mm
h_F	Height of FRP bar from the neutral axes	mm
h_s	Height of steel bar from the neutral axes	mm
h_{sp}	Height of ligament over the notch apex	mm
J_1	Coefficient related to the geometry and modulus of elasticity of reinforcing bar and surrounding concrete	-
k	Normalised neutral axis depth	-
k_{Lcs}^{mcr}	Coefficient for adjustment of crack spacing	-

Continued on next page

Notations (*Continued from previous page*)

k_f	Fibre effectiveness factor	-
k_1 to k_{16}	Constant parameter	-
l_{cb}	Crack bandwidth	mm
l_{ch}	Structural characteristic length	mm
l_d	Development length	mm
L_e	Embedded length	mm
l_f	Length of fibre	mm
$l_{s,\max}$	Maximum transmission length	mm
l_{tr}	Transmission length	mm
n	Axial stiffness ratio between reinforcement and surrounding concrete	-
n_b	Number of bars	-
n_{cr}	Number of cracks	-
n_L	Number of layers constituting the cross-section	-
n_L^c	Number of concrete layers in compressive zone	-
n_L^r	Number of layers with longitudinal reinforcing bars	-
n_L^t	Number of concrete layers in tensile zone	-
$s,\ s(x)$	Slip displacement	mm
s_b	Effective longitudinal bar spacing	mm
s_{fle}	Slip at loaded-end of the bar	mm
s_{le}	Slip at free loaded-end of the bar	mm
s_{mi}	Factor taking into account the influence of steel fibres by considering the number of fibres bridging a crack	$1/mm^2$
s_r	Spacing between each pair of adjacent cracks	mm
s_{rm}	Average crack spacing	mm
$s_{r,\max}$	Maximum crack spacing	mm
$s_{r,\min}$	Minimum crack spacing	mm
$s_{sec.1}$	Sliding at Section 1	mm

Continued on next page

Notations (*Continued from previous page*)

s_{tr}	Spacing between transverse reinforcement	mm
t_i	Thickness of i^{th} layer	mm
u_c	Elongation of concrete	mm
u_r	Elongation of reinforcing bar	mm
w	Crack width	mm
w_d	design value of crack width	mm
w_i^k	Crack width if i^{th} layer at k^{th} stage of loading	mm
w_k	Characteristic value of crack width	mm
w_m	Average crack width	mm
$w_{\max}$	Maximum crack width	mm
w_r	Crack width at the level of reinforcement	mm
w_{SLS}	crack width corresponding to the serviceability limit state	mm
w_u	Ultimate crack width	mm
y_{cc}	Internal arm of compressive force	mm
y_{ct}	Internal arm of tensile force	mm
y_F	Internal arm of tensile force of FRP bar	mm
y_s	Internal arm of tensile force of steel bar	mm
A_c	Area of cross-section of concrete	mm^2
$A_{c,eff}$	Effective area of concrete in tension	mm^2
$A_{Exp}^{(F-\delta)_i}$	Area beneath the experimental force-deflection curves up to the central deflection of δ^k	mm^2
A_F	Area of cross-section of longitudinal FRP reinforcement	mm^2
A_G	Area of cross-section of longitudinal GFRP reinforcement	mm^2
$A_{Num}^{(F-\delta)_i}$	Area beneath the numerical force-deflection curves up to the central deflection of δ^k	mm^2
A_r	Area of cross-section of longitudinal reinforcement	mm^2
A_{ri}	Area of cross-section of longitudinal reinforcement of i^{th} layer	mm^2
A_s	Area of cross-section of longitudinal steel reinforcement	mm^2

Continued on next page

Notations (*Continued from previous page*)

A_{tr}	Area of transverse reinforcement	mm^2
D_f	Diameters of spread concrete	mm
D_F	Deviation history in terms of force	-
D_i	Deformation of the generic i^{th} layer	mm
D_T	Deviation history in terms of toughness	-
E_c	Modulus of elasticity of concrete	N/mm^2
E_{cm}	Average modulus of elasticity of concrete	N/mm^2
E_{cr}	The post-cracking tensile modulus of FRC	N/mm^2
E_F	Modulus of elasticity of FRP	N/mm^2
E_G	Modulus of elasticity of GFRP bar	N/mm^2
E_r	Modulus of elasticity of reinforcement	N/mm^2
E_s	Modulus of elasticity of steel bar	N/mm^2
F	Applied force	N
F_{bond}	The load transmitted along with the interaction length	N
F_{cc}	Force of concrete compression zone	N
$F_{cc,i}^k$	Compressive force of the i^{th} layer of FRC at k^{th} stage of loading	N
F_{ct}	Force of concrete tensile zone	N
$F_{ct,i}^k$	Tensile force of the i^{th} layer of FRC at k^{th} stage of loading	N
F_{cr}	Force corresponding to crack initiation	N
F_{ct1}	Tensile force of concrete at section 1	N
F_{ct2}	Tensile force of concrete at section 2	N
F_F	Force of FRP bar	N
F_F^{pr}	Pre-stressing load of FRP bars	N
$F_{i,m}$	Average force corresponding to the $CMOD_i$	N
F_P	peak load	N
$\bar{F}_p^m$	Average peak load	N

Continued on next page

Notations (*Continued from previous page*)

F_{r1}	Internal force of reinforcing bar at section 1	N
$F_{r1,i}^{k}$	Tensile force of reinforcement at i^{th} layer and at k^{th} stage of loading at section 1	N
F_{r2}	Internal force of reinforcing bar at section 2	N
$F_{r2,i}^{k}$	Tensile force of reinforcement at i^{th} layer and at k^{th} stage of loading at section 2	N
$F_{r,cr}$	The internal force of the reinforcement at cracking initiation stage	N
$F_{r,i}^{k}$	Tensile force of reinforcement at i^{th} layer and at k^{th} stage of loading	N
$F_{r,\sigma-\varepsilon,i}^{k}$	Tensile force of reinforcement at i^{th} layer and at k^{th} stage of loading determined from stress-strain constitutive law	N
$F_{r,\tau-s,i}^{k}$	Tensile force of reinforcement at i^{th} layer and at k^{th} stage of loading determined from the bond	N
F_{SLS}	Force corresponding to the serviceability limit states	N
F_{SLS}^{m}	Average force corresponding to the serviceability limit states	N
F_{Exp}^{k}	Force registered experimentally corresponding to δ^{k}	N
$F^{e}(s_{sec.1})$	The load transmitted along with the elastic interaction length	N
$F_{\max}^{e}$	Maximum force that is transferred through elastic bond region	N
$F^{p}(s_{sec.1})$	The load transmitted along with the plastic interaction length	N
$F_{\max}^{p}$	Maximum force that is transferred through plastic bond region	N
$F^{s}(s_{sec.1})$	The load transmitted along with the softening interaction length	N
$F_{\max}^{s}$	Maximum force that is transferred through softening bond region	N
$F^{f}(s_{sec.1})$	The load transmitted along with the frictional interaction length	N
F_{Num}^{k}	Force determined numerically corresponding to δ^{k}	N
F_{s}	Force of steel bar	N
F_{s}^{pr}	Pre-stressing load of steel bars	N
F_{sy}	Force corresponding to yielding of steel reinforcement	N
F_{sy}^{m}	Average force corresponding to yielding of steel reinforcement	N
$F_{r,\sigma-\varepsilon}$	Internal force of reinforcing bar determined by stress-strain constitutive law	N
$F_{r,\tau-s}$	Internal force of reinforcing bar determined by bond-slip constitutive law	N

Continued on next page

Notations (*Continued from previous page*)

$F_{\delta_{SLS}=10n}^{\alpha\neq1.01}$	The load carrying capacity corresponding to the serviceability limit states obtained for the case $\alpha \neq 1.01$	N
$F_{\delta_{SLS}=10n}^{\alpha=1.01}$	The load carrying capacity corresponding to the serviceability limit states obtained for the case $\alpha = 1.01$	N
$F_{\delta_{SLS}=10n}^{\mu\neq0.0}$	The load carrying capacity corresponding to the serviceability limit states obtained for the case $\mu \neq 0.0$	N
$F_{\delta_{SLS}=10n}^{\mu=0.0}$	The load carrying capacity corresponding to the serviceability limit states obtained for the case $\mu = 0.0$	N
I_{cr}	Moment of inertia of cracked section	mm^4
I_e	Effective moment of inertia	mm^4
I_g	Moment of inertia of gross section	mm^4
I_{uncr}	Moment of inertia of uncracked section	mm^4
J_1	Constant parameter	-
K_{tr}	Transverse reinforcement index	-
L_{ch}	Characteristic length	mm
L_{cr}	The distance between two furthest crack at cracking stabilised stage	mm
L_{cs}	Spacing between cracks	mm
L_p	Length of perimeter of reinforcing bar	mm
L_{PBR}	Length of pure bending region	mm
L_{span}	Length of span	mm
L_{ss}	length of the beam's shear span	mm
L_{tr}	Transition length	mm
$L_{tr}^{e}(s_{sec1})$	Bond transfer length corresponding to the elastic region	mm
$L_{tr}^{f}(s_{sec1})$	Bond transfer length corresponding to the frictional region	mm
$L_{tr}^{p}(s_{sec1})$	Bond transfer length corresponding to the plastic region	mm
$L_{tr}^{s}(s_{sec1})$	Bond transfer length corresponding to the softening region	mm
M_a	Maximum applied moment	N.mm
M_{cr}	Cracking bending moment of cross-section	N.mm
M_F^{pr}	Bending moment corresponding to pre-stress load of FRP bars	N.mm

Continued on next page

Notations (*Continued from previous page*)

M_i	Bending moment in the i^{th} generic stage	N.mm
M_i'	Normalised bending moment in the i^{th} generic stage	N.mm
M_s	Bending moment at serviceability limit states	N.mm
M_s^{pr}	Bending moment corresponding to pre-stress load of steel bars	N.mm
R_r	Ratio of projected rib area normal to the bar axis to the product of nominal bar perimeter and centre-to-centre spacing of ribs	-
R_t	Area to spacing of ribs of reinforcement	-
T_{50}	Time was taken by mixture to spread up to a diameter of 500 mm	s
V_f	Volume fraction of fibres	-

List of Figures

Chapter 2: Literature Review

Chapter 4: Moment-Curvature Approach to Evaluate Flexural Response of R/SFRSCC Elements

Appendix A: Crack evolution in the SFRSCC beams reinforced by a steel bar

Appendix B: Crack evolution in tested SFRSCC beams reinforced by steel and GFRP bars

List of Tables

Chapter 2: Literature Review

Chapter 3: Experimental Evaluation of Flexural Response of R/SFRSCC Elements

Chapter 4: Moment-Curvature Approach to Evaluate Flexural Response of R/SFRSCC Elements

Chapter 5: Prediction of Crack Width and Spacing in R/FRC Flexural Elements

Chapter 1

Introduction

1.1 Motivation and objective

Concrete is the most-consumed manufactured material in today's world with a long history return to the when cementitious components were using to construct aqueducts in many ancient civilizations. During the last decades, the demand for concrete has grown with industrialisation, so that the worldwide production of concrete is believed revolving around 20 billion tonnes annually (Deluce and Vecchio 2013). When compared with steel material, concrete is neither as strong nor as tough. Nevertheless, the widespread usage of concrete is ascribed to its some peerless properties such as excellent resistance to water, plastic consistency in fresh state and consequent high potentiality to be formed into a variety of shapes and sizes as well as abundance and availability of its main components, which makes concrete the cheapest and most readily material for engineered structures. The latter, however in its turn is the origin of significant environmental criticisms. Nowadays, concrete dependent industries exploit the vastest amount of natural resource

and responsible for emitting up to 8 percent of global greenhouse gases (Scrivener and Kirkpatrick 2008).

Nevertheless, the durability of reinforced concrete structures remains a controversial subject. Due to its microstructure, concrete is inherently vulnerable in tension. Over the years, this weakness has been remedied by the use of steel reinforcements. This traditional treatment, however, comprises its own consequences. Steel is susceptible against corrosion and must be protected from environmental hostile agents by allocating a cover of concrete of proper thickness, which leads to the increase in height of cross-section. In this scheme, however, the early stage cracking is practically inevitable in plain concrete cover, which like micro streams facilitate traverse of aggressive agents toward the steel reinforcement leading to corrosion of steel and negative circumstances threaten the serviceability and safety of the structure.

The numerous researches conducted so far, to improve durability indexes of reinforced concrete structures can be overviewed generally, into two principal approaches. The first one comprises partially or entirely substitution of steel reinforcement by the ones of more significant resistance against corrosion, such as various types of fibre reinforced polymer (FRP) bars with fundamental differences in material properties or mechanical interaction to concrete. Therefore, substantial modifications should be mobilised in design approach and constitutive laws when FRP reinforced concrete structure is aiming.

The second approach to enhance the durability of concrete structures is aiming to control cracking in concrete. It is extensively documented that corrosion of steel reinforcement is considerably overcome when maximum crack width of the concrete cover is kept small. In this regard, the improvement of the post-cracking response of concrete is crucial which can be achieved by the use of discrete fibre in concrete. The randomly distributed fibres confer to the concrete the ability to form multiple cracks, resulting in a significant increase in energy absorption capacity and a pseudo-ductile behaviour owing to the fibre pullout mechanisms. Recent studies (Barros *et al.* 2015a, Mazaheripour *et al.* 2016b, Salehian and Barros 2017) have shown the potentialities of FRC as a supplement or even as a replacement of conventional longitudinal steel bars for elements failing in bending, mainly when having a strain-hardening character

(Mazaheripour *et al.* 2016b, Barros *et al.* 2015a, Salehian and Barros 2017). In this regard, it is fundamental to develop an integrated approach to mobilise accurately the post-cracking response of FRC, in a material point of view, for predicting the load carrying capacity of reinforced FRC (R/FRC) elements. Prediction of cracking behaviour of R/FRC remains a crucial aspect in such a comprehensive approach. Experimental studies have revealed the bar-to-concrete interaction and consequently, the tension stiffening effect tends to be improved by the increase in reinforcing contribution of fibres (Oliveira Júnior, 2016 #503). However, the scarcely available design approaches for prediction of cracking behaviour of R/FRC members are uncomprehensive and in some cases comprise arguable predictive performances.

1.2 Scope of the research

The present work aims to develop innovative numerical/analytical models to predict the force-deflection relationship and cracking behaviour of concrete elements failing in bending and reinforced by a hybrid-reinforcing scheme. Such an effective reinforcement solution in terms of durability and structural performance is obtained by placing the FRP bars near the outer surface of the tensile zone and steel bars at an inner level of the tensile zone. In this scheme, the steel bar provides a significant contribution in terms of ductility and stiffness and assure the safety of the structure in the case of a fire occurrence and the consequent loss of FRP reinforcing capacities. The reinforcing contribution of fibres is mobilised to eliminate conventional steel stirrups and concurrently to reduce the ratio of longitudinal reinforcements. In the aimed models, the post-cracking response of FRC is taken into account through two fundamental approaches proposed to simulate fracture mechanism of plain and fibrous concrete; the smeared crack and discrete crack approaches mobilised, respectively, into developed moment-curvature and moment-rotation models. Predictive performance of the models is assessed in a comprehensive experimental programme.

1.3 Outline of the dissertation

Chapter 2 aims to explain concrete morphology and overview various approaches proposed to reinforce concrete. Fundamental aspect relative to fibre reinforced concrete

is explained and fundamental approaches for simulation of fracture mechanism of plain and fibrous concrete is detailed. Applicable methods adopted to characterise the post-cracking response of FRC are also presented in this chapter. Furthermore, the concept of interaction between reinforcing bar and concrete is explained and relative key factors are overviewed.

A comprehensive experimental programme is introduced in details in chapter 3. The tes pogramme was conducted to evaluate load carrying capacity and cracking behaviour of flexural beams reinforced by a hybrid-reinforcing scheme. This study has been fulfilled by eighteen beams categorised in six series made of three types of steel fibre reinforced self-compacting concrete distinguished by different concrete strength classes and volume fraction of fibres. Two longitudinal reinforcing scheme is used in the tested beams.

In chapter 4 a closed-form solution is developed based on smeared crack approach for fibre reinforced concrete (FRC) elements reinforced with longitudinal steel and FRP bars failing in bending and is compared to the experimental results presented in the literature and the ones presented in Chapter 3. The proposed model is capable of analysing the mutual influence of the parameters that define the softening/stiffening character of an FRC as well as the pre-stressed percentage of longitudinal reinforcement, on the behaviour of R/FRC beams.

In chapter 5, is developed an integrated approach for the prediction of crack width and spacing in FRC flexural elements reinforced by longitudinal steel and FRP bars. The model is based on the discrete crack approach capable to take into consideration the post-cracking response of FRC in terms of stress-crack opening relationship and mobilises the shear bond-sliding characteristics of steel- and FRP-to-concrete interaction. The predictive performance of the proposed approach is compared to the experimental results recorded in the present research and the one presented in the literature. Finally, the significant conclusions and some suggestion for the future researches is presented in chapter 6.

Chapter 2

Literature Review

2.1 Introduction

This chapter performs a literature review on the most relevant key parameters affecting the load carrying capacity and cracking behaviour of flexurally reinforced concrete (RC) and fibre reinforced concrete (FRC) elements. The inherent vulnerability of concrete in tension is first ascribed to the structure of concrete, and the relevant conventional remedies are discussed. In this regard, the mechanism of crack formation in concrete and, particularly, in FRC is explained, and current methods for evaluating mechanical material properties of plain and fibrous concrete are detailed. The literature on concrete-to-reinforcing bar interaction is reviewed later, which comprises different local bond models proposed for steel and fibre reinforced polymer (FRP) bar embedment in plain and fibrous concrete, and finally, different approaches for predicting the cracking behaviour of RC and R/FRC flexural elements are introduced.

2.2 Morphology of concrete

Plain concrete is categorised as a two-phase composite comprising the aggregate and the bulk cement paste, which interconnect to each other through a so-called interfacial transition zone (ITZ). A wide range of 10 to 75 microns is reported for the thickness of the ITZ (Wei *et al.* 1986, Li and Stang 1997). The microstructure of the ITZ is schematised in Figure 2.1, according to which the ITZ contains two main features: a very thin surface layer of calcium silicate hydrate surrounding the aggregate, and greater concentration of larger calcium hydroxide crystals and needles of calcium sulphoaluminate (ettringite) than in the bulk cement paste.

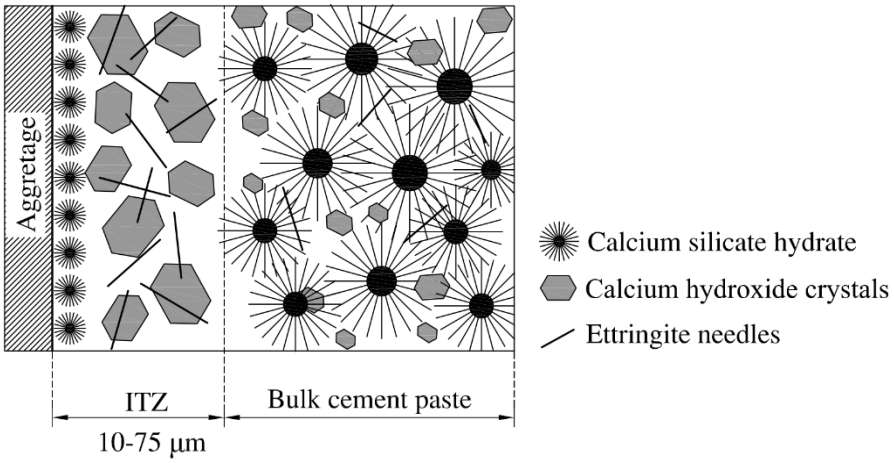

Figure 2.1: Features of the interfacial transition zone (ITZ) at the paste-aggregate interface (adopted from Li (2011))

The strength of the ITZ strongly depends on the volume and size of voids present. Even for a low water to cement ratio concrete, at premature ages, the volume and size of voids in the ITZ are larger than in the bulk cement paste because the cement grains cannot pack as efficiently near the surface of the aggregate due to the so-called wall effect. Besides, water to cement ratio increases next to the aggregates due to the hydrophilic phenomenon. Consequently, the ITZ is weaker in strength than the bulk cement paste. Therefore, the density of the stratum of calcium hydroxide crystals of the ITZ tends to decrease towards the surface of aggregate (Weerheijm 2013). The large calcium hydroxide crystals and the less content of calcium silicate hydrate formed in the ITZ lead to less adhesion capacity and consequently, the weak van der Waals forces of attraction. The presence of microcracks in the ITZ is another major and responsible factor for the

weakness of the ITZ. The differential movements occurring between aggregates and hydrated cement paste, either on drying or on the cooling of concrete, induce tensile stresses that form microcracks in the ITZ even before the material has been submitted to external loading. The amount of microcracks in the ITZ depends on the aggregate size and grading, water to cement ratio, the degree of consolidation of fresh concrete, curing conditions, environmental humidity and thermal history of concrete. Due to relatively weaker strength, the ITZ can be assumed as the strength-limiting phase in concrete that affects the mechanical properties and failure mode of concrete in compression and tension (Diamond and Huang 2001).

The compressive behaviour of plain concrete of moderate strength class can be identified by four distinct consecutive stages based on the initiation and propagation of cracks, as depicted in Figure 2.2 (Shah *et al.* 1995). When the stress is below about 30% of the peak stress, which can be considered as the concrete compressive strength (f_{cc}), the initiation of internal cracks is significant. In this stage (stage I in Figure 2.2) the stress-strain relationship is approximately linear. When the stress ranges between 30% and about 80% of the peak stress (stage II) the initial cracking at the ITZ starts to propagate and new micro-cracks develop. At approximately 60% of the peak stress, cracks at the cementitious matrix start to develop too. However, all these cracks are isolated and randomly distributed over the material volume. In stage III and for the stress ranging between 80% and 100% of the peak stress, all small internal cracks become unstable and start to localise into major cracks. The crack growth is stable until the peak load is reached, which means that cracks only propagate if the load is increased. For deformation above the corresponding to the peak stress (stage IV in Figure 2.2), the major cracks continuously propagate, even though the load is decreasing. Unloading (snap-back) may occur at the material outside the damage zone, while the deformation at the localised damage band keeps increasing.

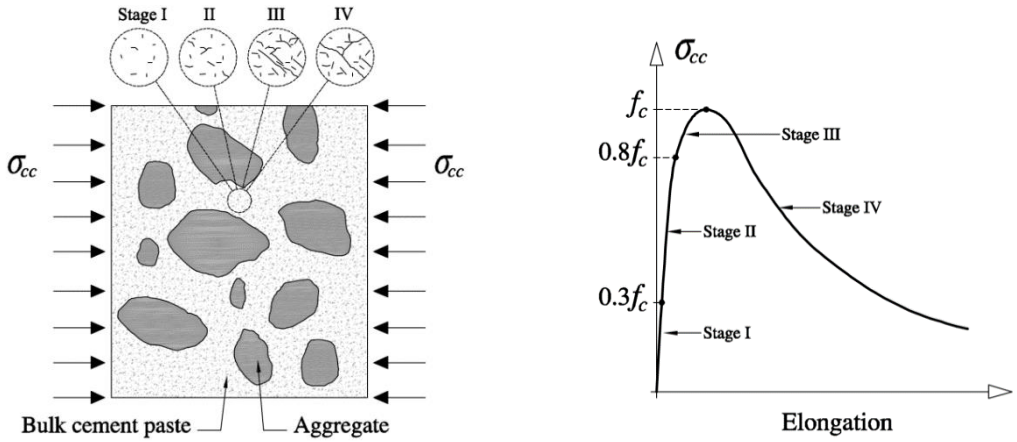

Figure 2.2: (a) Cracking mechanism of plain concrete in compression, (b) compressive stress-elongation response

The ITZ's weakness is much more pronouncedin tensile properties of concrete. As schematised in Figure 2.3, the direction of crack propagation in uniaxial tension is dominantly transverse to the stress direction, and consequently, relatively less energy is needed for the initiation and growth of cracks in the matrix due to the weakness of the ITZ. The failure in tension occurs with the formation of fewer numbers of cracks than in a failure in compression. Rapid propagation of the crack system, consisting of pre-existing cracks at the ITZ and newly formed cracks in the matrix, leads to the brittle failure of concrete in tension with significant less strength of 8 to 10 times of its compressive strengths (Raphael 1984).

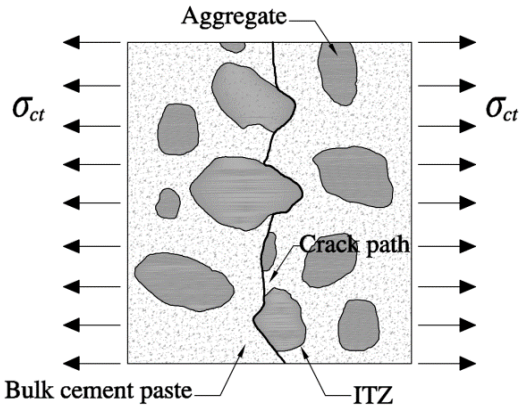

Figure 2.3: Cracking mechanism of plain concrete in tension

2.3 Longitudinal reinforcing steel bar

The tensile reinforcement of concrete by steel bars is a traditional remedy that has been widely used since the second half of the nineteenth century. The benefits ensured by the relatively high concrete compressive strength are combined with the tensile strength of steel reinforcement leading to a significant improvement of the load carrying capacity of the reinforced concrete (RC) structures. Nonetheless, corrosion of the steel reinforcement (SR) in reinforced concrete structures represents the main material pathology responsible for the significant amount of resources spent in the rehabilitation of the built patrimony. The corrosion of SR can be caused by a deficient concrete quality, a too-small concrete cover, inadequate construction practices, design inaccuracies, improper maintenance of the buildings, and an unexpectedly high level of aggressiveness of environmental agents. Consequently, due to the SR corrosion, the sound cross-sectional area of SR decreases, the concrete cover spalls, the concrete cross-sectional area diminishes, the bond between the steel bar and surrounding concrete deteriorates. These can lead to a significant deterioration of the load carrying capacity of an RC member, which can affect the structural safety indexes. Therefore, all the strategies that can prevent the occurrence of corrosion of the reinforcement systems applied in concrete structural elements are of paramount importance in terms of decreasing the maintenance costs of these structures. This contributes decisively to the development of a new generation of extremely durable and sustainable RC buildings.

2.4 Longitudinal reinforcing FRP bar

During last decades, the substitution of conventional steel reinforcement by fibre reinforced polymer (FRP) bars has been studied in numerous researches (Toutanji and Saafi 2009, Wang and Belarbi 2013, Mousa *et al.* 2018, Ribeiro *et al.* 2018). This is an effective remedy to prevent the corrosion problems of steel reinforcement and to improve the durability of concrete structures of near marine environments, near the ground, in the chemical and other industrial plants, and in thin structural elements. In fact, in comparison with steel, FRP materials have resistance against corrosion and their strength-to-weight ratio is noticeable (ACI 440R-07 2007). Furthermore, they are non-electrical conductive

and non-magnetic materials. Nevertheless, the major obstacles of the application of FRP bars as a sole reinforcing material for concrete structures are the relatively high initial costs, low modulus of elasticity, lack of ductility (linear stress-strain diagram up to rupture with no discernible yield point), and absence of well-consolidated design guidelines (Toutanji and Saafi 2009, Abdalla 2002, Alsayed *et al.* 2000). When compared with steel, the cost-comparative FRPs have a relatively low elastic modulus with considerably different bond properties in concrete (Abdalla 2002, Bakis *et al.* 2002, Tian and Yuan 2007). These often lead to a larger deflection and wider cracks in FRP reinforced concrete (FRP/RC) beams, so that the serviceability requirements of FRP/RC are often predominant (Almusallam 1997, Masmoudi *et al.* 1998). In addition, as a result of larger crack width and a smaller compressive stress blocks when using FRP bars for the flexural reinforcement, the shear capacity of FRP/RC beams is smaller than steel reinforced concrete (S/RC) beams of the same reinforcement ratio (ACI 440R-07 2007).

2.5 Hybrid longitudinal reinforcing scheme

In an attempt to overcome the drawbacks relative to the sole usage of steel or FRP bar as reinforcement of concrete, a combination of FRP and steel reinforcements is proposed in some literature for concrete elements (Aiello and Ombres 2002, Leung and Balendran 2003, Mazaheripour 2015, Mazaheripour *et al.* 2016a). In such a hybrid flexural reinforcing (HFR) scheme, an effective solution in terms of durability is obtained by placing the FRP bars near the outer surface of the tensile zone and steel bars at the inner level. Experimental evidence revealed that the deflection, crack width, and crack spacing of HFR/RC beams are typically smaller than that of FRP/RC beams (Tian and Yuan 2007, Aiello and Ombres 2002). In terms of the structural behaviour of the concrete member, the presence of the steel bars in this hybrid reinforcement system contributes significantly to enhance the ductility and stiffness. The few tests that were executed confirmed this idea. In fact, Tian and Yuan (2007) concluded that the deflection of concrete beams reinforced with FRP and steel bars was smaller than that of beams reinforced just with glass fibre reinforced polymer (GFRP). Aiello and Ombres (2002) also verified that, in comparison with beams exclusively reinforced with FRP bars, the presence of steel bars reduces the crack width and crack spacing values. These studies

also indicate that the hybrid longitudinal reinforcement system (steel and FRP) represent a competitive solution when the long-term costs of repairing activities are also taken into account. In the hybrid longitudinal reinforcing scheme, FRP and steel bars can be applied with a certain pre-stress to optimise their reinforcing capabilities. According to Nordin and Täljsten (2006), for the strengthening of reinforced concrete beams, there are four advantages when using pre-stressed FRP: better utilization of the strengthening material, smaller distance and width of cracks in concrete, unloading of the steel reinforcement, and higher steel yielding loads. Furthermore, with the pre-stress, a significant increase regarding load carrying capacity for deflection levels corresponding to the serviceability limit states can be obtained (Barros 2009). Some models were also developed in the literature to simulate the tension stiffening behaviour of fibre reinforced concrete (FRC) elements reinforced by hybrid fibre reinforced polymer (FRP) and steel bars (Mazaheripour *et al.* 2016a).

2.6 Fibre reinforced concrete

During the last decades, continuous advances have been made in concrete technology, leading to the advent of various kinds of micro-fillers such as fly ash and silica-fume that have been employed to densify the microstructure of concrete, with noticeable enhancements in terms of strength and durability. Furthermore, considerable scientific research has been conducted on the rheological properties of the fresh concrete, in parallel to the development of novel additives, such as superplasticizers and viscous admixture modifier employed to produce flowable concrete with a reduced water-to-cement ratio, currently called as self-compacting concrete (SCC) (Okamura 1997, Okamura and Ouchi 2003). The advent of fibre reinforced concrete (FRC) is also one of the advances in concrete technology, leading to a new generation of cement-based materials with several advantages regarding plain concrete. In particular, by merging the benefits of the fibre reinforcement to those derived from the self-consolidating character of the self-compacting concrete, a high-performance structural material is obtained designated by fibre reinforced self-compacting concrete (FRSCC) (Groth 2000, Grünewald 2004). The idea of reinforcing the brittle concrete with the addition of steel splinters was firstly patented by Bernard in 1874 (Maidl 1995). This idea, in fact, was inspired by an ancient

construction technique with a 3500-year-old history, when brittleness of sun-baked mud bricks was mitigated by the addition of organic or mineral fibres. Such a century-old structural construction technique is still present in some heritage. This technique is, even so, a competitive approach in the case of low-cost rural housing applications (Aziz *et al.* 1981, Balaguru and Shah 1985). The asbestos cement is the first widespread use of fibre in the cementitious composite, which was developed in about 1900 with the invention of the so-called Hatschek technology for the production of plates for roofing and pipes.

The interest in concrete reinforced with fibres grew noticeably when the enhanced properties of FRC were highlighted by Romualdi (Romualdi and Batson 1963, Romualdi and Mandel 1964). The discrete and randomly distributed fibres provide additional resistance to the opening of concrete microcracks by the so-called bridging mechanism which leads to a significant improvement of the fracture toughness, ductility, impact resistance, and fragmentation of concrete (Shah and Rangan 1971, di Prisco *et al.* 2004, Li *et al.* 1993, Naaman and Shah 1976, Naaman 2000, Barros *et al.* 2005). The bridging mechanism of fibres can equally contribute to enhance the shear resistance of concrete elements (Santos *et al.* 2008, Barros *et al.* 2004a, Casanova *et al.* 1997, Meda *et al.* 2005). In particular, when a high strength concrete is used and when beams are relatively shallow, fibres noticeably reduce the width of shear cracks and improve the durability of concrete. According to Wang and Belarbi (2013), an improvement of 30% of the durability index of RC beams was achieved by the addition of 0.5% volume fraction of fibres.

In the structural level, the influence of fibres on the reduction of shear cracks and improvement of the shear resistance of FRC beams is noticeable (Santos *et al.* 2008, Barros *et al.* 2004b, Susetyo *et al.* 2011). In shallow reinforced FRC (R/FRC) beams, steel stirrups can be replaced by reinforcing effects provided by the fibres, which accelerates the construction process and increases the durability of structure (Casanova *et al.* 1997). The discrete fibres also contribute to reduce the deflection of R/FRC beams under service loads and to increase the load carrying capacity at the ultimate limit states (Taheri *et al.* 2011, Barros *et al.* 2012). Experimental and numerical investigations revealed that the post-cracking behaviour of FRCs effectively improves the tension-stiffening behaviour of R/FRC elements (Abrishami and Mitchell 1997, Lee *et al.* 2013), which reduces the width and spacing of cracks (Bischoff 2003, Oliveira Júnior *et al.* 2016)

and can provide a higher post-yielding strength in S/FRC tensile members (Jordon and Frank 2013). In the study carried out by Meda *et al.* (2005), a reduction of 20% of crack spacing in FRC beams was observed when compared to reference beams of conventional concrete with and without stirrups. Presently, an extensive range of fibres of various geometrical, mechanical, physical and chemical properties have been considered and used for the reinforcement of cementitious materials (Brandt 1994), as summarised in Table 2.1. Nevertheless, steel fibres are the most commonly used type fibres in practical applications.

Table 2.1: Typical properties of fibres used in FRC composites (Bentur and Mindess 2007)

Fibre	Diameter [μm]	Specific gravity [-]	Modulus of elasticity [GPa]	Tensile strength [GPa]	Ultimate elongation [%]
Steel	5-500	7.87	200	0.5-2.0	0.5-3.5
Glass	9-15	2.6	70-80	2-4	2-3.5
Crocidolite Asbestos	0.02-0.4	3.4	196	3.5	2.0-3.0
Chrysotile Asbestos	0.02-0.4	2.6	164	3.1	2.0-3.0
Polypropylene (PP)	20-400	0.9-0.95	3.5-10	0.45-0.76	15-25
Poly Vinyl Alcohol (PVA)	14-600	1.31	25-40	0.88-1.60	6-10
Aramid (Kevlar)	10-12	1.44	63-120	2.3-3.5	2-4.5
Carbon (high strength)	8-9	1.6-1.7	230-380	2.5-4.0	0.5-1.5

The fracture mechanism of fibrous concrete is noticeably affected by the pullout response of fibres through the concrete matrix (Naaman *et al.* 1991, Taerwe and Gysel 1996). The pullout response of fibres, in turn, is influenced by the shape and geometry of fibres and structure of the matrix. Regarding smooth fibres, the pull out response is significantly affected by the elastic and frictional bond between the fibre and concrete, which are both improved by the refining of the microstructure of the cementitious matrix and consequent decreasing in its porosity. In conventional concrete, however, the chemical adhesion and frictional bond are negligible when a smooth fibre is utilised. In such a case, the mechanical anchorage of deformed fibres is required for offering extra resistance to crack opening (Banthia and Trottier 1994, Li and Stang 1997, Naaman and

Najm 1991). In this regard, deformed steel fibres of various types are utilised in concrete, some of which are schematised in Figure 2.4.

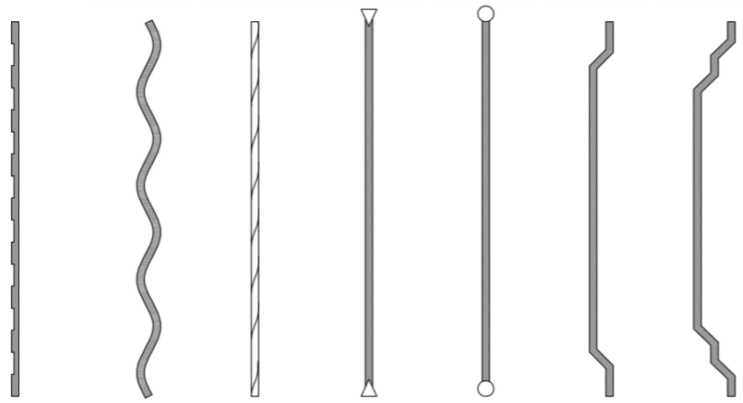

Figure 2.4: Various types of deformed steel fibres: (a) Indented, etched or roughened, (b) crimped or corrugated, (c) polygonal twisted, (d) flat-ended, (e) buttons-ended, (f) hooked ended, and (g) double hooked ended (adopted from Salehian (2015))

2.7 Mechanism of crack formation and propagation in the cementitious composites

Evaluating the mechanical properties of the cementitious composites based on fracture mechanics is a conventional approach explored in the literature. The advent of fracture mechanics turns back to World War I when Griffith (1921) presented his theory to explain the failure of materials. In this theory, it was assumed that formed crack becomes immediately stress-free up to the crack tip (Figure 2.5a) and the product of the square root of the crack length and the stress at the fracture is assumed constant. Experimental evidence proved the accuracy of this approach in the case of brittle materials, behaving according to the linear elastic fracture mechanics, like glass. Nevertheless, the Griffith theory was ignored for about three decades. The reason was that the energy required to cause a fracture in structural ductile materials is appreciably larger than that predicted by the Griffith theory. Furthermore, the non-linear response of material cannot be explained by this approach.

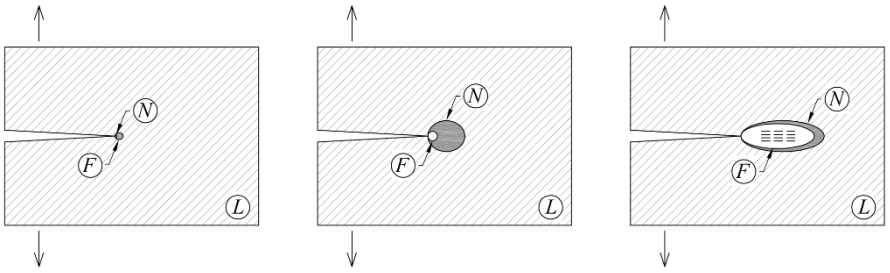

(a) (b) (c)

Figure 2.5: Typical representation of linear (L), non-linear (N) and fracture process (F) zones in Fracture of (a) brittle, (b) ductile, and (c) quasi-brittle materials (adopted from Bažant (1992)

In the late sixties, Irwin (1957) modified the Griffith theory by considering a nonlinear zone at the tip of a crack growing in ductile material, as depicted in Figure 2.5(b) and 2.5(c). The size of this zone extends by the increase in the applied load, while the elastically strained material behind the crack tip is unloading. Unlike the brittle materials, the nonlinear zone is large in ductile materials (Figure 2.5b), leading to plastic hardening or perfect plastic behaviour. In the case of ductile materials, in a very small part of the nonlinear zone, the fracture process zone forms in the vicinity of the crack apex. In the case of quasi-brittle materials, like concrete, the fracture process zone is significantly large and practically occupies the entire nonlinear zone as depicted in Figure (2.5c). This is attributed to the heterogeneity inherent of concrete and the presence of micro-cracks ahead of the crack tip. In fact, the existence of the fracture process zone in front of a crack constitutes the intrinsic reason for the size dependence of the fracture parameters in quasi-brittle materials. In this case, the plastic response of ductile materials is substituted by the strain-softening behaviour in tension where the stress normal to the crack plane decreases with the increase in strain (Zhang and Wu 1999). The fracture process zone of quasi-brittle materials is considered as a so-called “cohesive zone” in the literature (Dugdale 1960, Barenblatt 1959, Barenblatt 1962).

Hillerborg *et al.* (1976) have taken advantage of the concept of the cohesive zone in their “fictitious crack model”. In this approach, the fracture process zone together with the part of the localised crack where aggregate interlock is present, are substituted by a spurious crack as revealed in Figure 2.6(a).

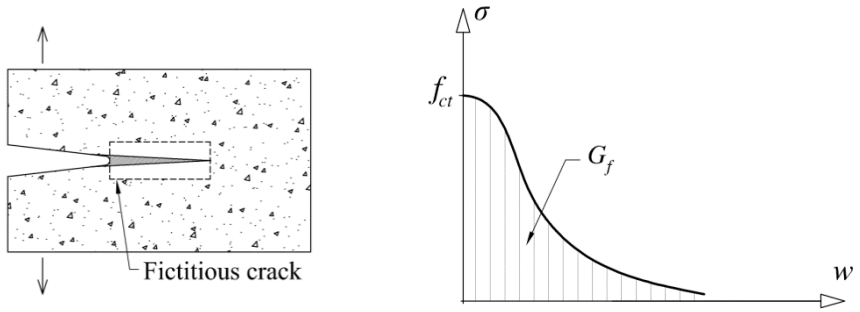

(a) (b)

Figure 2.6: (a) Fictitious crack at the tip of growing crack and (b) stress-crack opening constitutive laws assigned to the fictitious crack

The fictitious crack model of Hillerborg and his collaborators has been widely used in finite element analysis of the concrete fracture by using interface finite elements (IFE) in the simulations based on the finite element method (FEM). The constitutive law of the IFE simulates the crack opening process, by using a stress-crack opening $(\sigma - w)$ relationship (Figure 2.6b), where $\sigma(w)$ is the traction applied to the crack surfaces as a function of crack opening w, ranging between the tensile strength of concrete (f_{ct}) at the crack apex and zero at the ultimate crack widening. According to the literature, a bilinear softening curve suffices to characterise the fracture of concrete (Guinea *et al.* 1993). The fracture energy of concrete is defined by the area beneath the $\sigma - w$ curve:

$$G_f = \int_0^{w_u} \sigma(w)dw \tag{2.1}$$

The fictitious crack model was later used by Hillerborg (1980) to analyse the fracture of fibre reinforced concrete, as adopted by other authors to describe the bridging effects of fibres in fibre reinforced concrete (Lange-Kornbak and Karihaloo 1998, Li 1992). Due to the contribution of fibres in the pullout mechanism, the post-cracking behaviour of FRC is improved. In this regard, the higher the volume fraction of fibre, the higher the fracture energy was obtained in experimental research (Kooiman 2000). Nevertheless, since the length of fibres bridging the crack is significantly larger than the crack opening, the ultimate crack width (w_u) in FRC is not strictly relevant in a structural point of view. Therefore, the concept of fracture energy defined by Equation (2.1) may lose its meaning

from a practical point of view. For this reason, the actual shape of $\sigma - w$ curve in the range of acceptable crack opening (e.g. 0-1.5 mm) becomes more important than G_f (RILEM TC 162-TDF 2002).

The fracture of cement-based materials can also be analysed by a stress-strain relationship. This approach, firstly advanced by Bažant (Bažant and Oh 1983), is based on the fact that the microcracks are randomly distributed along with the fracture process zone, and growing the crack is roughly straight. Therefore, concerning smeared cracks band (or crack bandwidth) of l_{cb} in the fracture process zone (Figure 2.7a), the crack widening can be described by an equivalent strain so-called fracturing strain (ε^f) (Figure 2.7b). The concept of stress-strain relationship is quite familiar for the engineer. It is also fairly convenient for computer programming of the finite element method.

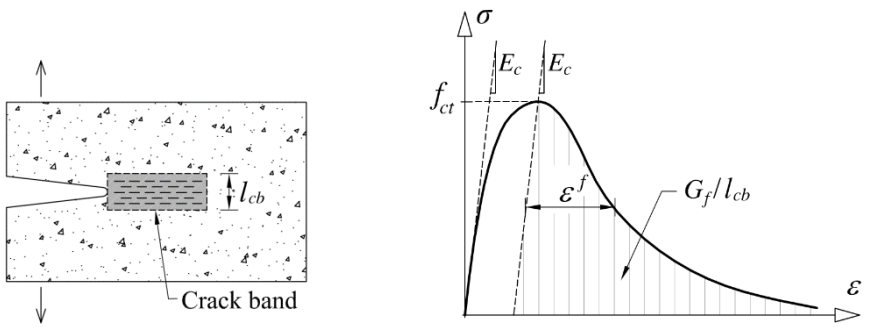

(a) (b)

Figure 2.7: (a) Crack band model at the tip of growing crack and (b) stress-strain diagram assigned to the crack band

In the crack band model, it is fundamental to adjust the material parameters controlling the smeared cracking such that the amount of energy dissipated during failure becomes independent of the mesh size. Therefore, the crack bandwidth is determined on the basis of the finite element size projected onto the direction of the maximum principal strain for the case of tensile cracking (Bažant 1984). Consequently, the crack opening displacement (w) is related to the fracturing strain (ε^f) through the following equation:

$$w = \varepsilon^{f} \, l_{cb} \tag{2.2}$$

For the structural elements, the crack bandwidth can be considered the same as the corresponding structural characteristic length (l_{ch}) of the element (RILEM TC 162-TDF 2002, *fib* Model Code 2010 2011) which is an indication of spacing between two adjacent cracks. l_{ch} is influenced by numerous parameters, such as compressive strength class of concrete, geometric properties of cross-section, percentage of longitudinal or transversal reinforcement, and the prescribed load level. Accordingly, there is not a consensus for determining l_{ch}. For FRC flexural elements without longitudinal reinforcement, a constant value of l_{ch} is often proposed in the literature equal to $h/2$ (RILEM TC 162-TDF 2001, Kooiman 2000, Iyengar *et al.* 1998, Massicotte 2004), $2h/3$ (AFGC-SETRA 2002), h (*fib* Model Code 2010 2011, CNR-DT 204 2006) or $2h$ (Strack 2008), where h is representative of the height of cross-section. In some literature, l_{ch} in R/FRC flexural elements is related to the level of prescribing load (Casanova and Rossi 1997, UNI 11188 2004) due to the fact that spacing between cracks changes by variation of the load level. Nevertheless, the minimum value between $h/2$ (Massicotte 2004) or depth of neutral axes (*fib* Model Code 2010 2011), and the average crack spacing (s_{rm}) is ordinarily considered for the derivation of characteristic length in R/FRC elements. s_{rm} can be estimated by following the approach represented by the *fib* Model Code 2010 (2011). The adopted magnitude of the characteristic length in a numerical modelling may affect deformational results and flexural capacity of the simulated element, whereas, by the increase in l_{ch}, the resisting bending moment reduces while a wider crack is predicted (Montaignac *et al.* 2012). Therefore, a large value l_{ch} is more appropriate when the maximum crack width at a localized crack is aiming, whereas, the smaller value of the characteristic length is recommended when the average crack spacing is concerned.

2.8 Characterization of the post-cracking response of FRC

2.8.1 Uniaxial tensile test

The uniaxial tensile test, when displacement controlled, represents the unique approach that directly yields the tensile constitutive laws of plain and fibre reinforced concrete (Hordijk 1991, Van Mier and Van Vliet 2002). According to Naaman and Reinhardt (2006), fibre reinforced concretes can be classified regarding the post-cracking responses in uniaxial tension: strain-softening and strain-hardening FRCs schematically compared in Figure 2.8. In the case of strain-softening FRCs, after initiation of the first crack at the stress that can be considered equal to the tensile strength of the cement matrix (f_{ct}), the tensile bearing capacity of the element is reduced abruptly by widening the localised crack until fibres efficiently bridge the crack by undergoing to the pullout mechanism. This mechanism leads to progressive deterioration of the tensile stress by widening of crack. Afterwards, and when debonding of fibres through the concrete matrix is fulfilled, the second drop may occur in stress-strain response up to ultimate separation. In fact, the increase in post-cracking strength of the strain-softening type FRCs is unexpected. Alternatively, significant improvement of toughness and increase in energy dissipation in tension with competitive cost are aimed in the strain-softening type FRCs (Naaman 2008, Bentur and Mindess 2007), in which, the volume fraction of fibres is often limited to 2%.

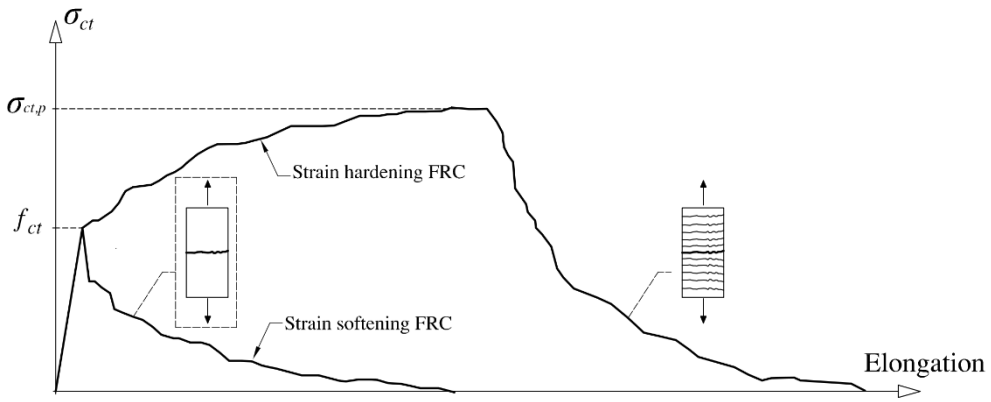

Figure 2.8: Schematic representation of tensile stress-elongation of strain-softening and strain-hardening FRC (adopted from Naaman (2008))

The strain-hardening FRCs comprise a significant characteristic of post-cracking tensile stress that is higher than their stress at crack initiation (Li 2003, Fantili et al. 2009, Kang et al. 2010, Pereira et al. 2010). Such a remarkable phenomenon is achieved by the use of higher volume fraction (up to 10% or even more) of microfibres in the cementitious matrix (Naaman 2008). The different types of strain-hardening FRCs have been developed in the recent years including slurry infiltrated fibre concrete (SIFCON) (Hackman *et al.* 1992, Naaman 1992), engineered cement composites (ECC) (Li and Leung 1992), and high-performance fibre reinforced concrete (HPFRC) (Markovic 2006, Lappa 2007, Naaman and Reinhard 2005). The typical feature of strain-hardening FRC represents the development of a diffuse crack pattern before the localization of the failure macro-crack (Pereira et al. 2010). After initiation of the first crack, the stress level is sustained equal or higher than the tensile strength of the cement matrix (f_{ct}) due to the contribution of a large number of fibres bridging the crack. In such a case, the post-cracking stress increases and multiple cracks diffuse along with the element. By attaining the tensile peak strength $(\sigma_{ct,p})$, which can be several times the cracking strength of the matrix (f_{ct}), a critical crack becomes localised and afterwards, the total elongation of the element in tension may lead to the opening of localised crack with reduction of tensile stress of the element while the other cracks are gradually closing. Although much higher load carrying capacity with noticeable energy absorption is obtained in the case of strain-hardening FRCs, this type of FRCs are usually more costly when compared to the strain-softening type due to the relatively high fibre content, requiring also particular considerations in the mix design.

2.8.2 Flexural Test

Despite the uniaxial tensile test (UTT) be, theoretically, the most suitable approach for determining the constitutive laws of FRC in tension, the UTT is, however, more expensive, tedious, time-consuming, and requires that several aspects be taken into consideration, like the boundary conditions, the geometry and size of the specimens (Hordijk 1991). Due to practical difficulties and ongoing debate about the test setup to execute the uniaxial tensile test, the flexural tests are widely utilised to evaluate, indirectly, the mechanical behaviour and the mode I fracture properties of fibre reinforced

concrete (Nanakorn and Horii 1996, Kitsutaka 1997). In this regard, the four-point bending test is recommended in some guidelines (JSCE-SF4 1984, ACI-544.2R 1988, ASTM-C-1018-97 1998). Depending on the force-deflection relationship determined in this type of test, FRCs are categorised into deflection-softening and deflection-hardening types. According to Naaman (2008), strain-hardening FRCs often present deflection-hardening in the four-point bending test, while the force-deflection response of the strain-softening composite may lead to either deflection-hardening or deflection-softening behaviour in flexure, depending on volume and aspect ratio of reinforcing fibres and compressive strength class of concrete matrices. Regarding the four-point bending test, and particularly in the case of deflection-hardening FRCs, several cracks may form along with the central pure bending region and consequently, the post-cracking response of a single crack is hardly extracted from bending test. Alternatively, the post-cracking response of FRC can be obtained from the three-point notched beam bending test configuration (EN 14651 2005, RILEM TC 162-TDF 2002, *fib* Model Code 2010 2011), where the presence of transversal notch promotes crack localisation at the mid-span of samples and facilitates determining the tensile constitutive laws of FRC in a single cracked cross-section. To derive the tensile constitutive laws of FRC from the flexural tests, it is mandatory to correlate the flexural test results, either the force versus deflection relationship or force-opening of the notch responses, to the key parameters defining the fracture characteristics of FRC. This can be achieved by following recommendations of reliable guidelines or through inverse analysis approach.

2.8.3 Inverse approach for evaluation of the post-cracking response of FRC

The inverse analysis is an indirect approach for determining the stress-strain or stress-crack width relationship of FRC through a trial computation, where the fracture mode I constitutive law of FRC is obtained by best fitting the force-deflection relationship registered in flexural tests. In this approach, a linear-elastic response is often assigned to FRC in compression to reduce, as much as possible, the intervening parameters and effectively speed up the computation. The overall tensile behaviour of FRC is a superimposition of the tensile strength of the cementitious matrix and contribution of fibres in tension through the pulling out mechanism (Figure 2.9).

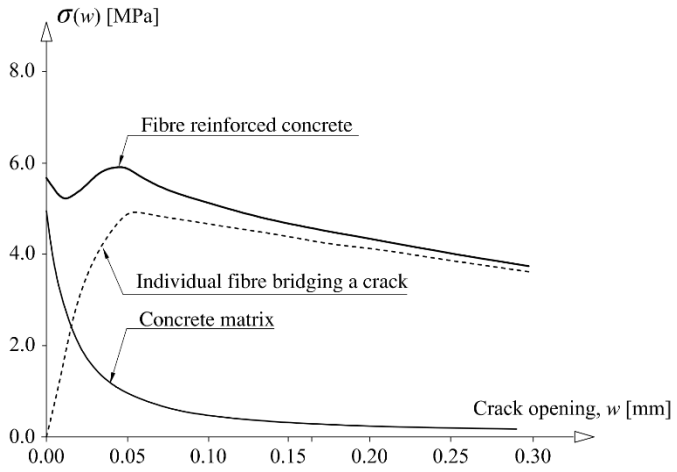

Figure 2.9: Stress-crack opening response of concrete matrix, individual fibres, and fibre reinforced concrete with 0.2% volume fraction of fibres (Li *et al*. 1993)

As indicated before, unlike plain concrete, the fracture energy is not an adequate parameter to represent the tensile behaviour of FRC. In particular, if longer fibres are utilised, the contribution of fibre in load bearing mechanism and consequent increase in fracture energy would not be diminished even for very large crack widths, which are not reliable in a structural design point of view. The shape of the tensile constitutive law of FRC is crucial, which is often complex and strongly dependent on the type and volume fraction of the used fibres (Stang and Olesen 1998). Since the 1980s, numerous researches have been conducted on the shape of stress-strain (or stress-crack width) relationship of concrete and fibre reinforced concrete in tension. In this regard, several models were developed considering the interaction between hydrated cement paste (HCP) and both aggregates and fibres, as well as the microstructure of the interfacial transition zone (Bentur *et al.* 1985, Wei *et al.* 1986). In some other studies, the pulling out response of an individual fibre is modelled to contribute for the simulation of the post-cracking response of FRC (Markovic *et al.* 2004, Markovic 2006, Jones *et al.* 2008). Finally, in the third type models, the fibrous cementitious composite is considered as an isotropic continuum, whose nonlinear behaviour due to the internal micro-mechanisms is entirely included in its constitutive law (Van Mier and Van Vliet 2002, Kooiman 2000, Barragán 2002). This kind of constitutive law is interesting for the inverse approach, due to the minimum intervening parameters and consequent simplicities.

In this regard, Li *et al.* (1993) proposed the bi-linear curve of Figure 2.10a, in which the first branch reflects a combination of the strength and toughness of the cementitious matrix and the initial bridging mechanism of fibres. The second branch, however, represents the bridging action of fibres. A similar model was utilised by Kooiman (2000). In the constitutive law proposed by Barragán (2002) an intermediate transition zone is considered. The similar model was utilised by Barros *et al.* (2005). The other and extremely suitable approach for the inverse analysis is the multi-linear curve proposed by some authors (Kitsutaka 1997, Kurihara *et al.* 2000, Löfgren *et al.* 2008), where the number and slop of the branches can be freely changed depending on the type, content or quality of fibre and the concrete matrix.

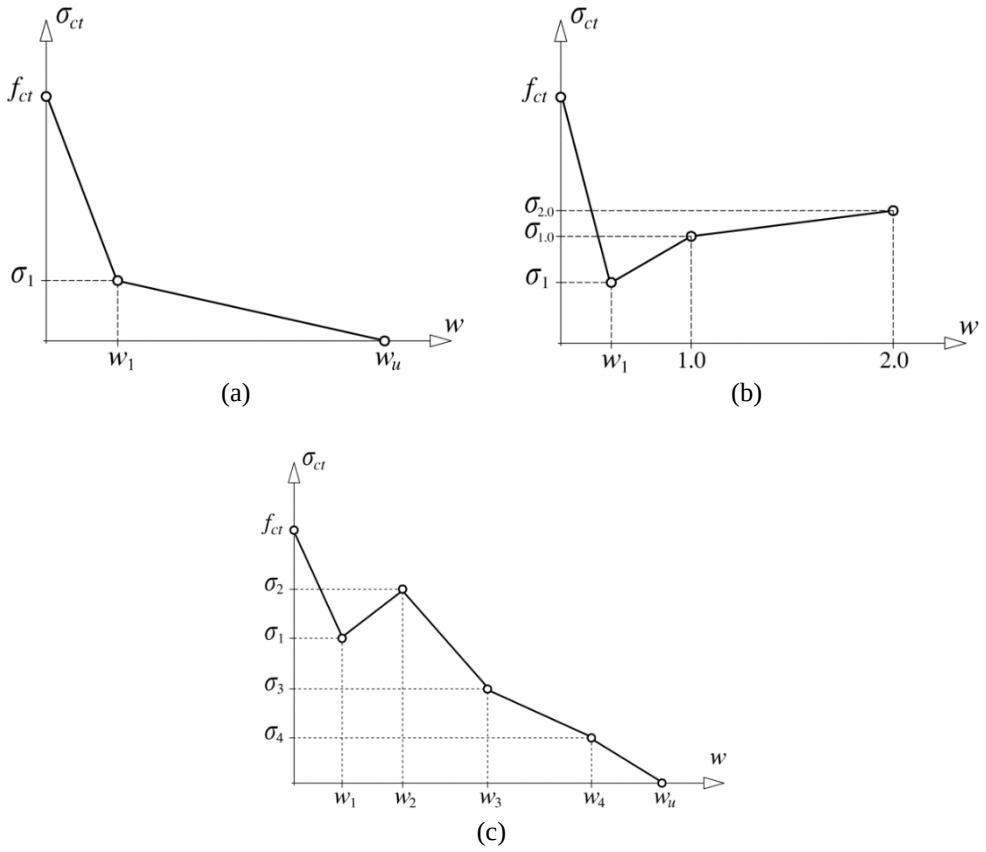

Figure 2.10: Typical stress-crack width relationship of FRC proposed by (a) Li *et al*. (1993), (b) Barragán (2002), and (c) Löfgren *et al.* (2008)

2.8.4 Recommendation of the guidelines for the post-cracking response of FRC

In the *fib* Model Code 2010 (2011), the tensile behaviour of FRC in the serviceability and ultimate limit states are derived from the experimental results recorded in the three-point notched beam bending test. For the serviceability limit states, *fib* Model Code 2010 (2011) considers the stress-strain diagram of Figure 2.11, according to which FRCs are categorised into three various cases. FRC-Case I has a strain-softening characteristic with a reduction of tensile stress when tensile strength is attained (point B). FRC-Case II and –Case III are two strain-hardening types FRC with a minor difference: in Case III the increase in the stress occurs just after the initial linear-elastic branch (point A) which is considered 90% of the tensile strength of concrete. In Case II, however, an intermediate zone is considered (AB branch) between the initial linear-elastic and the post-cracking curves.

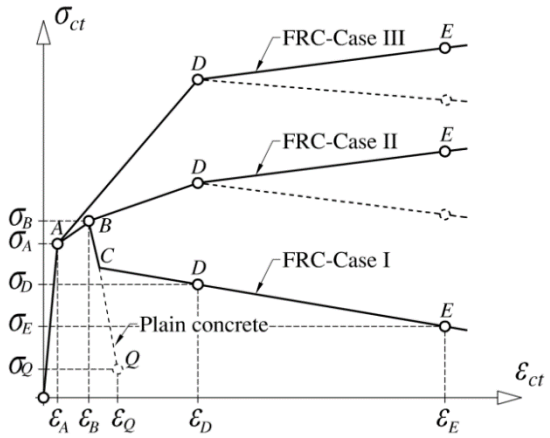

Figure 2.11: Tensile behaviour of FRC recommended by *fib* Model Code 2010 (2011) for the serviceability limit state analysis

Whether in the case of strain-softening or strain-hardening FRCs, the tensile strength of FRC is determined considering the strength class of concrete matrices. The post-cracking response of FRCs is, however, noticeably affected by the force-crack mouth opening displacement (*F-CMOD*) relationship recorded in the test. In this regard, *fib* Model Code 2010 (2011) utilises the concept of "residual flexural tensile strength".

For the ultimate limit state, the *fib* Model Code 2010 (2011) recommends two simplified constitutive laws in terms of stress-crack width $(\sigma - w)$ referred as the rigid-plastic model (Figure 2.12a) and the linear model (Figure 2.12b). The intervening parameters of these models are obtained from the *F-CMOD* curve.

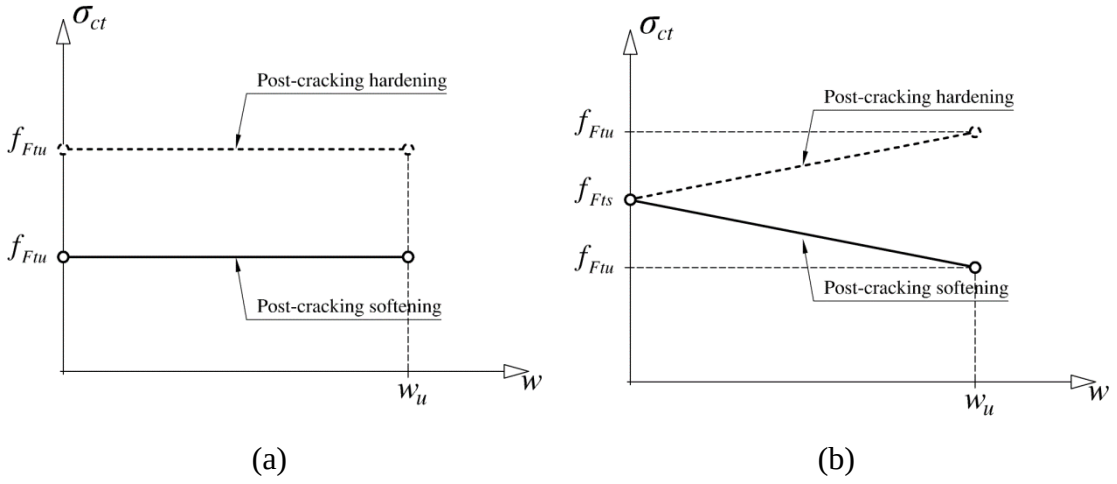

(a) (b)

Figure 2.12: Tensile behaviour of FRC recommended by *fib* Model Code 2010 (2011) for the ultimate limit state analysis; (a) the rigid-plastic model and (b) the linear model

Regarding the force-CMOD response of FRCs, *fib* Model Code 2010 (2011) proposes an approach to classify the toughness of FRC identified by the strength interval of $f_{R1,k}$ and a letter *a*, *b*, *c*, *d* or *e*, representing the $f_{R3,k}/f_{R1,k}$ ratio interval, being $f_{R1,k}$ and $f_{R3,k}$, the flexural residual strengths corresponding to CMOD of 0.5 mm and 2.5 mm, respectively (*fib* Model Code 2010 2011). For instance, according to Figure 2.13, a material denoted as "7b" possesses a strength $f_{R1,k}$ ranging between 7 and 8 MPa, and the $f_{R3,k}/f_{R1,k}$ ratio ranging between 0.7 and 0.9.

RILEM TC 162-TDF (2003) proposes a tri-linear stress-strain diagram for the tensile constitutive laws of the FRC used in a structural application, as illustrated in Figure 2.14. This constitutive law is derived by the force-CMOD responses registered in the three-point notched beam bending test.

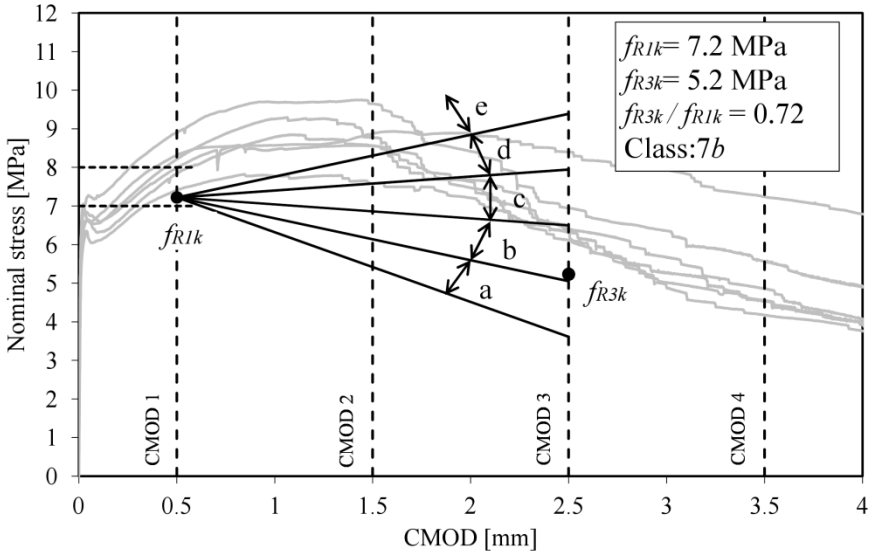

Figure 2.13: The concept of toughness class for FRC based on the relationship between the flexural stress and CMOD (*fib* Model Code 2010 2011)

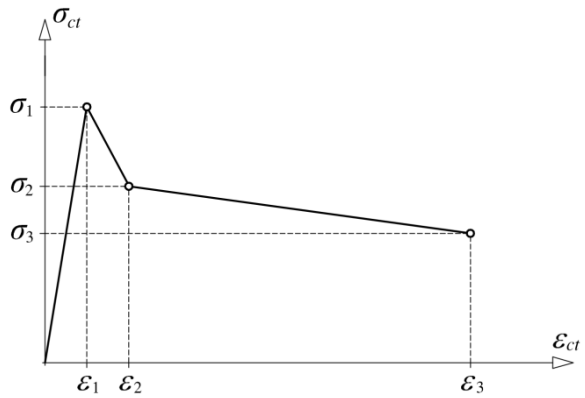

Figure 2.14: Tensile constitutive laws of FRC recommended by RILEM TC 162-TDF (2003)

2.9 Post-cracking behaviour of RC and R/FRC flexural members

Cracking in concrete is one of the dominant crucial aspects threaten the durability and structural performance of reinforced concrete (RC) structures. This problem is much more pronounced in the case of steel reinforced concrete (S/RC) structural elements since they are often subjected to tensile stress fields. The stiffness and load carrying capacity of RC elements decrease with the formation and propagation of cracks, which can

detrimentally affect their design requisites at the serviceability and ultimate limit state conditions (SLS and ULS, respectively). Crack propagation in S/RC elements also increases the permeability of concrete, facilitating the ingress of environmental adverse agents to the concrete zones where steel reinforcement is positioned, which promotes its corrosion as faster as wider are the cracks (Arya and Wood 2015). Number of cracks, is another key parameter that increases the rate of corrosion of reinforcement (Arya and Ofori-Darko 1996, Kaufmann and Marti 1998, Pimentel *et al.* 2010) (see Figure 2.15).

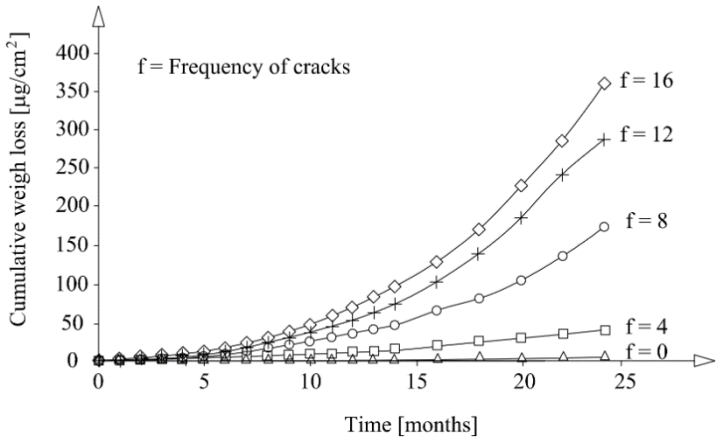

Figure 2.15: Effect of crack frequency on cumulative weight loss due to corrosion (Schiessl and Raupach 1997)

Reduction of the cross-section area of the steel reinforcement, deterioration of steel-to-concrete bond quality, and cracking and spalling out of the concrete cover, are all consequence of concrete cracking and responsible for the significant reduction of load carrying capacity of the element. Nevertheless, the influence of widening of cracks on the long-term durability of reinforced concrete can be negligible when the width of the crack is kept small according to the environmental conditions (Schiessl and Raupach 1997). When crack width is sufficiently small, penetration of aggressive agents, water and oxygen through the crack is suppressed due to the so-called self-healing phenomenon, resulting from calcium-bearing compounds and inoffensive dirt and dust deposits within the cracks. As a consequent, the rate of the corrosion process decreases. In this regard, the design guidelines often restrict the average crack width in the serviceability limit

states to a critical value ranging between 0.1 to 0.4 mm depending on the environment surrounding the structures (ACI 224R-01 2001, *fib* Model Code 2010 2011).

2.10 Tension Stiffening

Along a cracked region of a reinforced concrete member, the intact segments of concrete positioned between pairs of adjacent cracks sustain a significant portion of the total tension force due to the concrete-reinforcement interaction. Consequently, owing to the so-called tension stiffening effect, the average strain of the reinforcement between cracks is significantly lower than that one in the plane of a crack. In structural response point of view, the tension stiffening effect can be explained regarding the force-deflection relationship $(F-\delta)$ of a reinforced concrete beam schematised in Figure 2.16.

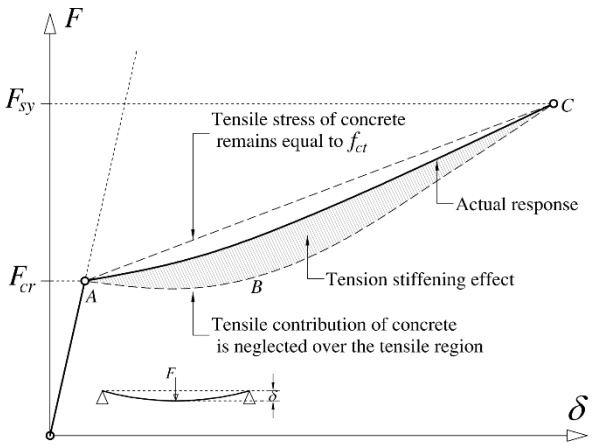

Figure 2.16: Schematic force-deflection response of the RC element (adopted from Gilbert (2007) and modified)

According to Figure 2.16, the force-deflection response of the beam is linear-elastic up to crack initiation, and the stiffness of this stage is proportional to the moment of inertia of the uncracked cross-section and the elasticity modulus of the constituent materials. When the extreme tensile fibre of the RC section attains the concrete tensile strength (f_{ct}), the first crack forms at the F_{cr} load level, followed by an abrupt reduction of the flexural stiffness. The genuine post-cracking response of the beam is ranging between the upper bound, which is based on the assumption that the tensile stress of concrete in cracked region remains equal to f_{ct}, and the lower bound that is determined

by neglecting the contribution of tensile concrete in cracked region, represented in Figure 2.16 by AC and ABC curves, respectively. In fact, the tension stiffening effect is defined as the difference between the actual response of the reinforced concrete flexural member and its zero-tension response (ABC curve) (Gilbert 2007). It should be, however, remarked that the amplitude of tension stiffening effect decreases up to the attainment of the force corresponding to the yield initiation in steel bar (F_{sy}) beyond which it would totally vanish.

To be specific, the contribution of tension stiffening increases by the decrease in the quantities of tensile reinforcement. For instance, in slab element with the percentage of longitudinal steel reinforcement (ρ_s) lower than 0.3%, more than 50% of the stiffness of the cracked member at service loads may be attained by the contribution of the tension stiffening effect (Gilbert 2007). In such a case, neglecting the tension stiffening may lead to overestimating the flexural deflection by a large proportion. It is, however, remarkable that significant decrease in longitudinal steel bar ratio, lower than the minimum reinforcement ratio recommended by design codes may lead to yielding of steel bar at almost crack initiation stage and frustrate the tension-stiffening effect.

Differently from the plain concrete assumed to carry tension just between the cracks only, fibre reinforced concretes are able to transmit significant tensile forces at a crack plane owing to the reinforcing effects provided by the fibres that cross the cracks. Therefore, the tension stiffening in fibre reinforced concrete elements comprises a combination of mechanisms between the cracks and at the cracks (Bischoff 2003). Therefore, the tension stiffening effect is more noticeable in R/FRC elements compared to RC members(Abrishami and Mitchell 1997).

In a simplified method, the contribution of tension stiffening to the post-cracking load-deflection response of reinforced concrete beams is taken into account by semi-empirical formulations proposed for determining the average effective moment of inertia (I_e) for a cracked member, such as the case of the equation developed by Branson (1965) for steel reinforced concrete, which is also recommended in ACI 318-05 (2005):

$$I_e = \left(\frac{M_{cr}}{M_a}\right)^3 I_g + \left[1 - \left(\frac{M_{cr}}{M_a}\right)^3\right] I_{cr} \leq I_g \quad (2.3)$$

being M_{cr} the cracking moment, M_a the maximum applied moment, I_{cr} the moment of inertia of the cracked transformed section, and I_g the moment of inertia of the gross section. According to some researches, the Branson's approach (Equation 2.3), however, overestimates noticeably the average stiffness of reinforced concrete members containing low percentages of steel reinforcement (Bischoff 2005), as the same as concrete beams reinforced with longitudinal FRP bars (Benmokrane *et al.* 1996).

Following the approach recommended by Eurocode 2 (1992), a more accurate prediction of the post-cracking response of reinforced concrete members (Gilbert 2007) may be obtained. In this approach, a reinforced concrete member is subdivided into the uncracked region, where the concrete and steel reinforcement both behave elastically and fully cracked region in which the tensile contribution of concrete is overlooked and the tensile force is entirely carried out by the steel bar. In this approach, the effective curvature of the element is obtained by Equation (2.4):

$$\chi_e = (1-\xi)\chi_{uncr,reg} + \xi\chi_{cr,reg} \quad (2.4)$$

where $\chi_{uncr,reg}$ and $\chi_{cr,reg}$ are the curvatures calculated for the uncracked and fully cracked regions, respectively. For the bending moment acting at the serviceability limit states (M_s), the compressive behaviour of concrete and the tensile response of reinforcement can be assumed linearly and elastic, and χ_e, $\chi_{uncr,reg}$ and $\chi_{cr,reg}$ are determined from the following equations:

$$\chi_e = \frac{M_s}{E_c I_e} \quad (2.5)$$

$$\chi_{uncr,reg} = \frac{M_s}{E_c I_{uncr}} \quad (2.6)$$

$$\chi_{cr,reg} = \frac{M_s}{E_c I_{cr}} \quad (2.7)$$

where I_e is the average effective moment of inertia and, I_{uncr} and I_{cr} are the moment of inertia of uncracked and cracked cross-section, respectively. In Equation (2.4), ξ is a distribution coefficient accounting for moment level and degree of cracking, given by:

$$\xi = 1 - \beta_1 \beta_2 \left(\frac{\sigma_{sr}}{\sigma_s} \right)^2 \tag{2.8}$$

being β_1 and β_2 constants taking into account the influence of duration of the loading or repeated loading on the average strain. In this equation, σ_{sr} is the stress in the tensile reinforcement in the cracked section under the loading conditions leading to the crack initiation (*i.e.* $M = M_{cr}$), and σ_s is the stress in the tensile reinforcement when the service moment (M_s) is acting. Substituting Equations (2.5) to (2.8) in Equation (2.4), for a flexural member with deformed bars under short-term loading, the effective moment of inertia is determined by the following equation:

$$I_e = \frac{I_{cr}}{1 - \left(1 - \frac{I_{cr}}{I_{uncr}}\right)\left(\frac{M_{cr}}{M_s}\right)^2} \tag{2.9}$$

Apart from the above-described approaches, the influence of tension stiffening effect on the post-cracking deflection response of reinforced concrete beams can be analysed through theoretical models adopting non-linear constitutive laws. Some of these models consider an average stress-strain relationship which was firstly introduced by Rashid (1968) based on the smeared crack model, which due to its simplicity and flexibility represent desirable methods for finite element simulation. In this approach, the tension stiffening effects are taken into account by modifying the constitutive law of tensile reinforcement (Feenstra and Borst de 1995) or more commonly, tensile concrete surrounding the reinforcement (Barros *et al.* 2001, Prakhya and Morley 1990).

In some other approaches, the tension stiffening effect is mobilised in the bond-slip relationship between the reinforcement and surrounding concrete along an interaction zone, which was first advanced by Saliger (1936). These models are developed for a

concrete prism with an embedded reinforcing bar subjected to the tensile force applied on the two protruding ends of the bar, as depicted in Figure 2.17.

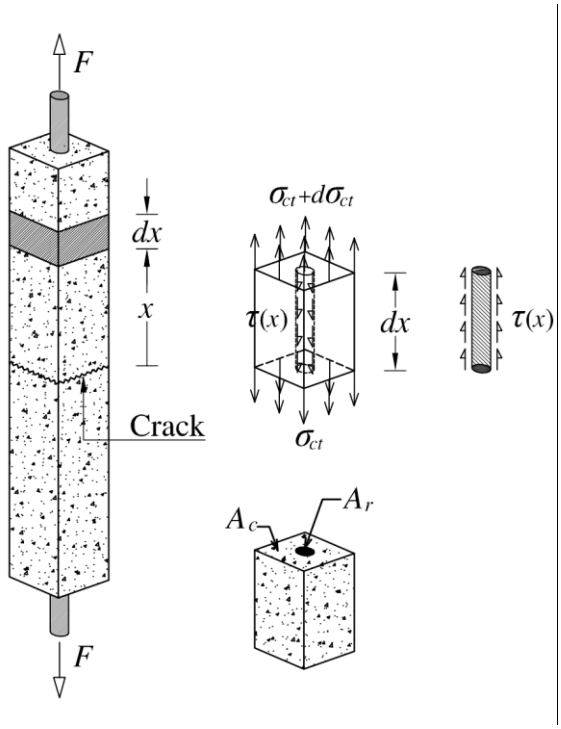

Figure 2.17: Conventionally reinforced direct tension specimen

When a crack initiates in a tensile reinforced concrete element, the bond between the concrete and the bar is stimulated by the movement of the bar ribs, leading to transfer a shear load to the intact concrete positioned between the cracks. This mechanism can be mathematically represented by the differential Equation (2.10), adopted in numerous formulations available in the literature (Balázs 1993, Fehling and Leutbecher 2007, Stang and Aarre 1992, Bianco *et al.* 2009):

$$\frac{d^2 s(x)}{dx^2} - J_1 \tau\left(s(x)\right) = 0 \tag{2.10}$$

where $s(x)$ and $\tau\left(s(x)\right)$ are, respectively, sliding and corresponding shear bond stress over the bond length, and J_1 is a constant determined from the following:

$$J_1 = \left(\frac{L_p}{E_r A_r} + \frac{L_p}{E_c A_c}\right) \tag{2.11}$$

being A_r and A_c the cross-sectional area of reinforcement and surrounding concrete, respectively (Figure 2.17), and $L_p (= \pi d_b)$ is the perimeter of the reinforcing bar of diameter d_b. E_r and E_c are also the elastic modulus of reinforcement and surrounding concrete, in turn. To solve the differential Equation (2.10), it is fundamental considering a proper local shear bond stress-slip (or in brief bond-slip) relationship $(\tau - s)$ between the reinforcing bar and surrounding concrete.

2.11 Bond Behaviour

The bond between the concrete and reinforcing bar is an integration of chemical adhesion, friction, and mechanical interaction (Lutz and Gergely 1967). For smooth bar, the mechanical interaction is caused by the micro-roughness of the bar surface and therefore, is extremely small. In deformed bars, however, the mechanical interaction is due to the presence of the ribs, which prevents relative movements at the interface (Figure 2.18).

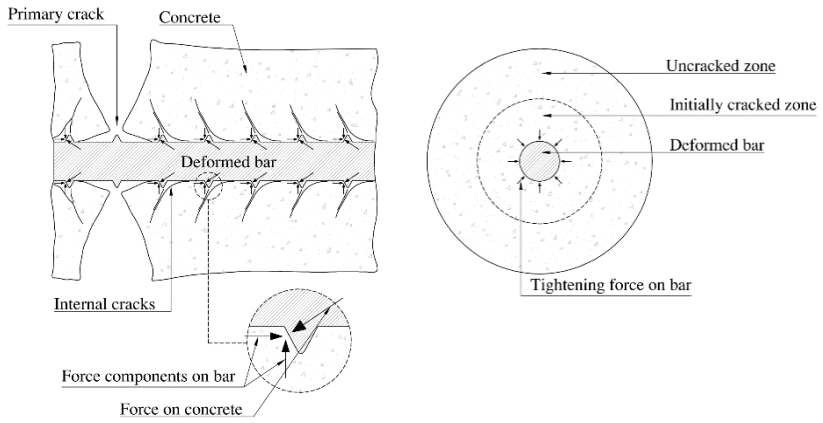

(a) (b)

Figure 2.18: Schematic deformation of concrete surrounding a deformed steel bar after the formation of internal cracks; (a) longitudinal section of the axially loaded specimen and (b) cross-section (Goto 1971);

In this case, the bond action spread out from the bar into surrounding concrete, which can be subdivided into a stress component parallel to the bar axis, denoted the bond stress, and radial components, designated as normal or splitting stress balanced by tensile stress ring in the concrete (Tepfers 1973). In concrete cover, where the ring is in its thinnest region, the tensile stress may exceed the tensile strength of the concrete, leading to the formation of longitudinal splitting cracks in concrete (Figure 2.19). In this regard, the bond strength is noticeably influenced by concrete strength class (*fib* Model Code 2010 2011, ACI 318-05 2005, Eurocode 2 1992).

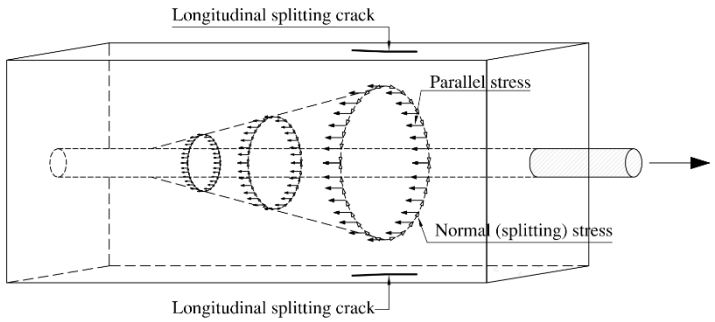

Figure 2.20: Schematic representation of radial components of the bond forces in an anchorage zone (Tepfers 1973)

Presence of the normal stress is quite necessary to assure transference of the load through the mechanical bond. Otherwise, the interaction between the concrete and reinforcement may be lost by the so-called splitting failure in which the concrete surrounding the reinforcement bar is penetrated by longitudinal splitting cracks (Lundgren 2005). On the contrary, if the concrete cover is large enough and concrete surrounding the reinforcement bar is well confined to withstand the normal stresses, splitting cracks do not form and surrounding concrete appears uncracked macroscopically until pullout failure occurs. The pullout failure is characterised by the propagation of shear cracks between the adjacent ribs, which represents the upper limit for the bond strength. The bond-slip relationship can be investigated experimentally through different groups of the test setup. The direct pullout test with a short anchorage (embedment length to bar diameter ratio less than 5) is a relatively convenient and inexpensive way for investigation the primary parameters affecting the bond behaviour. It is a test widely used in the literature for steel bar, FRP bar, or FRP laminates utilised in the near-surface

mounted (NSM) method (Eligehausen *et al.* 1983, Hungspreug 1981, Malvar and Warren 1992, Lundgren 2005). Typical setup of the direct pullout test is depicted in Figure 2.20, according to which the tensile force F is applied to the protruding end of the bar of the cross-sectional perimeter L_p, while the bar relative slip to concrete is measured at loaded-end and free loaded-end of the bar (s_{le} and s_{fle} in Figure 2.20). The bond behaviour is then represented by $\tau - s$ curve, where τ is the average bond stress over the embedded length (L_e) given by the following equation:

$$\tau = \frac{F}{L_e L_p} \tag{2.12}$$

In the pullout test, the tensile force applied to the bar is balanced by the compression introduced into concrete, which does not occur in a reality, since the bar and concrete are both in tension. Furthermore, due to confining effects in concrete at the bearing end (Aiello *et al.* 2007), higher resistance to splitting failure is determined when compared with real situations (Cairns and Plizzari 2003).

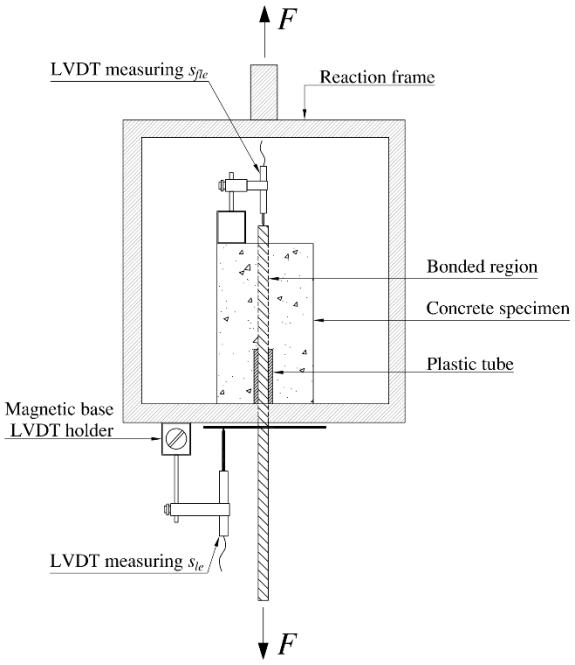

Figure 2.21: Typical direct pullout test setup

To investigate the bond condition within a flexural RC element, the pullout beam bending test is an appropriate choice utilised in the literature (De Lorenzis 2002, Cruz and Barros 2004, Mazaheripour 2015), which represents, as closely as possible, the actual stress state in a reinforced concrete structure.

In the beam test, the reinforced concrete specimen is composed of two blocks (left and right block) as depicted in Figure 2.21. The blocks are connected at two points; in the tensile zone of the bottom part by the longitudinal reinforcement and in the compressive zone by a steel hinge. To prevent the premature fracture of concrete in front of the blocks, the bar is covered for a specific length by plastic tubes to be kept unbounded. In one block, the bar is entirely bonded to concrete, while in the other one it is partially covered by plastic tube and is unbounded. The test is executed by four-point loading configuration, while the relative sliding of the bar at the loaded end and the free loaded end is measured. The applied bending moment in the central pure bending region is balanced by a couple of tensile and compressive force of the bar and steel hinge, respectively. Similarly to the direct pullout test, the τ is determined by Equation 2.12.

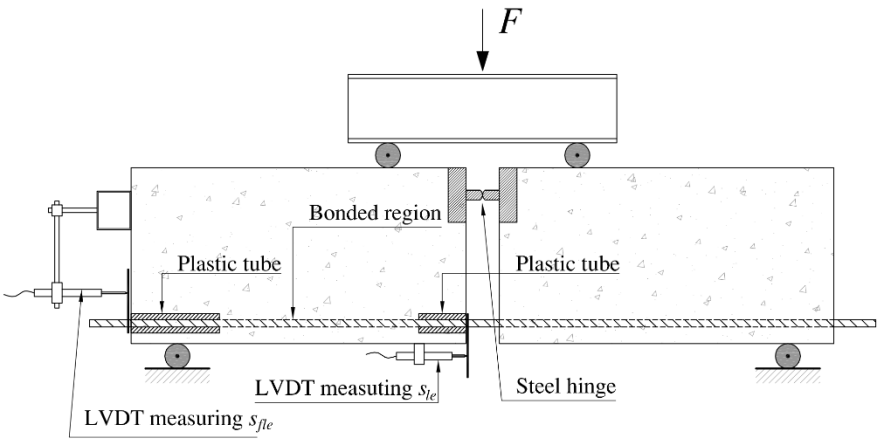

Figure 2.22: Typical flexural bond test setup

Although the beam tests closely approximate real applications, they may be challenged when the debonding of the reinforcing bar is combined with shear failure or crushing of concrete (Lundgren *et al.* 2019). Therefore, the geometry and span length of the samples and diameter of the reinforcing bar are the key parameters, when the beam test is designing.

2.11.1 Local bond models for steel/RC elements

If the imposed load is assumed monotonic and the pullout of reinforcing bar is considered as a predominant failure mode, the bond behaviour of deformed steel bar is modelled in the literature by a typical local bond stress-slip relationship $(\tau - s)$ of Figure 2.22 known as BPE Model, which was first proposed by Eligehausen *et al.* (1982).

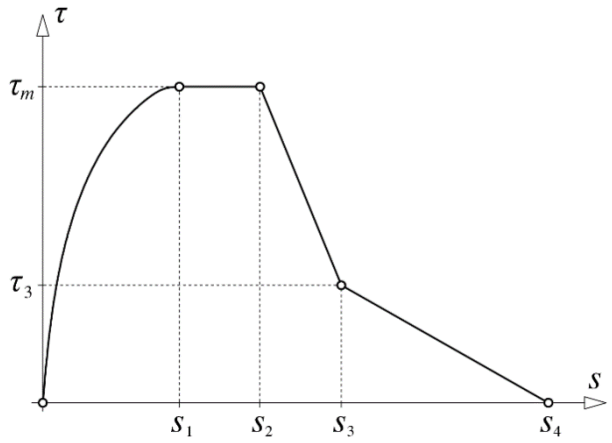

Figure 2.23: Typical local bond stress-slip model of deformed steel bar in concrete

Table 2.2: Proposed formulation for the initial branch of bond-slip relationship (adopted from *fib* Bulletin 10 (2000)

Author(s)	$\tau - S$ relationship
Rehm (1961)	$\tau = f_c^{cube}\left(\varphi s^{\alpha} \pm \psi s\right)$
Nilson (1968)	$\tau = 998.4s - 548\times10^{2}s^{2} + 852.2\times10^{3}s^{3}$
Mirza and Houde (1979)	$\tau = 539.8s - 256.1\times10^{2}s^{2} + 592.2\times10^{3}s^{3} - 557.4\times10^{4}s^{4}$
Martin (1973)	$\tau = \tau_0 + cs^{b}$
Ciampi *et al.* (1982)	$\tau = \tau_1\left(s/s_1\right)^{\alpha}$

The model comprises an initial ascending and often non-linear branch up to maximum bond stress τ_m and corresponding sliding s_1, represented by a large variety of

empirical expressions, some of which summarised in Table 2.2. The curve is followed by a plateau up to sliding s_2. Then the bond stress reduces up to the slip s_3 and corresponding bond stress τ_3, followed by a linearly softening branch up to the ultimate slip s_4.

2.11.2 Local bond models for FRP/RC elements

Comparing to steel reinforcement, different material properties or mechanical roughness of lateral surfaces of FRP reinforcement lead to a different interaction mechanism with concrete (Cosenza *et al.* 1997, Lee *et al.* 2008, Baena *et al.* 2013, Lin and Zhang 2014). A typical local bond-slip relationship of FRP bar into concrete is depicted in Figure 2.23, which is a modified version of the BPE Model (Eligehausen *et al.* 1982), in which the second branch of the BPE model, with constant maximum bond stress, is omitted to better describe the bond stress-slip relationship of FRP bars.

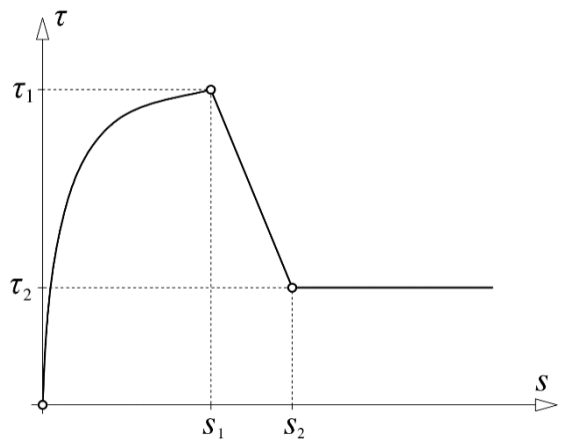

Figure 2.24: typical Local bond stress-slip model of FRP bar in concrete

2.11.3 Local bond models for R/FRC elements

If the bond failure is governed by the pullout of the bar, the addition of fibres to concrete would have no effect either on the bond-slip relationship and bond strength (Harajli *et al.* 1995, Rostásy and Hartwich 1988). However, the noticeable contribution of fibres is expected on the post-splitting behaviour (see Figure 2.24) since it is substantially influenced by the tensile behaviour of concrete and may positively be affected by the enhanced properties of FRC in tension. The use of fibres is also slow down the degradation of the bond strength by resisting widening of the cracks (Hota and Naaman 1997) which may cause a noticeable increase in ductility in cyclic loading (Balaguru *et al.* 1996). By the improvement of post-cracking behaviour and particularly when strain-hardening cementitious composites are used, initiation of failure crack is postponed, which may result in more uniform strain distribution along with the interaction and consequent reduction of interfacial bond stress. According to Fischer and Li (2002), the bond strength in reinforced engineering cementitious composites (R/ECC) members is not as significant as in reinforced concrete members. In experimental research conducted by Harajli and Mabsout (2002) the contribution of fibres on the bond behaviour is taken into account on the reduction of development length determined by the approach proposed by ACI Committee 408 (2003) as follows:

$$l_d = \left(\frac{\frac{f_y}{f_{cc}^{1/4}} - 2100}{68\left(\frac{c\vartheta + K_{tr}}{d_b} \right)} \right) d_b \qquad (2.13)$$

being f_{cc} and f_y the concrete compressive strength and the yield stress of steel bar, respectively, d_b is the bar diameter, c the concrete cover, and ϑ a coefficient related to concrete cover and bar spacing. K_{tr} is a transverse reinforcement index given by:

$$K_{tr} = \left(\frac{(0.39 d_b + 0.11) A_{tr}}{s_{tr} n_b} \right) f_{cc}^{1/2} \qquad (2.14)$$

where n_b is number of bars, and A_{tr} and s_{tr} are, respectively, the area and the spacing of transverse reinforcement. Harajli and Mabsout (2002) correlated the transverse

reinforcement index to the volume fraction (V_f) and aspect ratio (l_f / d_f) of the utilised steel fibres as below:

$$K_{tr}^{FRC} = \left(\frac{(0.39 d_b + 0.11)(9.6 R_r + 0.28) A_{tr}}{s_{tr} n_b} \right) f_{cc}^{1/2} + 0.16 \left(\frac{V_f l_f}{d_f} \right) c f_{cc}^{1/4} \qquad (2.15)$$

being R_r the ratio of projected rib area normal to the bar axis to the product of nominal bar perimeter and centre-to-centre spacing of ribs.

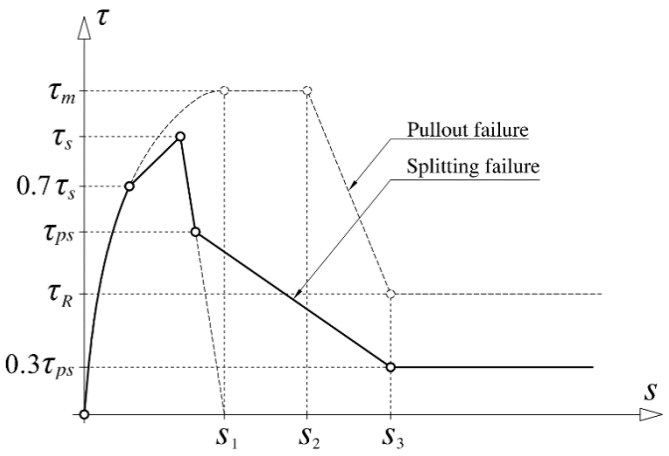

Figure 2.25: Local bond-slip relationship of deformed steel bar embedded in fibre reinforced concrete (Harajli *et al.* 2002)

2.12 The width and spacing of cracks in RC and R/FRC flexural elements

The concept of crack width and crack spacing in the reinforced concrete is often investigated in a tensile reinforced concrete prism depicted in Figure 2.17, where the tensile force is applied to the two protruding ends of the bar. Before cracking, the extension of the concrete and bar is uniform and strain of concrete and bar is compatible, determined by the following equation:

$$\varepsilon_r = \varepsilon_c = \frac{F}{E_r A_r + E_c A_c} \qquad (2.16)$$

being E_r, A_r, E_c, A_c, respectively, the elastic modulus and the cross-sectional area of reinforcement and concrete.

When a crack is initiated, the contribution of concrete at the crack plane reduces and the tensile force is typically transferred by the bar. However, owing to the bond, a portion of the total tensile force is gradually transferred to the concrete over a certain distance from the plane of the crack, which is so-called transmission length (l_{tr}). Therefore, the prism can be subdivided into two regions; incompatible region of length l_{tr} in the vicinity of the crack along which strain of concrete and reinforcement is different, and the compatible region beyond l_{tr} length where the strain compatibility (Equation 2.16) is restored to concrete and reinforcing bar.

With increasing load, when the stress of concrete $(\sigma_c = E_c \varepsilon_c)$ exceeds the concrete tensile strength (f_{ct}), a new pair of cracks may form in the compatibility regions (Beeby and Scott 2004, Murray *et al.* 2018) due to relatively higher average concrete strain comparing to that in the incompatible region. This means that the spacing of adjacent cracks may range between a lower and upper bound of $s_{r,\min} = l_{tr}$ and $s_{r,\max} = 2l_{tr}$, respectively (CEB 1993). Therefore, the cracking is assumed to be stabilised when the spacing between each pair of adjacent cracks along with the prism satisfies $s_{r,\min} \leq s_r \leq s_{r,\max}$.

According to EN 1992-1-1 (2004), the maximum spacing between the cracks $(s_{r,\max})$ in reinforced concrete elements can be determined using the following expression:

$$s_{r,\max} = k_1 c + k_2 k_3 k_4 \frac{d_b}{\rho_{s,eff}} \tag{2.17}$$

where c is the thickness of the concrete cover, d_b is the bar diameter, and $\rho_{s,eff}$ is the ratio between whole area of the longitudinal reinforcement (A_s) and the effective area of the concrete in tension $(A_{c,eff})$. The coefficients k_1 to k_4 are constant coefficients.

In the approach recommended by EN 1992-1-1 (2004), the characteristic crack width (w_k) is determined from the following equation:

$$w_k = s_{r,\max}\left(\varepsilon_{sm} - \varepsilon_{cm}\right) \tag{2.18}$$

where $s_{r,\max}$ is the maximum crack spacing determined by Equation (2.17) and the term $\varepsilon_{sm} - \varepsilon_{cm}$ is representative of the difference between the mean strain in the reinforcement and concrete between two adjacent cracks, given by the following equation:

$$\varepsilon_{sm} - \varepsilon_{cm} = \frac{\sigma_{st}}{E_s} - \frac{k_5}{E_s} \cdot \frac{f_{ctm}}{\rho_{s,eff}}\left(1 + \gamma_s \rho_{s,eff}\right) \tag{2.19}$$

In above equation, σ_{st} is the stress in the steel reinforcement at a cracked section, f_{ctm} is the mean tensile strength of concrete, E_s is the modulus of elasticity of steel reinforcement, γ_s is the ratio between modulus of elasticity of steel bar and concrete (*i.e.* E_s / E_c), and k_5 is a coefficient depends on short-term and long term loading. The maximum value of crack width $(w_{\max})$ can be considered equal to w_k (CEB-FIP 1978 1984) which is correlated to the average crack width (w_{m}) by the following equation:

$$w_{\max} = k_6\, w_{\mathrm{m}} \tag{2.20}$$

k_6 is a statistical coefficient recommended to be equal to 1.7 (Borosnyói and Balázs 2005). A numerous experimental researches presented in the literature to investigate crack width and spacing in fibre reinforced concrete (Abrishami and Mitchell 1997, Noghabai 2000, Bischoff 2003, Deluce and Vecchio 2013, Tan *et al.* 1995, Vandewalle 2000), which reveal a tendency of reduction of crack spacing and crack width by the increase in volume content and aspect ratio of fibres. In this regard, one of the most frequently used formulation for the prediction of crack spacing in fibre reinforced concrete elements is the one proposed by RILEM TC 162-TDF (Vandewalle *et al.* 2003) given by the following equation:

$$s_{rm} = \left(50 + 0.25 k_3 k_4 \frac{d_b}{\rho_{s,eff}}\right)\left(\frac{50}{l_f / d_f}\right) \tag{2.21}$$

Equation (2.21) is in fact, a modified feature of EN 1992-1-1 (2004) formulation for non-fibrous concrete (Equation 2.17) in which l_f / d_f is the fibre aspect ratio (being l_f

and d_f the fibre length and diameter). A more or less similar approach is proposed by Moffatt (2001) to estimate the average crack spacing of reinforced strain-softening type of fibre reinforced concrete elements as follows:

$$s_{rm} = \left(50 + 0.25k_3k_4\frac{d_b}{\rho_{s,ef}}\right)\left(1 - \frac{f_{res}}{f_{cr}}\right) \tag{2.22}$$

where f_{res} is the post-cracking residual concrete stress, and f_{cr} is the cracking stress of the concrete. In the approach proposed by RILEM TC 162-TDF (Vandewalle *et al.* 2003), the design value of the crack width (w_d) for R/FRC members subjected principally to flexure or tension is determined by the following equation:

$$w_d = k_7\, s_{rm}\, \varepsilon_{sm} \tag{2.23}$$

where k_7 is a constant coefficient correlating the average crack width to the design value and ε_{sm} is the average strain in the reinforcement.

Despite the main affecting parameters of fibre reinforced concrete have been included in the approach proposed by RILEM TC 162-TDF (Vandewalle *et al.* 2003) (Equation 2.21) and Moffatt (2001) (Equation 2.22), However, the predictive performance of these equations are arguable (Deluce and Vecchio 2013). Deluce *et al.* (2014) proposed Equation (2.24) for the average crack spacing of steel fibre reinforced concrete under uniaxial strain when cracking is stabilised.

$$s_{rm} = 2\left(c_{eff} + \frac{s_b}{10}\right)k_8 + \frac{k_9k_{10}}{s_{mi}} \tag{2.24}$$

The above formulation is based on the approach recommended by CEB-FIP (1978), in which c_{eff} is the effective concrete cover taken 1.5 times the maximum aggregate size, s_b is representative of the effective longitudinal bar spacing given as follows:

$$s_b = 0.5\sqrt{\frac{\pi d_b^2}{\rho_{s,eff}}} \le 15d_b \tag{2.25}$$

being d_b the bar diameter, and $\rho_{s,eff}$ the effective reinforcement ratio. In Equation (2.26), s_{mi} is a factor taking into account the influence of steel fibres by considering the number of fibres bridging a crack determined by the following equation:

$$s_{mi} = \frac{\rho_{s,eff}}{d_b^2} + k_f \frac{\alpha_f V_f}{d_f} \tag{2.26}$$

where d_f is the fibre diameter and V_f is the volume fraction of fibres, restricted to a maximum value of 0.015. Parameter α_f is also the fibre orientation factor can be taken equal to 0.5 for the random three-dimensional orientation of fibres in infinite elements (Stroeven and Hu 2006). In Equation (2.26), k_f is the fibre effectiveness factor given by:

$$k_f = \frac{l_f V_f}{50 d_f} \geq 1.0 \tag{2.27}$$

In Equation (2.24), the beneficial effects of steel fibres is also taken into consideration by the factor k_8 determined from the following equation:

$$k_8 = 1 - \left(\frac{\min(V_f, 0.015)}{0.015} \right) \left(1 - k_f^{-1} \right) \tag{2.28}$$

Furthermore, in this equation, the bond characteristics of the reinforcing bars are accounted by k_9 factor of 0.4 or 0.8 for deformed bar and plain bars or pre-stressing tendons, respectively. k_{10} also account the strain conditions in the concrete member determined by Equation (2.29):

$$k_{10} = \frac{0.25(\varepsilon_1 + \varepsilon_2)}{2\varepsilon_1} \tag{2.29}$$

being ε_1 and ε_2 the largest and smallest tensile strains in the concrete, respectively. In the approach proposed by *fib* Model Code 2010 (2011) the contribution of fibres on the cracking characteristics is taken into account using the concept of average residual strength of the fibre reinforced concrete at serviceability limit states ($f_{Fts,m}$) (see Figure

2.12). In this approach, the average spacing between cracks (s_{rm}) is estimated by multiplying a factor of 1.5 to the maximum transmission length given by the following equation:

$$l_{s,\max} = k_{11}\, c + \frac{\left(f_{ctm} - f_{Fts,m}\right)}{4\tau_{bm}} \frac{d_b}{\rho_{s,eff}} \tag{2.30}$$

where k_{11} is an empirical coefficient for simulating the influence of the concrete cover and τ_{bm} is the average bond strength between reinforcing bars and surrounding concreteRemark that Equation (2.30) is valid for FRCs whose average residual strength at serviceability limit states $(f_{Fts,m})$ is less than the crack strength of the concrete matrix (f_{ctm}). Regarding *fib* Model Code 2010 (2011) recommendations, the design values of crack width (w_d) is determined by equation below:

$$w_d = \frac{2 l_{s,\max}}{E_s}(\sigma_{st} - k_{12}\sigma_{sr} - k_{13}\varepsilon_{sh}E_s) \tag{2.31}$$

where σ_{st} is the stress of steel reinforcement in a crack, ε_{sh} is the shrinkage strain, and σ_{sr} is the steel stress at the crack section in the crack formation stage. k_{12} is also an empirical coefficient to assess the mean strain over $l_{s,\max}$, and k_{13} is a coefficient takes into account the shrinkage contribution.

2.13 Concluding remarks

In this chapter, the vulnerable of concrete in tension was explained by detailing its morphology and the different approaches employed to overcome the tensile weakness of concrete, including taking advantage of longitudinal steel or FRP bar lonely or simultaneously in a hybrid-reinforcing scheme were discussed.

The decrease in sound cross-sectional area, spalling the concrete cover, diminishing the concrete cross-sectional area, and deterioration of bond between reinforcing bar and concrete are the main eventuates of corrosion of steel bar affect negatively the load carrying capacity and the structural safety indexes. Although substitution of steel

reinforcement by the one made of FRP is an effective remedy against corrosion, the lack of ductility and the large deflection of FRP reinforced concrete (FRP/RC) elements are the main obstacles for using the FRP bar as the sole reinforcement.

These drawbacks can be overcome by a hybrid flexural reinforcing (HFR) scheme obtained by placing the FRP bars near the outer surface of the tensile zone and steel bars at the inner level. In this chapter, taking advantage of fibre in concrete was discussed as a novel approach to mitigate the tensile vulnerability in tension. Cracking mechanism of plain and fibre reinforced concrete was discussed and different approaches to simulate cracking behaviour of concrete were reviewed among which the fictitious crack model Hillerborg et al. (1976) and the crack band model of Bažant (Bažant and Oh 1983) were explained. The various approaches proposed in the literature to identify the post-cracking behaviour of fibre reinforced concrete were also presented. The chapter also includes a literature review on relevant aspects affecting the interaction between reinforcing bar and plain and fibre reinforced concrete, and its correlation to the tension-stiffening phenomenon was described. It was illustrated that the contribution of tension stiffening on the overall response of RC flexural elements is amplified by the reduction of tensile longitudinal reinforcement of the cross-section. In addition, the noticeable effect of fibres on the tension stiffening of R/FRC is highlighted.

Regarding the literature, the local bond models for steel/RC, FRP/RC, and R/FRC were presented and compared. Finally, the different approach proposed in the literature for predicting crack width and crack spacing of RC and R/FRC flexural elements were detailed.

Chapter 3

Experimental Evaluation of Flexural Response of R/SFRSCC Elements

3.1 Introduction

This chapter describes a comprehensive experimental programme conducted to evaluate the load carrying capacity and cracking behaviour of flexural elements reinforced with a hybrid system composed by discrete hooked-end steel fibres and longitudinal steel and fibre reinforced polymer (FRP) bars. In this evaluation, the influence of the key parameters affecting the material properties of SFRSCC, including the concrete strength class and volume fraction of fibres is assessed. Furthermore, the scheme and percentages of longitudinal reinforcement is studied.

3.2 Composition and Development of SFRSCC

The test programme was carried out on three series of steel fibre reinforced self-compacting concrete (SFRSCC) designated by C15-f45, C25-f60, and C45-f90, where the numbers after letters "C" and "f " represent, respectively, the average compressive strength of SFRSCC at 28 days in Mega Pascal, and the content of hooked-end steel fibres in kilograms per concrete cubic meter. The adopted contents of fibres of 45, 60, and 90 kg/m^3 are conventionally used in pavements, prefabricated elements, and elevated-SFRSCC slab systems, respectively.

Table 3.1: Composition of the developed SFRSCCs (per 1 m^3)

SFRSCC indication		C15-f45	C25-f60	C45-f90
Compressive strength [a]	[MPa]	15	25	45
Cement	[kg]	220	350	423
Water	[kg]	105	160	144
Water-to-cement ratio	[-]	0.48	0.46	0.34
Superplasticizer	[kg]	6.08	9.50	5.92
Limestone filler	[kg]	-	-	362
Fly-ash	[kg]	100	150	-
Fine river sand	[kg]	437	233	220
Coarse river sand	[kg]	693	698	671
Crushed granite	[kg]	615	580	491
VMA [b]	[g]	22	22	-
Fibre type	-	HESF1[c]	HESF1	HESF1
Supplier	-	IBERMIX	IBERMIX	IBERMIX
Content	[kg/m3]	45	60	90
Volume fraction	[%]	0.6	0.8	1.1
Fibre's length	[mm]	35	35	35
Fibre's diameter	[mm]	0.55	0.55	0.55
Aspect ratio	-	63	63	63
Tensile Strength	[MPa]	1300	1300	1300

[a] Nominal
[b] VMA: Viscosity modifying admixture
[c] HESF: Hooked end steel fibres

The compressive strength of SFRSCC of C15-f45 series is lower than the minimum strength often recommended in design guidelines for structural applications, and hence it was unplanned in the predefined test programme. Nevertheless, to evaluate the influence of variables of the research in a broader domain, this series of SFRSCC was additionally included. The SFRSCCs series were developed by using the following materials: Cement Cem 42.5R type I, water, three types of aggregates including fine river sand of maximum

diameter of 0.59 mm, coarse river sand of maximum diameter of 4.76 mm, crushed granite of maximum diameter of 12 mm, superplasticizer of third-generation based on polycarboxylates (SikaViscoCrete 3005), limestone filler, fly-ash, viscosity modifying admixture (Chryso®PlastV70), and hooked end steel fibres. The proportions of the constituents of the series of the developed SFRSCCs are detailed in Table 3.1.

3.2.1 Mixing procedure

To blend the components, a planetary mixer of the vertical axis and 360 litres capacity was used. The aggregates were put into the mixer from the highest to the lowest size (*i.e.* first the crushed granite, then the coarse river sand, and finally the fine river sand) and they were mixed for about one minute. Subsequently, a share of the water was added to the mixed aggregates to saturate the aggregates and mixing continued for one minute. Then the cement, fly ash or limestone filler, the viscosity modifying admixture, if any, the superplasticiser, and the remaining water were added. Mixing was continued for one more minute. Afterwards, the fibres were slowly added to the mixture for preventing fibres blockage in the mixture. The mixing process continued until proper homogeneity of the mixture was attained. Before casting, the flowability and the segregation resistance of the mixtures were examined through the slump flow test executed according to the recommendation of RILEM TC 188-CSC (2006) to assess the self-compacting nature of the developed concretes whose results are summarised in Table 3.2.

Table 3.2: Slump flow test results

		C15-f45	C25-f60	C45-f90
D_f	[mm]	740	660	570
T_{50}	[s]	1.5	2.1	2.9

3.2.2 Specimens

Regarding the shape, geometry, and reinforcing scheme, four types of specimen were built as shown in Figure 3.1, including standard cylinders of 150 mm diameter and 300 mm height and prismatic beams of 150×150 mm cross-section and 600 mm length used to evaluate, respectively, the compressive strength and post-cracking flexural tensile capacity of the developed SFRSCCs. Additionally, beams of 2500 mm length and

100×150 cross-section with two longitudinal reinforcing schemes were constructed to assess the influence of the investigated variables on the flexural capacity and cracking behaviour of SFRSCC flexurally reinforced beams. These beams were tested under four-point bending test configuration.

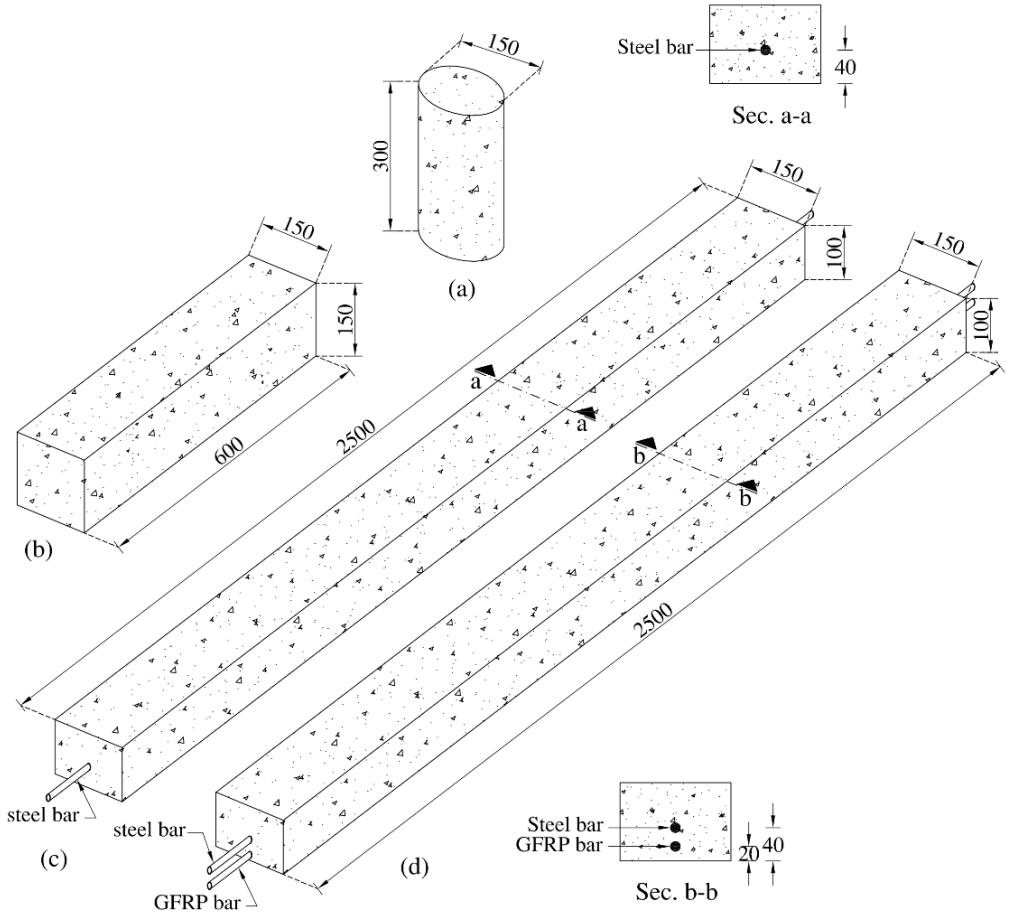

Figure 3.1: Geometry of the specimens: (a) standard cylinder for the uniaxial compression test; (b) SFRSCC beams used in three-point notched beam bending test; and beam reinforced longitudinally with (c) steel bar and (d) steel and GFRP bars used in four-point bending test (dimensions in mm)

The samples of each series of the developed SFRSCCs were built by three batches with the same composition according to the scheme detailed in Table 3.2.

Table 3.3: Adopted scheme for constructing the samples

SFRSCC series	C15-f45			C25-f60			C45-f90		
Batch number	1	2	3	1	2	3	1	2	3
	Number of samples								
Cylinder	2	2	3	2	2	3	3	2	2
Beam of 600 mm length	2	2	6	2	2	6	2	2	6
Beam of 2500 mm length	3[a]	3[b]	-	3[a]	3[b]	-	3[a]	3[b]	-

[a] with longitudinal steel bar

[b] with longitudinal steel and glass fibre reinforced polymer (GFRP) bar

3.2.3 Curing and preparation of specimens

After casting, the samples were covered by wet sack for a day to ensure proper moisture for the curing process. The samples were subsequently demoulded and kept covered with wet sack until the day before testing. In the day before testing, the irregular surface of the cylinders was rectified by a wet saw machine, and a transversal notch was introduced at mid-length of the prismatic beams of 600 mm.

3.3 Mechanical properties of the constituent materials

3.3.1 Compressive behaviour of the SFRSCCs

The compressive strength of each series of SFRSCCs at 28 days (f_{cm}) was obtained through the uniaxial compressive test detailed in Figure 3.2, where the compressive force was provided by a servo-controlled actuator of 3000 kN load carrying capacity. The test was displacement controlled by the internal linear variable displacement transducer (LVDT) of the loading machine. The test methodology was consistent with the specifications advanced by RILEM TC 148-SSC (2000) except, the prescribed rate of the deformation was increased to 10 μm/s as recommended in JSCE-SF4 (1984). This is due to the increase in compressive deformation of concrete by the addition of fibres (Barros and Figueiras 1999b, Cunha 2010).

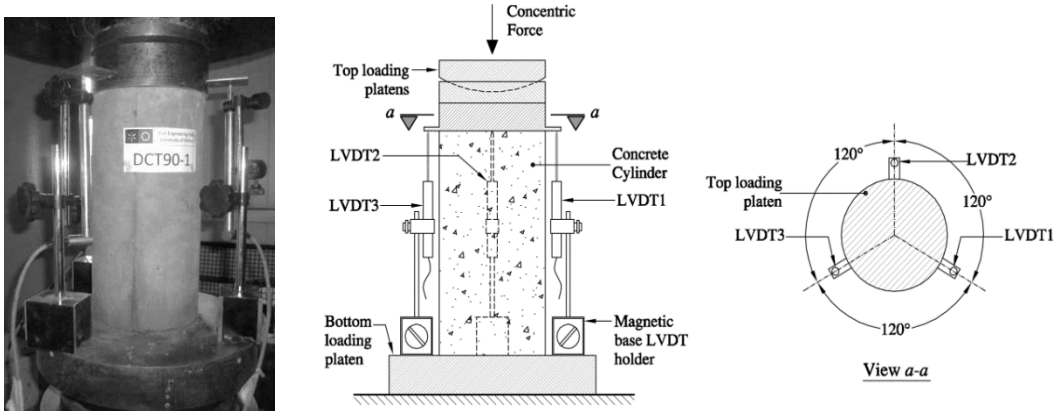

(a) (b)

Figure 3.2: Uniaxial compression test setup: (a) general view, (b) installation of LVDTs around the samples

The adopted prescribed rate of displacement ensures the stability of the test (Barros 1995). As shown in Figure 3.2b, the deformation of the specimen was measured by using three LVDTs with a linear stroke of +/- 5 mm that were mounted around the test sample by forming a relatively angle of 120 degrees. In Figure 3.3, the compressive stress-deformation relationship of the three series of the developed SFRSCCs is depicted, in which the stress was determined by dividing the axial force by the net cross-section area of 17671 mm^2.

The average compressive strength of the SFRSCCs (f_{cm}) is summarised in Table 3.4. In this table is presented the average tensile strength (f_{ctm}) and the average modulus of elasticity of the SFRSCCs (E_{cm}) determined by following the recommendations of *fib* Model Code 2010 (2011) through Equations (3.1) and (3.2), respectively:

$$f_{ctm} = \begin{cases} 0.30\, f_{ck}^{2/3} & \left[\text{for concrete class} \le C50/60\right] \quad (3.1a) \\ 2.12 \ln\left(1 + f_{cm}/10\right) & \left[\text{for concrete class} > C50/60\right] \quad (3.1b) \end{cases}$$

$$E_{cm} = 21.5\left(\frac{f_{cm}}{10}\right)^{1/3} \quad [f_{cm} \text{ in MPa, } E_{cm} \text{ in GPa}] \quad (3.2)$$

In Equation (3.1a) f_{ck} is the characteristic value of concrete compressive strength, considered equal to the mean strength (f_{cm}) minus 8 MPa (*fib* Model Code 2010 2011).

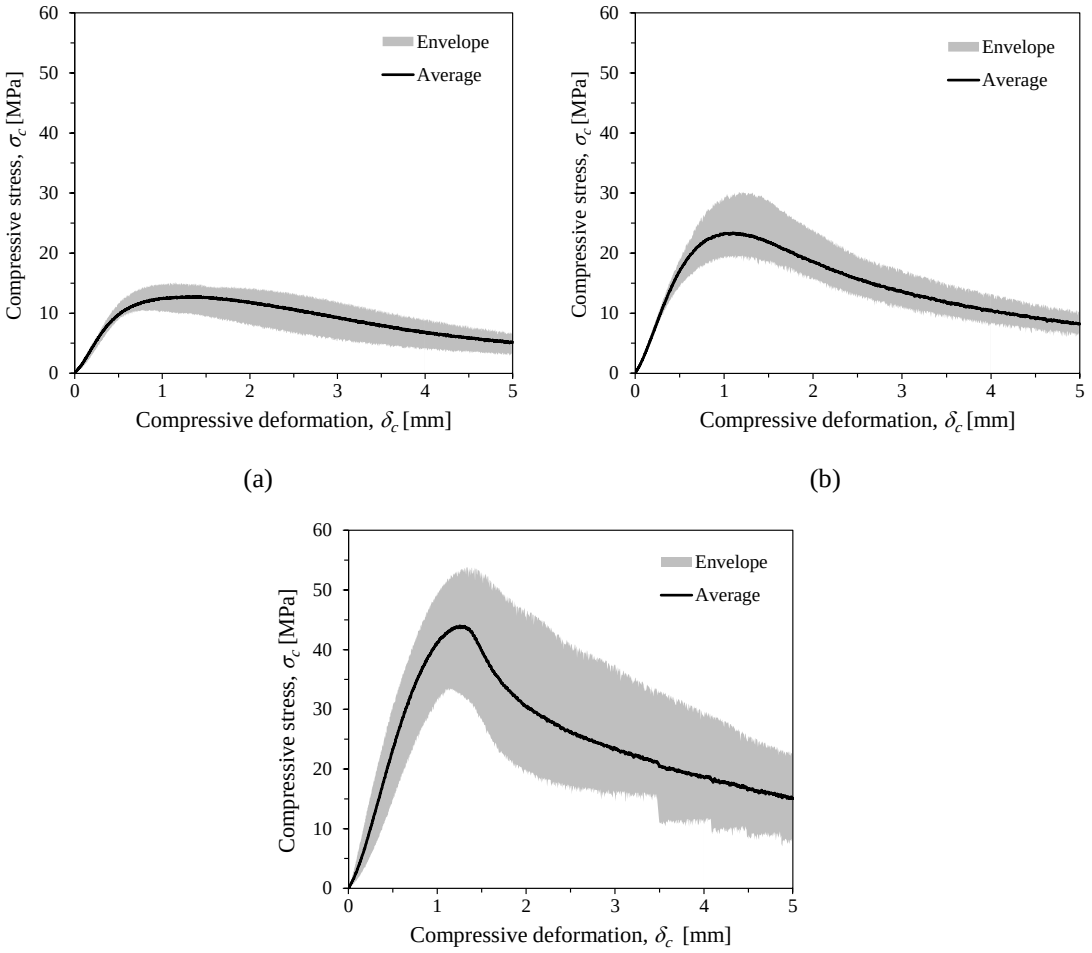

Figure 3.3: Compressive stress – deformation relationship for the (a) C15-f45, (b) C25-f60, and (c) C45-f90 series of SFRSCCs

Table 3.4: Material properties of the SFRSCCs

SFRSCC indication	f_{cm} [MPa]	f_{ctm} [MPa]	E_{cm} [GPa]
C15-f45	13.12	0.89	23.54
C25-f60	23.57	1.87	28.62
C45-f90	43.99	3.27	35.23

3.3.2 Post-cracking behaviour of the SFRSCCs

The post-cracking response of the SFRSCCs was evaluated by executing the three-point notched beam bending test according to the recommendations of *fib* Model Code 2010 (2011) in a test setup depicted in Figure 3.4.

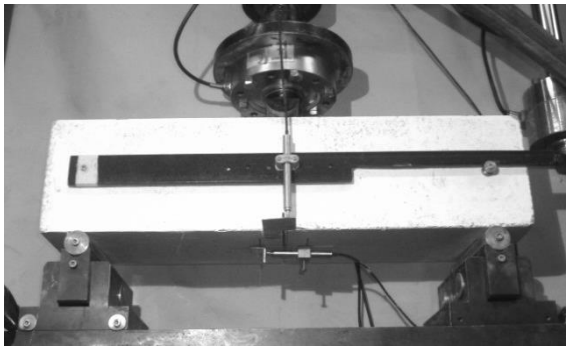

Figure 3.4: A view of the three-point notched beam bending test setup

The three-point notched beam bending test was performed on prismatic beams with 600 mm length and 150×150 mm^2 cross-section (Figure 3.1b). To promote crack localisation at the midsection of the specimen and in agreement with the recommendations of *fib* Model Code 2010 (2011), the beams were subjected to a transversal notch of 5 mm width and 25 mm depth at mid-length of a lateral side parallel to the casting direction.

The specimen was supported by a pair of roller supports that include two steel bars of 30 mm diameter, providing a free span length of 500 mm, as depicted in Figure 3.5. The vertical deflection of the beam at the mid-span was measured by LVDT1 of a linear stroke of +/-10 mm, supported in a steel yoke mounted to the front side of the beam by a simple hinge and a roller connection at extremities (Figure 3.5a). The crack mouth opening displacement (CMOD) was measured by LVDT2 of a linear stroke of +/-10 mm, installed on the bottom face of the beam with a measuring length of 30 mm (Figure 3.5b).

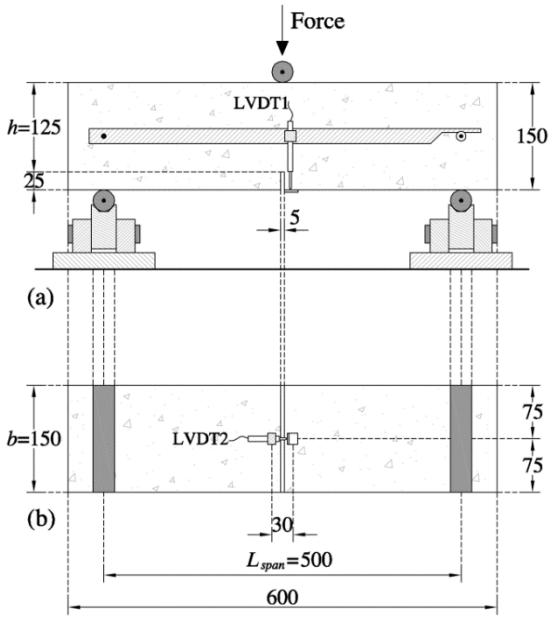

Figure 3.5: (a) front side and (b) bottom side of the notched beam (dimensions in mm)

The three-point notched beam bending test was displacement controlled at a constant rate of 2 μm/s, in a closed-loop system based on the readout of LVDT1, while the imposed force introduced by a servo-hydraulic actuator of 150 kN capacity was measured by a load cell of 200 kN capacity. The envelope and the average force-CMOD relationship of the three series of the tested notched beams are depicted in Figure 3.6.

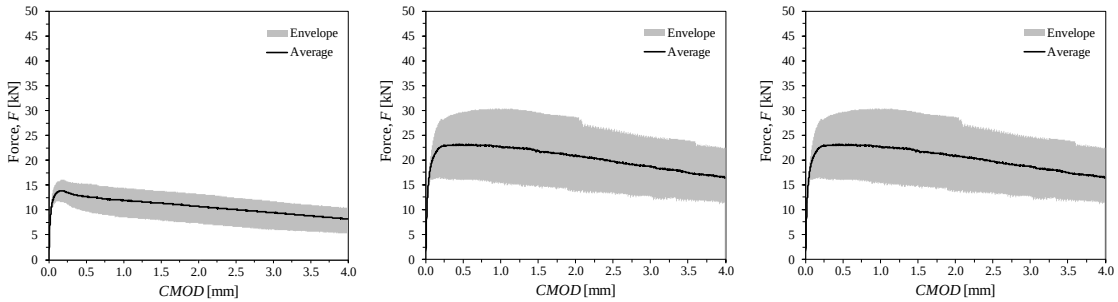

Figure 3.6: Force-CMOD relationship of (a) C15-f45, (b) C25-f60, and (c) C45-f90 registered in the three-point notched beam bending test

3.3.2.1 Characterisation of the post-cracking of the SFRSCCs by following recommendations of *fib* Model Code 2010 (2011)

By adopting the recommendation of *fib* Model Code 2010 (2011), the average flexural residual strength ($f_{Ri,m}$) is determined from the following equation:

$$f_{Ri,m} = \frac{3F_{i,m}\ L_{span}}{2\ b\ h_{sp}^2} \tag{3.3}$$

where $b = 150$ mm is the width of the beam, $h_{sp} = 125$ mm is the height of the ligament over the notch tip (fracture plane), and $L_{span} = 500$ mm is the length of the beam span. In addition, $F_{i,m}$ is the average force corresponding to the i^{th} crack mouth opening displacement ($CMOD_i$) equal to 0.5, 1.5, 2.5, and 3.5 mm. The average and characteristic values of flexural residual strengths (f_{Ri}) are summarised in Table 3.5. The latter was determined considering the *t*-student distribution for defining the lower bound of 80% confidence interval of the mean (Salehian 2015).

Table 3.5: The average and characteristic values of flexural residual strengths of the SFRSCCs

SFRSCC series	$f_{R1,m}$ [MPa]	$f_{R1,k}$ [MPa]	$f_{R2,m}$ [MPa]	$f_{R2,k}$ [MPa]	$f_{R3,m}$ [MPa]	$f_{R3,k}$ [MPa]	$f_{R4,m}$ [MPa]	$f_{R4,k}$ [MPa]
C15-f45	4.02	2.97	3.62	2.45	3.20	2.05	2.80	1.75
C25-f60	7.36	4.14	7.10	3.41	6.44	3.54	5.65	3.15
C45-f 90	11.59	8.73	11.15	8.86	9.70	7.40	8.47	7.01

For the ultimate limit states, *fib* Model Code 2010 (2011) recommends the linear stress-crack opening displacement schematised in Figure 3.7 for the post-cracking response of FRCs. In this figure, $f_{Fts,m}$ and $f_{Ftu,m}$ represent the average residual strength of FRC in the serviceability and the ultimate limit states, respectively, which are determined by the Equations (3.4) and (3.5), respectively.

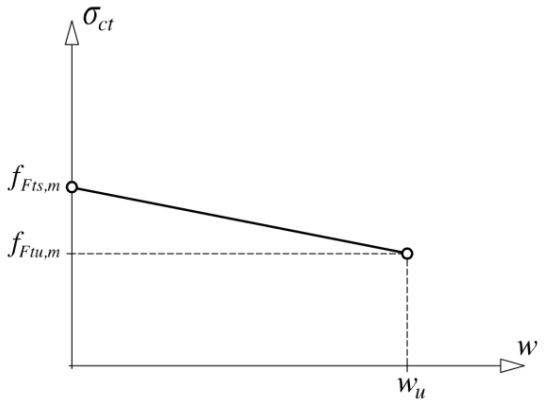

Figure 3.7: Stress-crack opening relationship of FRC recommended in *fib* Model Code 2010 (2011)

$$f_{Fts,m} = 0.45 f_{R1,m} \tag{3.4}$$

$$f_{Ftu,m} = f_{Fts,m} - \frac{w_u}{CMOD_3}(f_{Fts,m} - 0.5 f_{R3,m} + 0.2 f_{R1,m}) \geq 0 \tag{3.5}$$

where w_u is the ultimate value of crack opening, which depends on the level of required ductility, which can be considered equal to 2.5 mm. By adopting the abovementioned methodology, the post-cracking response of the developed SFRSCCs was characterised as represented in Figure 3.8.

For structural applications with normal and high-strength concrete, the FRC classification proposed by *fib* Model Code 2010 (2011) is based on the post-cracking residual strength. For this purpose, the f_{R1k} (representing the strength interval) and a letter *a, b, c, d* or *e* (representing the f_{R3k} / f_{R1k} ratio) are considered. For instance (Figure 3.9), a material denoted as "7b" has a strength f_{R1k} ranging between 7 and 8 MPa, and a f_{R3k} / f_{R1k} ratio ranging between 0.7 and 0.9. By adopting the methodology recommended by *fib* Model Code 2010 (2011), the toughness classes of the developed SFRSCC were determined summarised in Table 3.6.

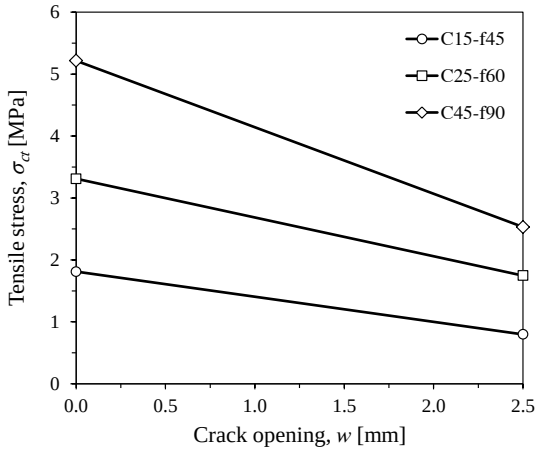

Figure 3.8: Post-cracking stress-crack width relationship of SFRSCCs determined by following the recommendations of *fib* Model Code 2010 (2011)

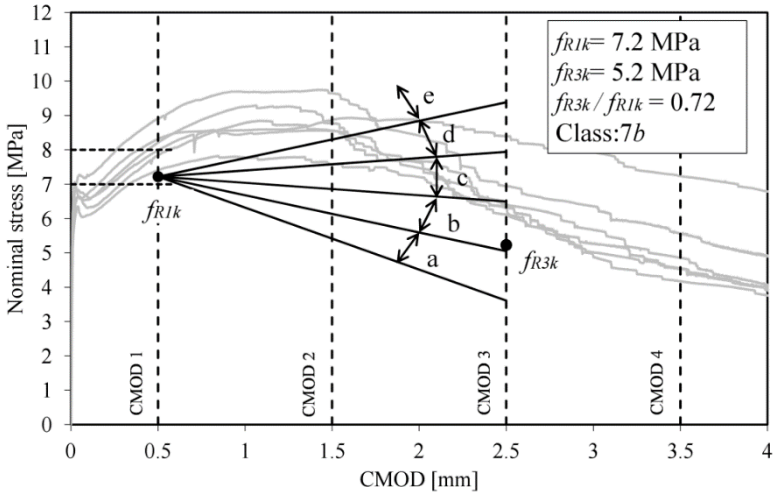

Figure 3.9: The concept of toughness class for FRC based on the relationship between the flexural stress and CMOD (*fib* Model Code 2010 2011)

Table 3.6: Toughness classes according to the *fib* Model Code 2010 (2011)

Case study	Interval of f_{R1k} [MPa]	Interval of f_{R3k} / f_{R1k}	Toughness classification
C15-f45	[2-3]	[0.5-0.7]	2a
C25-f60	[4-5]	[0.7-0.9]	4b
C45-f90	[8-9]	[0.7-0.9]	8b

3.3.2.2 Characterisation of the post-cracking of the SFRSCCs by inverse analysis

The mode I fracture parameters of the developed SFRSCCs were also determined by the inverse analysis (IA), by using the force-deflection results registered in the performed 3PNBBT. For this purpose, the 3PNBBT was simulated with a constitutive model implemented in a software based on the finite element method (FEM), FEMIX V4.0, which is described elsewhere (Ventura-Gouveia *et al.* 2011). By using the finite element mesh shown in Figure 3.10, a notched FRC beam with a span length of 500 mm, a cross-section of 150×150 mm^2, and a notch of 5 mm width and 25 mm depth was simulated.

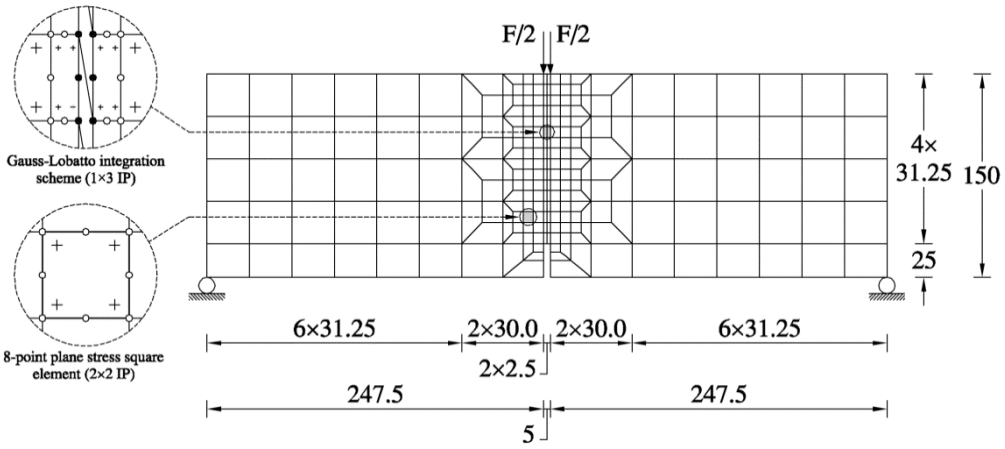

Figure 3.10: Finite element mesh, loading and support conditions of the specimen adopted for the simulation of three-point notched beam bending tests (dimensions in mm)

This beam was modelled by 8-node serendipity plane stress finite elements with Gauss-Legendre integration scheme of 2×2 integration points (IP). The opening of the crack over the notch was also simulated by introducing in the plane of symmetry of the specimen interface finite elements of six nodes with Gauss–Lobatto integration scheme of 1×3 IP for assuring the crack progresses along this plane.

Apart from the interface finite elements, the remaining finite elements were considered with linear-elastic behaviour in compression and tension depicted, respectively, in Figure 3.11(a) and (b). The compression and the tensile behaviour up to crack initiation of the material over the notch (simulated by the interface finite elements)

were also assumed linear-elastic, while its post-cracking tensile stage was simulated by a trilinear stress-crack opening relationship depicted in Figure 3.11(c). In the performed IA, a specific value of the tensile strength (f_{ctm}) was assumed, determined by Equation (3.1) (Table 3.3).

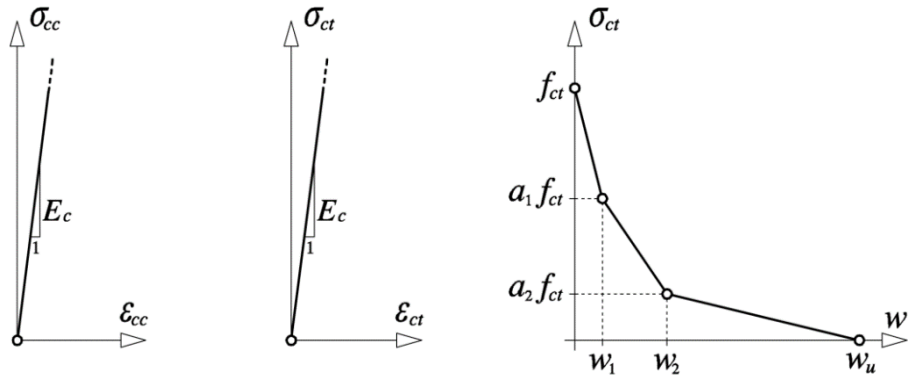

(a) (b) (c)

Figure 3.11: Constitutive laws of FRC adopted in the performed FEM simulation; (a) and (b) linear elastic stress-strain behaviour of intact concrete in compression and tension, respectively, and (c) mode I fracture property of cracked FRC in terms of the stress-crack opening relationship

In a trial computation, the $\sigma_{ct} - w$ of the fracture mode I constitutive law of the interface finite elements is obtained by best fitting the force-deflection relationship registered experimentally in the 3PNBBT. In a generic k^{th} step of the incremental procedure of the notched beam mid-span deflection (δ^k), the numerical force (F_{Num}^k) determined by the FEM is compared to the force registered experimentally (F_{Exp}^k) to evaluate the deviation history in terms of force (D_F) and toughness (D_T) during the loading process of the beam, by adopting the following equations:

$$D_F = \left| F_{Exp}^k - F_{Num}^k \right| / F_{Exp}^k \tag{3.6}$$

$$D_T = \left| A_{Exp}^{(F-\delta)_k} - A_{Num}^{(F-\delta)_k} \right| / A_{Exp}^{(F-\delta)_k} \tag{3.7}$$

where $A_{Exp}^{(F-\delta)_k}$ and $A_{Num}^{(F-\delta)_k}$ are the area beneath, respectively, the experimental and numerical force-deflection curves up to the central deflection of δ^k. In each step of the calculation, if D_F or D_T exceeds the considered tolerance (2%), the procedure is interrupted, and a new simulation is automatically started by adopting new values for the post-cracking parameters of the FRC.

Figure 3.12 represents the accuracy of performed inverse analysis by comparing the force-deflection responses obtained from the inverse approach with the ones registered in the experiment. Figure 3.13 represents the post-cracking response of the three series of SFRSCCs determined by the inverse approach in terms of stress-crack opening displacement, whose intervening parameters are summarised in Table 3.7.

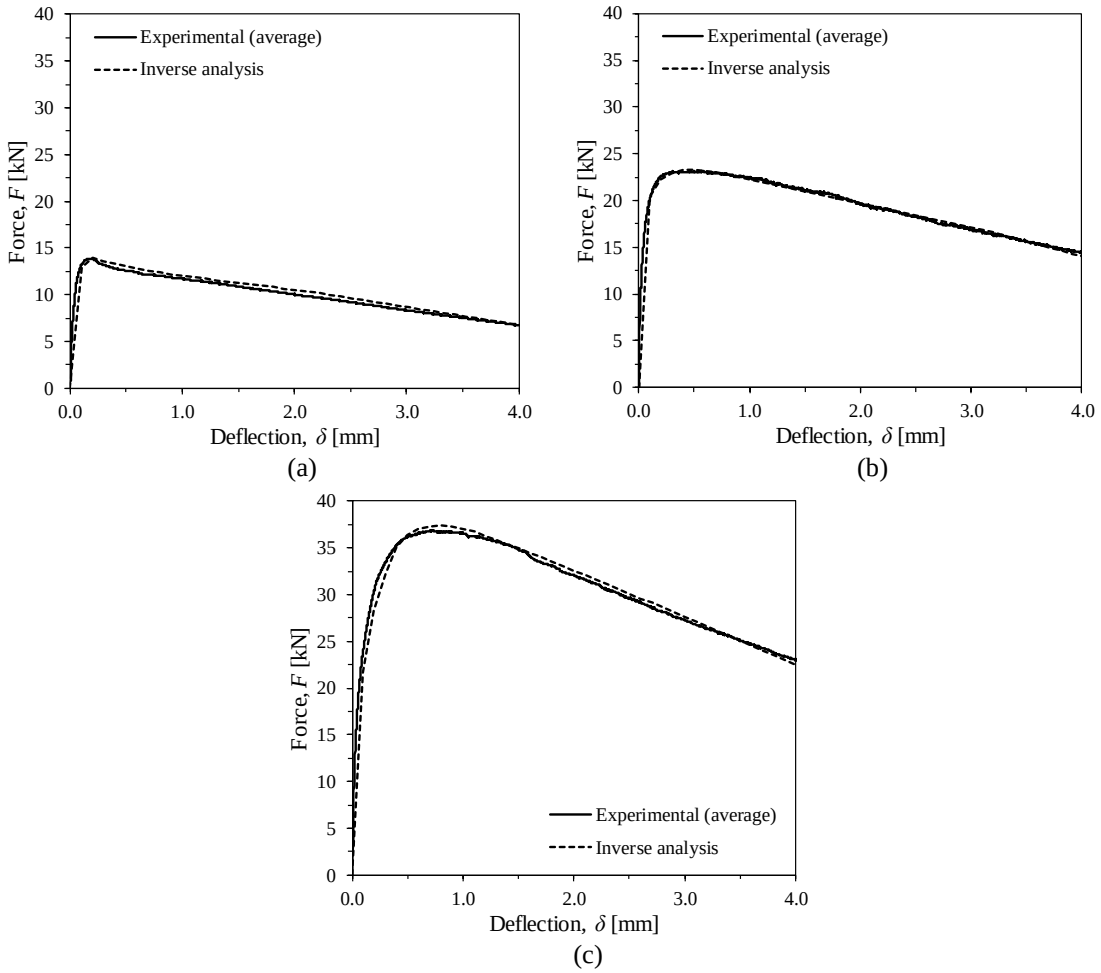

Figure 3.12: Predictive performance of the inverse analysis of the three-point notched beam bending tests performed on the (a) C15-f45, (b) C25-f60, and (c) C45-f90 series of specimens

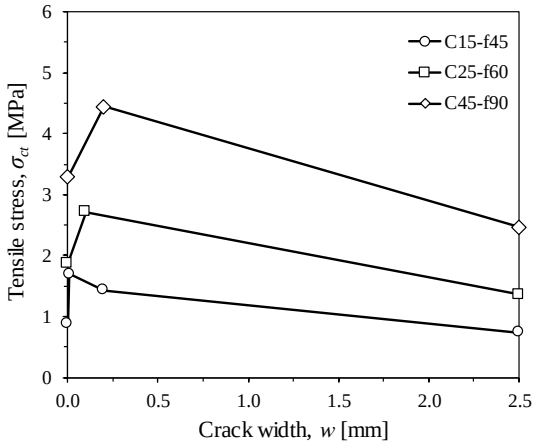

Figure 3.13: Post-cracking stress-crack width relationship of SFRSCCs determined by inverse analysis

Table 3.7: Values of parameters defining the constitutive laws of SFRSCCs

SFRSCC series	$f_{ct} = \sigma_{cr}$ [MPa]	a_1 [-]	a_2 [-]	w_1 [mm]	w_2 [mm]	w_u [mm]
C15-f45	0.89	1.90	1.60	0.01	0.20	5.00
C25-f60	1.87	1.45	0.20	0.10	4.90	5.00
C45-f90	3.27	1.35	0.60	0.20	3.00	5.00

3.3.2.3 Comparison between the prediction of *fib* model code 2010 and the results of inverse analysis

In Figure 3.14, the stress-crack opening relationship of the SFRSCCs obtained by the inverse analysis is compared to the ones determined by following the recommendations of *fib* Model Code 2010 (2011). This figure reveals following the recommendation of *fib* Model Code 2010 (2011) may lead to relatively higher post-cracking constitutive laws when compared to the inverse approach.

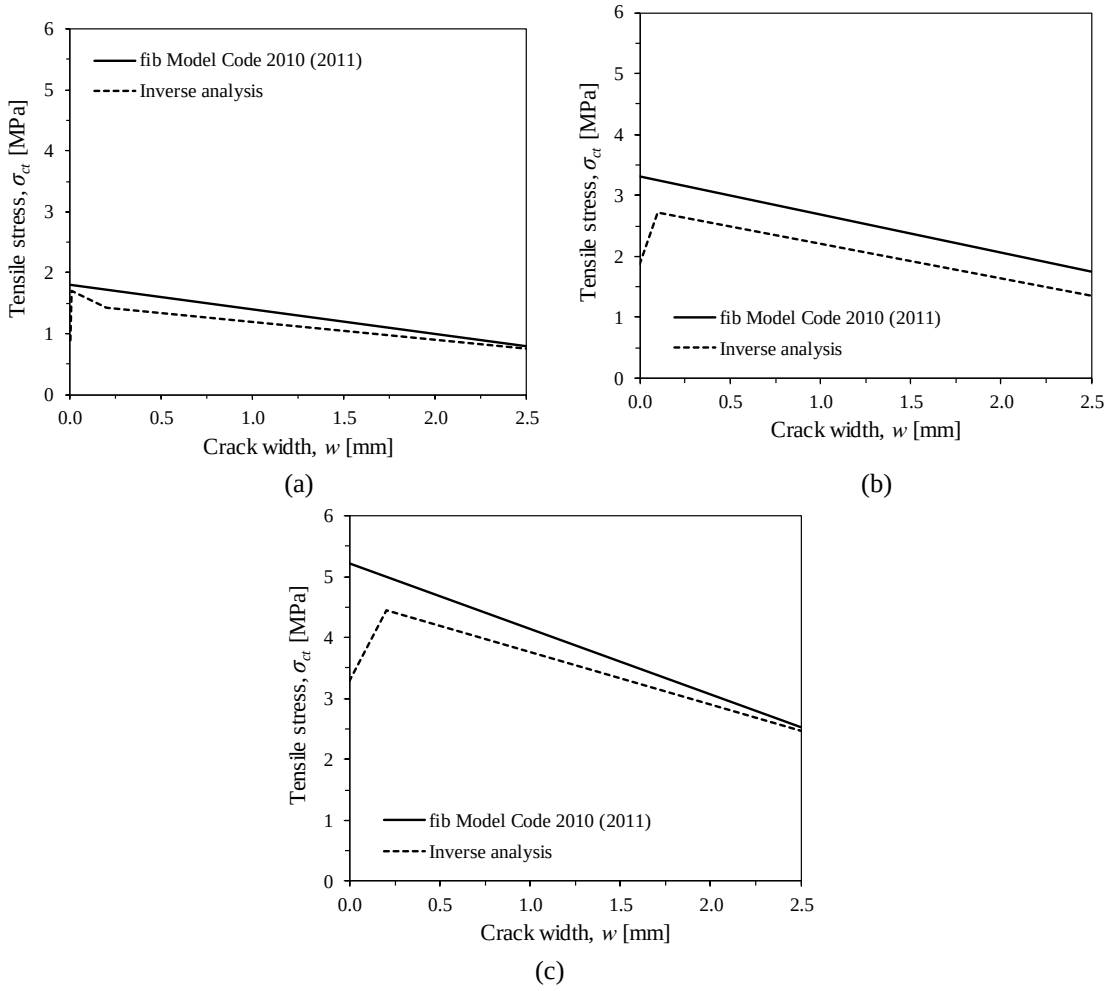

Figure 3.14: Comparison between the post-cracking response of SFRSCCs determined by inverse analysis and the ones recommended by fib Model Code 2010 (2011) for the (a) C15-f45, (b) C25-f60, and (c) C45-f90 series of specimens

3.3.3 Mechanical properties of longitudinal reinforcement

The tensile behaviour of steel and glass fibre reinforced polymer (GFRP) bars used in the test programme to reinforce the R/FRC beams were determined by executing the direct tensile test according to the ASTM A370 (2014) recommendation. The adopted test setup is depicted in Figure 3.15 according to which a pair of self-gripping clamps was utilised to transfer the tensile force to the bars. The bottom grip was fixed on the bottom surface of the loading machine while the top one, was pulled up by a hydraulic actuator of 100 kN. The clamping system consisted of interchangeable wedge jaws moved down and fixed into the bar by the initial gripping force generated by hydraulic pressure. The

direct tensile test was executed on three representatives steel and GFRP bars of 300 mm and 1200 mm length, respectively. The preliminary test conducted on GFRP bars presented undesirable slippage of GFRP bar because of its smooth surface. Furthermore, a premature failure was observed at clamped extremities of GFRP bars due to localisation of tensile stresses. To overcome these drawbacks, two extremities of the GFRP bars were covered by a pair of steel tubes of 300 mm length, 15 mm outer diameter, and 2 mm thickness (Figure 3.15b). The fixed connection between GFRP bar and steel tube was ensured by a high strength epoxy resin with a tensile strength of 30 MPa, which was cured for two weeks (Figure 3.15c).

The uniaxial tensile test executed on bars was displacement controlled with a constant rate of 3 μm/s. During loading, elongation of the bars was measured by a clip-on extensometer with a measuring length of 50 mm, mounted at mid-length of the specimens as shown in Figure 3.15(a) and (b). The test continued until the failure of specimens.

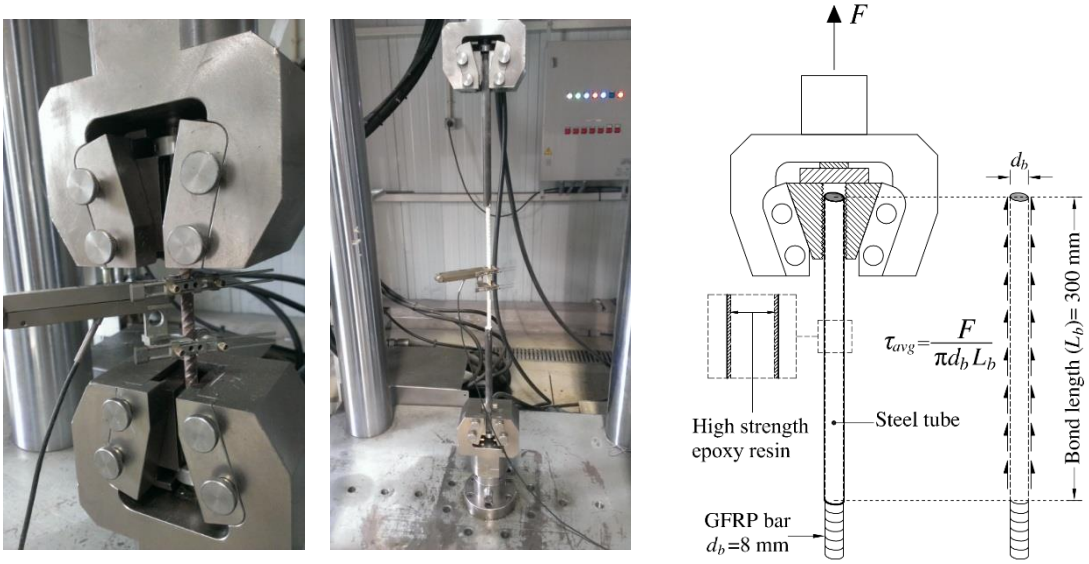

(a) (b) (c)

Figure 3.15: Direct tensile test conducted on (a) steel, (b) GFRP bars, and (c) details of transferring the applied load to GFRP

The average tensile stress-strain relationship of the steel and GFRP bars are depicted in Figure 3.16(a) and (b), respectively, where the stress and strain are determined, respectively, by dividing the total imposed axial force to the bar cross-section (=50.27 mm^2), and dividing the elongation measured by the extensometer to the initial measuring length (=50 mm). Considering diagrams of Figure 3.16, mechanical properties of reinforcing bars including, modulus of elasticity of steel and GFRP bars (E_s and E_G), stress and strain of steel bars at yielding (σ_{sy} and ε_{sy}) and ultimate stress and strain of steel bars (σ_{su} and ε_{su}), and ultimate stress and strain of GFRP bars (σ_{Gu} and ε_{Gu}) were determined, and are summarised in Table 3.8.

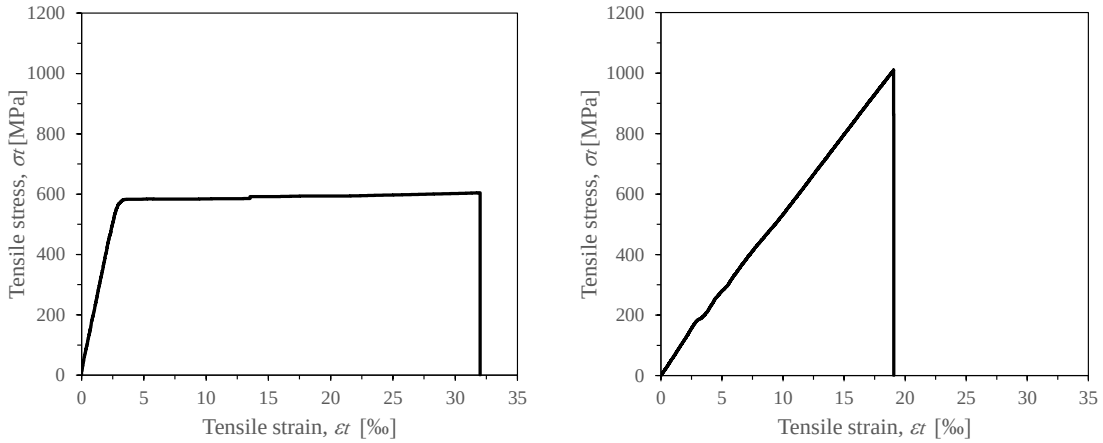

Figure 3.16: Average tensile stress-strain relationship of (a) steel and (b) GFRP bars

Table 3.8: Mechanical properties of steel and GFRP bars

Steel bar					GFRP bar		
E_s [GPa]	σ_{sy} [MPa]	ε_{sy} [‰]	σ_{su} [MPa]	ε_{su} [‰]	E_G [GPa]	σ_{Gu} [MPa]	ε_{Gu} [‰]
205	575	2.8	605	32	58	1058	18.0

3.4 Flexural behaviour of SFRSCC beams hybrid reinforced longitudinally

The flexural behaviour of reinforced FRC (R/FRC) beams was evaluated in a four-point bending test configuration. The test specimens were beams of 2500 mm length, with a cross-section of 100 mm height and 150 mm width, reinforced longitudinally by two different schemes. Three series of which were reinforced with a 8 mm diameter steel bar (SR beams) with a 40 mm concrete cover, and three others were reinforced by either steel and GFRP bars (SGR beams) both of 8 mm diameter, with a concrete cover of 40 mm and 20 mm, respectively (see Figures 3.1c and 3.1d). The adopted geometric properties of the R/FRC beams reduce the flexural capacity of the beams and prevent the occurrence of shear failure without using any transversal reinforcement.

Table 3.9: Designation and reinforcement details of the beams

Beam's designation	Num. of samples	Constituent SFRSCC	Long. steel bar	Long. GFRP bar	ρ_s [%]	ρ_G [%]
SR/FRC1545	3	C15-f45	1Φ8	-	0.56	-
SGR/FRC1545	3	C15-f45	1Φ8	1Φ8	0.56	0.42
SR/FRC2560	3	C25-f60	1Φ8	-	0.56	-
SGR/FRC2560	3	C25-f60	1Φ8	1Φ8	0.56	0.42
SR/FRC4590	3	C45-f90	1Φ8	-	0.56	-
SGR/FRC4590	3	C45-f90	1Φ8	1Φ8	0.56	0.42

Each series of beams includes three samples of similar geometric properties and reinforcement scheme. The beams are generally designated by xR/FRCyz (Table 3.9), where x represents the longitudinal reinforcement scheme, which can be "S" and "SG" in the case of beams reinforced exclusively with a steel bar, and with steel and GFRP bar, respectively. The letters "y" and "z" represent, respectively, the nominal compressive strength (in MPa) of the beam's SFRSCC and the content of fibres (in kg/m^3) in this composite (see Table 3.1).

It is well acknowledged that the contribution of the post-cracking response of FRC in R/FRC elements is much more pronounced when a lower percentage of longitudinal

reinforcement is utilised (Taheri *et al.* 2012). Therefore, a relatively small reinforcing ratio ($\rho_s = A_s / b\,d_s$ and $\rho_G = A_G / b\,d_G$ for steel and GFRP bar, respectively) were adopted for the SR and SGR series beams to assure yielding of steel bar before the ultimate failure. In this regard, ρ_s of lower than the balanced reinforcement ratio (ρ_b^{SR}) was utilised in the case of SR beams, which is obtained in a condition that the failure mode is attained by concrete crashing in compression while steel bar is yielded in tension, simultaneously, as depicted in Figure 3.17. Neglecting the contribution of pre-cracking tensile concrete ρ_b^{SR} can be determined from Equation (3.8):

$$\rho_b^{SR} = \frac{1}{d_s \sigma_{sy}} \left(\kappa_1 \kappa_2 f_{cm} d_{NA,b}^{SR} - f_{Ftu} (h - d_{cr,b}^{SR}) \right) \tag{3.8}$$

where f_{cm} and σ_{sy} are, respectively, the mean concrete compressive strength and the yield strength of steel bar, and $d_{NA,b}^{SR}$ and $d_{cr,b}^{SR}$ are depth of neutral axis for the balanced condition and depth of layer in which concrete cracking strain (ε_{cr}) is attained, respectively, which are obtained from the following equations:

$$d_{NA,b}^{SR} = \frac{\varepsilon_{cu}}{\varepsilon_{cu} + \varepsilon_{sy}} d_s \tag{3.9}$$

$$d_{cr,b}^{SR} = \frac{\varepsilon_{cu} + \varepsilon_{cr}}{\varepsilon_{cu}} d_{NA,b}^{SR} \tag{3.10}$$

being ε_{cu} the ultimate compressive strain of concrete considered equal to 3.5‰ (*fib* Model Code 2010 2011), ε_{sy} the strain of steel bar at yield initiation represented in Table 3.8, and $\varepsilon_{cr} = f_{ct} / E_c$ cracking strain of concrete. In Equation (3.9), d_s = 60 mm is the depth of steel reinforcement with respect to the upper face of the cross-section (Figure 3.17). In Equation (3.8) κ_1 and κ_2 are two constants defining, respectively, the equivalent concrete compressive strength and height of the compression zone (see Figure 3.17). For the concrete classes utilised in the present research, κ_1 and κ_2 are considered equal to 1.0 and 0.8, respectively (*fib* Model Code 2010 2011). Furthermore, $f_{Ftu,m}$ is

the ultimate residual strength and as *fib* Model Code 2010 (2011) recommends, it can be determined as follows:

$$f_{Ftu,m} = \frac{f_{R3,m}}{3} \tag{3.11}$$

being $f_{R3,m}$ the average residual flexural tensile strength of fibre reinforced concrete corresponding to the *CMOD* of 2.5 mm. The ρ_s / ρ_b^{SR} ratio of the SR series beams is lower than unity as represented in Table 3.10, which means that yielding of steel bar occurs before attainment of the flexural capacity of SR series beam.

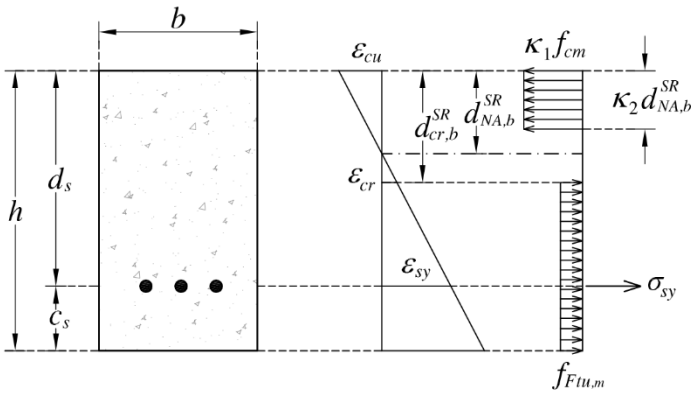

Figure 3.17: Variation of strain and stress of SR beams cross-section at balance condition

The balanced condition in FRP reinforced concrete elements either with or without steel reinforcement, is defined as a condition that the FRP bar ruptures, simultaneously, with the concrete crushing in compression (Soltanzadeh et al. 2016a). Since the tensile strength of FRP-type reinforcing bar is often extremely high, the above-defined balanced condition is just attainable when the height of the cross-section is long enough and concrete of higher strength class is utilised which is not the case of the SGR series beam built in the present research.

Table 3.10: Reinforcing ratio of SR and SGR series beam

Beam's designation	ρ_s [%]	ρ_b^{SR} [%]	ρ_s / ρ_b^{SR} [-]	ρ_G [%]	ρ_G^* [%]	ρ_G / ρ_G^* [-]
SR/FRC1545	0.56	0.81	0.7	-	-	-
SGR/FRC1545	0.56	-	-	0.42	0.4	1.0
SR/FRC2560	0.56	1.41	0.4	-	-	-
SGR/FRC2560	0.56	-	-	0.42	1.3	0.32
SR/FRC4590	0.56	2.78	0.2	-	-	-
SGR/FRC4590	0.56	-	-	0.42	3.4	0.12

It is notable that the structural behaviour of hybrid reinforced concrete element in the serviceability limit states is the primary objective of the present research and therefore, the balanced condition in SGR series beams is of less importance.

According to the adopted geometrical and material properties of built beams, the tensile rupture of the used GFRP bar is not expected in the SGR series beams and concrete crashing is likely the dominant failure mode. In this case, the employed reinforcement ratio of the GFRP bar (ρ_G) is lower than ρ_G^* which is the reinforcing ratio of GFRP bar by which yielding of steel reinforcement occurs simultaneously with concrete crushing in compression (Figure 3.18). ρ_G^* is determined from the following equation:

$$\rho_G^* = \frac{1}{d_G \sigma_G^*}\left(\kappa_1 \kappa_2 f_{cm} d_{NA}^* - f_{Ftu}(h - d_{cr}^*) - \frac{A_s \sigma_{sy}}{b}\right) \tag{3.12}$$

where d_{NA}^* and d_{cr}^* are equal to $d_{NA,b}^{SR}$ and $d_{cr,b}^{SR}$ determined by Equations (3.9) and (3.10), respectively, and σ_G^*, the actual stress of GFRP bar, is obtained by the Equations (3.13):

$$\sigma_G^* = E_G \varepsilon_{cu}(d_G - d_{NA}^*) / d_{NA}^* \leq \sigma_{Gu} \tag{3.13}$$

In Table 3.10, the ρ_G / ρ_G^* ratio in the SGR series beam are also summarised.

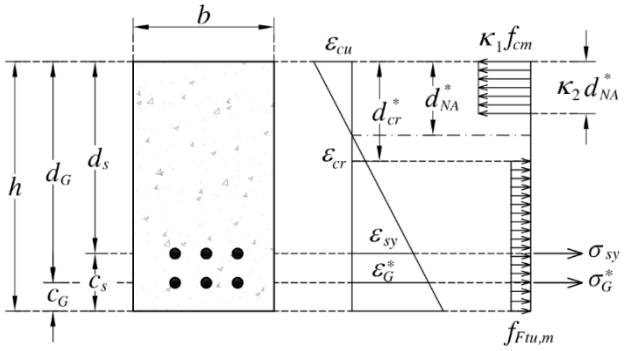

Figure 3.18: Variation of strain and stress of SGR beams cross-section when concrete is crashing in compression

3.4.1 Test setup

A view of the performed four-point bending test setup is shown in Figure 3.19, according to which the beams are positioned symmetrically on two roller supports with a span length of 2300 mm. By using an intermediate steel profile, the load introduced by a hydraulic actuator of 50 kN capacity was transmitted to the beam at two points located at a distance of 250 mm with respect to the span centre. This arrangement leads to a central pure bending region of 500 mm length.

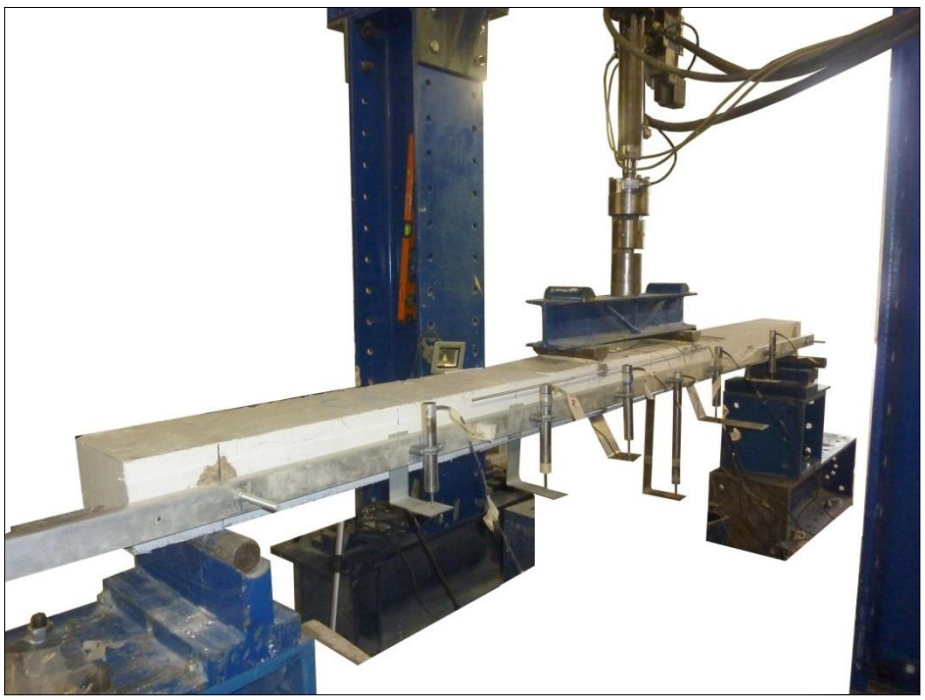

Figure 3.19: View of four-point bending test

By the use of an aluminium yoke, six vertical LVDTs (LVDT1 to LVDT6 in Figure 3.20a) were installed along with the beams to measure the vertical deflection of the beam in alignment of applied loads, centre of the span, and at each one-third of the left and middle of the right shear span of the beam, respectively.

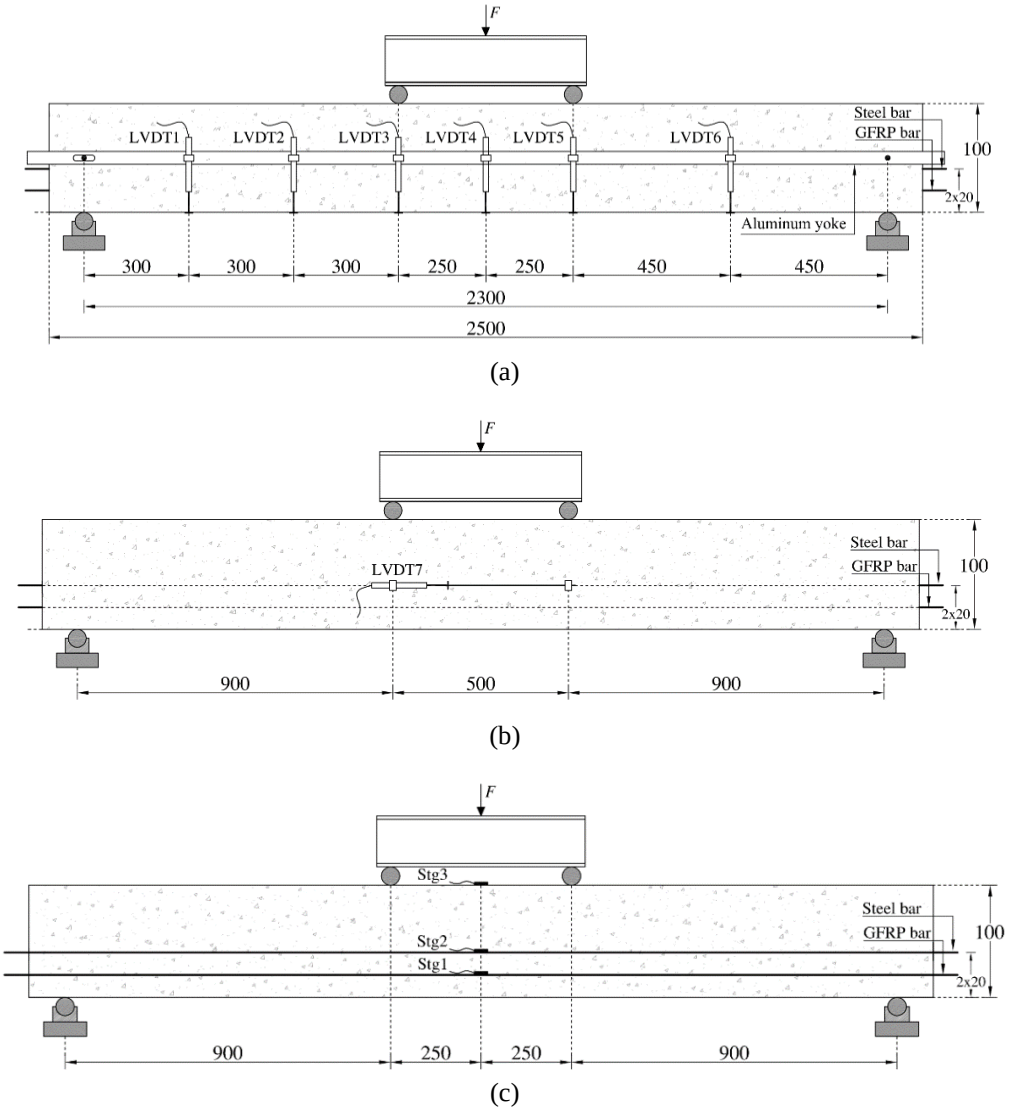

Figure 3.20: Four-point bending test setup; the position of (a) vertical LVDTs, (b) horizontal LVDT, and (c) strain gages (dimensions in mm)

Furthermore, a horizontal LVDT (LVDT7 in Figure 3.20b) was used to measure the longitudinal elongation of the central pure bending region at the level of steel bars. The readout of this LVDT was taken to determine the average crack width of the beams along with the pure bending region.

Additionally, the strain of the longitudinal reinforcements was measured by a pair of strain gages installed on the reinforcements at the mid-span, represented by the acronyms Stg1 and Stg2 in Figure 3.20(c). The compressive strain of concrete at the centre was also measured by a third strain gage (Stg3). The four-point bending test was displacement controlled with a rate of 1 μm/s considering vertical deflection measured at the centre (LVDT4 in Figure 3.20a).

3.4.2 Force-central deflection relationship

The envelope and average force-central deflection relationships of the tested SR and SGR beams are depicted in Figure 3.21.

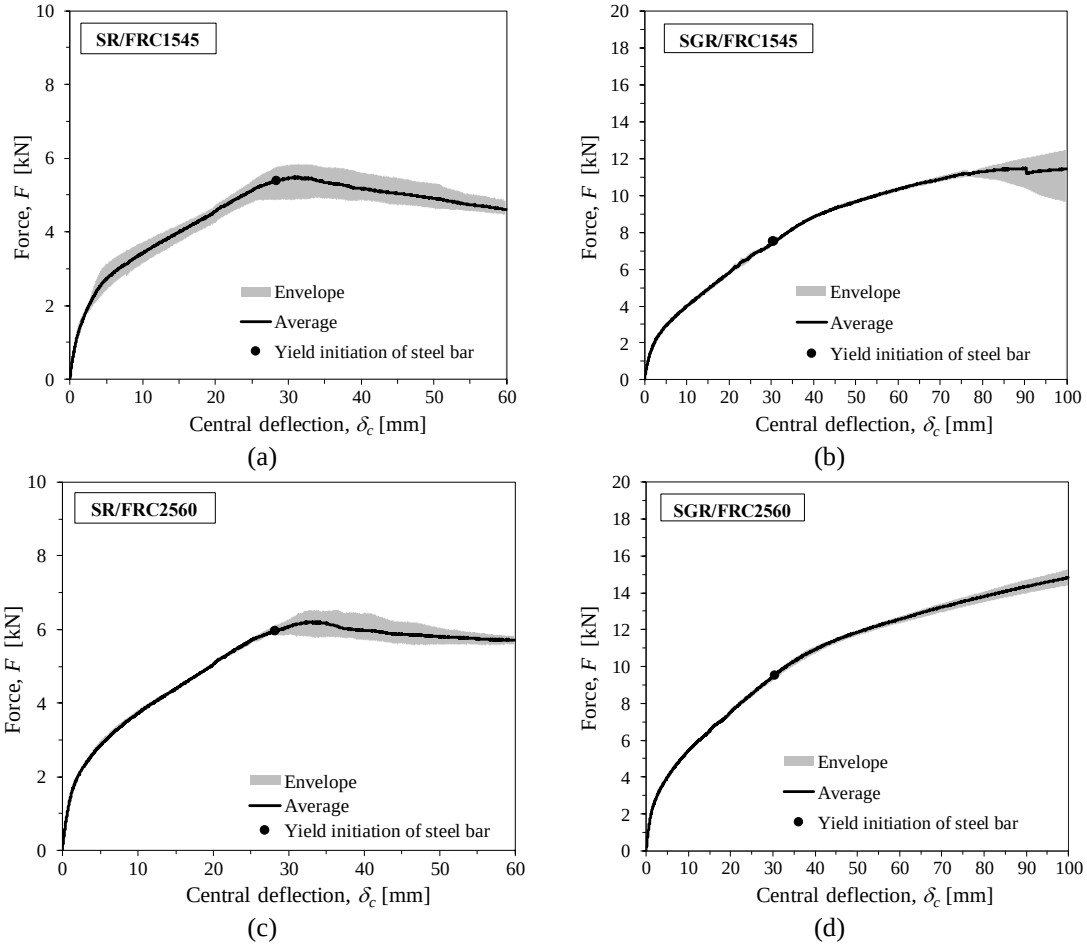

Figure 3.21: continuied

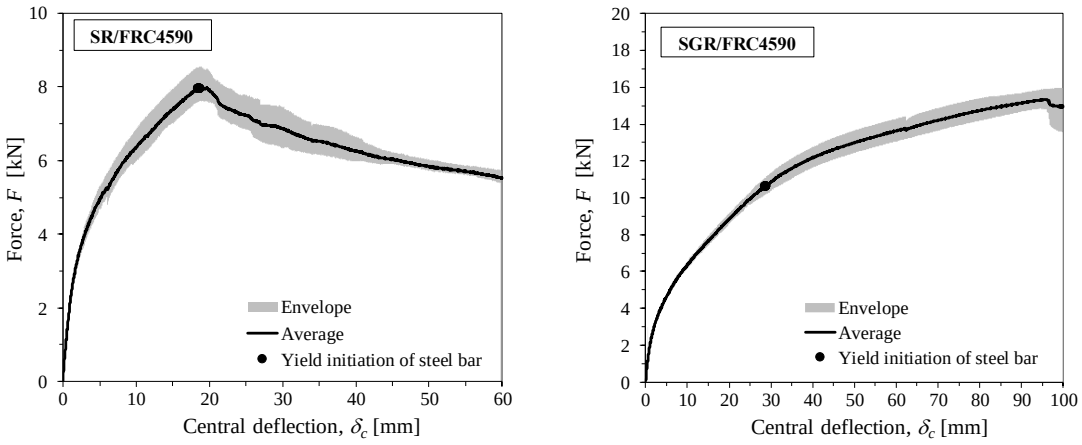

(e) (f)

Figure 3.22: Force-central deflection relationship of (a) SR/FRC1545, (b) SGR/FRC1545, (c) SR/FRC2560, (d) SGR/FRC2560, (e) SR/FRC4590, and (f) SGR/FRC4590

In these figures are also pointed the yield initiation of longitudinal steel bar regarding the readout of strain gage installed on steel bar (Stg2 in Figure 3.20c). Considering the test results, the average load at the limit of serviceability (F_{SLS}), which is assumed corresponding to the central deflection of $\delta_{SLS} = L_{span} / 250$ $(= 9.20\,\text{mm})$ as recommended by EN 1992-1-1 (2004), at yield initiation of steel bar (F_{sy}) and the peak load (F_P) were determined, and the corresponding values are provided in Table 3.11.

Table 3.11: Average load bearing of SR and SGR beams

Beam designation	F_{SLS} [kN]	F_{sy} [kN]	F_P [kN]	$\frac{\Delta F_{SLS}^m}{F_{SLS}^m}$	$\frac{\Delta F_{sy}^m}{F_{sy}^m}$	$\frac{\Delta F_P^m}{F_P^m}$
SR/FRC1545	3.33	5.38	5.51	-	-	-
SR/FRC2560	3.61	5.97	6.24	8%	11%	13%
SR/FRC4590	6.19	7.94	8.00	86%	48%	45%
SGR/FRC1545	3.86	7.47	12.18	-	-	-
SGR/FRC2560	5.21	9.52	15.18	35%	27%	25%
SGR/FRC4590	6.13	10.60	15.44	59%	42%	27%

As Figure 3.21 shows, the load-carrying capacity of all series of SR beams decreases after yielding of longitudinal steel bars, therefore, F_{sy} in Table 3.7 is very close to F_P. In fact, owing to the very low percentage of longitudinal reinforcement ($\rho_s / \rho_b^{SR} \leq 0.7$

) adopted in SR series beams, yielding of steel bar occurs in these series beams, which leads to the crack localisation phenomenon, with the widening of one or two distinct cracks at the ultimate limit state, which is shown in Figures 3.22 and 3.23.

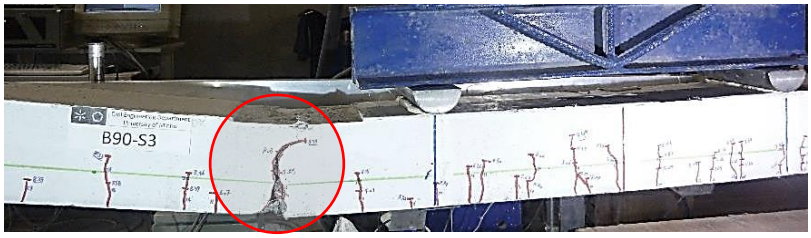

Figure 3.23: Crack failure localisation in SR/FRC beam

Figure 3.24: Ultimate crack pattern of (a) SR/FRC1545, (b) SR/FRC2560, and (c) SR/FRC4590 series beam

The crack localisation phenomenon is often accompanied by premature rupture of reinforcement at the localised failure crack, and reduction of the ductility of R/FRC elements as reported by Redaelli and Muttoni (2007), Deluce and Vecchio (2013) and Yang et al. (2009) in the case of R/FRC tensile element and Dancygier and Savir (2006), Yang et al. (2010), and Georgiadi-Stefanidi et al. (2011) for the R/FRC flexural beams. However, in the case of SR beams tested in the present research, rupture of steel bar did not occur while a large deflection was prescribed to the beams. This can be ascribed to the fact that the beams are quite shallow and the steel bar is located close to the neutral axes. Regarding the experimental results, it is revealed that the load decay after the localisation of the crack is more significant in the case of SR/FRC4590 (Figure 3.21e) where the higher dosage of fibres is utilised as emphasised by Yang et al. (2009).

The load decay due to crack localisation after yield initiation of steel bar is unobserved in the case of SGR series beams due to the increase in longitudinal reinforcement ratio. Accordingly, after yield initiation in steel bar, the load bearing capacity of the SGR beams continues to increases up to a large deflection (>100 mm) which is more than ten times the deflection corresponding to the serviceability limit states.

The average force-deflection response of SR and SGR beams are compared in Figure (3.24).

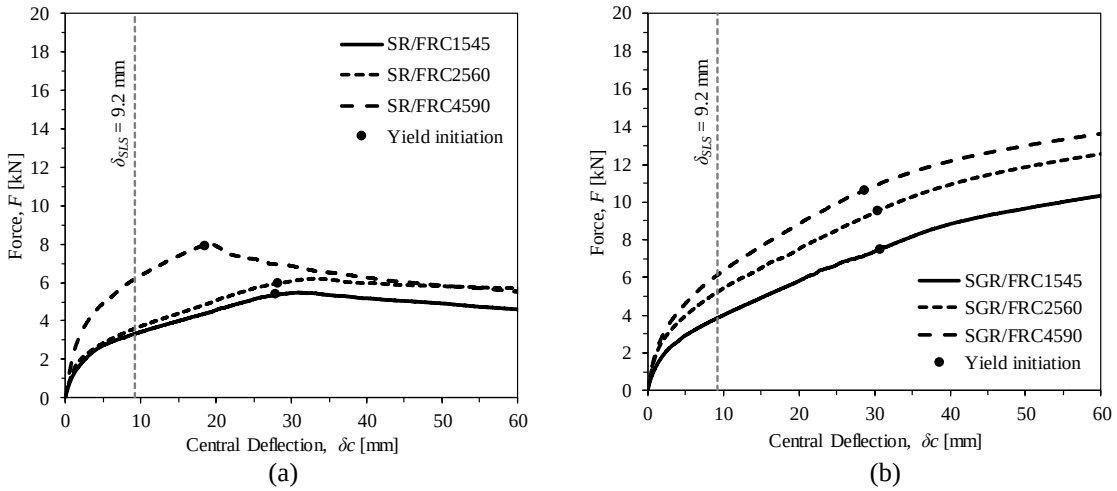

Figure 3.25: Average force-central deflection relationship of FRC beams reinforced with (a) steel bar, and (b) steel plus GFRP bars

Due to the influence of fibres, an increase of 8% and 86% in the load corresponding to the serviceability limit states (F_{SLS}) was obtained for the SR beams, when the content of fibres increases from 45 to 60 kg/m^3, and to 90 kg/m^3, respectively (Table 3.11). Correspondingly, the increasing rate of F_{SLS} in the case of SGR beams is 35% and 59%.

According to the test results, comparing to SR/FRC1545 beams, an increase of 11% and 13% was obtained for the load corresponding to the yield initiation (F_{sy}) and peak load (F_P), respectively for SR/FRC2560 beams, while in the case of SR/FRC4590 series beams, the increase in terms of F_{sy} and F_P was 48% and 45%, respectively.

In the case of SGR series beams, the increase in fibre content from 45 kg/m^3 to 60 kg/m^3 conducted to an increase of 27% and 25% of F_{sy} and F_P, respectively, while an increase of 42% and 27% of F_{sy} and F_P, respectively, is obtained for the SGR/FRC4590 beams with respect to the SGR/FRC1545 series beams.

Considering the test results depicted in Figure 3.24, using GFRP bar increases the flexural capacity of the SGR beams, which is more pronounced in the case of the load at yield initiation (F_{sy}) and peak load (F_P) of SGR beams. Regarding Table 3.7, an increase of 39%, 59%, and 33% of F_{sy}, and 121%, 143%, and 93% of F_P was obtained in the case of SGR/FRC1545, SGR/FRC2560, and SGR/FRC4590, respectively, when compared to corresponding SR beams with the same fibre reinforced concrete constituent. Moreover, an increase of 16% and 44% in service load of SGR/FRC1545 and SGR/FRC2560 was obtained with respect to SR/FRC1545 and SR/FRC2560, respectively.

Nevertheless, the use of GFRP longitudinal bar had a negligible influence on F_{SLS} of the SGR/FRC4590 when compared to that of SR/FRC4590. To be specific, the reinforcing effects of GFRP bar of the relatively low modulus of elasticity (=58 GPa), is mobilised in a relatively large deflection (higher than the one considered for the serviceability limit states).

3.4.3 Crack spacing

In Figure 3.25 is shown the force versus average crack spacing relationship $(F - s_{rm})$ measured along with the pure bending region (*i.e.* the 500 mm segment between the two applied forces, see Figures 3.19 and 3.20). The s_{rm} is determined at the level of steel bars in SR and SGR beams by the following equation:

$$s_{rm} = \frac{L_{cr}}{n_{cr} - 1} \tag{3.14}$$

where L_{cr} and n_{cr} are, respectively, the distance between two furthest crack at the level of steel reinforcement in the pure bending region and the total number of cracks formed at this level. L_{cr} and n_{cr} were obtained regarding the crack evolution in SR and SGR series beam are represented in Appendix A and B respectively. Figure 3.25 reveals that when cracking is stabilised the average crack spacing along with the pure bending region decreases marginally with the increase in fibres dosage as well as the addition of a longitudinal reinforcing bar. In the crack stabilised stage of SR series beams, the average crack spacing of 62.2, 58.6, and 58.4 mm is determined for SR/FRC1546, SR/FRC2560, and SR/FRC4590, respectively. s_{rm} in the crack stabilisation stage of SGR series beams ranges between 56.2 mm in SGR/FRC1545, 52.2 mm in SGR/FRC2560, and 46.8 mm in SGR/FRC4590.

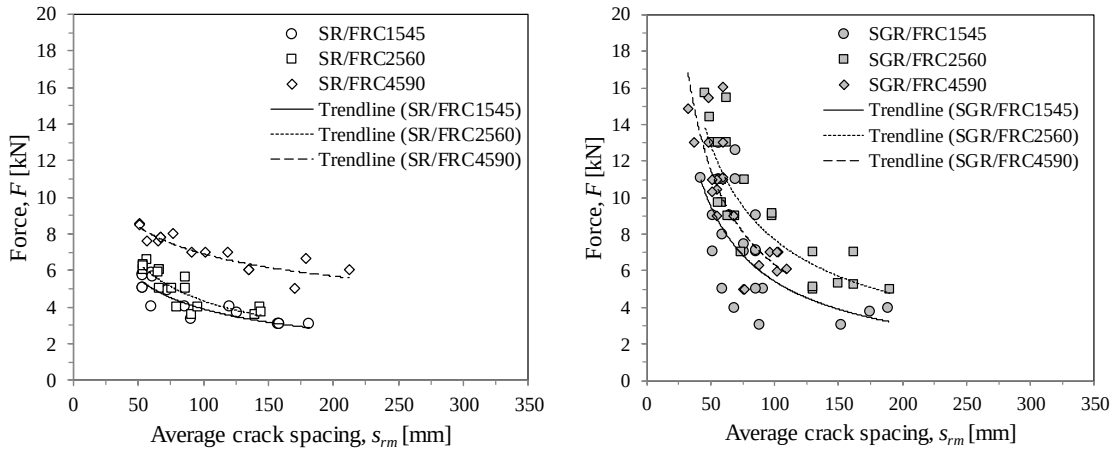

(a) (b)

Figure 3.26: Force-average crack spacing measured at steel bar level of the pure bending region in (a) SR and (b) SGR series beams

3.4.4 Crack width

The moment-average crack width relationships of SR and SGR beams are compared in Figure 3.26, in which the average crack opening was determined by the following equation:

$$w = \left[\Delta L - L_{PBR} \left(f_{ctm} / E_c \right) \right] / n_{cr} \tag{3.15}$$

where ΔL is the extension of the pure bending region area with a length (L_{PBR}) of 500 mm measured at level of steel bar by the readout of LVDT7 depicted in Figure 3.20b. In this equation, f_{ctm} and E_c are the average tensile strength and modulus of elasticity of concrete, respectively, and n_{cr} is the total number of cracks counted in the pure bending region at steel bar level. In Figure 3.26, $w_{SLS} = 0.1\,\text{mm}$ is indicated by a dashed line as the average crack width corresponding to the serviceability limit state recommended by EN 1992-1-1 (2004).

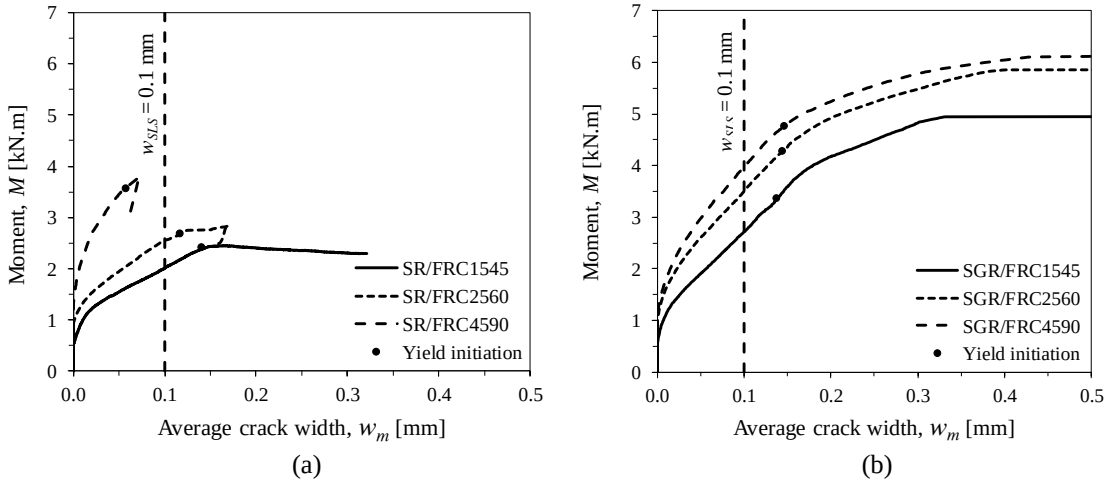

Figure 3.27: Comparison between moment-crack opening response (a) SR and (b) SGR beams

As Figure 3.26 shows, for a certain load level, the average crack width has decreased with the increase in the fibre content, in consequence of the improvement of the post-cracking response of FRCs. According to this figure, an increase of 27% was obtained in the bending moment of SR/FRC2560 at crack width of 0.1 mm (the average crack width corresponding to the serviceability limit states) when compared to SR/FRC1545. The moment-average crack width relationship of SR/FRC4590 beam increased up to a crack

width of around 0.07 mm and then the load and corresponding crack width reduces. This behaviour is due to the widening of failure crack outside the pure bending region (see Figure 3.23c) and consequent unloading of this region. This phenomenon is also observed in the case of SR/FRC2560 (see Figure 3.23b). The influence of the improved post-cracking response of FRCs is also noticeable in the case of SGR beams, where an increase of 29% and 46% in bending moment corresponding to the crack width of 0.1 mm was obtained in SGR/FRC2560 and SGR/FRC4590 when compared to SGR/FRC1545 series beam. Figure 3.27 depicts the influence of additional GFRP longitudinal reinforcement on the moment-crack width response of SGR beams.

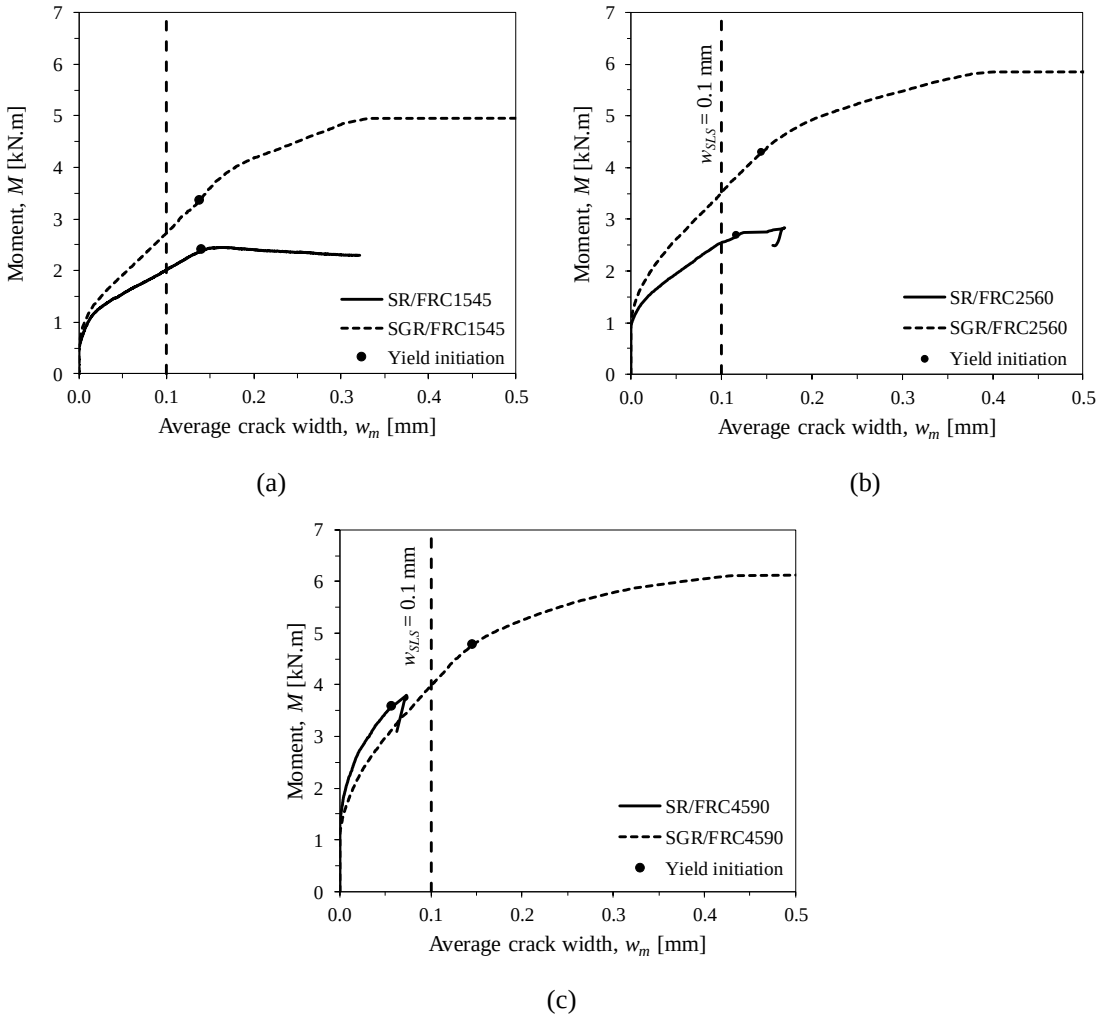

Figure 3.28: Comparison between moment-crack opening response of (a) SR/FRC1545 and SGR/FRC1545, (b) SR/FRC2560 and SGR/FRC2560, and (c) SR/FRC4590 and SGR/FRC4590

This figure reveals the noticeable contribution of GFRP bar to improve the flexural capacity of SGR/FRC1545 and SGR/FRC2560 series beam. An increase of 36% and 38% in bending moment was obtained at the crack opening of 0.1 mm (the considered crack width for the serviceability limit state), when compared to the corresponding SR/FRC1545 and SR/FRC2560 beams, respectively. In the case of SGR/FRC4590 beam, the initial flexural stiffness is lower than the one of SR/FRC4590, which is quite unexpected.

3.5 Concluding remarks

An experimental programme was carried out by developing three types of hooked-end steel fibre reinforced self-compacting concrete (SFRSCC) of nominal compressive strength of 15, 25, and 45 MPa reinforced, respectively, by 45, 60, and 90 kg/m^3 of fibres. The material properties of the SFRSCCs and reinforcing steel and GFRP bars were experimentally determined. In particular, the post-cracking response of the SFRCs was evaluated through three-point notched beam bending test (3PNBBT) by adopting the recommendation of *fib* Model Code 2010 (2011) and by inverse analysis of the force-deflection responses recorded in the 3PNBBT. It was revealed that the approach recommended by *fib* Model Code 2010 (2011) overestimates the stress-crack width response of the SFRCs when compared to the one determined through the inverse analysis.

The developed SFRSCCs were then utilised to build flexural beams reinforced longitudinally by one steel bar, designated by SR beams, and by one steel and one GFRP bars, designated by SGR series beam. The force-deflection response and cracking behaviour of the beams were evaluated at four-point bending test conditions. Due to the low percentage of longitudinal reinforcement utilised, failure crack localisation has occurred in SR series beam after yielding of the steel bar, followed by deflection-softening stage. This phenomenon became more pronounced when higher contents of fibres were utilised. Consequently, the peak load of the SR series beams was more or less equal to the load corresponding to the yield initiation in the steel bar. The load decay, however, was not observed in the case of SGR series beam.

Furthermore, an increase of 8% and 86% were obtained in SR beams, and 35% and 59% in SGR beams, in terms of the load corresponding to the serviceability limit state

(F_{SLS}), when the content of fibres increases from 45 to 60 kg/m^3, and to 90 kg/m^3, respectively and corresponding increase in strength class of concrete. For such an increase in the fibre content, the load corresponding to the yield initiation of the steel bar (F_{sy}) has increased 11% and 48% in SR series, and 27% and 42% in SGR series beam. Furthermore, according to the experimental results, it was revealed that the contribution of GFRP bar was more pronounced on the load at yielding of steel bar as well as the peak load of SGR beams.

The test results showed an increase of 39%, 59%, and 33% of F_{sy}, and 121%, 143%, and 93% of F_P in the case of SGR/FRC1545, SGR/FRC2560, and SGR/FRC4590, respectively, when compared to the SR series beams made of the same fibre reinforced concrete constituent. It was also revealed when a higher dosage of fibre was used (i.e. 90 kg/m^3, the use of additional GFRP longitudinal bar in SGR/FRC4590 beams, had a negligible influence on the load corresponding to the serviceability limit states.

Finally, it was revealed that the average crack spacing and crack width along with the pure bending region of the beams have tended to decrease with the increase in fibre dosage, as well as with the addition of GFRP bar.

Chapter 4

Moment-Curvature Approach to Evaluate Flexural Response of R/SFRSCC Elements

4.1 Introduction

The reinforcing contribution of discrete fibres diffused in concrete can decrease the crack opening and crack spacing in concrete elements, contributing to the increase in durability and integrity of concrete structures (ACI 544.5R-10 2010). Owing to the crack arrestment of fibres bridging the crack surfaces, the load carrying capacity, the energy dissipation, and the ductility at the serviceability and ultimate limit design states are increased (Barros 2008, Cunha *et al.* 2010). The nonlinear analysis is a fundamental approach for evaluating the influence of fibres on the increase in the post-cracking response of fibre reinforced concrete (FRC) and consequent improvement in the load-carrying capacity of reinforced FRC (R/FRC) flexural elements. For this aim, the finite element method (FEM) is indisputably a comprehensive approach with the capability of simulation of sophisticated structures and taking into account the intervening mechanisms (Tiejiong and Theodore 2019, Häussler-Combe and Hartig 2008). However, even if

implemented in computer software, FEM often comprises cumbersome computation when higher accuracy of the simulation is needed for which due to additional input data plugged into the approach the complexity of the simulation may be amplified significantly.

The nonlinear response of R/FRC flexural elements can be alternatively analysed by employing the principles of beam theory, according to which assuming plane sections remaining plane after bending, the strain at each layer of the cross-section is proportional to the distance of the layer with respect to the neutral axes. Accordingly, the deflectional response of the flexural element is dependent on the moment-curvature relationship of the element's cross-section. The moment to curvature ratio represents a macroscopic modified flexural toughness of the cross-section (Chen and Atsuta 1976), in which all non-linearity aspects due to cracking of concrete and yielding of steel reinforcement is entirely included.

The moment-curvature relationship of a reinforced concrete (RC) cross-section can be determined by a direct method, where the strains over the section and curvature are resulted from the imposed external bending moment and axial force (Pfeiffer and Quast 2003). In the other approach, the moment-curvature is determined in an inverse method in which a traditional iterative procedure is generally employed by incrementing the concrete strain at the extreme compression (or tension) fibre of the cross-section, whereas a numerical integration is used to determine the internal forces (Park and Paulay 1975).

The potentialities of fibres as a reinforcement system are not well explored in the moment-curvature models proposed in the literature. Some idealised moment-curvature relationships was employed for non-fibrous concrete elements with longitudinal reinforcement, such as the ones proposed by Charkas *et al.* (2002) and El-Mihilmy and Tedesco (2000) for FRP reinforced concrete elements. A few available models in a design practice format for R/FRC elements are not capable to embrace the variety of post-cracking response of FRC categorised as strain-softening or strain-hardening FRCs (Olesen 2001, Stang and Olesen 1998, Barragán 2002). The closed-form solution developed by Soranakom (2008) is capable of determining the moment-curvature relationship of a cross-section of a beam reinforced longitudinally with steel bars and made by strain-

softening FRC. In this model, the tensile post-cracking behaviour of FRC is simulated by an abrupt stress-decay branch (vertical branch) at crack initiation, followed by a constant residual tensile strength cut off at a certain ultimate tensile strain. This post-cracking tensile stress-strain diagram does not allow simulation of strain-hardening because the available experimental research on the tensile behaviour of these materials shows a gradual increase in stress after the crack initiation of the matrix up to the failure crack localization. Soranakom and Mobasher (2008) have proposed a stress-strain diagram for strain-softening and strain-hardening FRCs, but their model was not prepared to simulate the reinforcement provided by longitudinal steel bars. In the present chapter, a closed-form solution is developed by the generalization of two latter models for the design of cross-section of fibre reinforced concrete (FRC) elements reinforced with longitudinal steel and FRP bars failing in bending. The proposed model is capable of analysing the mutual influence of the parameters that define the softening/stiffening character of an FRC (Naaman and Reinhardt 2006), as well as the pre-stressed percentage of longitudinal reinforcement, on the behaviour of R/FRC beams. The predictive performance of the model is assessed by comparing to the experimental results presented in the literature and the ones presented in Chapter 3, as well as prediction of the layered model developed by Barros and Fortes (2005). Furthermore, the developed model is utilised in a comprehensive parametric study to evaluate the influence of the key characteristics of strain-softening and strain-hardening FRC materials (SS-FRC, SH-FRC) in the moment-curvature relationship and in the force-deflection response of beams failing in bending.

4.2 Geometry and reinforcing scheme of the cross-section

The proposed model is developed for an FRC rectangular cross-section of the width of b and height of h, reinforced by longitudinal steel and fibre reinforced polymer (FRP) bars in tension with a concrete cover of c_s and c_F, respectively (Figure 4.1).

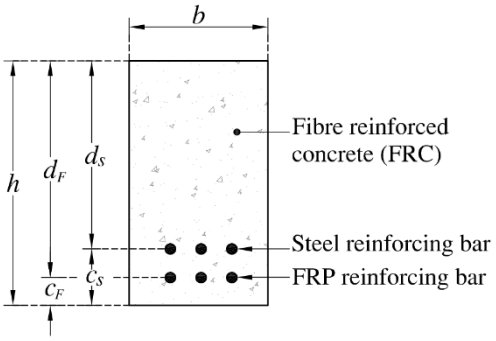

Figure 4.1: Geometry and reinforcing scheme of the cross-section

Considering the total area of steel (A_s) and FRP reinforcement (A_F), the reinforcement ratio of steel and FRP bars is determined by Equation (4.1) and (4.2), respectively:

$$\rho_s = \frac{A_s}{bd_s} \tag{4.1}$$

$$\rho_F = \frac{A_F}{bd_F} \tag{4.2}$$

being d_s $(= h - c_s)$ and d_F $(= h - c_F)$ the internal arms of steel and FRP bars, respectively.

4.3 Constitutive laws for the intervening materials

4.3.1 Tensile behaviour of FRC

The stress-strain diagram of Figure 4.2(a) proposed by Lim *et al.* (1987) is one of the first models presented for the constitutive laws of FRC in tension. In this model, the post-cracking behaviour of FRC is simulated by an abrupt stress-decay branch (vertical branch) at crack initiation, followed by a constant residual tensile strength (σ_R). Soranakom (2008) adopted this constitutive law to simulate the flexural behaviour of strain-softening FRC reinforced with longitudinal steel bars. However, despite the simplicity, this constitutive law does not allow the simulation of strain-hardening FRC where, as available experimental researches evidence, a gradual increase in stress is

expected just after the crack initiation of the matrix. In such a case, an extended model should be implemented like the one proposed by Lok and Xiao (1998) (Figure 4.2b) in which a transition branch is considered between the non-linear region corresponding to the pre-cracking and the residual strength.

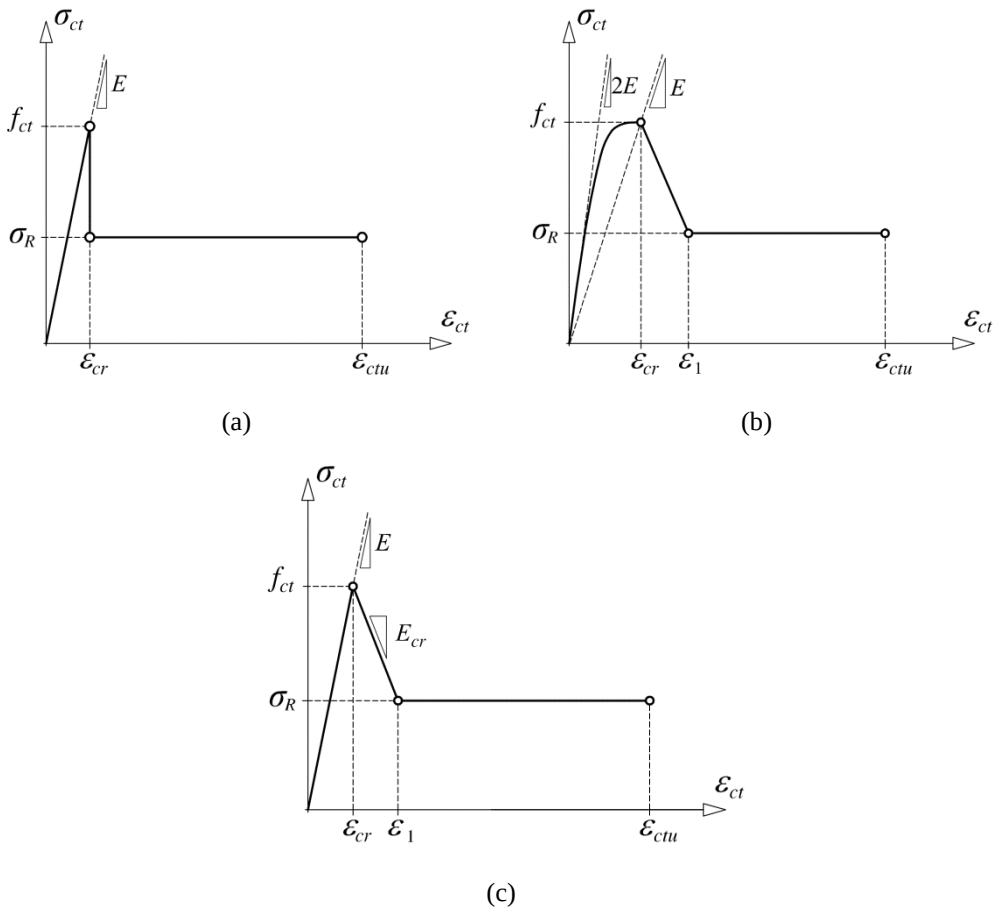

Figure 4.2: Typical stress-strain relationship of FRC proposed by (a) Lim *et al.* (1987), (b) Lok and Xiao (1998), (c) Soranakom and Mobasher (2008)

The model proposed by Lok and Xiao (1998) was simplified by Soranakom and Mobasher (2008) by adopting a trilinear diagram as represented in Figure 4.2(c) to develop a closed-form solution for the FRC flexural elements. In the present work, the constitutive law of Figure 4.2(c) is considered to develop a moment-curvature approach that takes into account the mutual influence of the parameters that define the softening/stiffening character of an FRC and the pre-stress percentage of two types of longitudinal reinforcement (*i.e.* steel and FRP bar), for simulation of the behaviour of

FRC elements failing in bending. The adopted tensile constitutive law of FRC is expressed by Equation (4.3), whose intervening parameters are indicated in Figure 4.3.

$$\sigma_{ct}(\varepsilon_{ct}) = \begin{cases} E_c \varepsilon_{ct} & \varepsilon_{ct} \le \varepsilon_{cr} \quad (4.3a) \\ E_c \varepsilon_{cr} + E_{cr}\left(\varepsilon_{ct} - \varepsilon_{cr}\right) & \varepsilon_{cr} < \varepsilon_{ct} \le \varepsilon_{trn} \quad (4.3b) \\ \sigma_R & \varepsilon_{trn} < \varepsilon_{ct} \le \varepsilon_{ctu} \quad (4.3c) \end{cases}$$

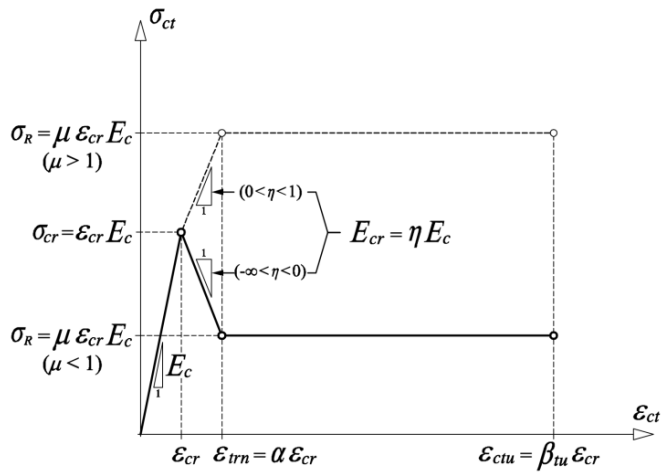

Figure 4.3: Tensile constitutive law of FRC

According to the previous figure, the tensile stress-strain response of FRC $(\sigma_{ct} - \varepsilon_{ct})$ is regarded to consist of three phases. When the stress is lower than cracking stress of FRC (σ_{cr}), the initial linear elastic behaviour is characterised by the concrete elastic modulus (E_c) and concrete crack strain (ε_{cr}). For practical application of FRC considered in the present work, fibre reinforcement mechanisms possess a negligible influence on this phase, therefore, σ_{cr}, E_c and ε_{cr} can be assumed equal to the corresponding values of the homologous plain concrete of the same strength class.

Regarding experimental evidence (Barragán 2002, Cunha *et al.* 2009, Oliveira 2010), after crack initiation in strain-softening FRCs, in general, an abrupt decay of the residual tensile strength occurs for a relatively low increase in tensile deformability. This stage is predominantly governed by concrete fracture characteristics. This is the second phase of the considered constitutive law, which is represented by a linear branch characterised by

the post-cracking tensile modulus $E_{cr}\ (=\eta E_c)$ and the transition strain $\varepsilon_{trn}\ (=\alpha\varepsilon_{cr})$. Note that in the case of strain-softening FRCs, E_{cr} is negative. These two variables are additionally manipulated to simulate the second phase of strain-hardening FRCs, but in this type of relatively significant tensile strength and ductile FRC, E_{cr} acquires a positive value and ε_{trn} can be several times higher than ε_{cr} due to the formation of a diffused crack pattern (Markovic 2006, Stähli *et al.* 2008, Fantilli *et al.* 2009, Kang *et al.* 2010).

Comparing with the model used by Soranakom (2008) (Figure 4.2a), by considering the intermediate branch defined by the strain-softening/stiffening modulus (E_{cr}) (Figure 4.2c and 4.3) the constitutive law becomes capable of simulating FRC of tensile strain-softening and tensile strain-hardening nature. This apparently minor alteration is quite relevant in the structural analysis of FRC elements failing in bending. In fact, as will be evidenced later in the parametric study, the introduction of a gradual stress variation after crack initiation, which depends on the values attributed to E_{cr} parameter, demonstrates a significant impact on the moment-curvature relationship, and consequently on the corresponding force-deflection responses of both strain-softening and strain-hardening FRC, mainly in the phase between crack initiation and yielding of the steel bars. This aspect is absolutely crucial since this is the phase when fibres can contribute for the verifications of the serviceability limit states imposed by design codes. Furthermore, material nonlinear analysis based on the finite element method (FEM) also evidences that the structural response of FRC structure is absolutely dependent on the value attributed to the softening/stiffening modulus corresponding to the branch just after crack initiation (Ventura-Gouveia *et al.* 2011).

The third phase of the considered tensile constitutive law of FRC is characterised by the residual tensile strength (σ_R) taken constantly up to the ultimate tensile strain (ε_{ctu}), beyond which it is assumed that FRC loses its tensile capacity. For the case of strain-softening FRCs, the third phase is substantially affected by the pullout mechanism of the fibres bridging the crack (Cunha *et al.* 2009, Oliveira 2010). In the case of strain-hardening FRCs, the third phase can be regarded as the transition phase between the stabilisation of the diffused crack pattern and the localisation of the critical crack just before ultimate

failure. The tensile behaviour of FRC can be normalised by utilising the cracking strain (ε_{cr}) and elastic modulus of concrete (E_c) as represented in the following equation:

$$\sigma'_{ct} = \begin{cases} \beta & \beta \le 1 \quad (4.4a) \\ 1+\eta(\beta-1) & 1<\beta\le\alpha \quad (4.4b) \\ \mu & \alpha<\beta\le\beta_{tu} \quad (4.4c) \end{cases}$$

where the dimensionless intervening parameters are defined as:

$$\sigma'_{ct} = \frac{\sigma_{ct}(\varepsilon_{ct})}{E_c\varepsilon_{cr}} \quad (4.5)$$

$$\beta = \frac{\varepsilon_{ct}}{\varepsilon_{cr}} \quad (4.6)$$

$$\eta = \frac{E_{cr}}{E_c} \quad (4.7)$$

$$\alpha = \frac{\varepsilon_{trn}}{\varepsilon_{cr}} \quad (4.8)$$

$$\mu = \frac{\sigma_R}{E_c\varepsilon_{cr}} \quad (4.9)$$

$$\beta_{tu} = \frac{\varepsilon_{ctu}}{\varepsilon_{cr}} \quad (4.10)$$

In above equations, σ'_{ct} and β are the normalised tensile stress and strain, respectively, α and β_{tu} are the normalised transition strain and ultimate strain, respectively, and μ is the normalised residual strength of FRC. η is the normalised softening/hardening modulus parameter that can be obtained from α and μ parameters:

$$\eta = -\frac{(1-\mu)}{(\alpha-1)} \quad (4.11)$$

Note that η is ranging between 0 to 1, and between -∞ to 0, in the case of strain-hardening and strain-softening FRCs, respectively (see Figure 4.3).

4.3.2 Compressive behaviour of FRC

Experimental research shows that for both SS- and SH-FRC the compressive strength is marginally affected by the presence of fibres unless a significant content of fibres is utilised (Barros and Figueiras 1999a). In fact, the benefits of fibre reinforcement for the compressive behaviour are most reflected in the compression softening phase, with an increase in the energy absorption that can be quite significant, depending on the characteristics of the fibres and surrounding matrix (Cunha *et al.* 2008).

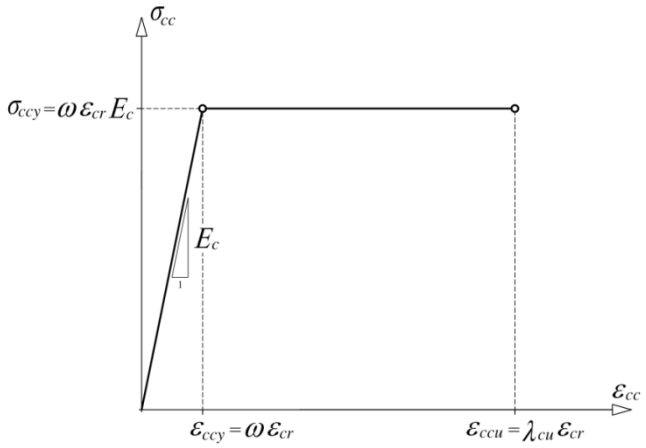

Figure 4.4: Constitutive law of FRC in compression

In the developed model the simplified bilinear stress-strain relationship of Figure 4.4 is considered for FRC in compression can be represented by the following equation:

$$\sigma_{cc}\left(\varepsilon_{cc}\right)=\begin{cases} E_c\varepsilon_{cc} & \varepsilon_{cc}\le\varepsilon_{ccy} \quad (4.12a) \\ E_c\varepsilon_{ccy} & \varepsilon_{ccy}<\varepsilon_{cc}\le\varepsilon_{ccu} \quad (4\text{-}12b) \end{cases}$$

The adopted constitutive law for the compression behaviour of a FRC is composed by an initial linear branch characterised by the elasticity modulus (E_c) up to the compressive "yield" strain (ε_{ccy}), and is continued with a constant value of compressive yield stress $(\sigma_{ccy}=E_c\varepsilon_{ccy})$ up to the ultimate compressive strain (ε_{ccu}), after which it is assumed that FRC loses the capacity of supporting compressive loads. The adopted constitutive law can be normalised by utilising the cracking stress $(=E_c\varepsilon_{cr})$:

$$\sigma'_{cc} = \begin{cases} \lambda & \lambda \le \omega \quad (4.13a) \\ \omega & \omega < \lambda \le \lambda_{cu} \quad (4.13b) \end{cases}$$

where the dimensionless parameters are determined from the following relations:

$$\sigma'_{cc} = \frac{\sigma_{cc}(\varepsilon_{cc})}{E_c \varepsilon_{cr}} \quad (4.14)$$

$$\lambda = \frac{\varepsilon_{cc}}{\varepsilon_{cr}} \quad (4.15)$$

$$\omega = \frac{\varepsilon_{ccy}}{\varepsilon_{cr}} \quad (4.16)$$

$$\lambda_{cu} = \frac{\varepsilon_{ccu}}{\varepsilon_{cr}} \quad (4.17)$$

In the above equations, σ'_{cc} and λ are the normalised compressive stress and strain, respectively, ω is the normalised compressive "yield" strain, and λ_{cu} is the normalised ultimate compressive strain of FRC.

4.3.3 Tensile behaviour of steel bar

Figure 4.5 depicts the tensile behaviour of the steel bars considered in the model simulated by a bilinear stress-strain diagram composed of a linear-elastic branch up to the yield strain (ε_{sy}), followed by a perfect plastic branch up to attain the ultimate tensile strain (ε_{su}), after which the steel tensile strength capacity is assumed null.

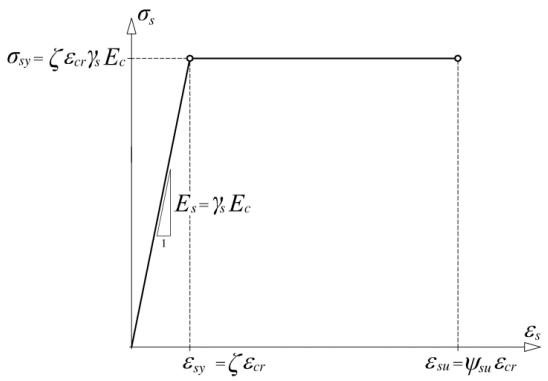

Figure 4.5: Tensile constitutive law of steel reinforcement

The constitutive law of steel reinforcement is defined by Equation (4.18), in which E_s is the elastic modulus of steel. The constitutive law of steel bar is represented in a normalised format by Equation (4.19).

$$\sigma_s\left(\varepsilon_s\right)=\begin{cases} E_s\varepsilon_s & \varepsilon_s \le \varepsilon_{sy} \quad (4.18a) \\ E_s\varepsilon_{sy} & \varepsilon_{sy} < \varepsilon_s \le \varepsilon_{su} \quad (4.18b) \end{cases}$$

$$\sigma_s'=\begin{cases} \gamma_s\psi & \psi \le \zeta \quad (4.19a) \\ \gamma_s\zeta & \zeta < \psi \le \psi_{su} \quad (4.19b) \end{cases}$$

In Equation (4.19) σ_s' and ψ are the normalised tensile stress and corresponding normalised strain of steel reinforcement, respectively, γ_s is the normalised stiffness factor of steel, and ζ and ψ_{su} are, respectively, the normalised yield strain and ultimate tensile strain of steel reinforcement. These parameters are determined from the following equations:

$$\sigma_s'=\frac{\sigma_s\left(\varepsilon_s\right)}{E_c\varepsilon_{cr}} \quad (4.20)$$

$$\gamma_s=\frac{E_s}{E_c} \quad (4.21)$$

$$\psi=\frac{\varepsilon_s}{\varepsilon_{cr}} \quad (4.22)$$

$$\zeta=\frac{\varepsilon_{sy}}{\varepsilon_{cr}} \quad (4.23)$$

$$\psi_{su}=\frac{\varepsilon_{su}}{\varepsilon_{cr}} \quad (4.24)$$

4.3.4 Tensile behaviour of FRP bar

The linear stress-strain relationship $(\sigma_F - \varepsilon_F)$ schematised in Figure 4.6 is considered to represent the tensile behaviour of FRP reinforcing bar, which is represented by Equation (4.25)

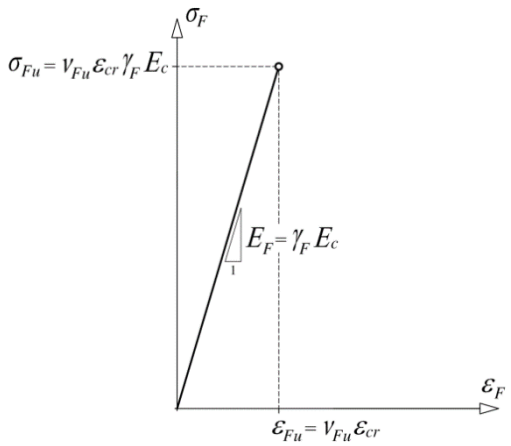

Figure 4.6: Tensile constitutive law of FRP reinforcement

$$\sigma_F(\varepsilon_F) = E_F\varepsilon_F \quad (\varepsilon_F \le \varepsilon_{Fu}) \tag{4.25}$$

In Equation (4.25) E_F is the elastic modulus and ε_{Fu} represents the ultimate tensile strain of the FRP bar. The normalised format of the tensile constitutive law of FRP reinforcement is represented in the following equation:

$$\sigma_F' = \gamma_F\nu \quad (\nu \le \nu_{Fu}) \tag{4.26}$$

where σ_F' and ν are the normalised tensile stress and corresponding stain of FRP reinforcement, respectively, γ_F is the normalised stiffness factor, and ν_{Fu} represents the normalised ultimate tensile strain of FRP reinforcement, respectively, that can be determined from the following equations:

$$\sigma_F' = \frac{\sigma_F(\varepsilon_F)}{E_c\varepsilon_{cr}} \tag{4.27}$$

$$\gamma_F = \frac{E_F}{E_c} \tag{4.28}$$

$$\nu = \frac{\varepsilon_F}{\varepsilon_{cr}} \tag{4.29}$$

$$\nu_{Fu} = \frac{\varepsilon_{Fu}}{\varepsilon_{cr}} \tag{4.30}$$

4.4 The closed-form solution to estimate the moment-curvature relationship

Assuming that a plane section remains plane after bending, and shear deformation of the section can be ignored, the strain profile along with the height of the cross-section is depicted in Figure 4.7 in which, the depth of the neutral axis is designated by d_{NA}. In Figure 4.7, $k\,(=d_{NA}/h)$ represents the normalised depth of the neutral axis, while $\Delta_s\,(=c_s/h)$ and $\Delta_F\,(=c_F/h)$ are the normalised concrete cover thickness of steel and FRP reinforcement, respectively.

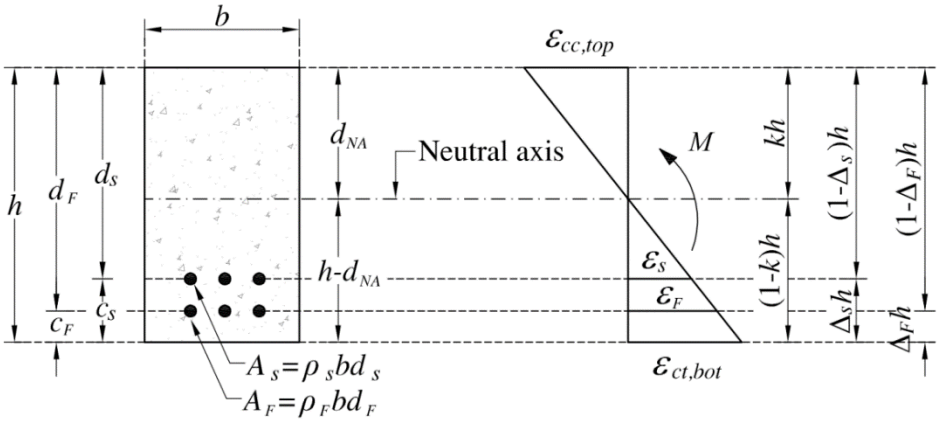

Figure 4.7: Strain profile of the section and intervening normalised parameters

Regarding Figure 4.7, the normalised tensile strain at the concrete bottom fibre (β), the normalised compressive strain at the concrete top fibre (λ), and the normalised tensile strain of the steel (ψ) and FRP bar (ν) are defined by the following equations:

$$\beta = \frac{\varepsilon_{ct,bot}}{\varepsilon_{cr}} \tag{4.31}$$

$$\lambda = \frac{\varepsilon_{cc,top}}{\varepsilon_{cr}} \tag{4.32}$$

$$\psi = \frac{\varepsilon_s}{\varepsilon_{cr}} \tag{4.33}$$

$$\nu = \frac{\varepsilon_F}{\varepsilon_{cr}} \tag{4.34}$$

In the proposed closed-form solution, a gradual increment is applied to the normalised tensile strain at the concrete bottom fibre (β), and corresponding values of the normalised compressive strain at the concrete top fibre (λ), and the normalised tensile strain of the steel (ψ) and FRP (ν) are obtained from Equation (4.35) to (4.37):

$$\lambda = \frac{k}{1-k}\beta \tag{4.35}$$

$$\psi = \frac{1-k-\Delta_s}{1-k}\beta \tag{4.36}$$

$$\nu = \frac{1-k-\Delta_F}{1-k}\beta \tag{4.37}$$

By assuming a perfect bond between the longitudinal bars and surrounding FRC, an independent pre-stress level can be assigned to steel and/or FRP bars. The pre-stress levels are defined by prescribing initial tensile strain to the steel and FRP bars, designated by ε_s^{pr} and ε_F^{pr}, respectively. The pre-stress level of steel and FRP bars, are respectively defined as the ratio of ε_s^{pr} to the steel tensile yield strain (ε_{sy}) and the ratio of ε_F^{pr} to the ultimate tensile strain of FRP (ε_{fu}), which depend on the type of bars and loading conditions, and should be in agreement with the recommendations of ACI 440R-07 (2007), ACI 440.1R-06 (2007), CAN/CSA-S806-02 (2007), and *fib* Bulletin No. 40 (2007). Assuming that variation of pre-stress levels ranging between zero and unitary value, the pre-stress strains are restricted to the linear elastic region of steel and FRP tensile stress-strain response. Therefore, the pre-stress loads for the steel (F_s^{pr}) and FRP (F_F^{pr}) are obtained from the following equations:

$$F_s^{pr} = \varepsilon_s^{pr}\gamma_s E_c \rho_s b d_s \tag{4.38}$$

$$F_F^{pr} = \varepsilon_F^{pr}\gamma_F E_c \rho_F b d_F \tag{4.39}$$

Regarding the depth of the neutral axis (kh), the bending moments corresponding to pre-stress loads are calculated by the following equations:

$$M_s^{pr} = F_s^{pr}(1-k-\Delta_s)\,h \tag{4.40}$$

$$M_F^{pr} = F_F^{pr}(1-k-\Delta_F)\,h \tag{4.41}$$

Due to the constitutive laws of the intervening materials considered in the model, (Figure 4.3 to 4.6), nine different stages should be considered for the range of strains as summarised in Table 4.1. According to this table, the stages are designated by a four digits number that, from the left to the right, representing the condition of the concrete in tension, concrete in compression, steel bar, and FRP bar, respectively.

Table 4.1: Variations of normalised strain parameters of the intervening materials

Stage	Concrete		Steel	FRP
	Tension	Compression		
1.1.1.1	$0<\beta\le 1$	$0<\lambda\le\omega$	$0<\psi\le\zeta$	$0<\nu\le\nu_{fu}$
2.1.1.1	$1<\beta\le\alpha$	$0<\lambda\le\omega$	$0<\psi\le\zeta$	$0<\nu\le\nu_{fu}$
2.1.2.1	$1<\beta\le\alpha$	$0<\lambda\le\omega$	$\zeta<\psi\le\psi_{su}$	$0<\nu\le\nu_{fu}$
2.2.1.1	$1<\beta\le\alpha$	$\omega<\lambda\le\lambda_{cu}$	$0<\psi\le\zeta$	$0<\nu\le\nu_{fu}$
2.2.2.1	$1<\beta\le\alpha$	$\omega<\lambda\le\lambda_{cu}$	$\zeta<\psi\le\psi_{su}$	$0<\nu\le\nu_{fu}$
3.1.1.1	$\alpha<\beta\le\beta_{tu}$	$0<\lambda\le\omega$	$0<\psi\le\zeta$	$0<\nu\le\nu_{fu}$
3.1.2.1	$\alpha<\beta\le\beta_{tu}$	$0<\lambda\le\omega$	$\zeta<\psi\le\psi_{su}$	$0<\nu\le\nu_{fu}$
3.2.1.1	$\alpha<\beta\le\beta_{tu}$	$\omega<\lambda\le\lambda_{cu}$	$0<\psi\le\zeta$	$0<\nu\le\nu_{fu}$
3.2.2.1	$\alpha<\beta\le\beta_{tu}$	$\omega<\lambda\le\lambda_{cu}$	$\zeta<\psi\le\psi_{su}$	$0<\nu\le\nu_{fu}$

Regarding Table 4.1, there are three possible main configurations for tensile strain at bottom fibre: $0<\beta\le 1$, $1<\beta\le\alpha$, and $\alpha<\beta\le\beta_{tu}$. Each configuration 2 and 3 has four possible conditions due to the value of concrete compressive strain at top fibre in either elastic $(0<\lambda\le\omega)$ or plastic $(\omega<\lambda\le\lambda_{cu})$ behaviour in compression, and regarding the value of steel tensile strain in either elastic $(0<\psi\le\zeta)$ or plastic $(\zeta<\psi\le\psi_{su})$ behaviour, and also due to the value of FRP tensile strain $(0<\nu\le\nu_{fu})$. For the nine considered stages, the profile of strain and stress along with the depth of cross-section is depicted in Figure 4.8.

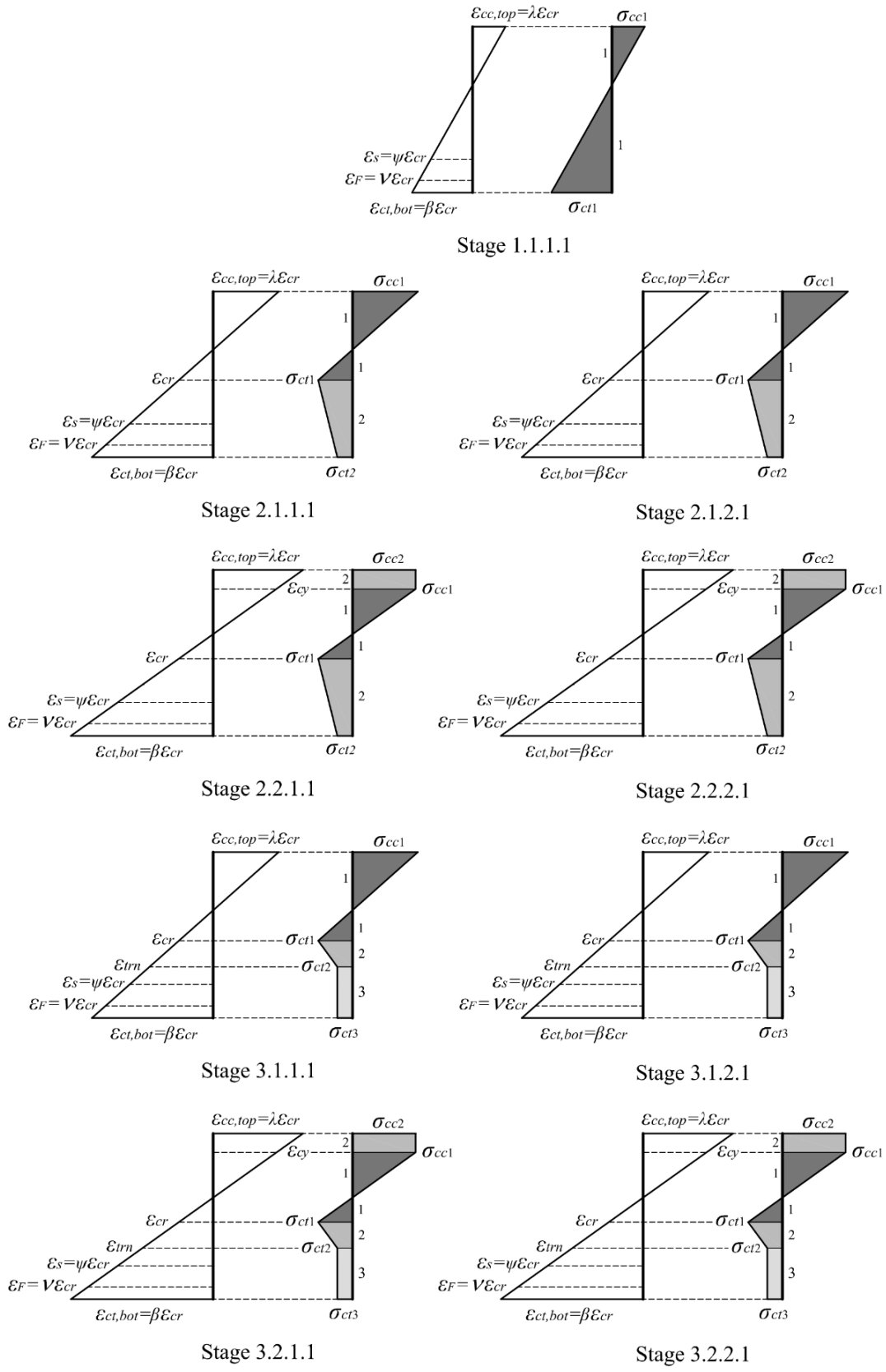

Figure 4.8: Profile of strain and stress along with the depth of cross-section for the considered stages

In Figure 4.9 the internal forces of compressive and tensile zone of concrete and the ones for steel and FRP bars are depicted for the adopted stages, according to which and corresponding to the priscribed tensile strain at bottom fibre (β), the normalised height of compression and tensile zones of the corss-section, the normalised stresses in concrete, and compressive and tensile force in concrete can be determined by the equations summarised represented in Tables 4.2, 4.3, and 4.4, respectively, whose deduction is presented in Appendix C, D, E, in turn. It is remarked that the force components for the steel and FRP bars are obtained multiplying their cross sectional area by the stress in these bars. In Table 4.5 is summarised the Normalised distance of the concrete forces in compression and tension and steel and FRP bars with respect to the neutral axess. The deduction of theses equations can also be found in Appendix F.

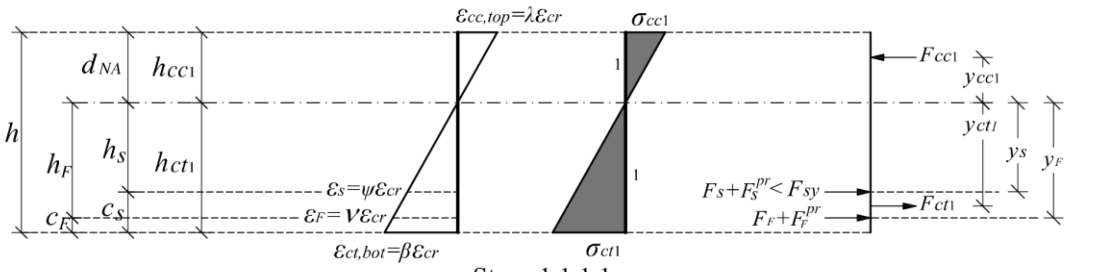

Stage 1.1.1.1

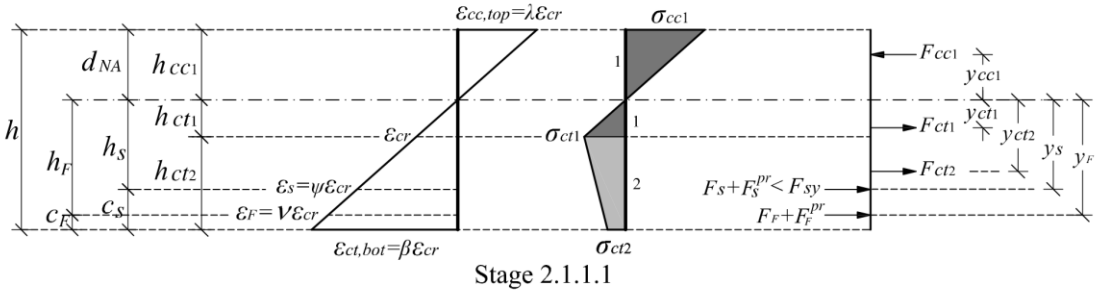

Stage 2.1.1.1

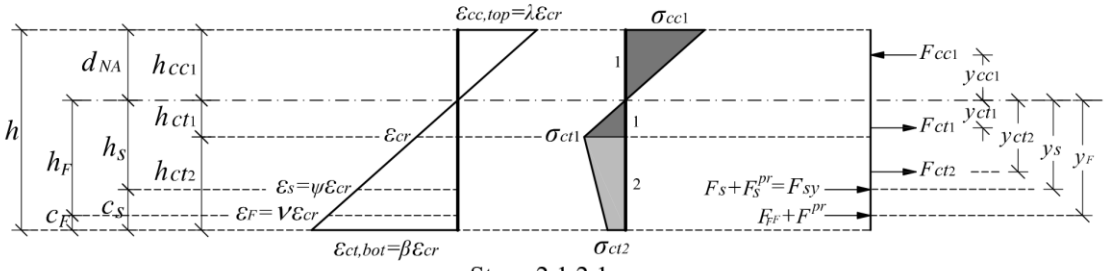

Stage 2.1.2.1

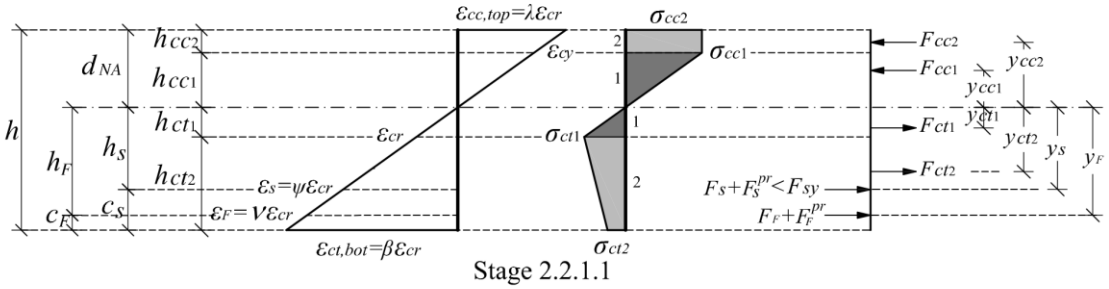

Stage 2.2.1.1

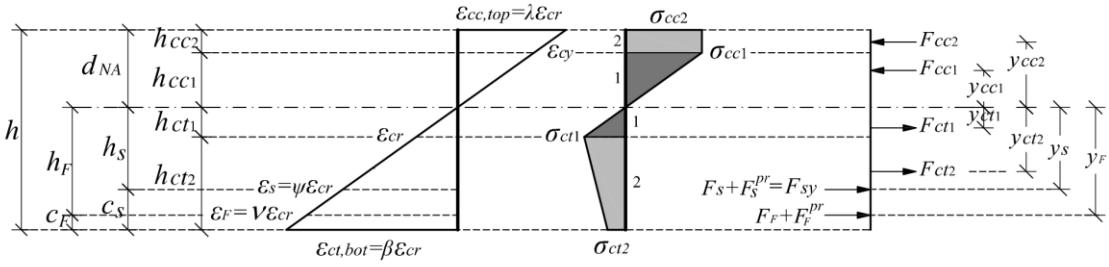

Stage 2.2.2.1

Figure 4.9: (*Continued*)

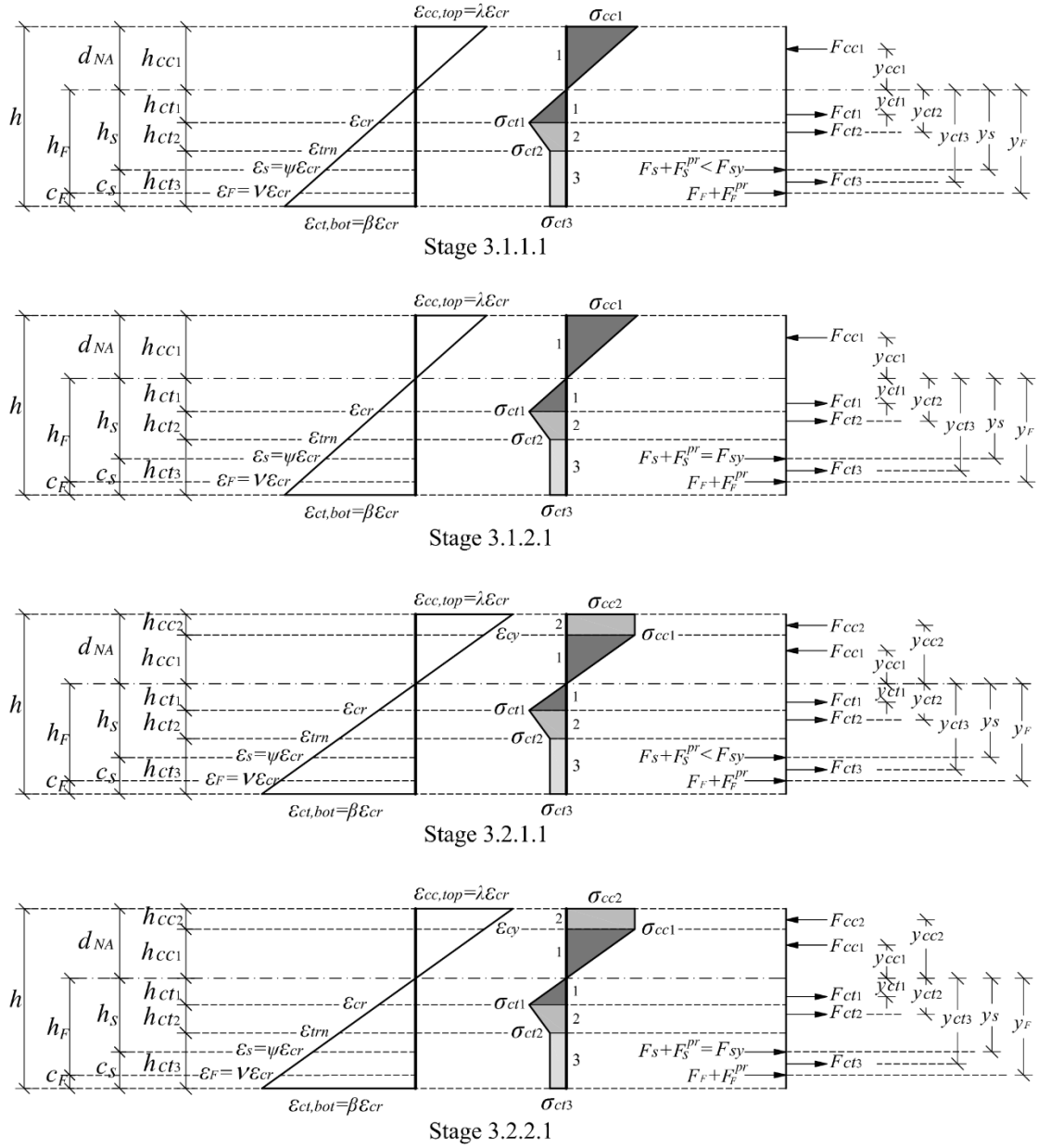

Figure 4.9: Iinternal forces of concrete and steel and FRP bars

Table 4.2: Normalised height of concrete compression and tension zones, and the normalised distance of the steel and FRP bars with respect to the neutral axes (see Figure 4.9)

Normalised Height	Stage 1	Stage 2.1.1.1	Stage 2.1.2.1	Stage 2.2.1.1	Stage 2.2.2.1
$\frac{h_{cc2}}{h}$		–	—	$\frac{k\beta-\omega(1-k)}{\beta}$	$\frac{k\beta-\omega(1-k)}{\beta}$
$\frac{h_{cc1}}{h}$	k	k	k	$\frac{\omega(1-k)}{\beta}$	$\frac{\omega(1-k)}{\beta}$
$\frac{h_{ct1}}{h}$	$1-k$	$\frac{1-k}{\beta}$	$\frac{1-k}{\beta}$	$\frac{1-k}{\beta}$	$\frac{1-k}{\beta}$
$\frac{h_{ct2}}{h}$		$\frac{(1-k)(\beta-1)}{\beta}$	$\frac{(1-k)(\beta-1)}{\beta}$	$\frac{(1-k)(\beta-1)}{\beta}$	$\frac{(1-k)(\beta-1)}{\beta}$
$\frac{h_{ct3}}{h}$	–	–	–	—	—
$\frac{h_s}{h}$	$1-k-\Delta_s$	$1-k-\Delta_s$	$1-k-\Delta_s$	$1-k-\Delta_s$	$1-k-\Delta_s$
$\frac{h_F}{h}$	$1-k-\Delta_F$	$1-k-\Delta_F$	$1-k-\Delta_F$	$1-k-\Delta_F$	$1-k-\Delta_F$

Continued

Table 4.2: Continue

Normalised height	Stage 3.1.1.1	Stage 3.1.2.1	Stage 3.2.1.1	Stage 3.2.2.1
$\frac{h_{cc2}}{h}$	–	–	$\frac{k\beta-\omega(1-k)}{\beta}$	$\frac{k\beta-\omega(1-k)}{\beta}$
$\frac{h_{cc1}}{h}$	k	k	$\frac{\omega(1-k)}{\beta}$	$\frac{\omega(1-k)}{\beta}$
$\frac{h_{ct1}}{h}$	$\frac{1-k}{\beta}$	$\frac{1-k}{\beta}$	$\frac{1-k}{\beta}$	$\frac{1-k}{\beta}$
$\frac{h_{ct2}}{h}$	$\frac{(1-k)(\alpha-1)}{\beta}$	$\frac{(1-k)(\alpha-1)}{\beta}$	$\frac{(1-k)(\alpha-1)}{\beta}$	$\frac{(1-k)(\alpha-1)}{\beta}$
$\frac{h_{ct3}}{h}$	$\frac{(1-k)(\beta-\alpha)}{\beta}$	$\frac{(1-k)(\beta-\alpha)}{\beta}$	$\frac{(1-k)(\beta-\alpha)}{\beta}$	$\frac{(1-k)(\beta-\alpha)}{\beta}$
$\frac{h_s}{h}$	$1-k-\Delta_s$	$1-k-\Delta_s$	$1-k-\Delta_s$	$1-k-\Delta_s$
$\frac{h_F}{h}$	$1-k-\Delta_F$	$1-k-\Delta_F$	$1-k-\Delta_F$	$1-k-\Delta_F$

Table 4.3: Normalised stresses of concrete in compression and tensile zones and in the steel and FRP bars (see Figure 4.9)

Normalised Stress	Stage 1	Stage 2.1.1.1	Stage 2.1.2.1	Stage 2.2.1.1	Stage 2.2.2.1
$\frac{\sigma_{cc2}}{E_c\varepsilon_{cr}}$	–	–	—	$\omega\gamma$	$\omega\gamma$
$\frac{\sigma_{cc1}}{E_c\varepsilon_{cr}}$	$\frac{\gamma\beta k}{1-k}$	$\frac{\gamma\beta k}{1-k}$	$\frac{\gamma\beta k}{1-k}$	$\omega\gamma$	$\omega\gamma$
$\frac{\sigma_{ct1}}{E_c\varepsilon_{cr}}$	β	1	1	1	1
$\frac{\sigma_{ct2}}{E_c\varepsilon_{cr}}$	–	$1+\eta(\beta-1)$	$1+\eta(\beta-1)$	$1+\eta(\beta-1)$	$1+\eta(\beta-1)$
$\frac{\sigma_{ct3}}{E_c\varepsilon_{cr}}$	–	–	–	—	—
$\frac{\sigma_s}{E_c\varepsilon_{cr}}$	$\frac{\gamma_s\beta(1-k-\Delta_s)}{1-k}$	$\frac{\gamma_s\beta(1-k-\Delta_s)}{1-k}$	$\zeta\gamma_s$	$\frac{\gamma_s\beta(1-k-\Delta_s)}{1-k}$	$\zeta\gamma_s$
$\frac{\sigma_F}{E_c\varepsilon_{cr}}$	$\frac{\gamma_F\beta(1-k-\Delta_F)}{1-k}$	$\frac{\gamma_F\beta(1-k-\Delta_F)}{1-k}$	$\frac{\gamma_F\beta(1-k-\Delta_F)}{1-k}$	$\frac{\gamma_F\beta(1-k-\Delta_F)}{1-k}$	$\frac{\gamma_F\beta(1-k-\Delta_F)}{1-k}$

Continued

Table 4.3: Continue

Normalised stress	Stage 3.1.1.1	Stage 3.1.2.1	Stage 3.2.1.1	Stage 3.2.2.1
$\frac{\sigma_{cc2}}{E_c\varepsilon_{cr}}$	–	–	$\omega\gamma$	$\omega\gamma$
$\frac{\sigma_{cc1}}{E_c\varepsilon_{cr}}$	$\frac{\gamma\beta k}{1-k}$	$\frac{\gamma\beta k}{1-k}$	$\omega\gamma$	$\omega\gamma$
$\frac{\sigma_{ct1}}{E_c\varepsilon_{cr}}$	1	1	1	1
$\frac{\sigma_{ct2}}{E_c\varepsilon_{cr}}$	$1+\eta(\alpha-1)$	$1+\eta(\alpha-1)$	$1+\eta(\alpha-1)$	$1+\eta(\alpha-1)$
$\frac{\sigma_{ct3}}{E_c\varepsilon_{cr}}$	μ	μ	μ	μ
$\frac{\sigma_s}{E_c\varepsilon_{cr}}$	$\frac{\gamma_s\beta(1-k-\Delta_s)}{1-k}$	$\zeta\gamma_s$	$\frac{\gamma_s\beta(1-k-\Delta_s)}{1-k}$	$\zeta\gamma_s$
$\frac{\sigma_F}{E_c\varepsilon_{cr}}$	$\frac{\gamma_F\beta(1-k-\Delta_F)}{1-k}$	$\frac{\gamma_F\beta(1-k-\Delta_F)}{1-k}$	$\frac{\gamma_F\beta(1-k-\Delta_F)}{1-k}$	$\frac{\gamma_F\beta(1-k-\Delta_F)}{1-k}$

Table 4.4: Normalised forces of concrete and steel and FRP bars (see Figure 4.9)

Normalised Force	Stage 1	Stage 2.1.1.1	Stage 2.1.2.1	Stage 2.2.1.1	Stage 2.2.2.1
$\frac{F_{cc2}}{bhE_c\varepsilon_{cr}}$	–	–	—	$\frac{\omega\gamma(\beta k+\omega k-\omega)}{\beta}$	$\frac{\omega\gamma(\beta k+\omega k-\omega)}{\beta}$
$\frac{F_{cc1}}{bhE_c\varepsilon_{cr}}$	$\frac{\beta\gamma k^2}{2(1-k)}$	$\frac{\beta\gamma k^2}{2(1-k)}$	$\frac{\beta\gamma k^2}{2(1-k)}$	$\frac{\omega^2\gamma(1-k)}{2\beta}$	$\frac{\omega^2\gamma(1-k)}{2\beta}$
$\frac{F_{ct1}}{bhE_c\varepsilon_{cr}}$	$\frac{\beta(1-k)}{2}$	$\frac{(1-k)}{2\beta}$	$\frac{(1-k)}{2\beta}$	$\frac{(1-k)}{2\beta}$	$\frac{(1-k)}{2\beta}$
$\frac{F_{ct2}}{bhE_c\varepsilon_{cr}}$	–	X_1	X_1	X_1	X_1
$\frac{F_{ct3}}{bhE_c\varepsilon_{cr}}$	–	–	–	—	—
$\frac{F_s}{bhE_c\varepsilon_{cr}}$	X_2	X_2	$\zeta\gamma_s\rho_s d_s/h$	X_2	$\zeta\gamma_s\rho_s d_s/h$
$\frac{F_F}{bhE_c\varepsilon_{cr}}$	X_3	X_3	X_3	X_3	X_3

$X_1=(1-k)(\beta-1)(\eta\beta-\eta+2)/2\beta$, $X_2=\gamma_s\beta\rho_s d_s(1-k-\Delta_s)/(1-k)h$, *Continued*
$X_3=\gamma_F\beta\rho_F d_F(1-k-\Delta_F)/(1-k)h$

Table 4.4: Continue

Normalised force	Stage 3.1.1.1	Stage 3.1.2.1	Stage 3.2.1.1	Stage 3.2.2.1
$\frac{F_{cc2}}{bhE_c\varepsilon_{cr}}$	–	–	$\frac{\omega\gamma(\beta k+\omega k-\omega)}{\beta}$	$\frac{\omega\gamma(\beta k+\omega k-\omega)}{\beta}$
$\frac{F_{cc1}}{bhE_c\varepsilon_{cr}}$	$\frac{\beta\gamma k^2}{2(1-k)}$	$\frac{\beta\gamma k^2}{2(1-k)}$	$\frac{\omega^2\gamma(1-k)}{2\beta}$	$\frac{\omega^2\gamma(1-k)}{2\beta}$
$\frac{F_{ct1}}{bhE_c\varepsilon_{cr}}$	$\frac{(1-k)}{2\beta}$	$\frac{(1-k)}{2\beta}$	$\frac{(1-k)}{2\beta}$	$\frac{(1-k)}{2\beta}$
$\frac{F_{ct2}}{bhE_c\varepsilon_{cr}}$	X_4	X_4	X_4	X_4
$\frac{F_{ct3}}{bhE_c\varepsilon_{cr}}$	$\frac{(1-k)(\beta-\alpha)\mu}{\beta}$	$\frac{(1-k)(\beta-\alpha)\mu}{\beta}$	$\frac{(1-k)(\beta-\alpha)\mu}{\beta}$	$\frac{(1-k)(\beta-\alpha)\mu}{\beta}$
$\frac{F_s}{bhE_c\varepsilon_{cr}}$	$\frac{\gamma_s\beta\rho_s d_s(1-k-\Delta_s)}{(1-k)h}$	$\zeta\gamma_s\rho_s d_s/h$	$\frac{\gamma_s\beta\rho_s d_s(1-k-\Delta_s)}{(1-k)h}$	$\zeta\gamma_s\rho_s d_s/h$
$\frac{F_F}{bhE_c\varepsilon_{cr}}$	$\frac{\gamma_F\beta\rho_F d_F(1-k-\Delta_F)}{(1-k)h}$	$\frac{\gamma_F\beta\rho_F d_F(1-k-\Delta_F)}{(1-k)h}$	$\frac{\gamma_F\beta\rho_F d_F(1-k-\Delta_F)}{(1-k)h}$	$\frac{\gamma_F\beta\rho_F d_F(1-k-\Delta_F)}{(1-k)h}$

$X_4=(1-k)(\alpha-1)(\eta\alpha-\eta+2)/2\beta$

Table 4.5: Normalised internal arm of force components for each stage (see Figure 4.9).

Normalised internal arm	Stage 1	Stage 2.1.1.1	Stage 2.1.2.1	Stage 2.2.1.1	Stage 2.2.2.1
$\frac{y_{cc2}}{h}$	–	–	—	$\frac{k\beta+\omega(1-k)}{2\beta}$	$\frac{k\beta+\omega(1-k)}{2\beta}$
$\frac{y_{cc1}}{h}$	$\frac{2}{3}k$	$\frac{2}{3}k$	$\frac{2}{3}k$	$\frac{2\omega(1-k)}{3\beta}$	$\frac{2\omega(1-k)}{3\beta}$
$\frac{y_{ct1}}{h}$	$\frac{2(1-k)}{3}$	$\frac{2(1-k)}{3\beta}$	$\frac{2(1-k)}{3\beta}$	$\frac{2(1-k)}{3\beta}$	$\frac{2(1-k)}{3\beta}$
$\frac{y_{ct2}}{h}$	–	X_5	X_5	X_5	X_5
$\frac{y_{ct3}}{h}$	–	–	–	—	—
$\frac{y_s}{h}$	$1-k-\Delta_s$	$1-k-\Delta_s$	$1-k-\Delta_s$	$1-k-\Delta_s$	$1-k-\Delta_s$
$\frac{y_F}{h}$	$1-k-\Delta_F$	$1-k-\Delta_F$	$1-k-\Delta_F$	$1-k-\Delta_F$	$1-k-\Delta_F$

$X_5=\frac{2\eta\beta^2-\eta\beta-\eta+3\beta+3}{3\beta(\eta\beta-\eta+2)}(1-k)$

Continued

Table 4.5: Continue

Normalised internal arm	Stage 3.1.1.1	Stage 3.1.2.1	Stage 3.2.1.1	Stage 3.2.2.1
$\frac{y_{cc2}}{h}$	–	–	$\frac{k\beta+\omega(1-k)}{2\beta}$	$\frac{k\beta+\omega(1-k)}{2\beta}$
$\frac{y_{cc1}}{h}$	$\frac{2}{3}k$	$\frac{2}{3}k$	$\frac{2}{3}\frac{\omega(1-k)}{\beta}$	$\frac{2}{3}\frac{\omega(1-k)}{\beta}$
$\frac{y_{ct1}}{h}$	$\frac{2(1-k)}{3\beta}$	$\frac{2(1-k)}{3\beta}$	$\frac{2(1-k)}{3\beta}$	$\frac{2(1-k)}{3\beta}$
$\frac{y_{ct2}}{h}$	X_6	X_6	X_6	X_6
$\frac{y_{ct3}}{h}$	$\frac{(\alpha+\beta)}{2\beta}(1-k)$	$\frac{(\alpha+\beta)}{2\beta}(1-k)$	$\frac{(\alpha+\beta)}{2\beta}(1-k)$	$\frac{(\alpha+\beta)}{2\beta}(1-k)$
$\frac{y_s}{h}$	$1-k-\Delta_s$	$1-k-\Delta_s$	$1-k-\Delta_s$	$1-k-\Delta_s$
$\frac{y_F}{h}$	$1-k-\Delta_F$	$1-k-\Delta_F$	$1-k-\Delta_F$	$1-k-\Delta_F$

$X_6=\frac{2\eta\alpha^2-\eta\alpha-\eta+3\alpha+3}{3\beta(\eta\alpha-\eta+2)}(1-k)$

For each strain configuration, the value of k parameter can be obtained by the equations presented in Table 4.6, which are determined by satisfying the equilibrium of forces in the cross-section as detailed in Appendix G. Note that in the developed

formulation the γ parameter is considered as the compressive to the tensile modulus of elasticity of concrete. Most often, the elastic modulus of concrete is considered equal in tension and compression, for which γ of unitary is adopted in the formulations. By determining k parameter, the internal moment (M) is obtained by multiplying the force components to their distance from the neutral axis. The corresponding curvature (χ) is equally determined as the ratio between the concrete compressive strain at the top fibre of the cross-section and the depth of the neutral axis.

For the i^{th} generic stage, the moment and curvature can be written in a normalised format in accordance with the following equations:

$$M_i' = M_i / M_{cr} \tag{4.42}$$

$$\chi'_i = \chi_i / \chi_{cr} \tag{4.43}$$

where M_{cr} and χ_{cr} are the cracking moment and the corresponding curvature, respectively, which are determined from the following equations:

$$M_{cr} = \frac{1}{6} bh^2 \left(E_c \varepsilon_{cr} \right) \tag{4.44}$$

$$\chi_{cr} = \frac{2\varepsilon_{cr}}{h} \tag{4.45}$$

In Table 4.7 are summarised the expressions generated for M_i' and χ'_i whose deduction is represented in Appendix H.

Table 4.6: Equations for the depth of the neutral axis parameter (k) of each stage

Stage	k
1.1.1.1	$k_{1111}=\begin{cases}\dfrac{2B_s d_s/h(1-\Delta_s)+2B_F d_F/h(1-\Delta_F)+1+(2F_{pr}/\beta)}{2\sqrt{D_{1111}}} & for\ \gamma=1\\ \dfrac{-\left(1+B_s d_s/h+B_F d_F/h+(F_{pr}/\beta)\right)+\sqrt{D_{1111}}}{(\gamma-1)} & for\ \gamma\neq 1\end{cases}$ $D_{1111}=(B_s d_s/h+B_F d_F/h+1+(1/\beta)F_{pr})^2-(1-\gamma)(1+2B_s d_s/h(1-\Delta_s)+2B_F d_F/h(1-\Delta_f)+(2/\beta)F_{pr})$
2.1.1.1	$k_{2111}=\dfrac{D_{2111}+\beta\left(\beta\left(B_s d_s/h+B_F d_F/h\right)+F_{pr}\right)}{D_{2111}-\beta^2\gamma}-\left(\dfrac{1}{D_{2111}-\beta^2\gamma}\right)\left[\left(D_{2111}+\beta\left(\beta\left(B_s d_s/h+B_F d_F/h\right)+F_{pr}\right)\right)^2-\left(D_{2111}-\beta^2\gamma\right)\left(D_{2111}+2\beta\left(\beta\left(B_s d_s/h(1-\Delta_s)+B_F d_F/h(1-\Delta_f)\right)+F_{pr}\right)\right)\right]^{0.5}$ $D_{2111}=\eta(\beta-1)^2+2\beta-1$
2.1.2.1	$k_{2121}=\dfrac{D_{2121}+\beta\left(\zeta B_s d_s/h+\beta B_F d_F/h+F_F^{pr}\right)}{D_{2121}-\beta^2\gamma}-\left(\dfrac{1}{D_{2121}-\beta^2\gamma}\right)\left[\left(D_{2121}+\beta\left(\zeta B_s d_s/h+\beta B_F d_F/h+F_F^{pr}\right)\right)^2-\left(D_{2121}-\beta^2\gamma\right)\left(D_{2121}+2\beta\left(\zeta B_s d_s/h+\beta B_F d_F/h(1-\Delta_F)+F_F^{pr}\right)\right)\right]^{0.5}$ $D_{2121}=\eta(\beta-1)^2+2\beta-1$
2.2.1.1	$k_{2211}=\dfrac{D_{2211}+\beta\left(\omega\gamma+\beta\left(B_s d_s/h+B_F d_F/h\right)+F_{pr}\right)}{D_{2211}+2\omega\gamma\beta}-\left(\dfrac{1}{D_{2211}+2\omega\gamma\beta}\right)\left[\left(D_{2211}+\beta\left(\omega\gamma+\beta\left(B_s d_s/h+B_F d_F/h\right)+F_{pr}\right)\right)^2-\left(D_{2211}+2\omega\gamma\beta\right)\left(D_{2211}+2\beta\left(\beta B_s d_s/h(1-\Delta_s)+\beta B_F d_F/h(1-\Delta_F)+F_{pr}\right)\right)\right]^{0.5}$ $D_{2211}=\eta(\beta-1)^2+2\beta-1+\omega^2\gamma$
2.2.2.1	$k_{2221}=\dfrac{D_{2221}+\beta\left(\beta B_F d_F/h+\zeta B_s d_s/h+\omega\gamma+F_F^{pr}\right)}{D_{2221}+2\omega\gamma\beta}-\left(\dfrac{1}{D_{2221}+2\omega\gamma\beta}\right)\left[\left(D_{2221}+\beta\left(\beta B_F d_F/h+\zeta B_s d_s/h+\omega\gamma+F_F^{pr}\right)\right)^2-\left(D_{2221}+2\omega\gamma\beta\right)\left(D_{2221}+2\beta\left(\zeta B_s d_s/h+\beta B_F d_F/h(1-\Delta_F)+F_F^{pr}\right)\right)\right]^{0.5}$ $D_{2221}=\eta(\beta-1)^2+2\beta-1+\omega^2\gamma$

$B_s=\gamma_s\rho_s,\ B_F=\gamma_F\rho_F,\ F_{pr}=F_s^{pr}+F_F^{pr}$

Continued

Table 4.6: Continue

Stage	k
3.1.1.1	$k_{3111}=\dfrac{D_{3111}+\beta\left(\beta\left(B_s d_s/h+B_F d_F/h\right)+F_{pr}\right)}{D_{3111}-\beta^2\gamma}-\left(\dfrac{1}{D_{3111}-\beta^2\gamma}\right)\left[\left(D_{3111}+\beta\left(\beta\left(B_s d_s/h+B_F d_F/h\right)+F_{pr}\right)\right)^2-\left(D_{3111}-\beta^2\gamma\right)\left(D_{3111}+2\beta\left(\beta\left(B_s d_s/h(1-\Delta_s)+B_F d_F/h(1-\Delta_F)\right)+F_{pr}\right)\right)\right]^{0.5}$ $D_{3111}=\eta(\alpha-1)^2+2\left(\alpha(1-\mu)+\mu\beta\right)-1$
3.1.2.1	$k_{3121}=\dfrac{D_{3121}+\beta\left(\beta B_F d_F/h+\zeta B_s d_s/h+F_F^{pr}\right)}{D_{3121}-\beta^2\gamma}-\left(\dfrac{1}{D_{3121}-\beta^2\gamma}\right)\left[\left(D_{3121}+\beta\left(\beta B_F d_F/h+\zeta B_s d_s/h+F_F^{pr}\right)\right)^2-\left(D_{3121}-\beta^2\gamma\right)\left(D_{3121}+2\beta\left(\zeta B_s d_s/h+\beta B_F d_F/h(1-\Delta_F)+F_F^{pr}\right)\right)\right]^{0.5}$ $D_{3121}=\eta(\alpha-1)^2+2\left(\alpha(1-\mu)+\mu\beta\right)-1$
3.2.1.1	$k_{3211}=\dfrac{D_{3211}+\beta\left(\beta\left(B_s d_s/h+B_F d_F/h\right)+\omega\gamma+F_{pr}\right)}{D_{3211}+2\omega\gamma\beta}-\left(\dfrac{1}{D_{3211}+2\omega\gamma\beta}\right)\left[\left(D_{3211}+\beta\left(\beta\left(B_s d_s/h+B_F d_F/h\right)+\omega\gamma+F_{pr}\right)\right)^2-\left(D_{3211}+2\omega\gamma\beta\right)\left(D_{3211}+2\beta\left(\beta\left(B_s d_s/h(1-\Delta_s)+B_F d_F/h(1-\Delta_F)\right)+F_{pr}\right)\right)\right]^{0.5}$ $D_{3211}=\eta(\alpha-1)^2+2\left(\alpha(1-\mu)+\mu\beta\right)+\omega^2\gamma-1$
3.2.2.1	$k_{3221}=\dfrac{D_{3221}+\beta\left(\zeta B_s d_s/h+\omega\gamma+F_F^{pr}\right)+\beta^2 B_F d_F/h}{D_{3221}+2\omega\gamma\beta}-\left(\dfrac{1}{D_{3221}+2\omega\gamma\beta}\right)\left[\left(D_{3221}+\beta\left(\zeta B_s d_s/h+\omega\gamma+F_F^{pr}\right)+\beta^2 B_F d_F/h\right)^2-\left(D_{3221}+2\omega\gamma\beta\right)\left(D_{3221}+2\beta\left(\zeta B_s d_s/h+\beta B_F d_F/h(1-\Delta_F)+F_F^{pr}\right)\right)\right]^{0.5}$ $D_{3221}=\eta(\alpha-1)^2+2\left(\alpha(1-\mu)+\mu\beta\right)+\omega^2\gamma-1$

$B_s=\gamma_s\rho_s,\ B_F=\gamma_F\rho_F,\ F_{pr}=F_s^{pr}+F_F^{pr}$

Table 4.7: Equations for the evaluation of the normalised moment for each stage

Stage (i)	M_i'	χ_i'
1.1.1.1	$\frac{2\beta\left(\gamma k^3 h + h(1-k_{1111})^3\right)}{(1-k_{1111})h} + \frac{6B_s\beta d_s(1-k_{1111}-\Delta_s)^2}{(1-k_{1111})h} + \frac{6B_F\beta d_F(1-k_{1111}-\Delta_F)^2}{(1-k_{1111})h} + (M_{pr}^{'})_{1111}$	$\frac{\beta}{2(1-k_{1111})}$
	$\left(M_{pr}^{'}\right)_{1111} = \frac{6}{bhE_c\varepsilon_{cr}}\left(F_s^{pr}(1-k_{1111}-\Delta_s) + F_F^{pr}(1-k_{1111}-\Delta_F)\right)$	
	$B_s = \gamma_s\rho_s,\ B_F = \gamma_F\rho_F$	
2.1.1.1	$\frac{\left[2\beta^3\gamma k^3 h + 2h(1-k_{2111})^3 + h(1-k_{2111})^3(\beta-1)C_{2111}\right]}{\beta^2(1-k_{2111})h} + \frac{\left[6B_s\beta^3 d_s(1-k_{2111}-\Delta_s)^2 + 6B_F\beta^3 d_F(1-k_{2111}-\Delta_F)^2\right]}{\beta^2(1-k_{2111})h} + \left(M_{pr}^{'}\right)_{2111}$	$\frac{\beta}{2(1-k_{2111})}$
	$C_{2111} = 2\eta\beta^2 - \eta\beta - \eta + 3\beta + 3$	
	$\left(M_{pr}^{'}\right)_{2111} = \frac{6}{bhE_c\varepsilon_{cr}}\left(F_s^{pr}(1-k_{2111}-\Delta_s) + F_F^{pr}(1-k_{2111}-\Delta_F)\right)$	
	$B_s = \gamma_s\rho_s,\ B_F = \gamma_F\rho_F$	
2.1.2.1	$\frac{\left[2\beta^3\gamma k^3 h + 2h(1-k_{2121})^3 + h(1-k_{2121})^3(\beta-1)C_{2121}\right]}{\beta^2(1-k_{2121})h} + \frac{6B_s\beta^2\xi d_s(1-k_{2121})(1-k_{2121}-\Delta_s)}{\beta^2(1-k_{2121})h} + \frac{6B_F\beta^3 d_F(1-k_{2121}-\Delta_F)^2}{\beta^2(1-k_{2121})h} + \left(M_{pr}^{'}\right)_{2121}$	$\frac{\beta}{2(1-k_{2121})}$
	$C_{2121} = 2\eta\beta^2 - \eta\beta - \eta + 3\beta + 3$	
	$\left(M_{pr}^{'}\right)_{2121} = \frac{6F_F^{pr}(1-k_{2121}-\Delta_F)}{bhE_c\varepsilon_{cr}}$	
	$B_s = \gamma_s\rho_s,\ B_F = \gamma_F\rho_F$	

Continued

Table 4.7: Continue

Stage (i)	M_i'	χ_i'
2.2.1.1	$\frac{2h\omega^3\gamma(1-k_{2211})^3+2h(1-k_{2211})^3}{\beta^2(1-k_{2211})h} + \frac{3h\omega\gamma(\beta k_{2211}+\omega k_{2211}-\omega)(k_{2211}\beta+\omega(1-k_{2211}))(1-k_{2211})}{\beta^2(1-k_{2211})h} + \frac{h(1-k_{2211})^3(\beta-1)C_{2211}+6B_s\beta^3 d_s(1-k_{2211}-\Delta_s)^2}{\beta^2(1-k_{2211})h} + \frac{6B_F\beta^3 d_F(1-k_{2211}-\Delta_F)^2}{\beta^2(1-k_{2211})h} + \left(M_{pr}^{'}\right)_{2211}$	$\frac{\beta}{2(1-k_{2211})}$
	$C_{2211}=2\eta\beta^2-\eta\beta-\eta+3\beta+3$	
	$\left(M_{pr}^{'}\right)_{2211}=\frac{6}{bhE_c\varepsilon_{cr}}\left(F_s^{pr}(1-k_{2211}-\Delta_s)+F_F^{pr}(1-k_{2211}-\Delta_F)\right)$	
	$B_s=\gamma_s\rho_s,\ B_F=\gamma_F\rho_F$	
2.2.2.1	$\frac{2h\omega^3\gamma(1-k_{2221})^3++2h(1-k_{2221})^3}{\beta^2(1-k_{2221})h} + \frac{3h\omega\gamma(\beta k_{2221}+\omega k_{2221}-\omega)(k_{2221}\beta+\omega(1-k_{2221}))(1-k_{2221})}{\beta^2(1-k_{2221})h} + \frac{h(1-k_{2221})^3(\beta-1)C_{2221}+6B_s\beta^2\xi d_s(1-k_{2221})(1-k_{2221}-\Delta_s)}{\beta^2(1-k_{2221})h} + \frac{6B_F\beta^3 d_F(1-k_{2221}-\Delta_F)^2}{\beta^2(1-k_{2221})h} + \left(M_{pr}^{'}\right)_{2221}$	$\frac{\beta}{2(1-k_{2221})}$
	$C_{2221}=2\eta\beta^2-\eta\beta-\eta+3\beta+3$	
	$\left(M_{pr}^{'}\right)_{2221}=\frac{6F_F^{pr}(1-k_{2221}-\Delta_F)}{bhE_c\varepsilon_{cr}}$	
	$B_s=\gamma_s\rho_s,\ B_F=\gamma_F\rho_F$	
3.1.1.1	$\frac{2\gamma\beta^3{k_{3111}}^3h+2(1-k_{3111})^3h+(1-k_{3111})^3(\alpha-1)C_{3111}h}{\beta^2(1-k_{3111})h} + \frac{3(1-k_{3111})^3(\beta-\alpha)(\alpha+\beta)\mu h}{\beta^2(1-k_{3111})h} + \frac{6B_s\beta^3 d_s(1-k_{3111}-\Delta_s)^2+6B_F\beta^3 d_F(1-k_{3111}-\Delta_F)^2}{\beta^2(1-k_{3111})h} + \left(M_{pr}^{'}\right)_{3111}$	$\frac{\beta}{2(1-k_{3111})}$
	$C_{3111}=2\eta\alpha^2-\eta\alpha-\eta+3\alpha+3$	
	$\left(M_{pr}^{'}\right)_{3111}=\frac{6}{bhE_c\varepsilon_{cr}}\left(F_s^{pr}(1-k_{3111}-\Delta_s)+F_F^{pr}(1-k_{3111}-\Delta_F)\right)$	
	$B_s=\gamma_s\rho_s,\ B_F=\gamma_F\rho_F$	

Continued

Table 4.7: Continue

Stage (i)	M_i'	χ_i'
3.1.2.1	$\frac{2\gamma\beta^3 k_{3121}^3 h + 2(1-k_{3121})^3 h + (1-k_{3121})^3(\alpha-1)C_{3121}h}{\beta^2(1-k_{3121})h} + \frac{3(1-k_{3121})^3(\beta-\alpha)(\alpha+\beta)\mu h + 6B_s\beta^2\xi d_s(1-k_{3121})(1-k_{3121}-\Delta_s)}{\beta^2(1-k_{3121})h} + \frac{6B_F\beta^3 d_F(1-k_{3121}-\Delta_F)^2}{\beta^2(1-k_{3121})h} + (M_{pr}^{'})_{3121}$	$\frac{\beta}{2(1-k_{3121})}$
	$C_{3121} = 2\eta\alpha^2 - \eta\alpha - \eta + 3\alpha + 3$	
	$(M_{pr}^{'})_{3121} = \frac{6F_F^{pr}(1-k_{3121}-\Delta_F)}{bhE_c\varepsilon_{cr}}$	
	$B_s = \gamma_s\rho_s,\ B_F = \gamma_F\rho_F$	
3.2.1.1	$\frac{2h\omega^3\gamma(1-k_{3211})^3 + 2(1-k_{3211})^3 h}{\beta^2(1-k_{3211})h} + \frac{(1-k_{3211})^3(\alpha-1)C_{3211}h + 3(1-k_{3211})^3(\beta-\alpha)(\alpha+\beta)\mu h}{\beta^2(1-k_{3211})h} + \frac{6B_s\beta^3 d_s(1-k_{3211}-\Delta_s)^2 + 6B_F\beta^3 d_F(1-k_{3211}-\Delta_F)^2}{\beta^2(1-k_{3211})h} + \left(M_{pr}^{'}\right)_{3211}$	$\frac{\beta}{2(1-k_{3211})}$
	$C_{3211} = 2\eta\alpha^2 - \eta\alpha - \eta + 3\alpha + 3$	
	$\left(M_{pr}^{'}\right)_{3211} = \frac{6}{bhE_c\varepsilon_{cr}}\left(F_s^{pr}(1-k_{3211}-\Delta_s) + F_F^{pr}(1-k_{3211}-\Delta_F)\right)$	
	$B_s = \gamma_s\rho_s,\ B_F = \gamma_F\rho_F$	
3.2.2.1	$\frac{3h\omega\gamma(\beta k_{3221} + \omega k_{3221} - \omega)(k_{3221}\beta + \omega(1-k_{3221}))(1-k_{3221})}{\beta^2(1-k_{3221})h} + \frac{2h\omega^3\gamma(1-k_{3221})^3 + 2(1-k_{3221})^3 h + (1-k_{3221})^3(\alpha-1)C_{3221}h}{\beta^2(1-k_{3221})h} + \frac{3(1-k_{3221})^3(\beta-\alpha)(\alpha+\beta)\mu h + 6B_s\beta^2\xi d_s(1-k_{3221})(1-k_{3221}-\Delta_s)}{\beta^2(1-k_{3221})h} + \frac{\left[6B_F\beta^3 d_F(1-k_{3221}-\Delta_F)^2\right]}{\beta^2(1-k_{3221})h} + (M_{pr}^{'})_{3221}$	$\frac{\beta}{2(1-k_{3221})}$
	$C_{3221} = 2\eta\alpha^2 - \eta\alpha - \eta + 3\alpha + 3$	
	$(M_{pr}^{'})_{3221} = \frac{6F_F^{pr}(1-k_{3221}-\Delta_F)}{bhE_c\varepsilon_{cr}}$	
	$B_s = \gamma_s\rho_s,\ B_F = \gamma_F\rho_F$	

4.5 Model to estimate the force-deflection relationship

The force-deflection response of a statically determinate beam failing in bending is obtained by the algorithm schematically represented in Figure 4.10. According to this approach, for the successive increment of χ_k of the $M-\chi$ relationship of the beam mid-span cross-section, the corresponding M_k is read, and the total applied force F_k ($=2M_k / L_{ss}$, see Figure 4.10) is determined. The bending moment at the middle of the i^{th} segment (M_i) is also obtained according to the beam bending diagram.

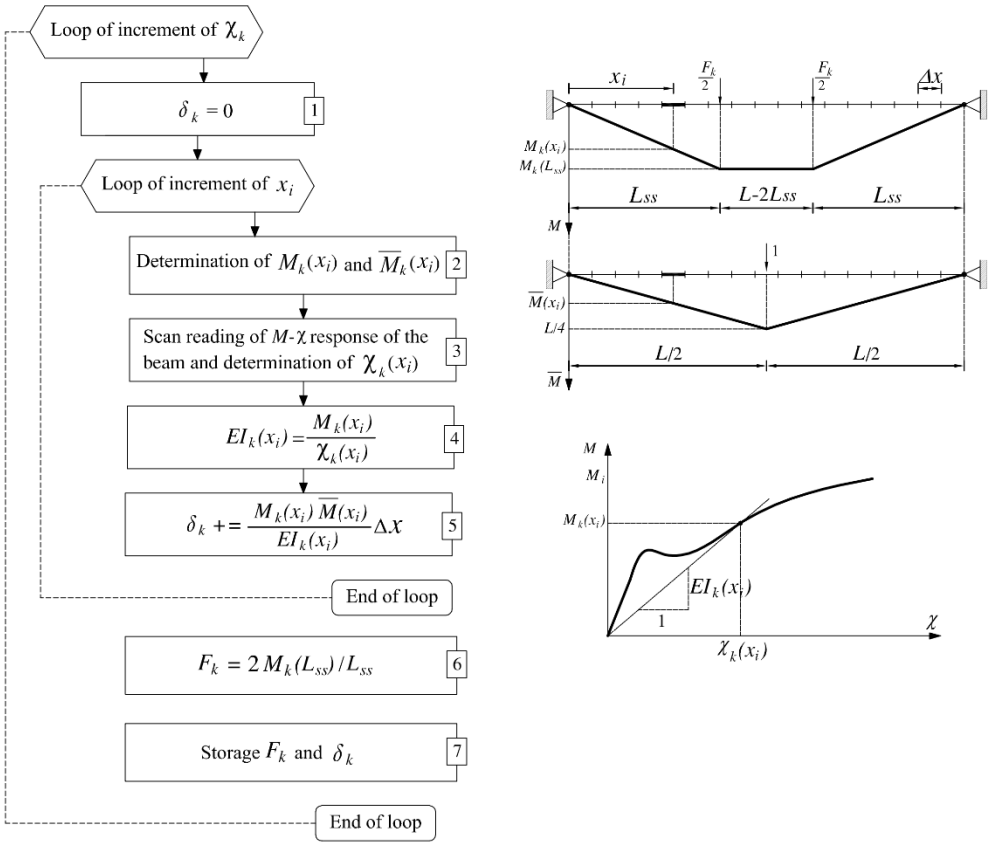

Figure 4.10: Numerical approach to simulate the force-deflection response of simply supported beams failing in bending

Decomposing the beam in small segments, the bending moment in a generic cross-section at a distance X can be designated by $M_i(x)$. From the $M-\chi$ relationship of this cross-section, the corresponding flexural stiffness $EI_i(x)$ is obtained, as well as the bending moment in this section for the base system corresponding to the evaluation

of the deflection at the beam mid-span $\bar{M}(x)$. By applying the Virtual Work Method, the mid-span deflection of the beam for the k^{th} loading step $(\delta_{mid})_k$, is determined, which, jointly with F_k provides a point of the $F-\delta$ curve.

4.6 Model appraisal

To evaluate the accuracy of the proposed model, the results obtained with it are compared to the ones determined from DOCROS software (Basto and Barros 2008). The model implemented in DOCROS assumes that a plane section remains plane after deformation, and the bond between materials is perfect. The section is divided into layers, and the thickness and width of each layer are user-defined and depend on the cross-section geometry. DOCROS can analyse sections of irregular shape and size, composed of various types of materials subjected to an axial force. DOCROS provides a wide database of constitutive laws for the simulation of monotonic and cyclic behaviour of cement-based materials, polymer-based materials and steel bars.

The predictive performance of the model was assessed by evaluating the moment-curvature relationship for a rectangular cross-section of 250 mm width and 500 mm depth depicted in Figure 4.11. The cross-section is reinforced longitudinally with steel and FRP bars whose reinforcing ratio is 0.2% and 0.1%, respectively. Furthermore, a concrete cover of 30 mm is considered for FRP bars, while steel bars are positioned deeper, at a distance of 80 mm from the tensile face of the section. The steel bars and FRP bars are applied with a pre-stress percentage of 50%.

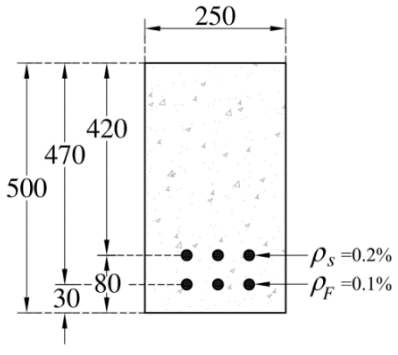

Figure 4.11: Geometry and reinforcing scheme of the cross-section considered in the model appraisal (dimensions in mm)

Concerning material properties of steel and GFRP bars commonly used in practical applications, the considered values of the parameters defining the constitutive laws of the intervening materials of Figures 4.3 to 4.6 are included in Table 4.8.

Table 4.8: Values of the parameter defining the constitutive laws

FRC							Steel bar		FRP bar		
Tension					Compression						
ε_{cr}	E_c	α	β_{tu}	μ	ω	λ_{cu}	ζ	γ_s	ψ_{su}	ν_{Fu}	γ_F
[‰]	[GPa]	[-]	[-]	[-]	[-]	[-]	[-]	[-]	[-]	[-]	[-]
0.1	30	10	150	0.33[a] /1.10[b]	10	40	20	6.67	120	300	1

[a] Strain-softening / [b] Strain-hardening

The moment-curvature relationships predicted by the proposed model and those obtained from DOCROS software are compared in Figures 4.12a and 4.12b for the cross-section of beams made by strain-softening and strain-hardening FRC, respectively, according to which the excellent accuracy of the developed model is verified.

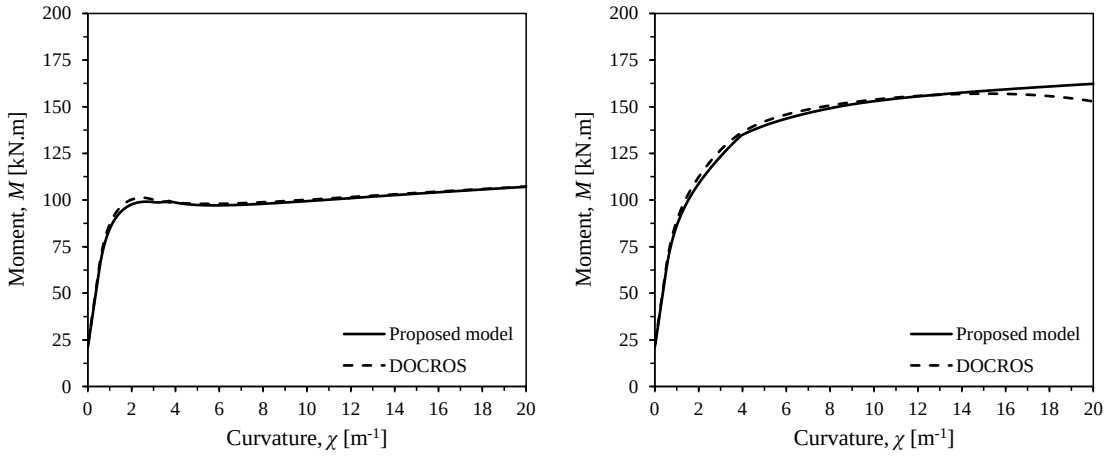

Figure 4.12: Moment-curvature responses predicted by the proposed model and DOCROS for the cross-section of reinforced FRC of (a) strain-softening and (b) strain-hardening behaviour

The predictive performance of the model was also evaluated by simulating two experimental tests carried out by Badawi and Soudki (2009), and by Xue *et al.* (2010). As Figure 4.13 shows the two various strengthening techniques have been employed in the

considered test programs. The first one applying a pre-stressed longitudinal GFRP (glass fibres reinforced polymer) bar placed into a groove open on the concrete cover of the beam, in agreement with the procedures of the near-surface mounted (NSM) technique (Badawi and Soudki 2009); and the second one applying a pre-stressed carbon fibre reinforced polymer (CFRP) laminate according to the externally bonded reinforcement (EBR) technique (Badawi and Soudki 2009).

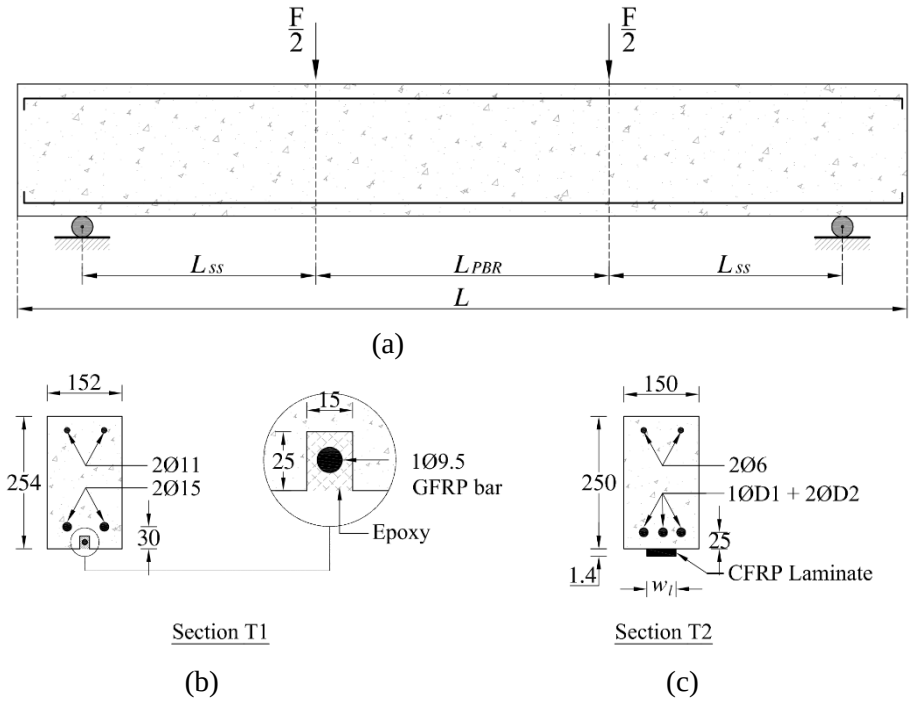

Figure 4.13: (a) Geometry and loading scheme of the beams considered for model appraisal, reinforcement and strengthening configurations of the beams (b) B1 and B2 tested by Badawi and Soudki (2009), and (c) B3 and B4 tested by Xue *et al.* (2010) (dimensions in mm)

The geometric properties of the beams and strengthening arrangements are included in Table 4.9. In Tables 4.10 and 4.11 are presented the relevant values of the parameters that define the constitutive laws of the intervening materials. Since non-fibrous concrete was used in these RC beams, the contribution of the post-cracking residual strength of the concrete was neglected by assigning a null value to μ parameter.

Table 4.9: Data to define the geometry, the reinforcement and the strengthening systems of the beams represented in Figure 4.13

Beam Designation	L [mm]	l_{ss} [mm]	l_{PBR} [mm]	Section type	W [mm]	D_1 [mm]	D_2 [mm]	Pre-stressing
B1	3500	1100	1100	T1	-	-	-	40.0%
B2	3500	1100	1100	T1	-	-	-	60.0%
B3	2700	950	600	T2	50	12	14	42.1%
B4	2700	950	600	T2	20	12	12	50.6%

Table 4.10: Data to define the constitutive laws of the intervening materials in the beams of Figure 4.11

Beam Designation	σ_{cy} [MPa]	σ_{cr} [MPa]	E_c [GPa]	σ_{sy} [MPa]	E_s [GPa]	σ_{Fu} [MPa]	E_F [GPa]
B1	53	3.79	30.20	440	190	1970	136
B2	53	3.79	30.20	440	190	1970	136
B3	50.3	3.60	32.50	383	142	2500	150
B4	50.3	3.60	32.50	429	145	2500	150

Table 4.11: Values considered for the constitutive parameters for the simulation of the beams

	FRC [a]						Steel bar					GFRP bar			
Beams	ε_{cr} [‰]	α [-]	μ [-]	β_{tu} [-]	ω [-]	λ_{cu} [-]	ρ_s [%]	γ_s [-]	ζ [-]	ψ_{su} [-]	ε_s^{pr} [%]	ρ_F [%]	γ_F [-]	ν_{Fu} [-]	ε_F^{pr} [%]
B1	0.125	2	0	150	13.98	28	1.04	6.29	18.53	120	0	0.19	4.5	116	0.56
B2	0.125	2	0	150	13.98	28	1.04	6.29	18.53	120	0	0.19	4.5	116	0.84
B3	0.111	2	0	150	13.97	32	1.25	4.36	24.30	120	0	0.186	4.62	150	0.7
B4	0.111	2	0	150	13.97	32	1.00	4.46	26.65	120	0	0.074	4.62	150	0.84

[a] $\gamma = 1$

Figure 4.14 compares the load-deflection responses predicted by the proposed formulation and those recorded in the experimental tests, which evidences the capability of the model to predict with good accuracy the deflection response of this type of structural elements.

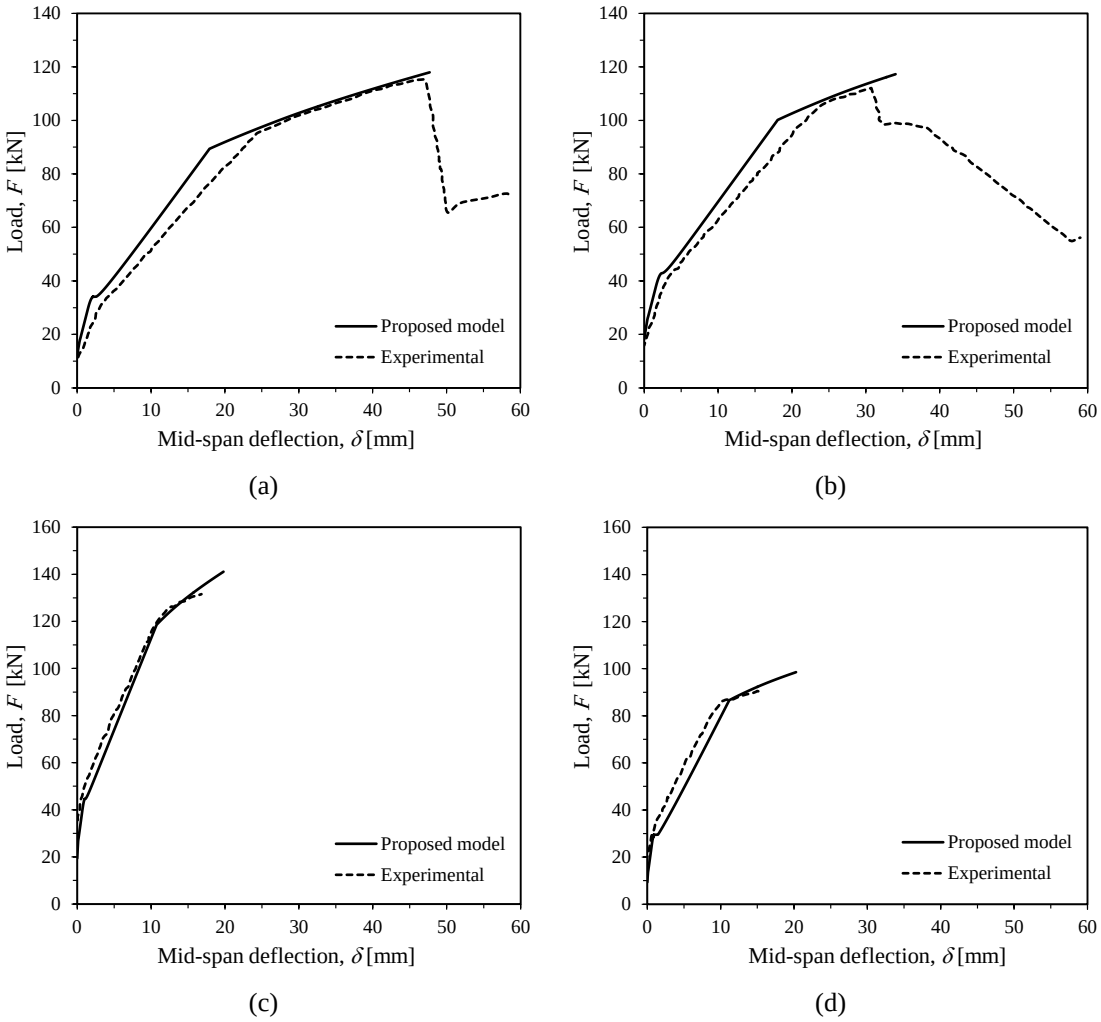

Figure 4.14: Force-deflection relationships determined by the proposed model and the ones registered in the experimental tests for (a) B1, (b) B2, (c) B3, and (d) B4

To assess the predictive performance of the developed model, it was adopted to simulate the load-deflection response of the R/SFRSCC beams tested in the experimental programme detailed in Chapter 3. The considered values of parameters defining the constitutive laws of the intervening materials are summarised in Table 4.12 and 4.13.

Table 4.12: Values considered for the constitutive parameters of SFRSCCs developed in the present study

SFRSCC	ε_{cr} [‰]	α [-]	μ [-]	β_{tu} [-]	ω [-]	λ_{cu} [-]
C15-f45	0.0378	79.36	1.46	661.37	14.74	92.59
C25-f60	0.0653	45.94	1.35	382.85	12.61	53.60
C45-f90	0.0928	32.33	1.18	269.40	13.45	37.71

Table 4.13: Values considered for the constitutive parameters of reinforcing bars adopted in the present study

SFRSCC	ρ_s [%]	γ_s [-]	ζ [-]	ψ_{su} [-]	ρ_F [%]	γ_F [-]	ν_{Fu} [-]
C15-f45	0.56	8.71	74.07	846.56	0.42	2.46	476.19
C25-f60	0.56	7.16	42.88	490.04	0.42	2.03	275.65
C45-f90	0.56	5.82	30.17	344.83	0.42	1.65	193.96

Note that the post-cracking response of the developed SFRSCCs in the experimental programme was determined by converting the linear post-cracking of the SFRSCCs in terms of stress-crack width relationship recommended by *fib* Model Code 2010 (2011) (Figure 3.7) to the trilinear stress-strain diagram adopted in the proposed model (Figure 4.3). For this aim, the residual strength of FRC (σ_R) in Figure 4.3 was taken the average of $f_{Fts,m}$ and $f_{Ftu,m}$, the residual strengths of FRC in the serviceability and the ultimate limit states, respectively. In this simulation ε_{ctu} was also obtained by dividing the ultimate value of crack opening ($w_u = 2.5\,mm$) by $h = 100\ mm$, the height of the beam's cross-section, while ε_{trn} was assumed 0.003. In Figure 4.15 the force-deflection relationships determined by the model are compared to the experimental result, according to which it can be concluded that the model is capable to predict with a broadly reasonable accuracy the force-deflection responses recorded in the experiment.

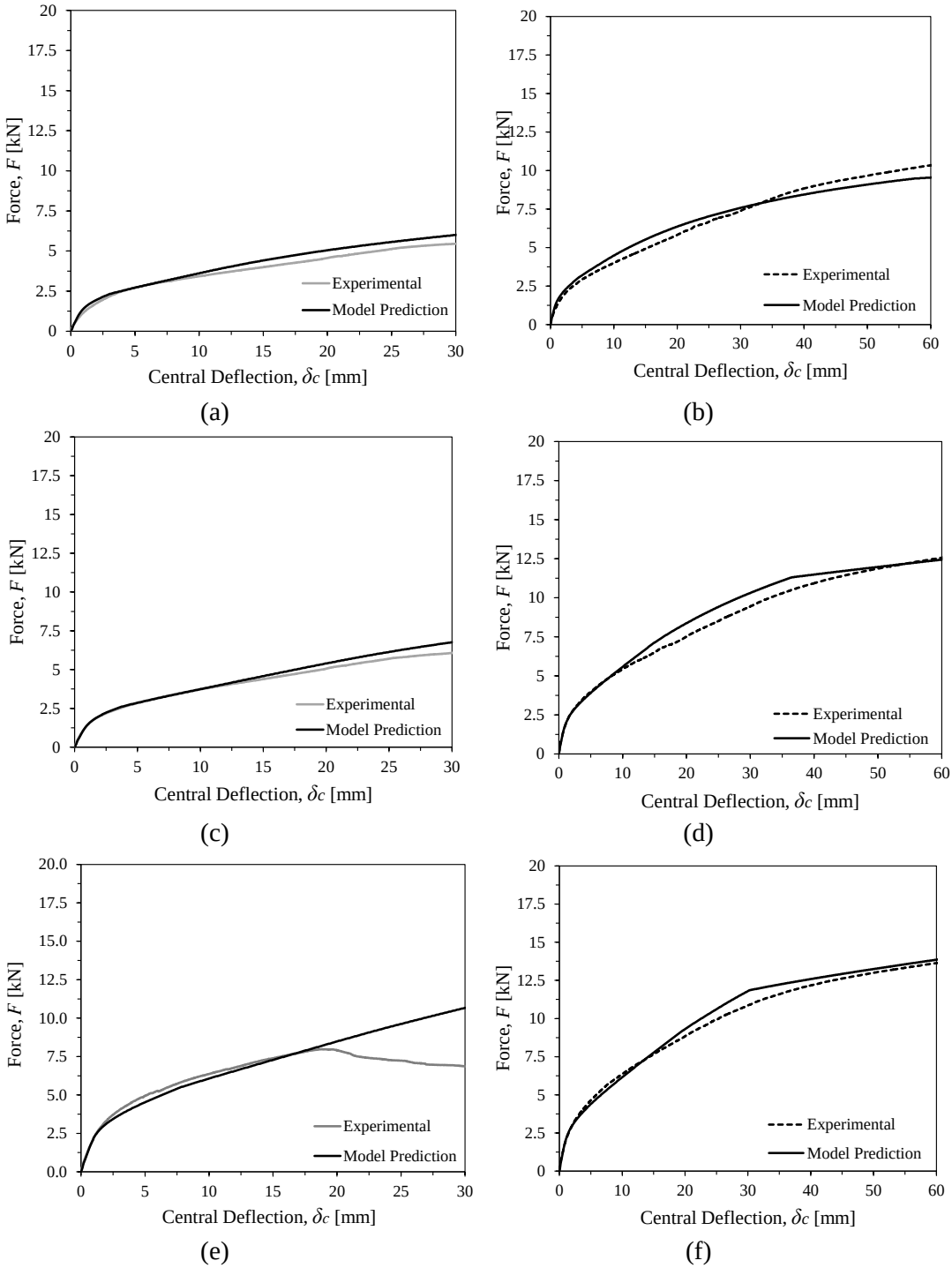

Figure 4.15: Force-deflection relationships determined by the proposed model and the ones registered in the experimental program explained in Chapter 3, (a) SR/FRC1545, (b) SGR/FRC1545, (c) SR/FRC2560, (d) SGR/FRC2560, (e) SR/FRC4590, and (f) SGR/FRC4590

4.7 Parametric studies

To assess the influence of the relevant mechanical properties of FRC, and the pre-stress level applied to FRP and steel bars, on the moment-curvature relationship and on the force-deflection of hybrid reinforced FRC beams, a parametric study was carried out adopting a simply supported beam with the geometry, the reinforcement arrangement and the loading configuration represented in Figure 4.16.

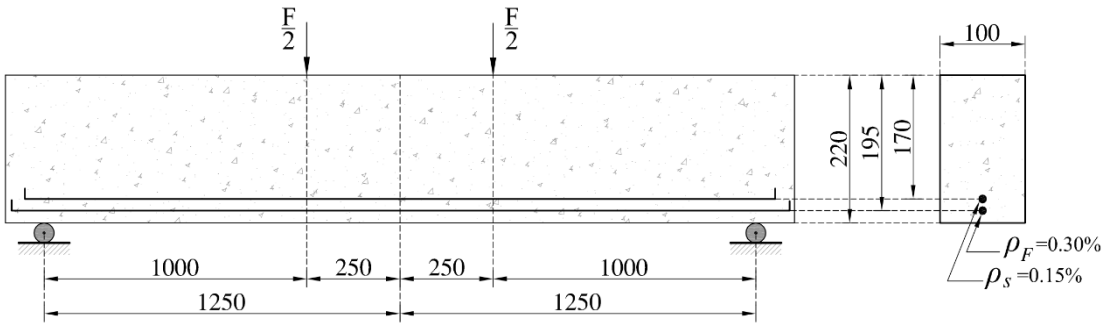

Figure 4.16: Geometry and reinforcement data for the beam of the parametric study (dimensions in mm).

Three distinct pre-stress levels including 0% (non-prestressed), 25%, and 50% are considered for the steel and FRP bars, which are, respectively, a percentage of the yield stress of the steel bars and a percentage of the tensile strength of the FRP bars. However, due to the susceptibility to creep rupture of some types of FRP bars (mainly those made by glass fibres, GFRP), the limits recommended by some standards (ACI 440R-07 2007, ACI 440.1R-06 2007, CAN/CSA-S806-02 2007, *fib* Bulletin No. 40 2007) for the stress level in these reinforcements under sustained stresses should be considered. If FRP bars are subjected to cyclic or fatigue loading, the stress limits proposed by these standards should be also taken into account. For the influence of the post-cracking performance of FRC, the values of 0.0, 0.4, 0.8, and 1.2 are adopted for the normalised residual strength (μ), maintaining constant the normalised transition strain of $\alpha = 10$. In this context, the influence of the α parameter is also assessed by adopting values of 1.01, 10, 50, and 150, keeping constant the normalised residual strength $(\mu = 0.4)$. For the parametric study, the values of the parameters that define the constitutive laws of the intervening materials are indicated in Table 4.14. For this parametric study GFRP bars were considered.

Table 4.14: Values for the parameters of the materials constitutive laws adopted in the parametric study

FRC							Steel bar			FRP bar	
Tension				Compression							
ε_{cr}	E_c	α	β_{tu}	μ	ω	λ_{cu}	ζ	γ_s	ψ_{su}	ν_{Fu}	γ_F
[‰]	[GPa]	[-]	[-]	[-]	[-]	[-]	[-]	[-]	[-]	[-]	[-]
0.1	35	1.01 10[a] 50 150	150	0.0 0.4[b] 0.8 1.2	20	35	75	5.71	150	166.7	1.71

[a] Constant values considered for α to evaluate the influence of μ

[b] Constant values considered for μ to evaluate the influence of α

4.7.1 Influence of α parameter and pre-stress level on the moment-curvature and load-deflection responses of hybrid reinforced FRC beams

For each adopted pre-stress level of FRP and steel bars, the influence of α parameter on the moment-curvature and load-deflection responses is represented in Figures 4.17(a)-(c) and 4.17(d)-(f), respectively. The points corresponding to the concrete crack initiation and the steel yield initiation are also signalised in the curves of Figure 4.17.

Since α is a post-cracking parameter of FRC, it has no effect on the responses before crack initiation. However, after cracking the flexural capacity of the cross-section and the load carrying capacity of the beam are significantly increased with the increase in α parameter. In fact, the moment and the load at yield initiation of steel bars increase with α, and this tendency is also observed for the corresponding curvatures and deflections. Therefore, the residual strength of FRC between ε_{cr} and $\varepsilon_{trn} = \alpha\varepsilon_{cr}$ (see Figure 4.3) has a significant favourable impact on the flexural and load carrying capacities corresponding to the level of curvatures and deflections installed in this type of structural elements at serviceability limit states.

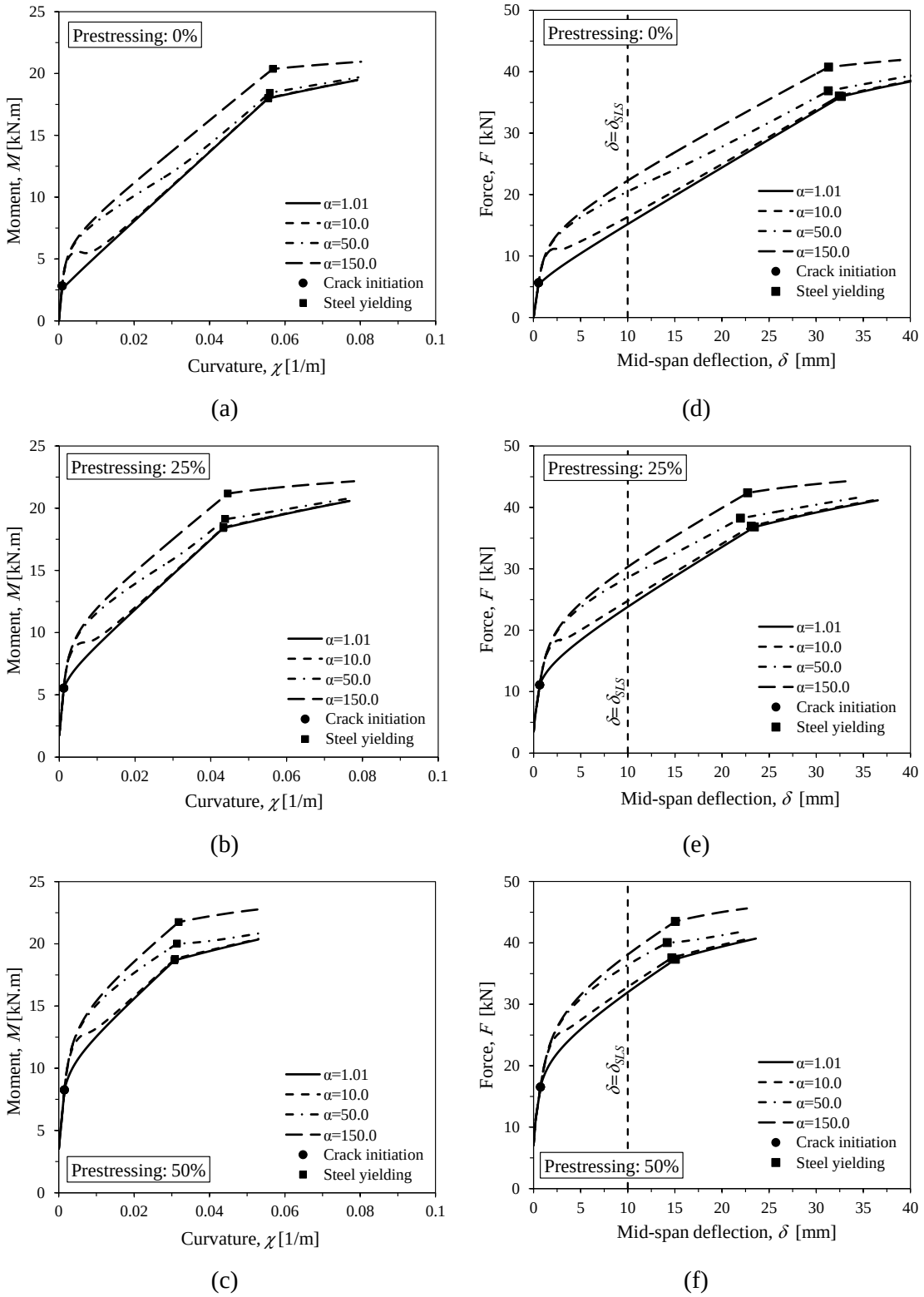

Figure 4.17: Effect of the α parameter on the moment-curvature and load-deflection responses for steel and FRP bars pre-stressed at level of 0.0, 25, and 50%

According to Figure 4.17, the moment-curvature and load-deflection diagrams corresponding to the two lowest adopted values of normalised transition strain (α =1.01 and α =10) only differ in a relatively small amplitude of curvature and deflection, just after crack initiation. The increase in α parameter from 10 to 150, however, provides significant improvement of those responses.

The increasing percentage of the load carrying capacity of the beam at serviceability limit states is determined by the following equation:

$$\Delta F_{SLS}^{\alpha} = \frac{\left(F_{\delta_{SLS}=10mm}^{\alpha\neq1.01} - F_{\delta_{SLS}=10mm}^{\alpha=1.01}\right)}{F_{\delta_{SLS}=10mm}^{\alpha=1.01}} \tag{4.46}$$

where δ_{SLS} $(=10\,\mathrm{mm})$ is the deflection corresponding to the serviceability limit state determined by dividing the beam span length ($L_{span} = 2500mm$) by 250 (EN 1992-1-1 2004). Furthermore, $F_{\delta_{SLS}=10mm}^{\alpha\neq1.01}$ and $F_{\delta_{SLS}=10mm}^{\alpha=1.01}$ are the load carrying capacity corresponding to the serviceability limit states obtained for the case $\alpha \neq 1.01$ (*i.e.* α =10, 50, or 150) and $\alpha = 1.01$, respectively.

It is verified that by adopting the α values of 10, 50 and 150, ΔF_{sls}^{α} of 8%, 35% and 47% is determined for the pre-stressing level of 0%; 4%, 20% and 27% for the pre-stressing level of 25%; and 3%, 14% and 19% for the pre-stressing level of 50%, respectively. Due to the linear behaviour of FRP bars, the moment-curvature and the load-deflection diagrams vary almost linearly between steel yield point and ultimate condition (all the analysis was interrupted when the tensile strength of FRP was attained).

The influence of the pre-stress percentage on the moment-curvature and load-deflection responses is illustrated in Figures 4.18(a)-(d) and 4.19(a)-(d), respectively, for the considered values of α. As expected, for a given α value, the moment and the load at crack initiation have increased with the applied pre-stress, but the moment and the load at yield initiation of the steel bars were not significantly affected by the pre-stress level.

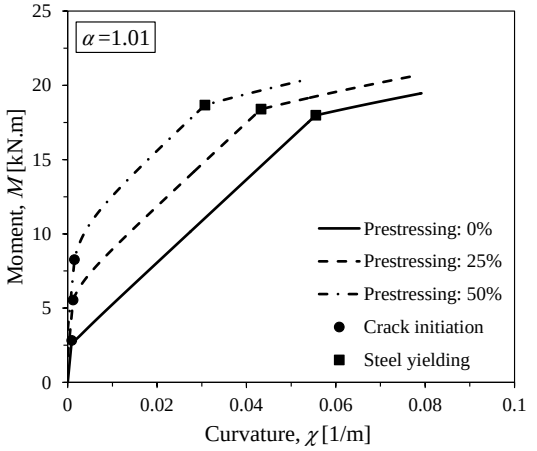

(a)

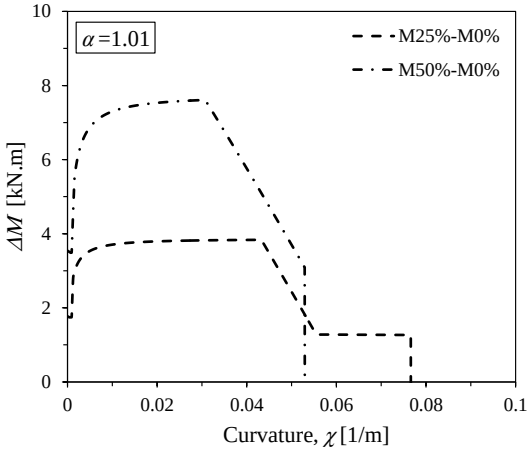

(e)

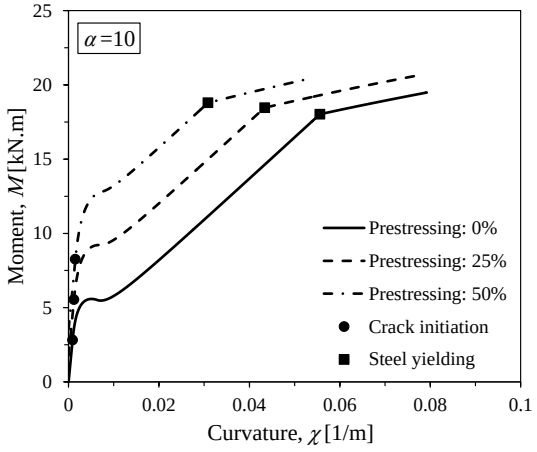

(b)

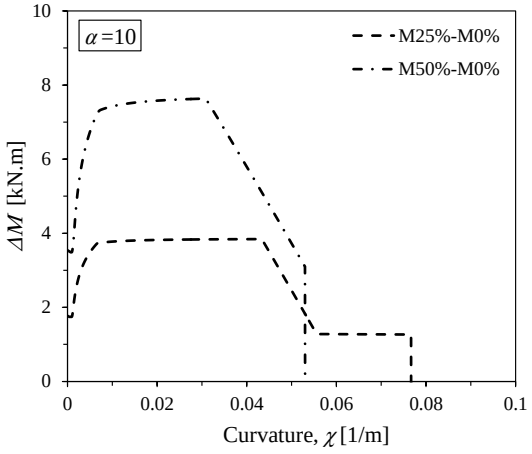

(f)

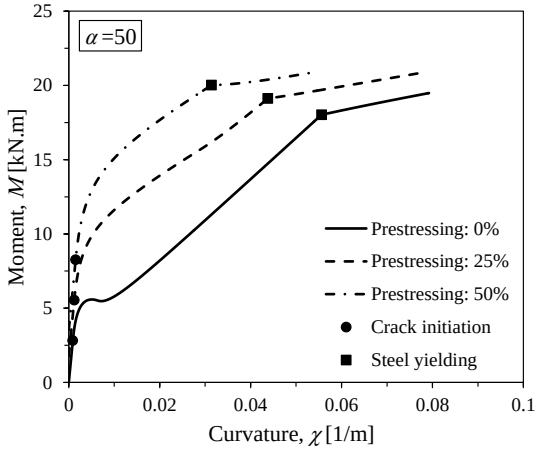

(c)

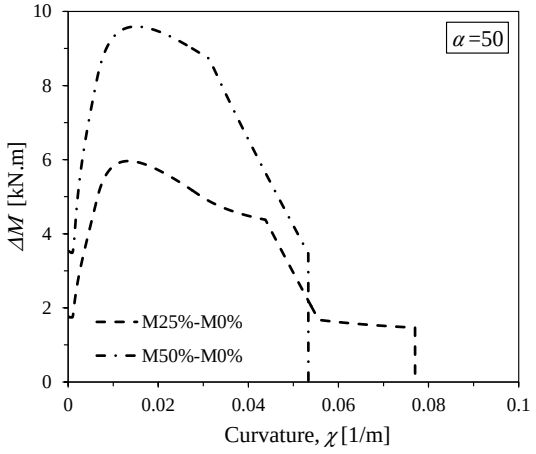

(g)

Figure 4.18 (*Continued*)

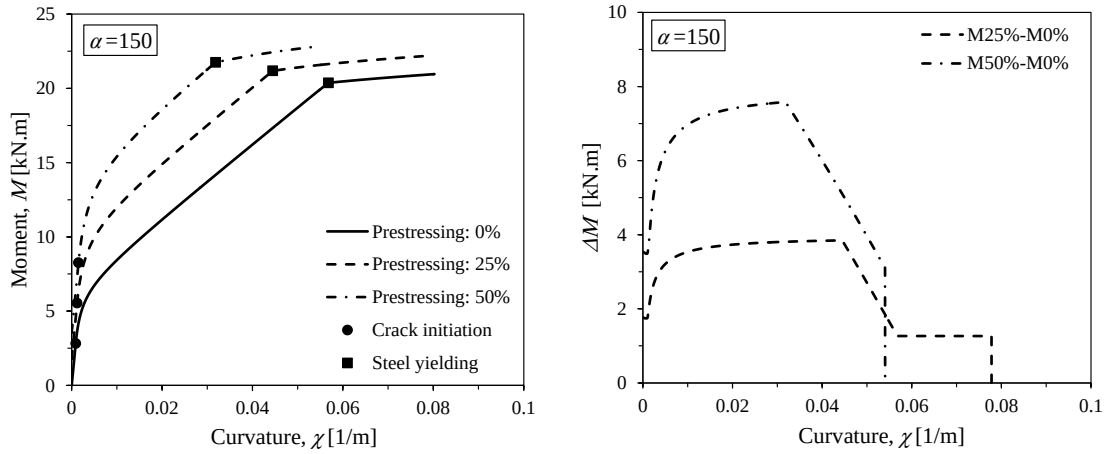

(d) (h)

Figure 4.18: Effect of the pre-stress level on the: (a-d) moment-curvature response; (e-h) increase in the resisting bending moment; for μ =0.4 and α equal to 1.01, 10, 50 and 150.

However, due to the initial tensile strain introduced in the steel bars when pre-stress is applied, the curvature and the deflection at yield initiation decrease with the increase in the pre-stress level. Due to similar reason, the curvature and the deflection at the rupture of the FRP bars decrease with the increase in the pre-stress level applied to these bars. Figures 4.18(e)-(h) show that the $\Delta M = M^{pr=25/50} - M^{pr=0.0}$ increases with the pre-stress level, being $M^{pr=25/50}$ the moment for a pre-stress level of 25% or 50%, and $M^{pr=0.0}$ the moment for non pre-stressed beam. However, the maximum increase in ΔM is almost the same regardless of the value of α considered. The similar tendency is observed for the increase in $\Delta F = F^{pr=25/50} - F^{pr=0.0}$ with the pre-stress level (Figures 4.19e-h).

Figures 4.18(a)-(d) and 4.19(a)-(d) also show that the curvature and the deflection at steel yield initiation decrease with the increase in the pre-stress level applied to steel and FRP bars, while the curvature and deflection at crack initiation is not affected significantly. Therefore, the curvature and deflection amplitude between crack initiation and steel yield initiation decreases with the increase in the pre-stress level, reducing the ductility of the response of the beams. However, a hybrid reinforced FRC beam can be designed in order the maximum ΔF occurs at a deflection level larger than the deflection at serviceability limit states (with an amplitude decided by the designer), as is the case of the present analysis.

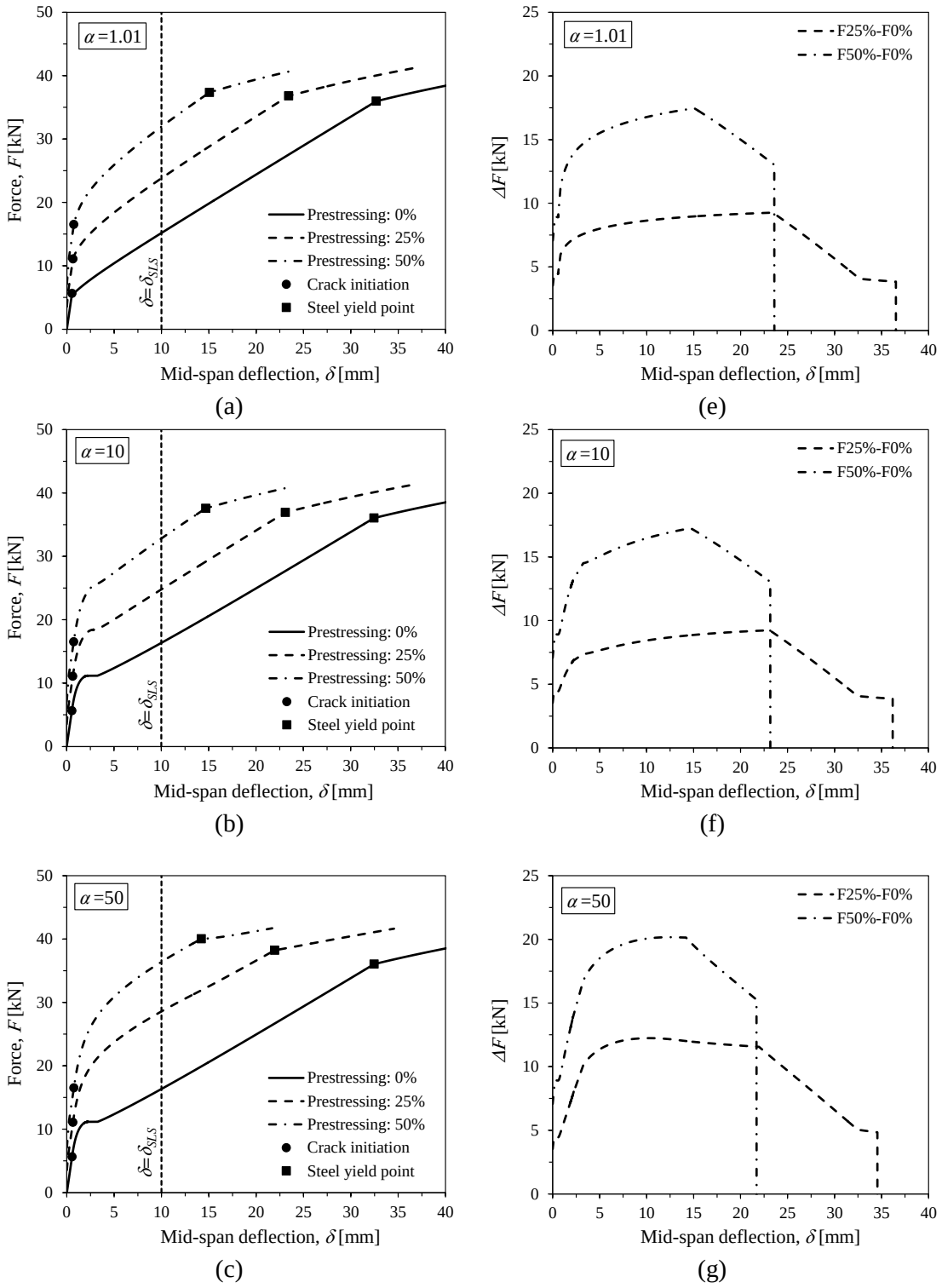

Figure 4.19 (*Continued*)

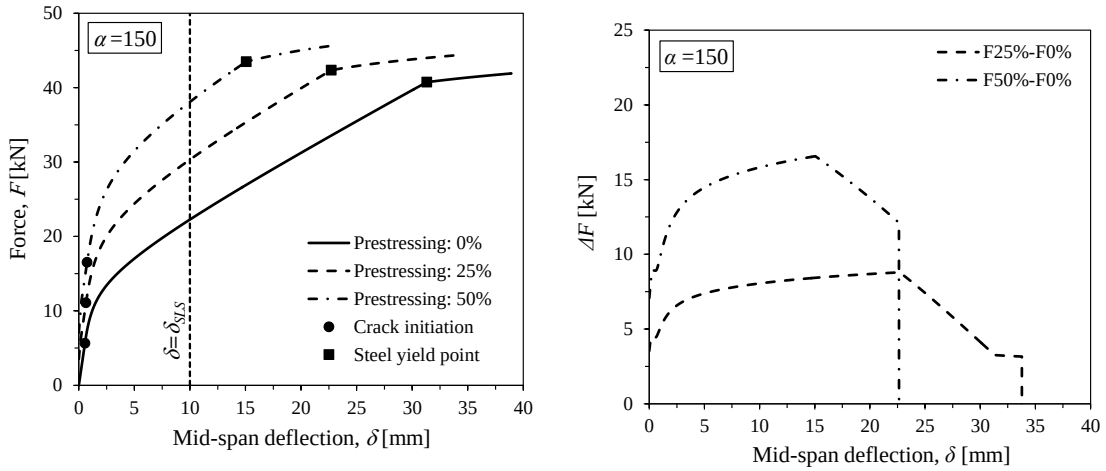

(d) (h)

Figure 4.19: Effect of the pre-stress level on the: (a-d) Load-deflection response; (e-h) increase in the load carrying capacity; for μ =0.4 and α equal to 1.01, 10, 50 and 150

4.7.2 Influence of μ parameter and pre-stress level on moment-curvature and load-deflection responses of hybrid reinforced FRC beams

Figures 4.20(a)-(c) and 4.20(d)-(f) represent the influence of normalised residual strength, μ, in terms of moment-curvature and force-deflection responses, respectively. The increase in this parameter provides a significant increase in the flexural strength and load carrying capacity. For the deflection corresponding to the serviceability limit states conditions (δ_{SLS} =10 mm), the increasing percentage of the load carrying is determined by the equation below:

$$\Delta F_{SLS}^{\mu} = \frac{\left(F_{\delta_{SLS}=10mm}^{\mu\neq 0.0} - F_{\delta_{SLS}=10mm}^{\mu=0.0}\right)}{F_{\delta_{SLS}=10mm}^{\mu=0.0}} \tag{4.47}$$

being $F_{\delta_{SLS}=10mm}^{\mu\neq 0.0}$ and $F_{\delta_{SLS}=10mm}^{\mu=0.0}$ the load carrying capacity corresponding to the serviceability limit states obtained for the case $\mu \neq 0.0$ (*i.e.* $\mu = 0.4$, 0.8, or 1.2) and $\mu = 0.0$, respectively. Regarding the results of the parametric study, ΔF_{SLS}^{μ} of 31%, 68% and 103.7% is obtained for the pre-stressing level of 0%; 20%, 41% and 61% for the pre-stressing level of 25%; and 14%, 29% and 42% for the pre-stressing level of 50%.

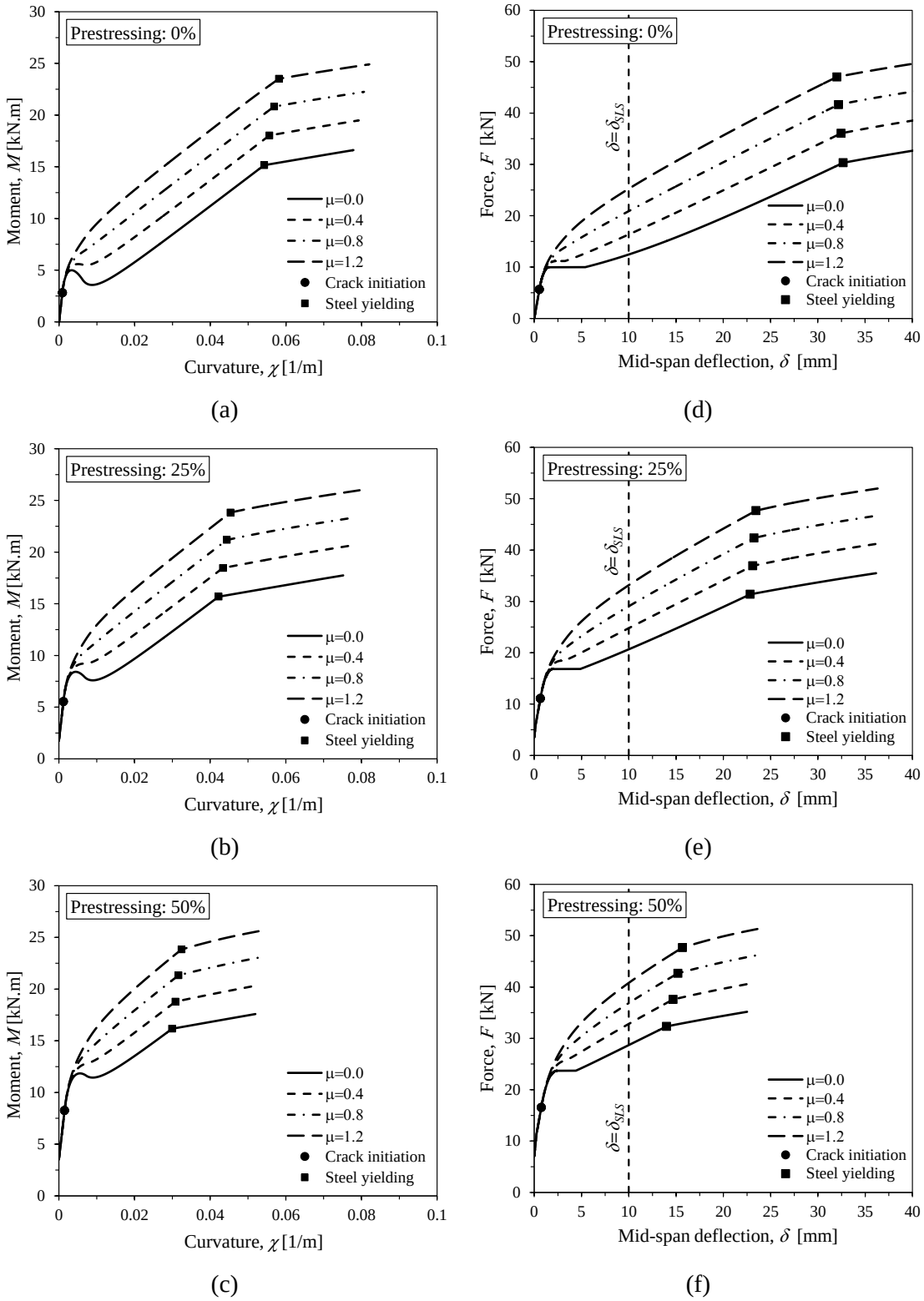

Figure 4.20: Effect of the μ parameter on the moment-curvature and load-deflection responses for α =10, and steel and FRP bars pre-stressed at 0.0, 25, 50%.

The increased level in terms of flexural strength and load carrying capacity is provided with the increase in μ remains almost constant up to the rupture of the FRP (the occurred failure condition). The moment at yield initiation of steel bars and its corresponding curvature increase with μ. The similar tendency occurs in the load carrying capacity at yield initiation of steel bars.

The influence of the pre-stress percentage on the moment-curvature and load-deflection responses is illustrated in Figures 4.21(a)-(d) and 4.22(a)-(d), respectively, for the values of μ considered.

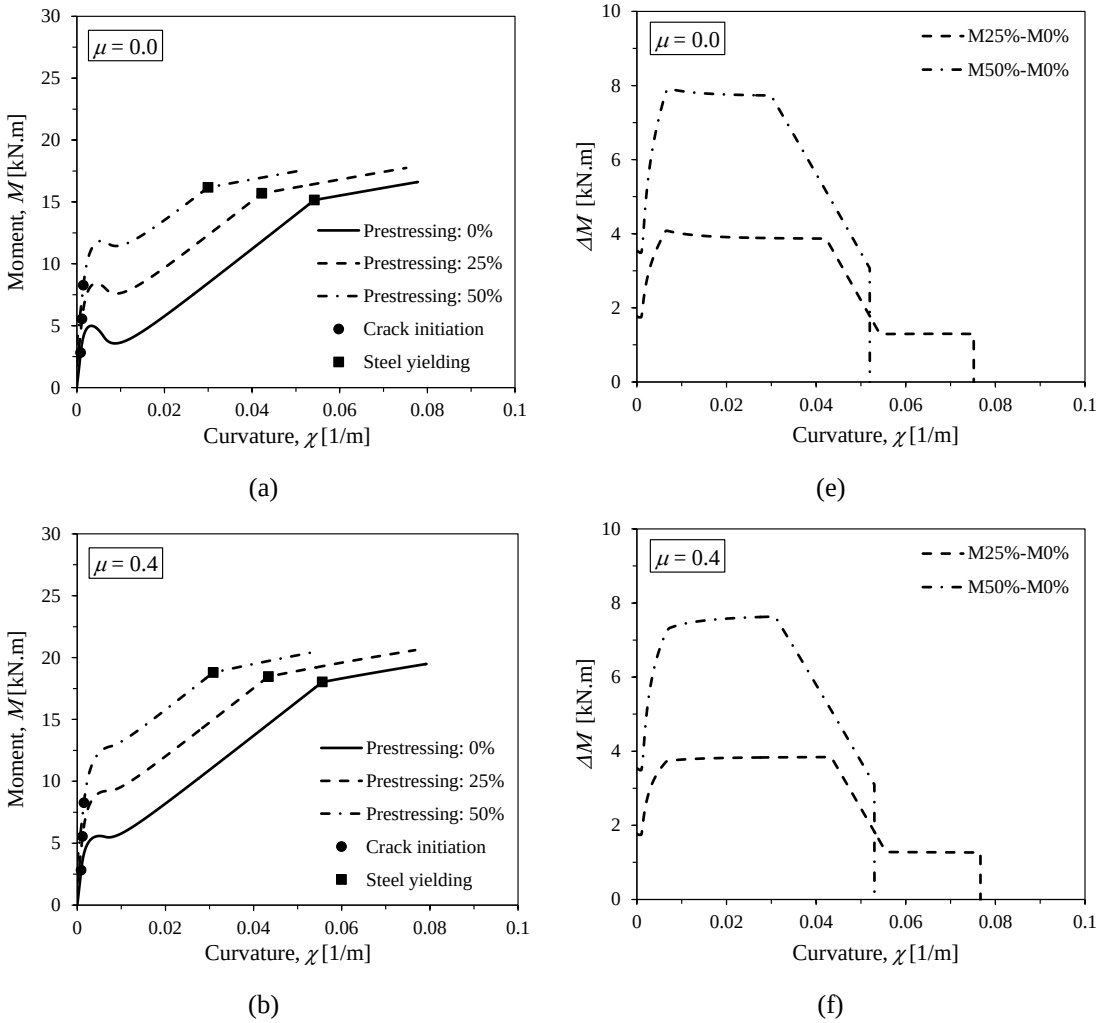

Figure 4.21 *(Continued)*

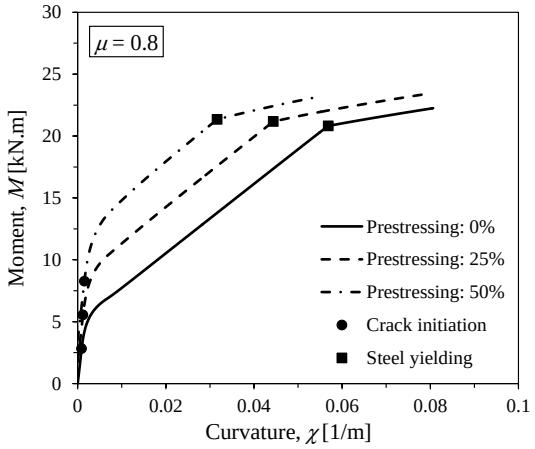

(c)

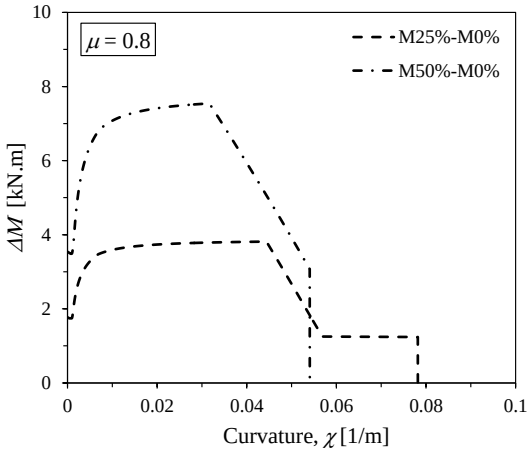

(g)

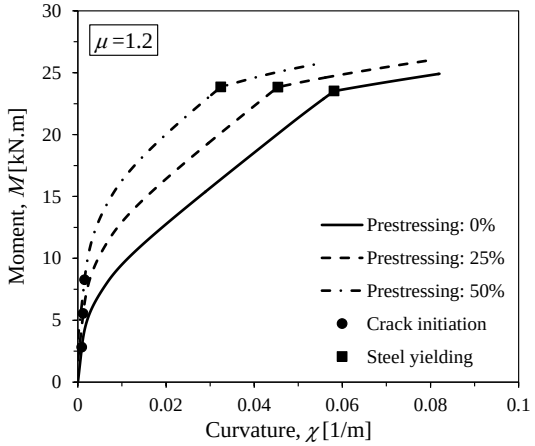

(d)

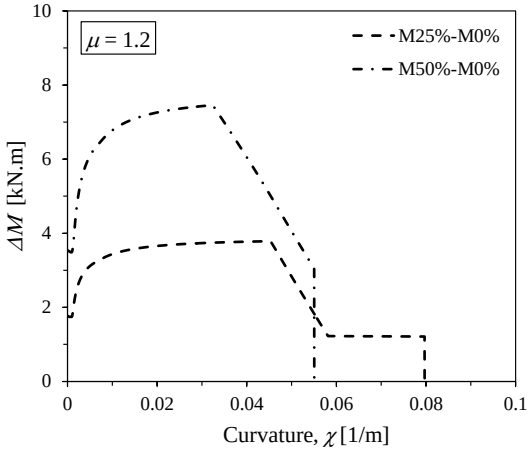

(h)

Figure 4.21: Effect of the pre-stress level on the: (a-d) moment-curvature response; (e-h) increase in the resisting bending moment; for α = 10 and μ equal to 0.0, 0.4, 0.8, 1.2.

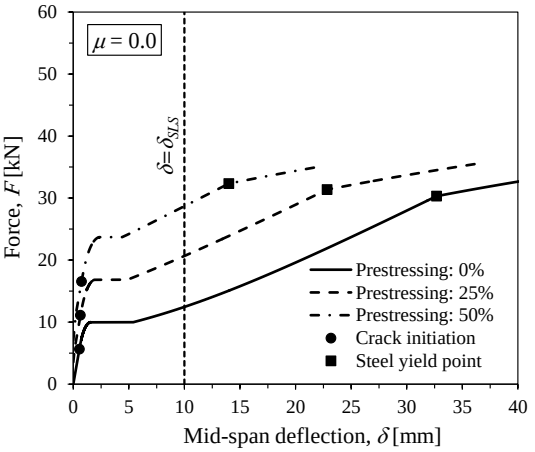

(a)

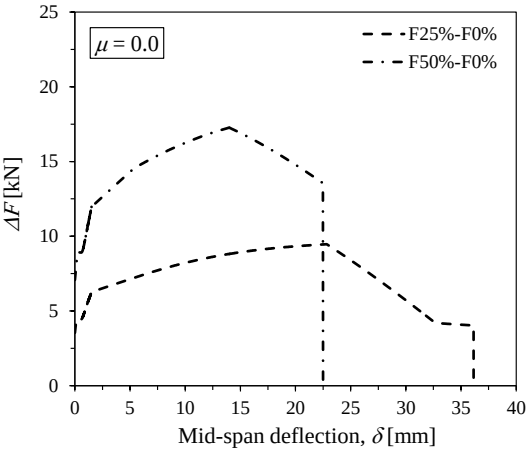

(e)

Figure 4.22 *(Continued)*

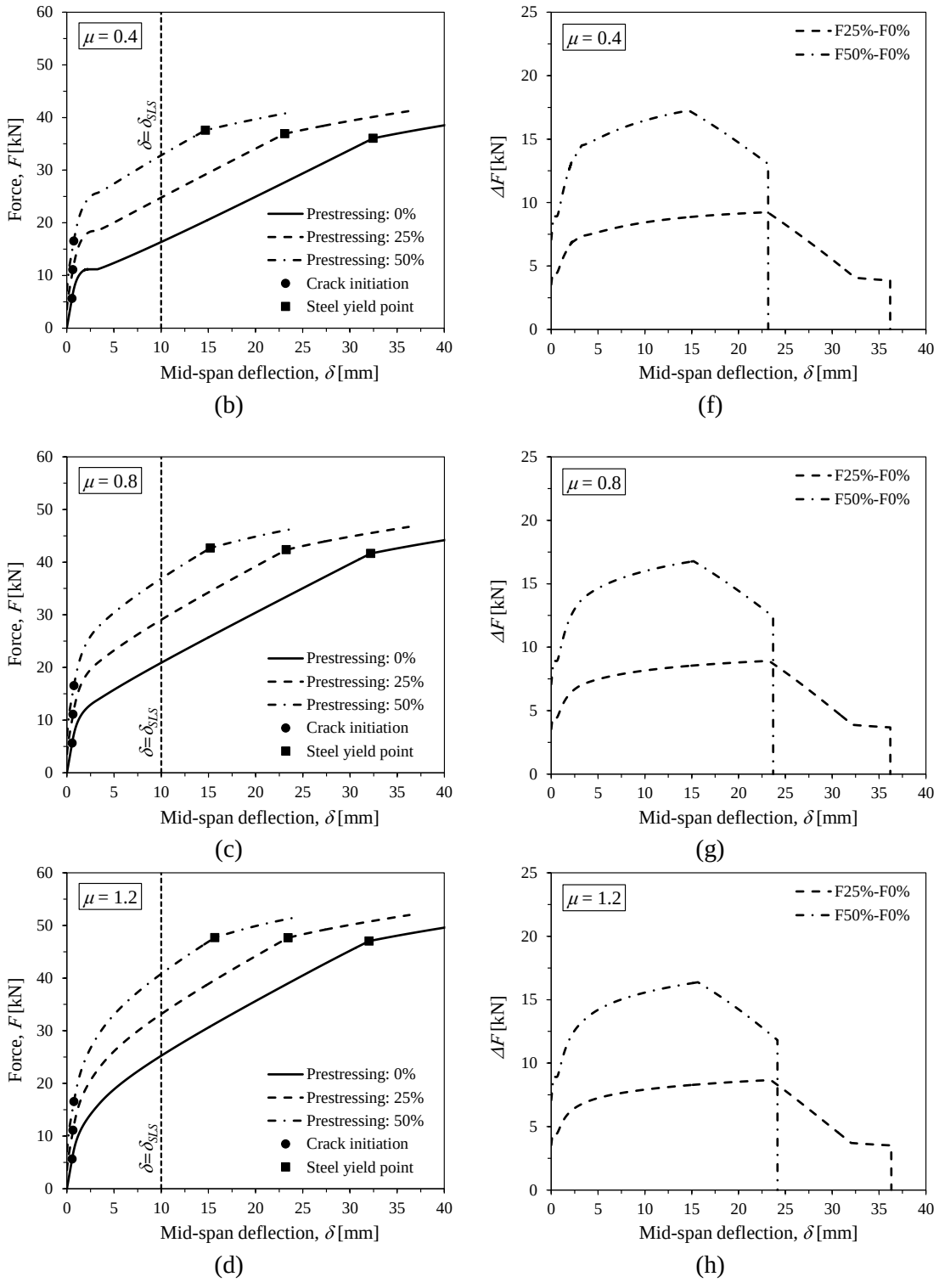

Figure 4.22: Effect of the pre-stress level on the: (a-d) Load-deflection response; (e-h) increase in the load carrying capacity; for α = 10 and μ equal to 0.0, 0.4, 0.8, 1.2.

As expected, for a given μ value, the moment and the load at crack initiation increase with the applied pre-stress, but the moment and the load at yield initiation of the steel bars

were not significantly affected by the pre-stress level. The difference between the curvatures at yield and crack initiation decreases with the increase in the pre-stress level, which equally occurs in the load-deflection response, indicating a decrease in the ductility performance of the beam. As expected, the curvature and the deflection at the failure of the FRP also decrease with the increase in the pre-stress level.

Figures 4.21(e)-(h) show that the $\Delta M = M^{pr=25/50} - M^{pr=0.0}$ increases with the pre-stress level. However, the maximum increase in ΔM is almost the same regardless of the value of μ considered. A similar tendency is observed for the increase in $\Delta F = F^{pr=25/50} - F^{pr=0.0}$ with the pre-stress level (Figures 4.20(e)-(h)).

4.8 Concluding remarks

In this chapter, a design-oriented model was proposed for determining the moment-curvature response of rectangular cross-section of FRC members reinforced by longitudinal pre-stressed steel and FRP bars that fail in bending. By using a trilinear stress-strain diagram for the tensile behaviour of FRC, the proposed model is capable of simulating both strain-softening and strain-hardening FRC materials. A relatively limited number of parameters is necessary to characterize the FRC behaviour in tension and compression, as well as the behaviour of steel and FRP bars in tension. Using the moment-curvature relationship predicted by the model and implementing an algorithm based on the virtual work method, a numerical strategy was developed for the prediction of the force-deflection response of statically determinate beams. The excellent predictive performance of the model was assessed by simulating the force-deflection responses registered in experimental programs. The model is capable of simulating the behaviour of beams internally reinforced with steel and FRP bars, and can additionally be used to predict the force-deflection relationship of RC beams flexurally strengthened with pre-stressed FRP systems applied according to the near-surface mounted (NSM) and externally bonded reinforcement (EBR) techniques.

The proposed methodology was employed to execute a parametric study to evaluate the influence of the following parameters on the moment-curvature and force-deflection

responses: $\alpha = \varepsilon_{trn} / \varepsilon_{cr}$ (normalised transition strain) and $\mu = \sigma_R / E_c \varepsilon_{cr}$ (normalised residual strength) FRC-related parameters and pre-stress level. It was observed that the flexural capacity of the cross-section and the load carrying capacity of the beam increase significantly with μ and α parameters. Furthermore, it was revealed that the moment at yield initiation of steel bars and its corresponding curvature increase with the increase in μ and α parameters. The similar tendency occurs for the load carrying capacity at yield initiation of steel bars. For the deflection corresponding to the serviceability limit states conditions, the increase in μ and α causes a significant increase in the load carrying capacity.

It was also observed that by increasing the pre-stress level in the steel and FRP bars, the curvature and the deflection at steel yield initiation, as well as the curvature and the deflection at failure decrease. Therefore, since the deflection at crack initiation is not affected significantly by the applied pre-stress level, the deflection amplitude between crack initiation and steel yield initiation decreases with the increase in the pre-stress level, reducing the ductility of the response of the beams. However, the FRC can be optimised to provide values for the μ and α parameters that guarantee the aimed degree of ductility when applying a certain pre-stress level in a hybrid reinforced beam.

Chapter 5

Prediction of Crack Width and Spacing in R/FRC Flexural Elements

5.1 Introduction

Cracking in concrete is one of the crucial aspects threaten the durability and structural performance of reinforced concrete (RC) structures. This problem is much more pronounced in the case of steel reinforced concrete (S/RC) structural elements since they are often subjected to tensile stress fields. The stiffness and load carrying capacity of RC elements decrease with the formation and propagation of cracks, which can threaten their design requisites at the serviceability and ultimate limit state conditions (SLS and ULS, respectively). Crack propagation in S/RC elements also increases the permeability of concrete, facilitating the ingress of environmental adverse agents through the concrete zones where steel reinforcement is disposed, which promotes its corrosion as faster as wider are the cracks (Arya and Wood 2015). This typically results in a reduction of the cross-section area of the steel reinforcement, deterioration of steel-to-concrete bond

quality, and concrete spalling and disintegration, which are all responsible for a reduction of load carrying capacity of structural S/RC elements.

Substitution of steel reinforcements by non-corrodible ones made of fibre reinforced polymer (FRP) has been investigated during the last decades, in an attempt of improving the durability of RC structural elements (Wang and Belarbi 2013, Abdalla 2002). Hereinafter these elements will be designated by the acronym F/RC to distinguish them from those reinforced with steel bars (S/RC). The use of FRP as internal reinforcement of concrete structures may have, however, some detrimental consequences in structural design viewpoint. When compared to steel, the frequently used and cost-competitive FRPs have lower elasticity modulus and weaker bond characeristics. Furthermore, mechanical properties of FRPs are negatively affected when surrounding temperature exceeds the transition temperature of their polymer-based matrix. These aspects often lead to a larger deflection and wider cracks in F/RC elements subjected to flexural loading conditions, such as the case of beams and slabs, so accomplishing the design requisites at SLS of F/RC are often predominant in the design framework (Almusallam 1997, Masmoudi *et al.* 1998). Furthermore, due to the larger crack width, the shear capacity of F/RC beams is smaller than S/RC beams of the same reinforcement ratio due to the detrimental impact on the favourable aggregate interlock resisting mechanism (ACI 440R-07 2007). The previously pointed out drawbacks can be mitigated by adopting hybrid flexural reinforcements (HFR), where FRP bars are placed with the minimum possible concrete cover thickness to take advantage of their immunity to corrosion, while steel bars are disposed with higher concrete cover thickness for being better protected from corrosion agents (Aiello and Ombres 2002). Elements with HFR are, hereinafter, abbreviated by the acronym H/RC, where the extraordinary tensile strength of FRPs combined with the elasto-plastic behaviour of steel reinforcements can be mobilised for ensuring adequate performance at SLS and ULS design conditions. Experimental evidence revealed that the deflection, crack width, and crack spacing of H/RC beams are generally smaller than that of F/RC beams, and failure mode can be more ductile (Tian and Yuan 2007, Aiello and Ombres 2002). The potentialities of HFR can be increased when used with fibre reinforced concrete (FRC) for the development of hybrid flexurally reinforced FRC (H/FRC) beams (Taheri *et al.* 2011). When cracks are formed in concrete, the discrete fibres bridging these cracks offer resistance to their widening by fibre pull-

out mechanisms (Naaman 2000, Barros *et al.* 2005), leading to significant benefits in terms of SLS and ULS design requisites and on the durability of S/RC, F/RC and H/RC elements (Soltanzadeh *et al.* 2016b, Mazaheripour *et al.* 2016b). According to Wang and Belarbi (2013), an improvement of 30% of the durability index of RC beams was achieved by the addition of 0.5% volume fraction of fibres. The influence of fibres for minimising the occurrence of shear cracks and increasing the shear resistance of FRC beams is noticeable (Santos *et al.* 2008, Barros *et al.* 2004b, Susetyo *et al.* 2011). It has been demonstrated that in shallow reinforced FRC (R/FRC) beams, steel stirrups can be replaced by fibres with technical and economic advantages (Casanova *et al.* 1997). In addition, the discrete fibres contribute to reduce the deflection of R/FRC beams under service loads and to increase the maximum load carrying capacity (Taheri *et al.* 2011, Barros *et al.* 2012). Experimental and numerical investigations have revealed that the favourable fibre reinforcement mechanisms on the post-cracking behaviour of concrete have effectively improved the tension-stiffening effect owing to stress transference between flexural reinforcements and surrounding concrete during the concrete cracking process (Mazaheripour *et al.* 2016a, Abrishami and Mitchell 1997, Lee *et al.* 2013), resulting in reduction in the width and spacing of cracks (Bischoff 2003, Oliveira Júnior *et al.* 2016, Chiaia *et al.* 2008), as well as in maximum stress level in the flexural reinforcement (Jordon and Frank 2013).

In the present chapter an integrated approach for the prediction of crack width and spacing in H/FRC flexural elements is developed, where mechanical properties of intervening materials, the post-cracking response of FRC in terms of stress-crack opening relationship $(\sigma - w)$, and the shear bond-sliding characteristics of steel- and FRP-to-concrete interaction is mobilised in a model developed based on a moment-rotation approach (Taheri and Barros 2012). The predictive performance of the proposed approach is evaluated considering the results of the experimental program detailed in chapter 3, as well as the ones present in the literature (Vandewalle 2000, Tan *et al.* 1995, Montaignac *et al.* 2012). The predictive performance in terms of crack width and spacing of the formulations proposed by two international organizations (*fib* Model Code 2010 2011, RILEM TC 162-TDF 2003) is also assessed and commented.

5.2 Model developed based on the moment-rotation approach

Figure 5.1(a) depicts an idealised crack propagation stage in a pure bending region (PBR) of L_{PBR} length of an R/FRC element subjected to bending moment (M) and consequent overall rotation (θ). It is assumed that the geometry of the beam's cross-section and reinforcing scheme of the section is constant along with the L_{PBR}. The considered R/FRC element is assumed to have symmetric cross-section as shown in Figure 5.1(b), where the width can vary along its depth, h. The total height of the cross-section is decomposed in *n* layers to take into account the appropriate constitutive law for each material layer during the loading procedure.

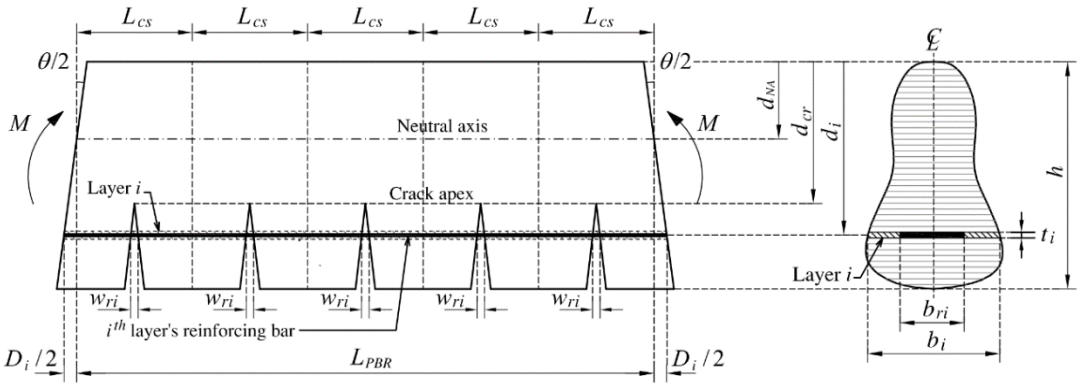

Figure 5.1: (a) Cracking propagation in a pure bending region of R/FRC beams, (b) layer approach to model the cross-section

The width, the thickness and the depth of the generic i^{th} layer (numbered from the beam's top surface) are represented by b_i, t_i, and d_i, respectively. The i^{th} layer may additionally include reinforcing bars of cross-sectional area A_{ri}. In this case, the total width of the layer (b_i) is subdivided into the equivalent width of reinforcement b_{ri} $(=A_{ri}/t_i)$ and the width of concrete b_c $(=b_i-b_{ri})$ (see Figure 5.1b). By progressively increasing the applied bending moment, the most tensioned concrete surface (in Figure 5.1a is the bottom surface) attains the concrete strain at crack initiation $(\varepsilon_{ct}=\varepsilon_{cr})$ and, consequently, several flexural cracks may propagate along with the PBR, subdividing the

L_{PBR} into several R/FRC prisms of L_{cs} length. Due to the constant bending moment and similarity of geometry and reinforcing scheme of the beam's cross-section along with the PBR, the cracks geometry (*i.e.* the width and depth) and spacing are assumed equal.

5.2.1 Mechanical properties of intervening materials

5.2.1.1 Compressive behaviour of FRC

The compressive behaviour of FRC can be subdivided into the pre-peak and the post-peak responses. Imposing strains lower than the one corresponding to the concrete compressive strength ($\varepsilon_{cc,p}$, Figure 5.2), only small isolated and randomly distributed cracks exist and hence, the continuous mechanics is valid. When $\varepsilon_{cc,p}$ is exceeded, internal microcracks coalesce into macro-cracks leading to crack localisation. Consequently, the use of strain as a state variable in constitutive laws for compressive concrete is not valid anymore. (Van Mier 1997). In this case, the post-peak behaviour of concrete in compression can be analysed by the wedge sliding mechanism (Barros *et al.* 2015b). However, since the present research is aiming to analyse the behaviour of R/FRC flexural beams during the cracking propagation stage, by estimating the crack width and average crack spacing for serviceability limit state design conditions, the maximum concrete compressive strain level is less than $\varepsilon_{cc,p}$. Therefore, and for the sake of simplicity, the stress-strain relationship $(\sigma_{cc}-\varepsilon_{cc})$ schematised in Figure 5.2 was adopted for simulating the concrete compression behaviour, which is represented by the following equations (Vipulanandan and Paul 1990):

$$\sigma_{cc}\left(\varepsilon_{cc}\right)=f_{cc}\frac{\varepsilon_{cc}/\varepsilon_{cc,p}}{(1-p-q)+q\left(\varepsilon_{cc}/\varepsilon_{cc,p}\right)+p\left(\varepsilon_{cc}/\varepsilon_{cc,p}\right)^{\frac{1-q}{p}}} \tag{5.1}$$

$$q=1-p-\frac{E_{c,\sec}}{E_c},\ p+q\in]0,1[,\frac{1-q}{p}>0 \tag{5.2}$$

where $\varepsilon_{cc,p}$ is the strain corresponding to the concrete compressive strength (f_{cc}), $E_{c,\sec}$ is the secant modulus of elasticity of concrete ($= f_{cc} / \varepsilon_{cc,p}$), and p is a parameter ranging between zero to one. For concrete reinforced with hooked ends steel fibres the following equations were adopted for determining $\varepsilon_{cc,p}$ and *p* parameters (Barros and Figueiras 1999b):

$$\varepsilon_{cc,p}^{SFRC} = \varepsilon_{cc,p}^{PC} + 0.000654 V_f \tag{5.3}$$

$$p = 1.0 - 0.919 \exp\left(-1.289 V_f\right) \tag{5.4}$$

where V_f is the fibre volume percentage, and $\varepsilon_{cc,p}^{PC}$ is the strain at the compressive strength of the plain concrete of the same strength class of the FRC (*fib* Model Code 2010 2011). The superscript *SFRC* and *PC* in Equation (5.3) indicate that the entity is measured in specimens of steel fibre reinforced concrete or plain concrete of the same strength class, respectively. For concrete reinforced with fibres other than of steel material, specific equations for the $\varepsilon_{cc,p}$ and *p* should be derived based on experimental results with the FRC.

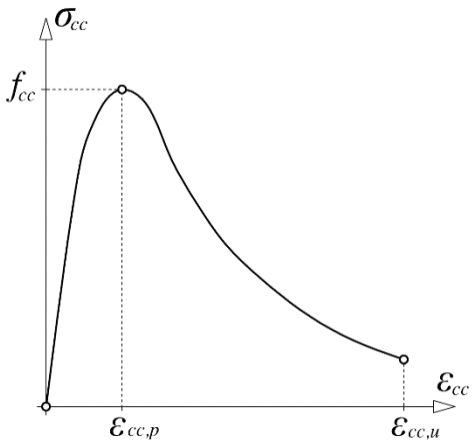

Figure 5.2: Stress-strain diagram for simulating the compressive behaviour of an FRC

5.2.1.2 Tensile behaviour of FRC

The constitutive law adopted to simulate the tensile behaviour of FRC is presented in Figure 5.3, which is capable of simulating FRC of strain-softening and strain-hardening nature (SS-FRC and SH-FRC, respectively). In fact in SS-FRC, after crack initiation, at $(\varepsilon_{cr}, f_{ct})$, the tensile behaviour is governed by a stress-crack width like the one schematically represented in Figure 5.3(b), therefore, the second branch of the stress-strain diagram is almost inexistent, *i.e.*, $\varepsilon_{ct,p} = \varepsilon_{cr}$ and $\sigma_{ct,p} = f_{ct}$. In the case of SH-FRC, after crack initiation, several cracks are progressively formed up to the degeneration of one of these cracks into a macro-crack. This stage is simulated by the second branch of the $\sigma_{ct} - \varepsilon_{ct}$ relationship, whose stiffness depends on the reinforcement mechanisms developed between fibres and the surrounding matrix.

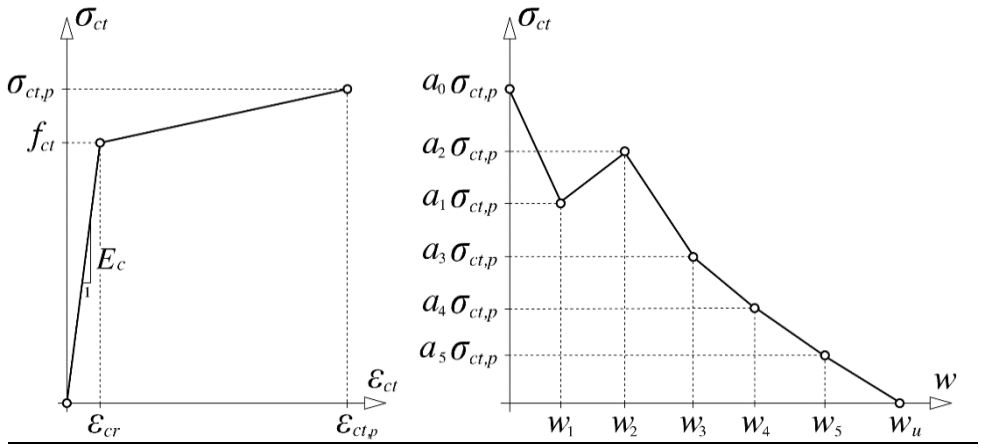

(a) (b)

Figure 5.3: Tensile behaviour of FRC: (a) stress-strain diagram before macro-cracking localization, (b) post-cracking stress-crack width response

The stress-strain diagram is simulated by the following equations (Figure 5.3):

$$\sigma_{ct}(\varepsilon_{ct}) = \begin{cases} E_c \varepsilon_{ct} & 0 \le \varepsilon_{ct} \le \varepsilon_{cr} \quad (5.5a) \\ f_{ct} + \left(\frac{\varepsilon_{ct} - \varepsilon_{cr}}{\varepsilon_{ct,p} - \varepsilon_{cr}}\right)\left(\sigma_{ct,p} - f_{ct}\right) & \varepsilon_{cr} < \varepsilon_{ct} \le \varepsilon_{ct,p} \quad (5.5b) \end{cases}$$

where $\varepsilon_{cr} = f_{ct}/E_c$ is the strain at crack initiation, and f_{ct} and E_c present the tensile strength and Young's modulus of FRC that can be obtained from the recommendations of *fib* Model Code 2010 (2011):

$$f_{ct} = \begin{cases} 0.30\, f_{ck}^{2/3} & \left[\text{for concrete strength class} \le C50/60\right] \quad (5.6a) \\ 2.12 \ln\left(1 + f_{cm}/10\right) & \left[\text{for concrete strength class} > C50/60\right] \quad (5.6b) \end{cases}$$

$$E_c = 21.5\left(\frac{f_{cm}}{10}\right)^{1/3} \quad [\, f_{cm} \text{ in MPa, } E_c \text{ in GPa}] \quad (5.7)$$

being f_{ck} and f_{cm} the characteristic and average value of compressive strength of concrete, respectively. In Equation (5.5b) $\sigma_{ct,p}$ and $\varepsilon_{ct,p}$ are the tensile strength and corresponding strain of SH-FRC, respectively. Macro-cracking propagation is described by a stress-crack opening diagram that can be formed by multi-linear segments (Figure 5.3b) to embrace the potential of capturing, with excellent accuracy, the behaviour of the softening response of cement-based materials reinforced with mono- or hybrid fibre systems (RILEM TC 162-TDF 2003):

$$\sigma_{ct}(w) = \left[a_i + (a_{i+1} - a_i)\frac{w - w_i}{w_{i+1} - w_i}\right]\sigma_{ct,p} \quad (\textit{for } w_i \le w \le w_{i+1}) \quad (5.8)$$
$$(i = 0 \text{ to } 6,\ a_0 = 1,\ w_0 = 0,\ a_6 = 0, w_6 = w_u)$$

where $a_i = \sigma_i / f_{ct}$ is the normalised stress parameter corresponding to crack width w_i, and w_u represents the ultimate crack width. The shape of the $\sigma - w$ diagram is typically determined by performing uniaxial tensile tests with notched FRC specimens (Salehian 2015, Pereira *et al.* 2012), or by inverse analysis by fitting with a target accuracy the force-deflection registered in notched FRC beam bending tests (Salehian and Barros 2015, Barros *et al.* 2007).

5.2.1.3 Behaviour of longitudinal reinforcing bars

The bilinear stress-strain relationship represented in Figure 5.4 is adopted for the longitudinal reinforcement in both compression and tension that can be described by the following equation:

$$\sigma_r\left(\varepsilon_r\right)=\begin{cases} E_r\varepsilon_r & \varepsilon_r \le \varepsilon_{ry} \quad (5.9a) \\ \sigma_{ry}+\left(\varepsilon_r-\varepsilon_{ry}\right)\left(\dfrac{\sigma_{ru}-\sigma_{ry}}{\varepsilon_{ru}-\varepsilon_{ry}}\right) & \varepsilon_{ry}<\varepsilon_r \le \varepsilon_{ru} \quad (5.9b) \end{cases}$$

where E_r, σ_{ry}, and σ_{ru} represent, respectively, the modulus of elasticity, the yielding stress, and ultimate strength of the reinforcement, while ε_{ry} and ε_{ru} are the strains corresponding to σ_{ry} and σ_{ru}, respectively. The constitutive law of Figure 5.4 can also simulate reinforcement of elastoplastic behaviour, such as the case of some steel bars, by considering the identical value for σ_{ry} and σ_{ru}. This diagram is also adaptable for simulating the behaviour of FRP bars since their linear-brittle nature can be model by assuming $\varepsilon_{ru}=\varepsilon_{ry}$ and $\sigma_{ru}=\sigma_{ry}$.

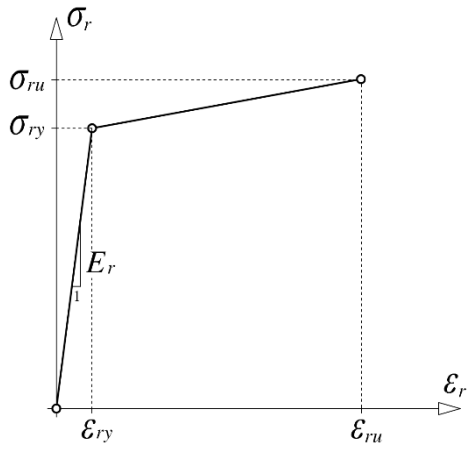

Figure 5.4: Stress-strain relationship for simulating the tension and compression behaviour of longitudinal reinforcements

5.2.2 FRC-to-longitudinal reinforcement interaction

5.2.2.1 Local bond stress-slip relationship

In the developed model, the multi-linear shear bond stress-slip relationship $(\tau - s)$ represented in Figure 5.5 is adopted for simulating the bond mechanisms between longitudinal reinforcements and surrounding FRC. The adopted configuration for the $\tau - s$ is sufficiently flexible for simulating the bond conditions of FRP bars (Baena *et al.* 2009) and steel bars (Harajli *et al.* 2002). This model is based on the one originally developed by Eligehausen *et al.* (1982) to describe the local bond stress-slip behaviour of deformed bars, as recommended in (*fib* Model Code 2010 2011), with the difference of replacing the pre-peak parabolic curve by a linear bond-slip relationship to simplify the numerical approach.

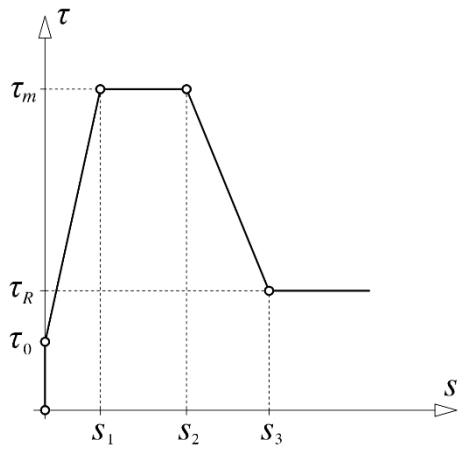

Figure 5.5: Shear bond stress-slip relationship for embedded reinforcement

$$\tau\left(s(x)\right)=\begin{cases}\tau_0+\left(\dfrac{\tau_m-\tau_0}{s_1}\right)s(x) & 0\le s(x)\le s_1 & \text{(elastic phase)} & (5.10a)\\ \tau_m & s_1<s(x)\le s_2 & \text{(plastic phase)} & (5.10b)\\ \tau_m-\left(\dfrac{\tau_m-\tau_R}{s_3-s_2}\right)\left[s(x)-s_2\right] & s_2<s(x)\le s_3 & \text{(softening phase)} & (5.10c)\\ \tau_R & s_3<s(x) & \text{(frictional phase)} & (5.10d)\end{cases}$$

The adopted shear bond stress-slip relationship includes five distinct phases; 1) an adhesion stage with a bond strength of τ_0 for null sliding; 2) a linear-elastic response

up to attain the slip s_1 that corresponds to the occurrence of the shear bond strength (τ_m); 3) a perfect plastic slipping stage up to the slip s_2 where bond stress remains constant; 4) a slipping softening phase up to s_3; 5) a frictional phase where a constant residual bond stress (τ_R) is considered due to frictional mechanisms between reinforcing bar and surrounding concrete. A similar model was adopted by Bianco *et al.* (2009) to simulate the bond-sliding response of carbon FRP (CFRP) laminates used in shear strengthening of RC beams by near-surface mounted (NSM) technique.

5.2.2.2 Bond interaction between flexural reinforcement and surrounding FRC in the cracking process of an R/FRC element

In Figure 5.6, a longitudinal reinforcing bar is shown with an effective area of the surrounding concrete. When a longitudinal bar of relatively large embedment length is crossed by a crack, the slip of this bar in the cracked cross-section can be assumed equal to half of the crack width at the level of this bar $(s_r = w_r / 2)$.

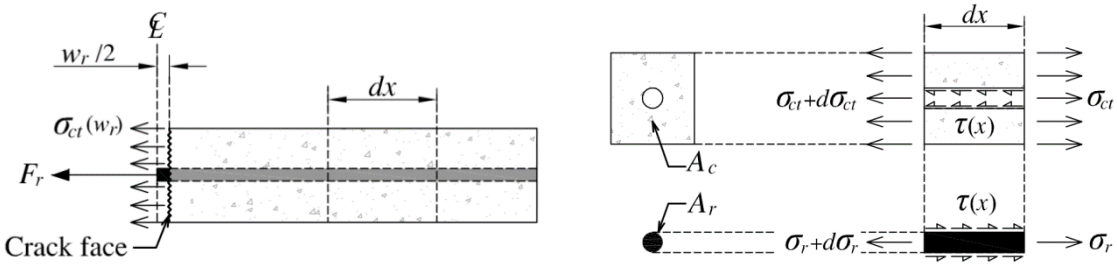

(a) (b)

Figure 5.6: (a) Reinforcing bar and surrounding concrete, (b) force equilibrium of reinforcement and surrounding concrete along an infinitesimal bond transference length of dx

In Figure 5.6(a), the internal force of the reinforcing bar and tensile stress of the surrounding concrete at crack face are designated by F_r and $\sigma_{ct}(w_r)$, respectively. The latter can be determined from the post-cracking constitutive law of concrete in tension, according to the diagram represented in Figure 5.3(b). In Figure 5.6(b) is depicted the force equilibrium of reinforcement and surrounding concrete along with the bond transference length dx. By satisfying equilibrium between tensile forces of reinforcement

$(\sigma_r A_r)$, the surrounding concrete ($\sigma_{ct} A_c$), and also the contribution of shear bond force along with the bond transference length $(\tau(x) L_p dx)$, it can be formulated as bellow:

$$(\sigma_{ct} + d\sigma_{ct})A_c + \tau(x)L_p dx - \sigma_{ct}A_c = 0 \quad \Rightarrow \quad \frac{d\sigma_{ct}}{dx} = -\frac{\tau(x)L_p}{A_c} \tag{5.11}$$

$$(\sigma_r + d\sigma_r)A_r - \tau(x)L_p dx - \sigma_r A_r = 0 \quad \Rightarrow \quad \frac{d\sigma_r}{dx} = \frac{\tau(x)L_p}{A_r} \tag{5.12}$$

where A_r and A_c are the cross-sectional area of reinforcement and surrounding concrete, respectively (Figure 5.6b), and $L_p (= \pi d_b)$ is the perimeter of the reinforcement bar of diameter d_b. The interfacial slip along with the bond transference length can be defined as the relative deformation between reinforcement (u_r) and surrounding concrete (u_c):

$$s(x) = u_r - u_c \tag{5.13}$$

By two times differentiating the two sides of the previous equation and considering the Hooke's law for the reinforcement

and concrete, results:

$$\frac{d^2 s(x)}{dx^2} = \frac{1}{E_r}\left(\frac{d\sigma_r}{dx}\right) - \frac{1}{E_c}\left(\frac{d\sigma_{ct}}{dx}\right) \tag{5.14}$$

Furthermore, by substituting $d\sigma_{ct}/dx$ and $d\sigma_r/dx$, respectively, from Equations (5.11) and (5.12) into Equation (5.14), the following equation is obtained:

$$\frac{d^2 s(x)}{dx^2} - J_1 \tau(x) = 0 \tag{5.15}$$

where J_1 is a coefficient related to the geometry and modulus of elasticity of reinforcing bar and surrounding concrete:

$$J_1 = \left(\frac{L_p}{E_r A_r} + \frac{L_p}{E_c A_c}\right) \tag{5.16}$$

As depicted in Figure 5.7, the relative sliding between the reinforcing bar and surrounding concrete tends to zero at section 2 (Sec. 2) located at a distance L_{tr} from the crack face (Sec. 1).

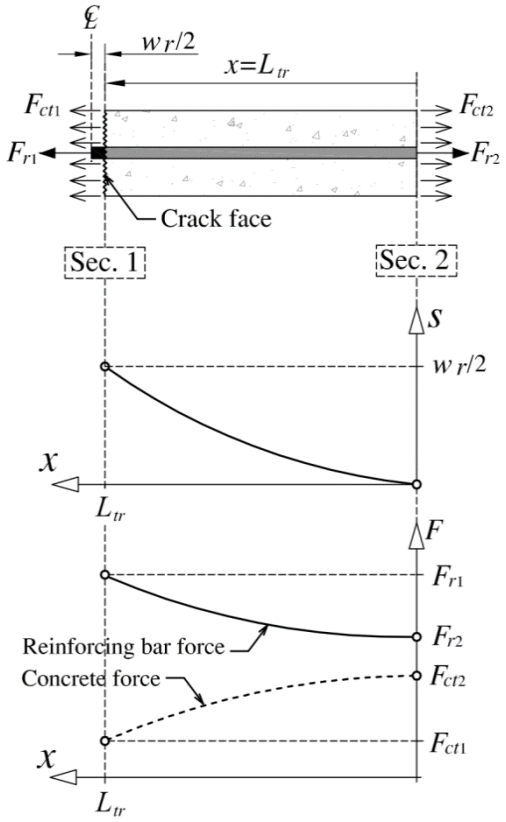

Figure 5.7: Force equilibrium along bond transference length

Beyond Sec. 2 perfect bond condition can be assumed between reinforcement and concrete. Thus, equating the elastic strain of reinforcement $(\varepsilon_{r2} = \sigma_{r2} / E_r)$ and surrounding concrete $(\varepsilon_{ct2} = \sigma_{ct2} / E_c)$ at Sec. 2, and considering $\sigma_{r2} = F_{r2} / A_r$ and $\sigma_{ct2} = F_{ct2} / A_c$, results:

$$\frac{F_{ct2}}{F_{r2}} = \frac{E_c A_c}{E_r A_r} \tag{5.17}$$

By satisfying the equilibrium of the forces at Sec. 1 and Sec. 2 in Figure 5.7 $(i.e.\ F_{r1} + F_{ct1} = F_{r2} + F_{ct2})$ it can be written:

$$F_{r1} + F_{ct1} = F_{r2}(1 + \frac{E_c A_c}{E_r A_r}) \tag{5.18}$$

where $F_{ct1}(= \sigma_{ct}(w_r) A_c)$ is the tensile force transferred at the localised crack of a width w_r. On the other hand, from the equilibrium of force of reinforcement along with the bond transference length it can be written:

$$F_{r2} = F_{r1} - \int_0^{L_{tr}} \tau(x) L_p dx \tag{5.19}$$

By substituting Equation (5.19) into Equation (5.18) yields:

$$F_{r1} + F_{ct1} = (F_{r1} - \int_0^{L_{tr}} \tau(x) L_p dx)(1 + \frac{E_c A_c}{E_r A_r}) \tag{5.20}$$

according to which:

$$F_{r1}(\frac{E_c A_c}{E_r A_r}) = F_{ct1} + (1 + \frac{E_c A_c}{E_r A_r}) \int_0^{L_{tr}} \tau(x) L_p dx \tag{5.21}$$

or:

$$F_{r1} = nF_{ct1} + (n+1)\,\mathrm{F}_{bond} \tag{5.22}$$

where $F_{bond} = \int_0^{L_{tr}} \tau(x) L_p dx$ is the total force transmitted along with the intraction length and n is the axial stiffness ratio between reinforcement and surrounding concrete:

$$n = \frac{E_r A_r}{E_c A_c} \tag{5.23}$$

On the other hand, by differentiating the two sides of Equation (5.13) results:

$$\frac{ds(x)}{dx} = \frac{du_r}{dx} - \frac{du_c}{dx} \tag{5.24}$$

where du_r / dx and du_c / dx are the strain of reinforcing bar (ε_r) and surrounding concrete (ε_c), respectively. By considering Equation (5.24) at Sec. 1 and the Hooke's law ($\varepsilon_{r1} = F_{r1} / (E_r A_r)$, $\varepsilon_{ct1} = F_{ct1} / (E_c A_c)$), yields:

$$\frac{ds(x)}{dx} = \frac{F_{r1}}{E_r A_r} - \frac{F_{ct1}}{E_c A_c} \tag{5.25}$$

according to which:

$$F_{r1} = E_r A_r \frac{ds(x)}{dx} + nF_{ct1} \tag{5.26}$$

Equation (5.26) provides the second formula for the evaluation of F_{r1}, the internal force of the reinforcing bar at the cracked section (see Figure 5.7). By equating Equations. (5.22) and (5.26), the bond transference length (L_{tr}) can be determined from:

$$\frac{ds(x)}{dx} = \frac{(n+1)}{E_r A_r} F_{bond} \tag{5.27}$$

5.2.2.3 Resolving the differential equations

Regarding the various phases of the considered shear bond-slip relationship (Figure 5.5), the differential Equation (5.15) is solved as described in the following sections.

Elastic phase

When sliding of the reinforcement at the localised crack ($s_{\text{sec.1}} = w_r / 2$) is smaller than s_1 , the interaction between reinforcement and concrete is defined by the elastic phase of the bond-sliding relationship as schematised in Figure 5.8(a). The variation of the elastic sliding $s(x^e)$ from Sec. 2 (the most adjacent section at perfect bond conditions) to Sec. 1 (cracked section) is represented by Equation (5.28), which is determined by solving Equation (5.15) when $\tau(x)$ is replaced by Equation (5.10a):

$$s(x^e) = C_1^e e^{\lambda_1 x^e} + C_2^e e^{-\lambda_1 x^e} - C_3^e \qquad (s(x^e) \le s_1) \qquad (5.28)$$

where λ_1 and C_3^e are constants determined by the following equations:

$$\lambda_1 = \sqrt{\frac{(\tau_m - \tau_0) J_1}{s_1}} \qquad (5.29)$$

$$C_3^e = \frac{J_1 \tau_0}{\lambda_1^2} \qquad (5.30)$$

By considering the following boundary conditions:

$$\begin{cases} at\ x^e = 0: & s(x^e) = 0 \\ at\ x^e = L_{tr}^e(s_{\text{sec.1}}): & s(x^e) = s_{\text{sec.1}} \end{cases} \qquad (5.31)$$

the C_1^e and C_2^e can be determined:

$$C_1^e = \left[s_{\text{sec.1}} + C_3^e (1 - e^{-\lambda_1 L_{tr}^e (s_{\text{sec.1}})}) \right] \frac{1}{e^{\lambda_1 L_{tr}^e (s_{\text{sec.1}})} - e^{-\lambda_1 L_{tr}^e (s_{\text{sec.1}})}} \qquad (5.32)$$

$$C_2^e = C_3^e - C_1^e \qquad (5.33)$$

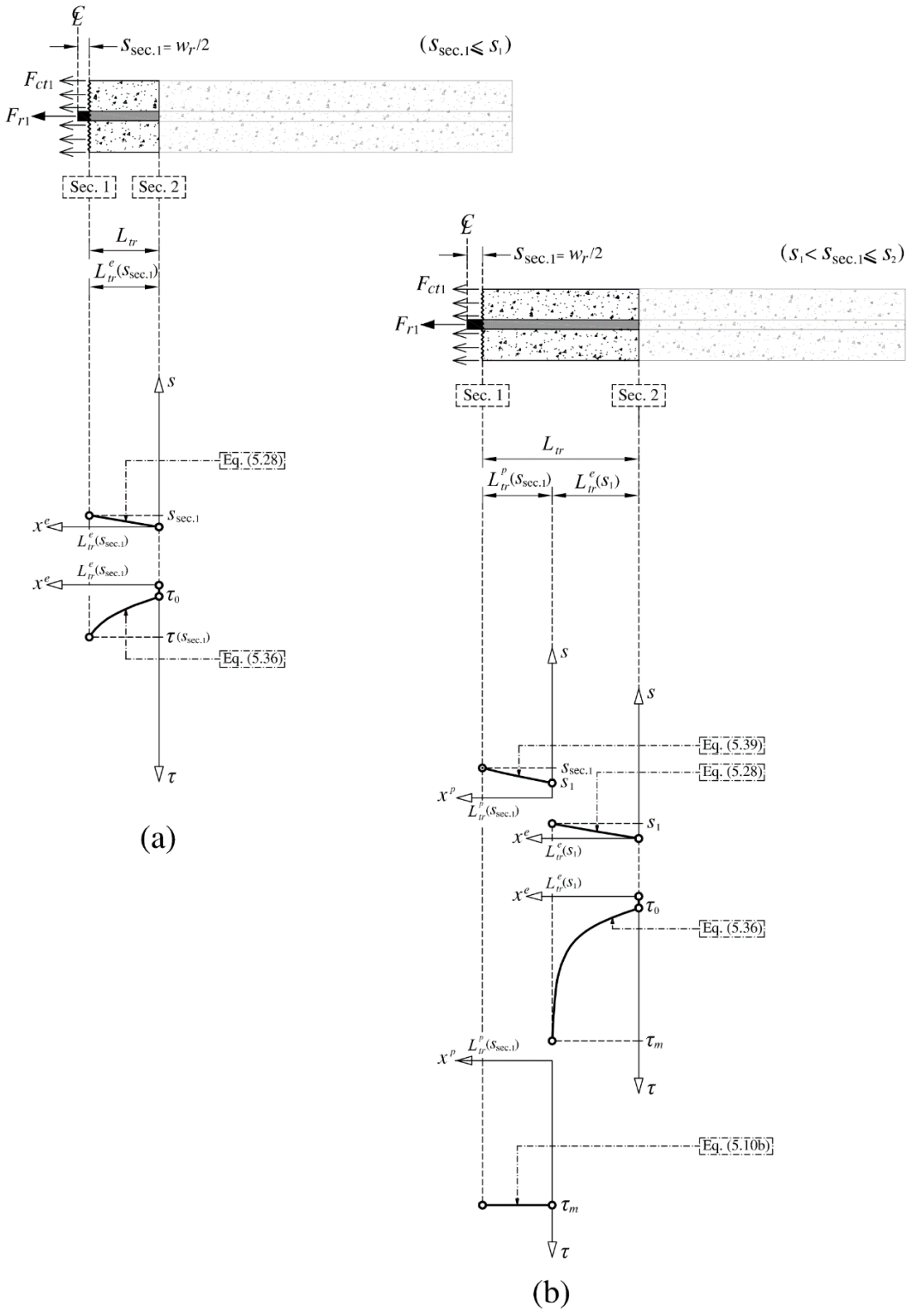

Figure 5.8: Variation of shear bond stress and sliding along with the interaction zone when activated (a) the elastic and (b) the plastic phases of bond

In Equation (5.32), $L_{tr}^{e}(s_{\sec.1})$ is the bond transfer length corresponding to the elastic region. The load transmitted along with the interaction length ($F_{bond} = \int_{0}^{L_{tr}} \tau(x) L_p dx$) is obtained from the following equation:

$$F_{bond} = F^{e}(s_{\sec.1}) = \int_{0}^{L_{tr}^{e}(s_{\sec.1})} \tau(x^{e}) L_p dx^{e} = \left[L_p \tau_0 L_{tr}^{e}(s_{\sec.1}) + L_p \left(\frac{\tau_m - \tau_0}{s_1} \right) \times \left(\frac{C_1^{e}}{\lambda_1} \left(e^{\lambda_1 L_{tr}^{e}(s_{\sec.1})} - 1 \right) + \frac{C_2^{e}}{\lambda_1} \left(1 - e^{-\lambda_1 L_{tr}^{e}(s_{\sec.1})} \right) - C_3^{e} L_{tr}^{e}(s_{\sec.1}) \right) \right] \tag{5.34}$$

$F^{e}(s_{\sec.1})$ in Equation (5.34) is the load transmitted along with the elastic interaction length. By substituting Equation (5.34) into Equation (5.27) and considering $ds(x^{e} = L_{tr}^{e}(s_{\sec.1})) / dx = C_1^{e} \lambda_1 e^{\lambda_1 L_{tr}^{e}(s_{\sec.1})} - C_2^{e} \lambda_1 e^{-\lambda_1 L_{tr}^{e}(s_{\sec.1})}$, the $L_{tr}^{e}(s_{\sec.1})$ is determined from:

$$L_{tr}^{e}(s_{\sec.1}) = \frac{1}{\lambda_1} \operatorname{acosh}\left(\frac{s_{\sec.1} + C_3^{e}}{C_3^{e}} \right) \tag{5.35}$$

Substituting the sliding determined from Equation (5.28) into Equation (5.10a), the variation of the shear bond stress along with the elastic bond transfer length is obtained from the following equation:

$$\tau(x^{e}) = \left[\tau_0 + \left(\frac{\tau_m - \tau_0}{s_1} \right) \right] \left[C_1^{e} e^{\lambda_1 x} + C_2^{e} e^{-\lambda_1 x} - C_3^{e} \right] \tag{5.36}$$

Finally, by substituting Equation (5.34) into Equation (5.22), the internal force of the reinforcement at the localised crack (F_{r1}) is determined from:

$$F_{r1} = n F_{ct1} + (n+1) F^{e}(s_{\sec.1}) \tag{5.37}$$

where $F_{ct1} = \sigma_{ct} \left[w_r = 2s\left(x^{e}\right) \right] A_c$. To determine the axial stiffness ratio of reinforcement versus concrete (n), the effective area of tensile concrete, $A_c (= b \times c_{eff})$, is obtained

by following the recommendations of *fib* Model Code 2010 (2011), as schematically represented in Figure 5.9:

$$c_{eff} = \begin{cases} \min\left[\, 2.5(h-d),\ (h-d_{NA})/3 \,\right] & \text{(for beams)} \quad (5.38a) \\ \min\left[2.5(c+d_b/2),\ (h-d_{NA})/3\right] & \text{(for slabs)} \quad (5.38b) \end{cases}$$

being d_b the diameter of the reinforcing bar and *c* the concrete cover thickness.

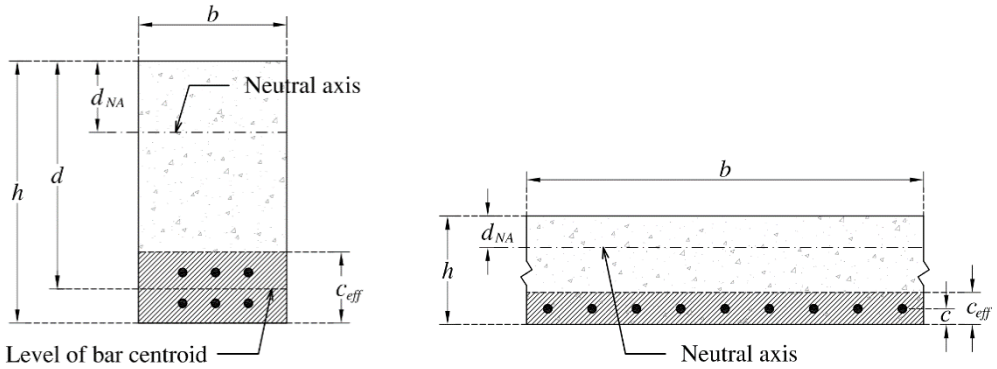

(a) (b)

Figure 5.9: Recommendations of *fib* Model Code 2010 (2011) for the evaluation of the effective tension area of the concrete surrounding reinforcing bar in (a) beams, and (b) slabs

Plastic phase

By the gradual opening of the localised crack, $s_{\text{sec.1}}$ may range between s_1 and s_2 (Figure 5.5), which means that the plastic stage of bond-slip constitutive law contributes in the interaction length. In this case, the actual bond length comprises a part in the elastic stage ($L_{tr}^{e}(s_1)$), which is simulated according to the formulation that has already been described, and a part ($L_{tr}^{p}(s_{\text{sec.1}})$) that is the plastic stage of the bond stress transfer process (Figure 5.8b). The plastic sliding of this region is obtained by solving the differential Equation (5.15) when $\tau(x)$ is substituted by Equation (5.10b) leading to the following equation:

$$s(x^p) = C_1^p (x^p)^2 + C_2^p x^p + C_3^p \qquad (s_1 < s(x^p) \le s_2) \tag{5.39}$$

where:

$$C_1^p = \frac{J_1 \tau_m}{2} \tag{5.40}$$

and the other C_2^p and C_3^p parameters are determined by considering the boundary conditions (Figure 5.8b):

$$\begin{cases} at\ x^p = 0: & s = s_1 \\ at\ x^p = L_{tr}^p(s_{\text{sec.1}}): & s = s_{\text{sec.1}} \end{cases} \tag{5.41}$$

resulting,

$$C_2^p = \frac{(s_{\text{sec.1}} - s_1) - C_1^p \left[L_{tr}^p(s_{\text{sec.1}}) \right]^2}{L_{tr}^p(s_{\text{sec.1}})} \tag{5.42}$$

$$C_3^p = s_1 \tag{5.43}$$

where $L_{tr}^p(s_{\text{sec.1}})$ is the bond transfer length corresponding to the plastic region. The load transmitted along with the interaction length ($F = \int_0^{L_{tr}} \tau(x) L_p dx$) is obtained from the following equation:

$$F_{bond} = F_{\max}^e + F^p(s_{\text{sec.1}}) = F_{\max}^e + \int_0^{L_{tr}^p(s_{\text{sec.1}})} \tau(x^p) L_p dx^p = F_{\max}^e + L_p \tau_m L_{tr}^p(s_{\text{sec.1}}) \tag{5.44}$$

where $F_{\max}^e$ is the maximum force that is transferred in the elastic region:

$$\begin{aligned} F_{\max}^e = F^e(s_1) = \int_0^{L_{tr}^e(s_1)} \tau(x) L_p dx = L_p \tau_0 L_{tr}^e(s_1) + \\ L_p \left(\frac{\tau_m - \tau_0}{s_1} \right) \left(\frac{C_1^e}{\lambda_1} \left(e^{\lambda_1 L_{tr}^e(s_1)} - 1 \right) + \frac{C_2^e}{\lambda_1} \left(1 - e^{-\lambda_1 L_{tr}^e(s_1)} \right) - C_3^e L_{tr}^e(s_1) \right) \end{aligned} \tag{5.45}$$

$F^p(s_{\text{sec.1}})$ in Equation (5.44) is the load transmitted along with the plastic interaction length. By substituting Equation (5.44) into Equation (5.27) and considering $ds(x^p = L_{tr}^p(s_{\text{sec.1}}))/dx = 2C_1^p L_{tr}^p(s_{\text{sec.1}}) + C_2^p$, the $L_{tr}^p(s_{\text{sec.1}})$ is determined from:

$$L_{tr}^p(s_{\text{sec.1}}) = \frac{-(1+n)F_{\max}^e}{K^p} + \frac{\sqrt{(1+n)^2(F_{\max}^e)^2 + 2K^p(A_r E_r(s_{\text{sec.1}} - s_1))}}{K^p} \qquad (5.46)$$

and K^p is a factor obtained from the following equation:

$$K^p = 2\left[(1+n)L_p\tau_m - A_r E_r C_1^p\right] \qquad (5.47)$$

As Figure 5.8(b) shows, when the plastic phase of the bond-slip relationship is mobilized, the total bond transfer length is:

$$L_{tr}(s_{\text{sec.1}}) = L_{tr}^e(s_1) + L_{tr}^p(s_{\text{sec.1}}) \qquad (5.48)$$

In this case, and according to the considered bond-slip relationship, the shear bond for the plastic phase is constant $(=\tau_m)$. By substituting F_{bond} into Equation (5.22), the internal force of the reinforcement at the cracked section (F_{r1}) is determined:

$$F_{r1} = nF_{ct1} + (n+1)\left(F^p(s_{\text{sec.1}}) + F_{\max}^e\right) \qquad (5.49)$$

Softening phase

When sliding of reinforcement at the cracked section ranges between s_2 and s_3 (see Figure 5.5), the softening phase of bond-sliding behaviour is activated, as schematised in Figure 5.10(a). In this case, the variation of sliding along with the softening region is obtained from the following equation:

$$s(x^s) = C_1^s \sin(\beta x^s) + C_2^s \cos(\beta x^s) + C_3^s \qquad (s_2 < s(x^s) \le s_3) \qquad (5.50)$$

where:

$$\beta_3 = \sqrt{\frac{(\tau_m - \tau_R)J_1}{(s_3 - s_2)}} \tag{5.51}$$

$$C_3^s = s_2 + \frac{J_1 \tau_m}{\beta_3^2} \tag{5.52}$$

while C_1^s and C_2^s are determined by implementing the following boundary conditions:

$$\begin{cases} at\ x^s = 0: & s = s_2 \\ at\ x^s = L_{tr}^s(s_{\text{sec.1}}): & s = s_{\text{sec.1}} \end{cases} \tag{5.53}$$

resulting:

$$C_1^s = \frac{1}{\sin\left(\beta_3 L_{tr}^s(s_{\text{sec.1}})\right)}\left[s_{\text{sec.1}} - s_2 + \left(\frac{\tau_m J_1}{\beta_3^2}\right)\left(\cos\left(\beta_3 L_{tr}^s(s_{\text{sec.1}})\right) - 1\right)\right] \tag{5.54}$$

$$C_2^s = s_2 - C_3^s \tag{5.55}$$

where $L_{tr}^s(s_{\text{sec.1}})$ is the bond transfer length corresponding to the softening phase. The total transmitted load ($F_{bond} = \int_0^{L_{tr}} \tau(x) L_p dx$) is obtained from the following equation:

$$\begin{aligned} F = F_{\max}^e + F_{\max}^p + F^s(s_{\text{sec.1}}) &= F_{\max}^e + F_{\max}^p + \int_0^{L_{tr}^s(s_{\text{sec.1}})} \tau(x^s) L_p dx^s \\ &= F_{\max}^e + F_{\max}^p + \frac{L_p \beta_3}{J_1}\Big[C_1^s\left(\cos\left(\beta_3 L_{tr}^s(s_{\text{sec.1}})\right) - 1\right) \\ &\qquad - C_2^s \sin\left(\beta_3 L_{tr}^s(s_{\text{sec.1}})\right)\Big] \end{aligned} \tag{5.56}$$

where $F_{\max}^p$ is the maximum force that is transferred in the plastic region:

$$F_{\max}^p = F^p(s_2) = \int_0^{L_{tr}^p(s_2)} \tau(x^p) L_p dx^p = L_p \tau_m L_{tr}^p(s_2) \tag{5.57}$$

$F^s(s_{\text{sec.1}})$ in Equation (5.56) is the load transmitted along with the softening interaction length. By substituting Equation (5.56) into Equation (5.27) and considering

$ds(x^s = L_{tr}^s(s_{\text{sec.1}}))/dx = C_1^s\beta_3\cos(\beta_3 x^s) - C_2^s\beta_3\sin(\beta_3 x^s)$, the $L_{tr}^s(s_{\text{sec.1}})$ is determined from:

$$L_{tr}^s(s_{\text{sec.1}}) = \frac{1}{\beta_3}(\phi + \arcsin\frac{c_s}{\sqrt{a_s^2 + b_s^2}}) \tag{5.58}$$

where:

$$\phi = \arcsin\frac{b_s}{\sqrt{a_s^2 + b_s^2}} \tag{5.59}$$

$$a_s = F_{\max}^e + F_{\max}^p \tag{5.60}$$

$$b_s = \frac{L_p\tau_m}{\beta_3} \tag{5.61}$$

$$c_s = \frac{L_p\beta_3}{J_1}(s_{\text{sec.1}} - C_3^s) \tag{5.62}$$

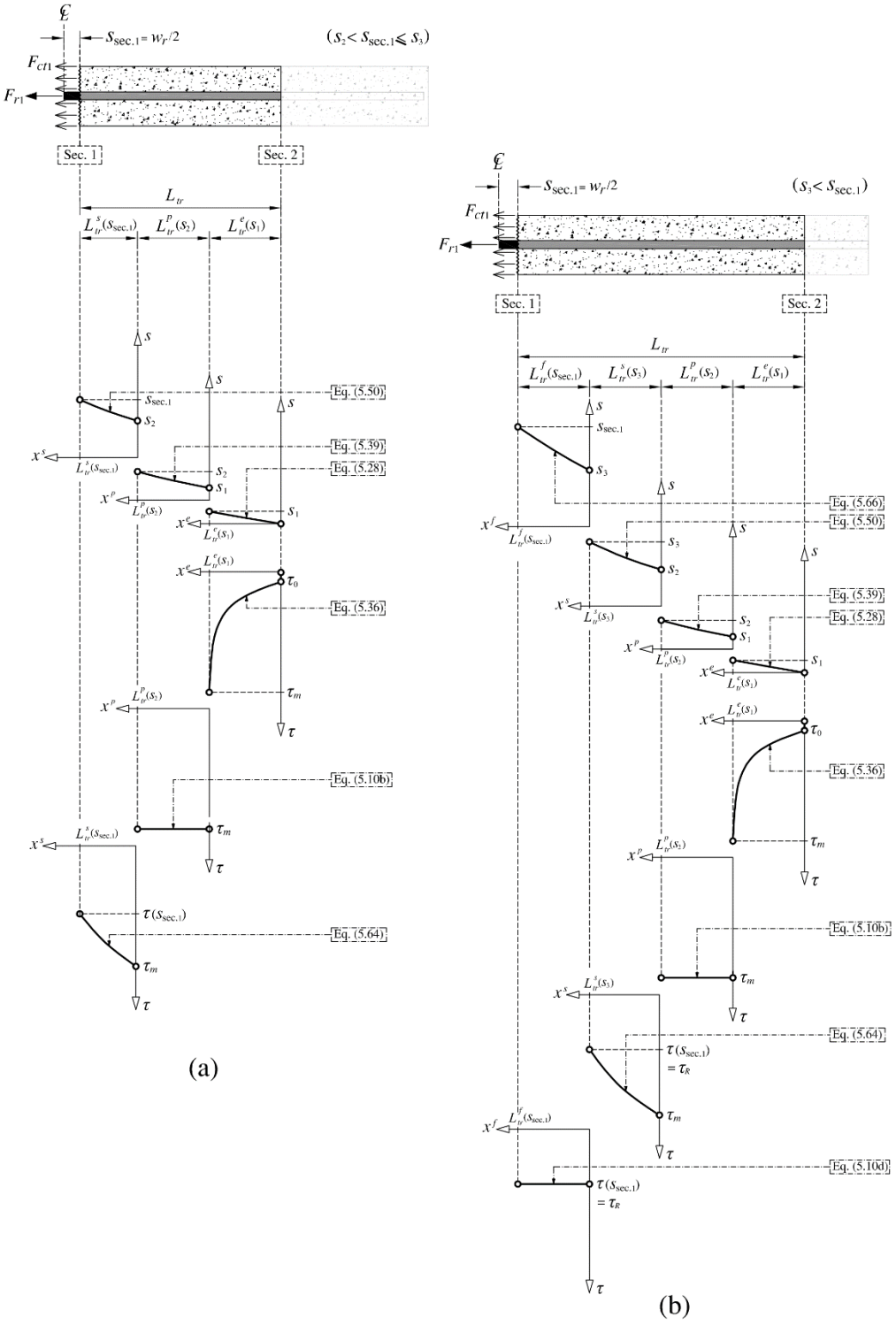

Figure 5.10: Variation of shear bond stress and sliding along with the interaction zone when activated (a) the softening and (b) the frictional phases of bond

Regarding Figure 5.10(a), the total bond transfer length $(L_{tr}(s_{\sec.1}))$ is determined by the following equation:

$$L_{tr}(s_{\sec.1}) = L_{tr}^{e}(s_1) + L_{tr}^{p}(s_2) + L_{tr}^{s}(s_{\sec.1}) \tag{5.63}$$

Substituting $s(x^s)$ from Equation (5.50) into Equation (5.10c), the shear bond stress for the softening phase is obtained:

$$\tau(x^s) = \tau_m - \left(\frac{\tau_m - \tau_R}{s_3 - s_2}\right)\left[\left(C_1^s \sin(\beta_3 x^s) + C_2^s \cos(\beta_3 x^s) + C_3^s\right) - s_2\right] \tag{5.64}$$

Furthermore, replacing F_{bond} obtained from Equation (5.56) into Equation (5.22), the internal force of the reinforcement at the localised crack is determined:

$$F_{r1} = nF_{ct1} + (n+1)\left(F^s(s_{\sec.1}) + F_{\max}^{p} + F_{\max}^{e}\right) \tag{5.65}$$

Frictional phase

By further increasing the sliding of reinforcement at the cracked section, the frictional bond-slip behaviour is activated when $s_{\sec.1}$ exceeds s_3 (Figure 5.10b), and the sliding field in this frictional bond transfer length is determined from the following equation:

$$s(x^f) = C_1^f (x^f)^2 + C_2^f x^f + C_3^f \qquad (s_3 < s(x^f)) \tag{5.66}$$

where:

$$C_1^f = \frac{J_1 \tau_R}{2} \tag{5.67}$$

while the C_2^f and C_3^f parameters are obtained by imposing the following boundary conditions:

$$\begin{cases} at\ x^f = 0: & s = s_3 \\ at\ x^f = L_{tr}^f(s_{\text{sec.1}}): & s = s_{\text{sec.1}} \end{cases} \tag{5.68}$$

resulting,

$$C_3^f = s_3 \tag{5.69}$$

$$C_2^f = \frac{(s_{\text{sec.1}} - s_3) - C_1^f \left[L_{tr}^f(s_{\text{sec.1}}) \right]^2}{L_{tr}^f(s_{\text{sec.1}})} \tag{5.70}$$

where $L_{tr}^f(s_{\text{sec.1}})$ is the bond transfer length corresponding to the frictional region. The load transmitted along with the interaction length ($F_{bond} = \int_0^{L_{tr}} \tau(x) L_p dx$), is obtained from the following equation:

$$\begin{aligned} F_{bond} = F_{\max}^e + F_{\max}^p + F_{\max}^s + F^f(s_{\text{sec.1}}) &= F_{\max}^e + F_{\max}^p + F_{\max}^s + \int_0^{L_{tr}^f(s_{\text{sec.1}})} \tau(x^f) L_p dx^f \\ &= F_{\max}^e + F_{\max}^p + F_{\max}^s + L_p \tau_R L_{tr}^f(s_{\text{sec.1}}) \end{aligned} \tag{5.71}$$

where $F_{\max}^s$ is the maximum force that is transferred in the softening region:

$$\begin{aligned} F_{\max}^s = \int_0^{L_{tr}^s(s_3)} \tau\left(x^s\right) L_p dx^s = \frac{L_p \beta_3}{J_1} \Big[& C_1^s \left(\cos\left(\beta_3 L_{tr}^s(s_3)\right) - 1 \right) \\ & - C_2^s \sin\left(\beta_3 L_{tr}^s(s_3)\right) \Big] \end{aligned} \tag{5.72}$$

$F^f(s_{\text{sec.1}})$ in Equation (5.71) is the load transmitted along with the frictional interaction length. By substituting Equation (5.71) into Equation (5.27) and considering $ds(x^f = L_{tr}^f(s_{\text{sec.1}})) / dx = 2C_1^f L_{tr}^f(s_{\text{sec.1}}) + C_2^f$, the $L_{tr}^f(s_{\text{sec.1}})$ is determined from:

$$L_{tr}^f(s_{\text{sec.1}}) = \frac{-(1+n)F_{\max}^{eps} + \sqrt{(1+n)^2 (F_{\max}^{eps})^2 + 2K^f (A_r E_r (s_{\text{sec.1}} - s_3)}}{K^f} \tag{5.73}$$

being:

$$F_{\max}^{eps} = F_{\max}^e + F_{\max}^p + F_{\max}^s \tag{5.74}$$

$$K^f = 2\left[(1+n)L_p\tau_R - A_rE_rC_1^f\right] \tag{5.75}$$

As depicted in Figure 5.10(b), the total bond transfer length corresponding to the activation of the frictional phase is determined by the following equation:

$$L_{tr}(s_{\text{sec.1}}) = L_{tr}^e(s_1) + L_{tr}^p(s_2) + L_{tr}^s(s_3) + L_{tr}^f(s_{\text{sec.1}}) \tag{5.76}$$

The internal force of the reinforcement at the cracked section corresponding to the frictional phase is obtained from:

$$F_{r1} = nF_{ct1} + (n+1)\left(F^f(s_{\text{sec.1}}) + F_{\max}^s + F_{\max}^p + F_{\max}^e\right) \tag{5.77}$$

5.2.2.4 Order of formation and spacing of cracks in flexural elements

In Figure 5.11 is depicted a flexural R/FRC beam subjected to four-point bending load configuration. It is assumed this type of elements has sufficient shear reinforcement in the critical shear zones to do not fail in shear. This can be achieved by deposing of conventional shear reinforcement or/and fibre reinforcement (Barros and Foster 2018, Conforti et al. 2013, Ortiz Navas et al. 2018).

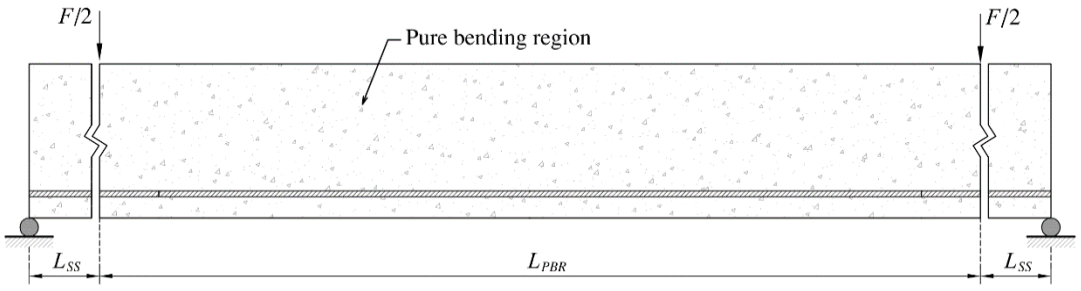

Figure 5.11: Reinforced concrete beam subjected to four-point bending load configuration

In the proposed model, the moment-rotation relationship (Taheri and Barros 2012, Barros *et al.* 2015b) is used to determine the crack profile in the cross-section for the applied moment, from which the crack opening evolution is evaluated considering the $\sigma - w$ constitutive low of FRC, as well as the slip and the internal forces in the

reinforcements according to the adopted bond-slip approach. Considering the overall rotation (θ) prescribed to the extremities of the pure bending region (PBR) of L_{PBR} length (see Figure 5.1), the deformation of the generic i^{th} layer (D_i) and the corresponding effective strain $(\varepsilon_{ef,i} = D_i / L_{PBR})$ is determined. For the layer positioned at the level of reinforcing bars, hereafter designated by Rlayer, its strain, $\varepsilon_{ef,r}$, is compared to the cracking strain of FRC (ε_{cr}) (see Figure 5.3a), and the analysis should proceed according to the following possible scenarios.

Pre-cracking stage

As long as $\varepsilon_{ef,r}$ is smaller than ε_{cr}, the Rlayer does not crack. Consequently, the entire PBR is considered as an intact prism. In this case, the interaction between concrete and embedded bar is considered as a perfect bond condition. Hence, the internal force of the bar (F_r) is equal to the force originated by the strain of the reinforcement, designated herein by $F_{r,\sigma-\varepsilon}$, which is determined by multiplying the cross-sectional area of the reinforcing bars (A_r) to the stress corresponding to $\varepsilon_{ef,r}$, *i.e.* $\sigma_r(\varepsilon_{ef,r})$, obtained by adopting the stress-strain constitutive law of the reinforcement depicted in Figure 5.4.

Crack propagation stage

For a certain value of rotation imposed to the extremities of the PBR, $\varepsilon_{ef,r}$ becomes equal to ε_{cr}, representing the load configuration to the initiation of the first crack at Rlayer. Due to the disordered nature of concrete when regarded at micro- and meso-level, the first crack occurs at the cross-section of the most pronounced defects along with the PBR. Nevertheless, for the convenience of simulation, it is assumed that the first crack forms at mid-span of the PBR (Figure 5.12a). In this case, $F_r = F_{r,\sigma-\varepsilon}$ is kept as $F_{r,cr}$, which represents the internal force of the reinforcement at cracking initiation stage. $F_{r,cr}$ is utilised for detecting if new cracks initiate in next steps of loading. Note

that, in the proposed model, the geometric properties of cross-section and reinforcing scheme of the beam is assumed constant over the PBR, and therefore, $F_{r,cr}$ is valid for any other section of this region. Further increase in rotation prescribed to the extremities may lead to the widening of the crack at Rlayer (w_r) with the consequent increase in sliding in the reinforcing bar $(s_{\sec.1} = w_r / 2)$. Therefore, the internal force of the reinforcement (F_r) is determined by superimposing the force due to the strain of the reinforcing bar $(F_{r,\sigma-\varepsilon})$ to the one resulting from the sliding of the bar from the surrounding concrete $(F_{r,\tau-s})$. The latter is equal to the internal force of reinforcing bar at the crack section (Sec. 1), which is simulated by F_{r1} in the approach described in section 5.1.2.3.

In case the flexural beam is constituted of strain-hardening FRCs, due to the enhanced post-cracking characteristic of this type of material, the increase in rotation leads to the formation of new micro-cracks (Naaman 2003) as long as $\varepsilon_{ef,r}$ is smaller than $\varepsilon_{ct,p}$, which represent the strain corresponding to the tensile peak stress (see Figure 5.3a). During the hardening stage, the tensile deformation of the prism is assumed being represented by the strain concept (Naaman 2008). Hence, the internal force of the reinforcement is evaluated from $F_{r,\sigma-\varepsilon}$ during the tensile strain-hardening stage of the surrounding FRC. When $\varepsilon_{ef,r}$ exceeds $\varepsilon_{ct,p}$, the critical crack, considered to be the one initiated in Sec. 1, begins to be widened accompanied by the contribution of the post-cracking tensile softening stage of the FRC (Figure 5.3b), as well as the contribution of the term $F_{r,\tau-s}$ relative to the occurrence of sliding. Therefore, for tensile strain-hardening FRC, debond of the reinforcements is only considered for tensile strain higher than $\varepsilon_{ct,p}$, due to the relatively narrow width of the cracks formed during the tensile strain-hardening stage. Concurrently to the increase in sliding of the reinforcing bar at the first crack (Sec. 1), the internal force of reinforcement at section 2 (F_{r2} in Figure 5.12a) and the bond transfer length between the bar and surrounding concrete (L_{tr}) increase gradually.

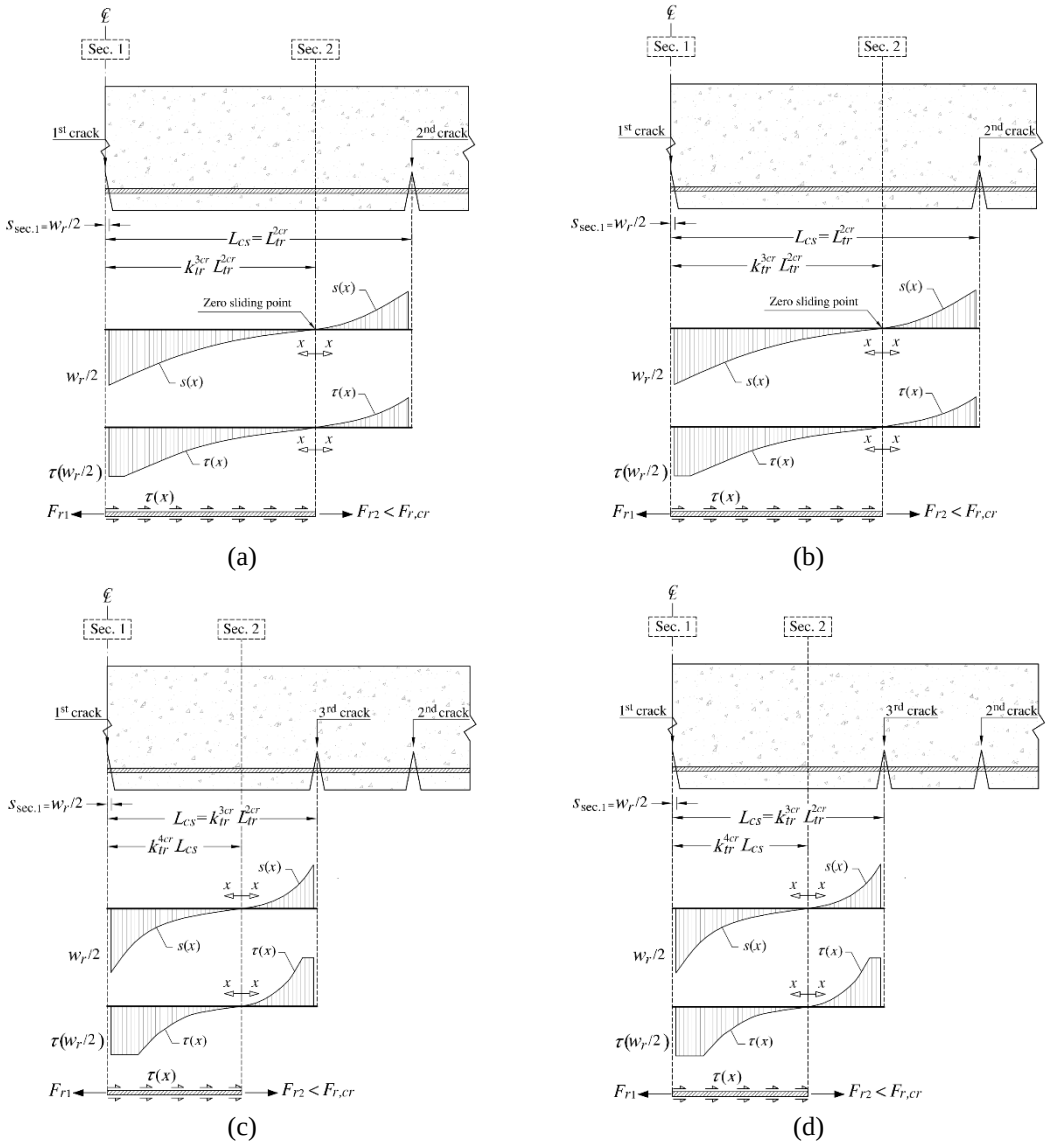

Figure 5.12: Crack propagation and bond stress-slip distribution between two adjacent cracks just before initiation of a (a) second crack, (b) third crack, (c) fourth crack, and (d) fifth crack

It is assumed that the interaction length of the beam is long enough to provide an infinite bond transfer length between the reinforcing bar and concrete. In each loading step, the value of F_{r2} is determined from Equation (5.19) and compared to $F_{r,cr}$ to verify the eventual formation of new crack. As long as F_{r2} is less than $F_{r,cr}$, the increase in the imposed rotation causes the widening of the actual crack and to the increase in the elastic deformation of the intact region. When F_{r2} attains $F_{r,cr}$, a pair of second cracks

(2nd crack in Figure 5.12b; due to symmetry only one of these cracks is represented) is formed at a distance L_{tr}^{2cr} from the 1st crack. From now on and up to the formation of the pair of 3rd cracks, the actual length of the prism (L_{cs}) is set to L_{tr}^{2cr}. In the newly formed prism, the reinforcing bar is tensioned on both sides by widening of the cracks located at the extremities. Therefore, due to the equilibrium of the internal forces, the sliding and bond stress tend, necessarily, to zero at a point positioned along with the prism. By the further increase in the overall rotation imposed to the pure bending region, the new crack may form at the zero sliding point. Beforehand initiation of a new crack with generic identifier *m*cr (e.g. 3cr, 4cr, or 5cr in Figure 5.12), the zero sliding point is assumed located at a distance of $k_{Lcs}^{mcr} L_{cs}$ from the 1st crack, where k_{Lcs}^{mcr} is a coefficient determined from Equation (5.78):

$$k_{Lcs}^{mcr} = \begin{cases} 0.5 & (\text{if } L_{cs} \le 0.5L_{PBR}) \quad (5.78a) \\ \dfrac{L_{ss}}{0.5L_{PBR} + 2L_{ss} - L_{cs}} & (\text{if } L_{cs} > 0.5L_{PBR}) \quad (5.78b) \end{cases}$$

where L_{ss} is the length of the beam's shear span (Figure 5.11). Note that in Equation (5.78), L_{cs} is the actual prism length, which is updated during the proposed computational procedure. Before initiation of the crack *m*cr, if $L_{cs} \le 0.5L_{PBR}$ this means the prism is entirely inside the PBR. In this case, since the widening of the crack and, consequently, sliding of the reinforcing bar at both extremities of the prism is the same, the zero sliding point is located right at midst of the prism and therefore, by adopting k_{Lcs}^{mcr} of 0.5 from Equation (5.78a), the length of the prism by formation crack *m*cr is set to $0.5L_{cs}$. However, when Sec. 2 is outside the PBR, (*i.e.* $L_{cs} > 0.5L_{PBR}$), the width of the crack at the extremity of the prism outside the PBR is smaller than that of the 1st crack due to relatively lower bending moment. In this case, the sliding of the bar is not equal at the cracks of the two extremities of the prism, since the wider the crack the larger the sliding. Therefore, the zero sliding point moves toward the extremity located outside the PBR to provide longer transition length in the part corresponding to the crack where larger

sliding occurs (1st crack in Figure 5.12b) (Piyasena 2002). In such a case, a linear correlation between transition length and bending moment is assumed in the evaluation of k_{Lcs}^{mcr} according to Equation (5.78b). Therefore, when the third crack forms, the length of the prism is set to $k_{Lcs}^{3cr}L_{cs}$, which is equal to $k_{Lcs}^{3cr}L_{tr}^{2cr}$ (Figure 5.12b). Once F_{r2} exceeds $F_{r,cr}$, a new pair of cracks is detected at the zero sliding point of the prisms. Consequently, as shown in Figures 5.12c and d, the distance between cracks is reduced to $k_{Lcs}^{4cr}\left(k_{Lcs}^{3cr}L_{tr}^{2cr}\right)$ and $k_{Lcs}^{5cr}\left[k_{Lcs}^{4cr}\left(k_{Lcs}^{3cr}L_{tr}^{2cr}\right)\right]$, when the fourth and the fifth cracks are formed, respectively. The possibility of developing new cracks is successively evaluated, being the crack spacing limited to half the height of cross-section (Massicotte 2004).

5.3 Algorithm to predict the moment-rotation response of H/FRC element

In the developed incremental-iterative algorithm, the rotation of the extremities of the pure bending region of L_{PBR} length in a k^{th} generic step of the computation is increased by considering a constant increment of $\Delta\theta$:

$$\theta^k = k\Delta\theta \tag{5.79}$$

Correspondingly, the axial elongation of an i^{th} layer (D_i^k) is determined by considering its position along with the depth of the cross-section (d_i), and assuming an initial value for the depth of the neutral axis (d_{NA} in Figure 5.1):

$$D_i^k = \theta^k \left|d_i - d_{NA}\right| \tag{5.80}$$

It should be noted that d_{NA} is determined iteratively through the bisectional approach by satisfying the force equilibrium according to the adopted tolerance of 10 N. Therefore, the increment is the rotation and iterative procedure is for d_{NA}. The corresponding effective strain of the pure bending region is obtained from the following equation:

$$\varepsilon_{ef,i}^k = \frac{D_i^k}{L_{PBR}} \tag{5.81}$$

For the layers placed above the neutral axes where $d_i < d_{NA}$, the compressive force of concrete $(F_{cc,i}^k)$ is determined by the following equation:

$$F_{cc,i}^k = \sigma_{cc}\left(\varepsilon_{ef,i}^k\right) b_i t_i \tag{5.82}$$

where $\sigma_{cc}\left(\varepsilon_{ef,i}^k\right)$ is the compressive constitutive low of concrete depicted in Figure 5.2. Tensile force ($F_{ct,i}^k$) of the layers positioned below the neutral axis $(d_i > d_{NA})$ is determined by the following equation:

$$F_{ct,i}^k = \begin{cases} \sigma_{ct}\left(\varepsilon_{ef,i}^k\right) b_i t_i & (\varepsilon_{ef,i}^k \le \varepsilon_{cr}^*) \quad \left(\begin{array}{l}\text{for SS-FRC: } \varepsilon_{cr}^* = \varepsilon_{cr} \\ \text{for SH-FRC: } \varepsilon_{cr}^* = \varepsilon_{ct,p}\end{array}\right) & \text{(5.83a)} \\ \sigma_{ct}\left(w_i^k\right) b_i t_i & (\varepsilon_{ef,i}^k > \varepsilon_{cr}^*) & \text{(5.83b)} \end{cases}$$

where $\sigma_{ct}\left(\varepsilon_{ef,i}^k\right)$ is the pre-cracking (pre-macrocracking localisation in the case of strain-hardening FRCs) tensile stress of concrete obtained from the constitutive law represented in Figure 5.3a, while the crack width of the i^{th} layer (w_i^k) and corresponding post-cracking tensile stress (softening stage) of concrete $(\sigma_{ct}(w_i^k))$ is obtained by adopting the diagram represented in Figure 5.3b and performing an iterative procedure for solving the following equation:

$$\varepsilon_{ef,i}^k - \frac{\sigma_{ct}\left(w_i^k\right)}{E_c} - \frac{w_i^k}{L_{ch}} = 0 \tag{5.84}$$

where L_{ch} is the characteristic length considered equal to the length of prisms when cracking is stabilised. On the other word L_{ch} in Equation (5.84) is the average crack spacing (s_{rm}) at the end of the cracking stage, which is equal to the minimum value of L_{cs} determined by the developed formulation. L_{ch} is primarily initiated by the length of the pure bending region (L_{PBR}) and is modified iteratively in a procedure described in Figure 5.13. When cracking is stabilised, *i.e.* when new cracks do not form any more,

L_{ch} is compared with the determined average crack spacing (s_{rm}). If the deviation of L_{ch} and s_{rm} is less than the adopted tolerance of 1%, the computation is continued. Otherwise, the procedure is resumed by the new value of L_{ch} which is equal to s_{rm}. In Equation (5.84) is assumed that when the crack crosses the i^{th} layer, the effective tensile strain of the layer along with the prism of L_{ch} length $(\varepsilon_{ef,i}^{k})$ is a superimposition of the equivalent strain due to the average widening of the crack (w_i^k / L_{ch}) and the elastic strain of the prism in the vicinity of the crack $(\sigma_{ct}\left(w_i^k\right)/E_c)$.

In case the i^{th} layer includes a longitudinal reinforcing bar, the internal force of the reinforcement $(F_{r,i}^{k})$ is a superimposition of the force due to the elongation of reinforcing bar along with the pure bending region $(F_{r,\sigma-\varepsilon,i}^{k})$ and the ones originated from sliding of the bar in the cracked section $(F_{r,\tau-s,i}^{k} = F_{r1,i}^{k})$.

$$F_{r,i}^{k} = F_{r,\sigma-\varepsilon,i}^{k} + F_{r,\tau-s,i}^{k} \tag{5.85}$$

$$F_{r,\sigma-\varepsilon,i}^{k} = b_{r,i}\, t_i \sigma_r\left(\varepsilon_{ef,i}^{k}\right) \tag{5.86}$$

$$F_{r,\tau-s,i}^{k} = F_{r1,i}^{k} = \begin{cases} nF_{ct1} + (n+1)F^{e}(s_{\text{sec.1}}^{k,i}) & s_{\text{sec.1}}^{k,i} \le s_1 \quad (5.87a) \\ nF_{ct1} + (n+1)\left(F^{p}(s_{\text{sec.1}}^{k,i}) + F_{\max}^{e}\right) & s_1 < s_{\text{sec.1}}^{k,i} \le s_2 \quad (5.87b) \\ nF_{ct1} + (n+1)\left(F^{s}(s_{\text{sec.1}}^{k,i}) + F_{\max}^{p} + F_{\max}^{e}\right) & s_2 < s_{\text{sec.1}}^{k,i} \le s_3 \quad (5.87c) \\ nF_{ct1} + (n+1)\left(F^{f}(s_{\text{sec.1}}^{k,i}) + F_{\max}^{s} + F_{\max}^{p} + F_{\max}^{e}\right) & s_3 < s_{\text{sec.1}}^{k,i} \quad (5.87d) \end{cases}$$

In Equation (5.86), $\sigma_r\left(\varepsilon_{ef,i}^{k}\right)$ is the stress of the bar determined regarding the constitutive law schematised in Figure 5.4. The intervening parameters in Equation (5.87) can be obtained according to the formulation described in Section 5.1.2.3. If the reinforcement is uncrossed by a crack (*i.e.* $\varepsilon_{ef,i}^{k} \le \varepsilon_{cr}^{*}$), null $F_{r,\tau-s,i}^{k}$ is adopted in Equation (5.85). Once $\varepsilon_{ef,i}^{k}$ attains ε_{cr}^{*}, value of $F_{r,\sigma-\varepsilon,i}^{k}$ determined by Eq. (5.86) is allocated to $F_{r,i}^{cr}$ which is representative of force of the reinforcing bar at the i^{th} layer

when the layer is onset by the crack. From now on $F_{r1,i}^{k}$, $F_{r2,i}^{k}$, and $L_{tr,i}^{k}$ are determined regarding slippage of reinforcement at the crack section by taking advantage of the formulation described in Section 5.1.2.3. Once $F_{r2,i}^{k}$ exceeds $F_{r,i}^{cr}$, a new crack is formed, and the prism length is updated accordingly. For a i^{th} layer positioned in the compressive zone (*i.e.* $d_i < d_{NA}$), Equation (5.86) provides a negative value for $F_{r,\sigma-\varepsilon,i}^{k}$, while $F_{r,\tau-s,i}^{k}$ in Equation (5.85) is null.The depth of the neutral axis is obtained by the equilibrium of the axial forces in the cross-section:

$$\sum F = \sum_{i=1}^{n_L^c} F_{cc,i}^{k} + \sum_{i=1}^{n_L^t} F_{ct,i}^{k} + \sum_{i=1}^{n_L^r} F_{r,i}^{k} \tag{5.88}$$

where n_L^c and n_L^t are, respectively, the number of concrete layers positioned in the compressive and tensile zone, and n_L^r represents the number of layers with longitudinal reinforcing bars. In case the unbalanced force of cross-section (ΣF) is greater than the adopted tolerance (=10 N), the value of the depth of the neutral axis (d_{NA}) utilised in Equation (5.80) is modified and the abovementioned procedure is rehearsed by a new value of d_{NA} until the equilibrium condition is satisfied, after which the following bending moment of the k^{th} loading step is determined:

$$M^{k} = \sum_{i=1}^{n_L^c} F_{cc,i}^{k} d_{cc,i} + \sum_{i=1}^{n_L^t} F_{ct,i}^{k} d_{ct,i} + \sum_{i=1}^{n_L^r} F_{r,i}^{k} d_{r,i} \tag{5.89}$$

Equations. (5.79) and (5.89) define a point of the moment-rotation relationship $(\theta^k - M^k)$. The developed model is described in the flowchart depicted in Figure 5.13.

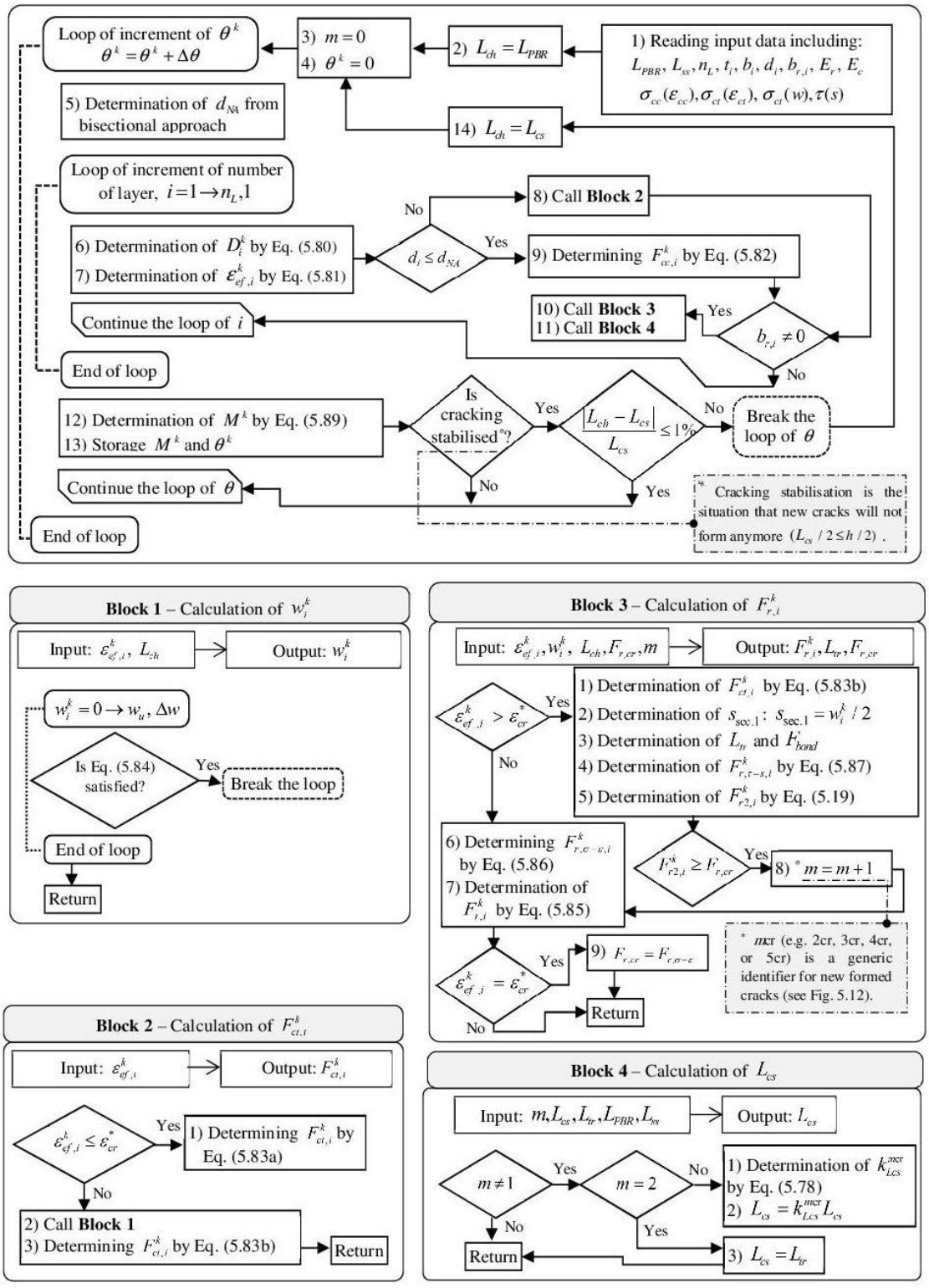

Figure 5.13: Algorithm of the model

5.4 Model appraisal

The predictive performance of the proposed model was evaluated simulating the moment versus average crack width and average crack spacing of R/SFRSCC beams, detailed in Chapter 3 (Table 3.9), designated herein B1 to B6, and the ones registered in the experimental research conducted by other authors (B7 to B10). The beams were loaded under four-point bending configuration, as schematised in Figure 5.14.

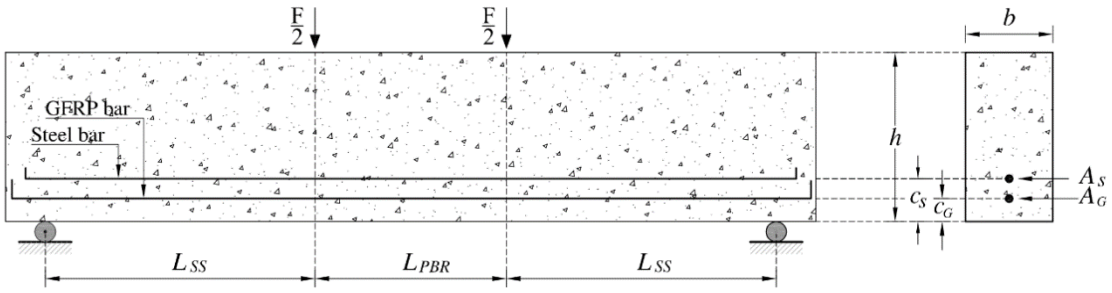

Figure 5.14: Four-point bending test setup (G represents GFRP)

Table 5.1: Geometry and reinforcing scheme of the beams (G: GFRP; dimensions are in mm)

Beams	Designation in Chapter 3 or in the Reference	SFRC type	Geometrical prop.		Steel bar			GFRP bar		
			$b \times h$	L_{ss}/L_{PBR}	type	num. and diam.	c_s	type	num. and diam.	c_G
B1	SR/FRC1545	C15-f45	150×100	900/500	S1	1Φ8	40	-	-	-
B2	SR/FRC2560	C25-f60	150×100	900/500	S1	1Φ8	40	-	-	-
B3	SR/FRC4590	C45-f90	150×100	900/500	S1	1Φ8	40	-	-	-
B4	SGR/FRC1545	C15-f45	150×100	900/500	S1	1Φ8	40	G1	1Φ8	20
B5	SGR/FRC2560	C25-f60	150×100	900/500	S1	1Φ8	40	G1	1Φ8	20
B6	SGR/FRC4590	C45-f90	150×100	900/500	S1	1Φ8	40	G1	1Φ8	20
B7	Vandewalle (2000)	SFRC1	200×350	750/1750	S2	2Φ20	45	-	-	-
B8	Tan et al. (1995)	SFRC2	100×125	600/600	S2	2Φ10	25	-	-	-
B9	Montaignac et al. (2012)	SFRC3	400×300	900/600	S3	2Φ16	50	-	-	-
B10	Montaignac et al. (2012)	SFRC4	400×300	900/600	S3	2Φ16	50	-	-	-

The designation of the constitutive SFRSCC, the geometric properties of the beams, and the beams longitudinal reinforcing schemes are indicated in Table 5.1. Accordingly, except B4, B5, and B6, which were hybrid reinforced with a GFRP and a steel bar, the remains are reinforced solely with longitudinal steel bars. The mechanical properties of the reinforcing bars are summarised in Tables 5.2. According to Table 5.1, the beams are made of seven types of SFRCs, which are distinguished by the concrete strength class and volume content and geometry of hooked-end steel fibres, as detailed in Table 5.3.

Table 5.2: Mechanical properties of the reinforcing bars

Steel/GFRP bar type	E_r [GPa]	σ_{ry} [MPa]	ε_{ry} [‰]	σ_{ru} [MPa]	ε_{ru} [‰]
S1	205	575	2.8	575	32
S2	200	500	2.5	500	15
S3	200	400	2.0	400	15
G1*	58	-	-	1058	18

* Grooved surface

The 28-day average compressive strength of the SFRCs (f_{cm}) is summarised in Table 5.3, according to which the tensile strength (f_{ctm}) and modulus of elasticity (E_{cm}) of the SFRCs were determined by Equations (5.6) and (5.7), respectively.

In the case of C15-f45, C25-f60, and C45-f90, the post-cracking responses were evaluated by the inverse analysis of the force-deflection relationship registered in three-point notched beam bending tests executed according to the recommendations of *fib* Model Code 2010 (2011), as described in detail in chapter 3. The adopted post-cracking responses for the SFRC3 and 4, are the ones provided in (Montaignac et al. 2012). In the case of SFRC1 and 2, however, due to lack of information, the post-cracking response of SFRCs was estimated by following the recommendations *fib* Model Code 2010 (2011), according to which a linear stress-crack width diagram represented in Figure 5.15 is adopted for modelling the FRC in tension.

Table 5.3: Relevant properties of the used SFRCs

		C15-f45	C25-f60	C45-f90	SFRC1	SFRC2	SFRC3	SFRC4
f_{cm}	MPa]	13.12	23.57	43.99	37.50	34.50	46.90	63.20
f_{ctm}	[MPa]	0.89	1.87	3.27	2.86	2.67	3.44	6.34
E_{cm}	[GPa]	23.54	28.61	35.23	33.40	32.50	36.00	39.75
f_{R1} / f_{R3}	[-]	4.02/3.20	7.36/6.44	11.59/9.70	3.52/3.10	2.86/2.58	5.22/4.37	6.27/5.13
f_{Fts} / f_{ctm}	[-]	2.03	1.77	1.60	0.55	0.48	0.68	0.99
V_f	[%]	0.6	0.8	1.1	0.6	0.5	1.0	1.0
l_f	[mm]	35	35	35	35	30	35	60
d_f	[mm]	0.55	0.55	0.55	0.54	0.50	0.55	0.75
a_1	[-]	1.90	1.45	1.35	0.55	0.48	0.62	0.49
a_2	[-]	1.60	1.22	1.27	0.50	0.44	0.68	0.61
a_3	[-]	1.33	0.96	1.14	0.45	0.40	0.65	0.75
a_4	[-]	1.00	0.69	0.87	0.40	0.35	0.33	0.76
a_5	[-]	0.67	0.20	0.60	0.30	0.27	0.58	0.47
w_1	[mm]	0.01	0.10	0.20	0.00	0.00	0.01	0.01
w_2	[mm]	0.20	1.00	0.50	0.50	0.50	0.11	0.05
w_3	[mm]	1.00	2.00	1.00	1.00	1.00	0.45	0.26
w_4	[mm]	2.00	3.00	2.00	1.50	1.50	0.86	0.67
w_5	[mm]	3.00	4.90	3.00	2.50	2.50	2.78	2.32
w_u	[mm]	5.00	5.00	5.00	2.55	2.55	5.00	6.00

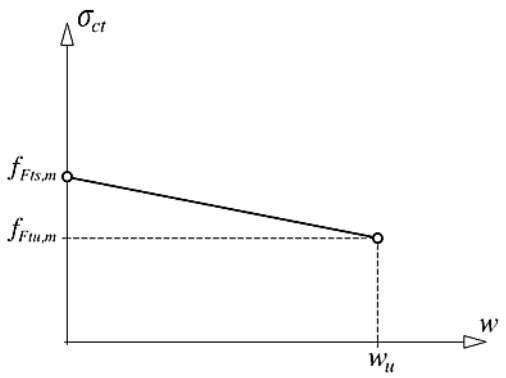

Figure 5.15: Tensile stress *vs.* crack opening diagram recommended by *fib* Model Code 2010 (2011)

In Figure 5.15 $f_{Fts,m}$ and $f_{Ftu,m}$ are, respectively, the average serviceability and ultimate residual strength of FRC determined from the following equations:

$$f_{Fts,m} = 0.45 f_{R1,m} \tag{5.90}$$

$$f_{Ftu,m} = f_{Fts,m} - \frac{w_u}{CMOD_3}(f_{Fts,m} - 0.5 f_{R3,m} + 0.2 f_{R1,m}) \geq 0 \tag{5.91}$$

being $f_{R1,m}$ and $f_{R3,m}$ the average residual flexural tensile strength of FRC at a $CMOD_1$= 0.5 mm and $CMOD_3$ = 2.5 mm evaluated from the force-CMOD relationship determined in three-point notched beam bending tests carried out according to the recommendations of *fib* Model Code 2010 (2011). In Equation (5.91) w_u is the ultimate value of crack width depends on the level of required ductility. In the case of elements failing in bending w_u is considered equal to 2.5 mm (*fib* Model Code 2010 2011). Since the flexural residual strength parameters are unavailable for SFRC1 and 2, they were estimated according to the following equations, whose adequate predictive performance was demonstrated elsewhere (Moraes-Neto et al. 2013):

$$f_{R1,m} = 7.5\left(V_f l_f / d_f\right)^{0.8} \tag{5.92}$$

$$f_{R3,m} = 6.0\left(V_f l_f / d_f\right)^{0.7} \tag{5.93}$$

being V_f , l_f and d_f the volume percentage, length and diameter of the used fibres, respectively.

The values of the parameters that define the local bond-slip constitutive law (Figure 5.5) are indicated in Table 5.4. Regarding some literature, considering the *fib* Model Code 2010 (2011) equations, the maximum bond stress of steel bars (τ_m) (see Figure 5.5) is determined independently from the bar geometry. Despite the simplicity, prediction of these equation is noticeably underestimated, even up to 60%, compared with the real value measured in the test (Desnerck et al. 2010). Therefore, In the proposed model the maximum bond stress and corresponding slippage (s_1) of steel bars were determined by the following equations (Desnerck et al. 2010):

$$\tau_m = \left[1.77 + 0.49(c_s / d_b)\right]\sqrt{f_{cm}} \tag{5.94}$$

$$s_1 = c_0\left(0.0035c_0 + 0.006\right) \tag{5.95}$$

where c_s is the concrete cover thickness in mm, d_b is the diameter of the reinforcement bar in mm, f_{cm} is the concrete compressive strength in MPa, and c_0 is the clear rib spacing of the steel bars and taken equal to 5.7, 6.5, 9.6, and 11.5 mm, respectively, for the 8, 10, 16, and 20 mm diameter bars according to the DIN 488 (1986). Furthermore, regarding the recommendations of *fib* Model Code 2010 (2011), s_2 and s_3 are taken equal to 2 mm and c_0, respectively, and τ_R is considered $0.4\tau_m$. The values of the parameters that define the local bond-slip relationship of GFRP bar are also included in Table 5.4. In the case of C15-f45 and C25-f60, these parameters were determined by Mazaheripour (2015) by the inverse analysis of pull-out bending test results of the same GFRP type and concrete strength class. In the case of C45-f90, however, due to lack of information, the bond-slip constitutive law of the GFRP bar was linearly extrapolated regarding the results presented in (Mazaheripour 2015).

Table 5.4: Bond-slip parameters adopted in the simulations

Type of bar	SFRC	τ_0 [MPa]	τ_m [MPa]	s_1 [mm]	s_2 [mm]	τ_R [MPa]	s_3 [mm]
GFRP	C15-f45	1.00	12.50	0.12	1.80	5.10	7.00
	C25-f60	1.00	14.90	0.11	1.20	5.90	8.60
	C45-f90	1.00	17.30	0.10	0.60	6.70	10.20
Steel	C15-f45	0.00	15.28	0.15	2.00	6.11	5.70
	C25-f60	0.00	20.49	0.15	2.00	8.20	5.70
	C45-f90	0.00	27.99	0.15	2.00	11.20	5.70
	SFRC1	0.00	16.09	0.53	2.00	6.44	11.50
	SFRC2	0.00	17.59	0.19	2.00	7.04	6.50
	SFRC3	0.00	22.61	0.38	2.00	9.04	9.60
	SFRC4	0.00	26.24	0.38	2.00	10.50	9.60

In the case of specimens tested in the present research (B1 to B6), the average crack spacing at cracking stabilized stage (when no new more cracks were formed) was determined by dividing the distance between two furthest crack at the level of steel

reinforcement in PBR, by the number of uncracked segments between these two cracks. The crack patterns of the tested beams (B1 to B6) are shown in Figure 5.16. The average crack width was determined by dividing the deformation of the pure bending region at the steel bar level, measured by the LVDT7 shown in Figure 3.20(b) mounted at this level mines equivalent elastic deformation of concrete, by the total number of cracks that have crossed the concrete at this level. In the case of the remaining beams, the values reported in the literature were taken into consideration.

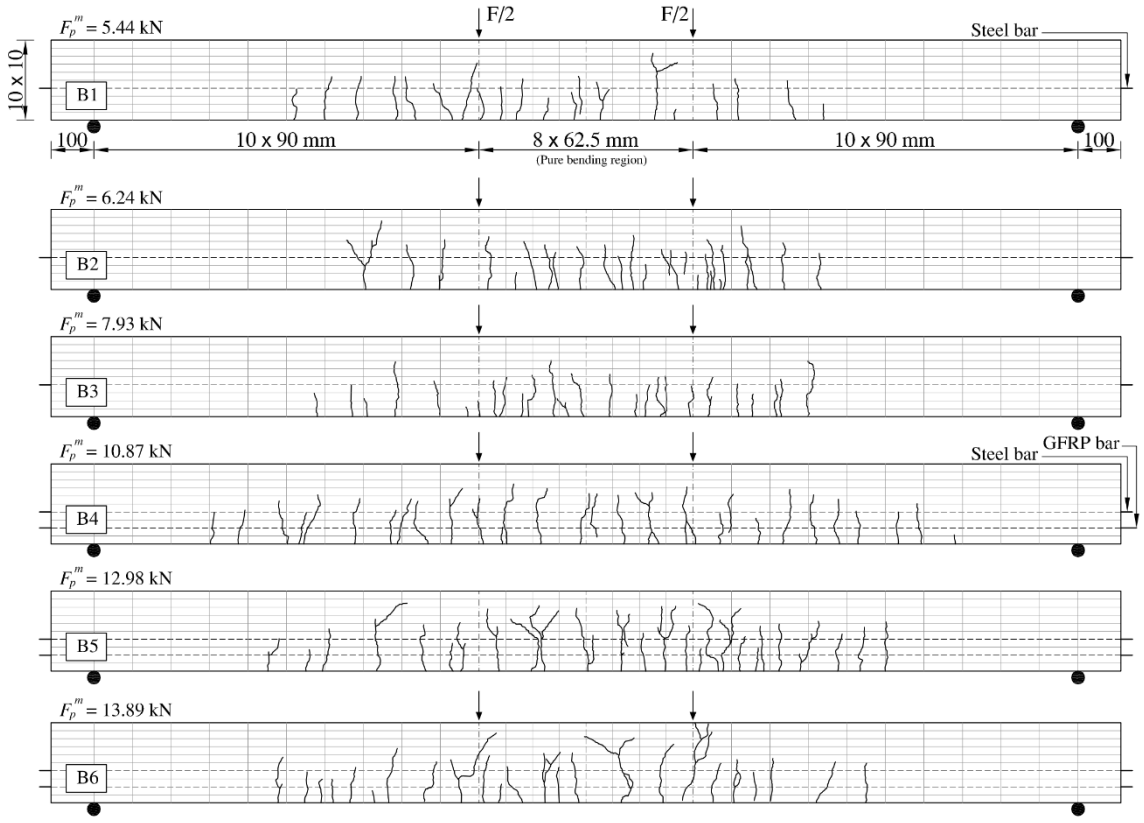

Figure 5.16: Typical crack patterns in the tested beams (F_p^m is the average peak load of the corresponding series of beams)

In Figure 5.17, the prediction of the proposed model in terms of the force-deflection response is assessed regarding the tested beams (B1 to B6) comparing the results registered in the experimental programmes, which reveals good accuracy of the developed model. It is remarked that for each level of prescribed bending moment, the central deflection of the beams is determined by the algorithm represented in Figure 4.10,

in which the corresponding curvature is resulted by dividing the overall rotation of the pure bending region of (θ), determined by the model, by the length of this region $(L_{PBR} = 500\,mm)$.

The moment-average crack width relationships predicted by the model are compared with the ones recorded in the experimental programs in Figure 5.18 and 5.19. In this figure is also indicated the adopted value of the characteristic length (L_{ch}) determined by the developed algorithm of Figure 5.13. Considering Figure 5.18 and 5.19, the excellent predictive performance of the developed model is assessed.

In Figure 5.20 the model prediction in terms of average crack spacing is compared to the test results, which reveals that the predictive performance of the model is reasonable. Nevertheless, when compared with the test results, the proposed model predicted lower bending moments at crack initiation. This is ascribed to the fact that crack detection during the performed tests was based on a visual inspection and hence the first microcracks, which are predicted theoretically by formulation, should be widened enough by the increase of the prescribed load to be detectable by unarmed eyes. Figure 5.20 also shows that the rate of cracking (i.e. reduction of crack spacing) differs, to some extent, in the case of model prediction and the performed test. It is remarkable that in the proposed model concrete is considered as a homogeneous material with constant cracking strain over the beam length implemented to the procedure. Therefore, the presence of the porosities and microcracks in the tested beams never can be taken into consideration in the model while they directly dictate the position of cracks over the length.

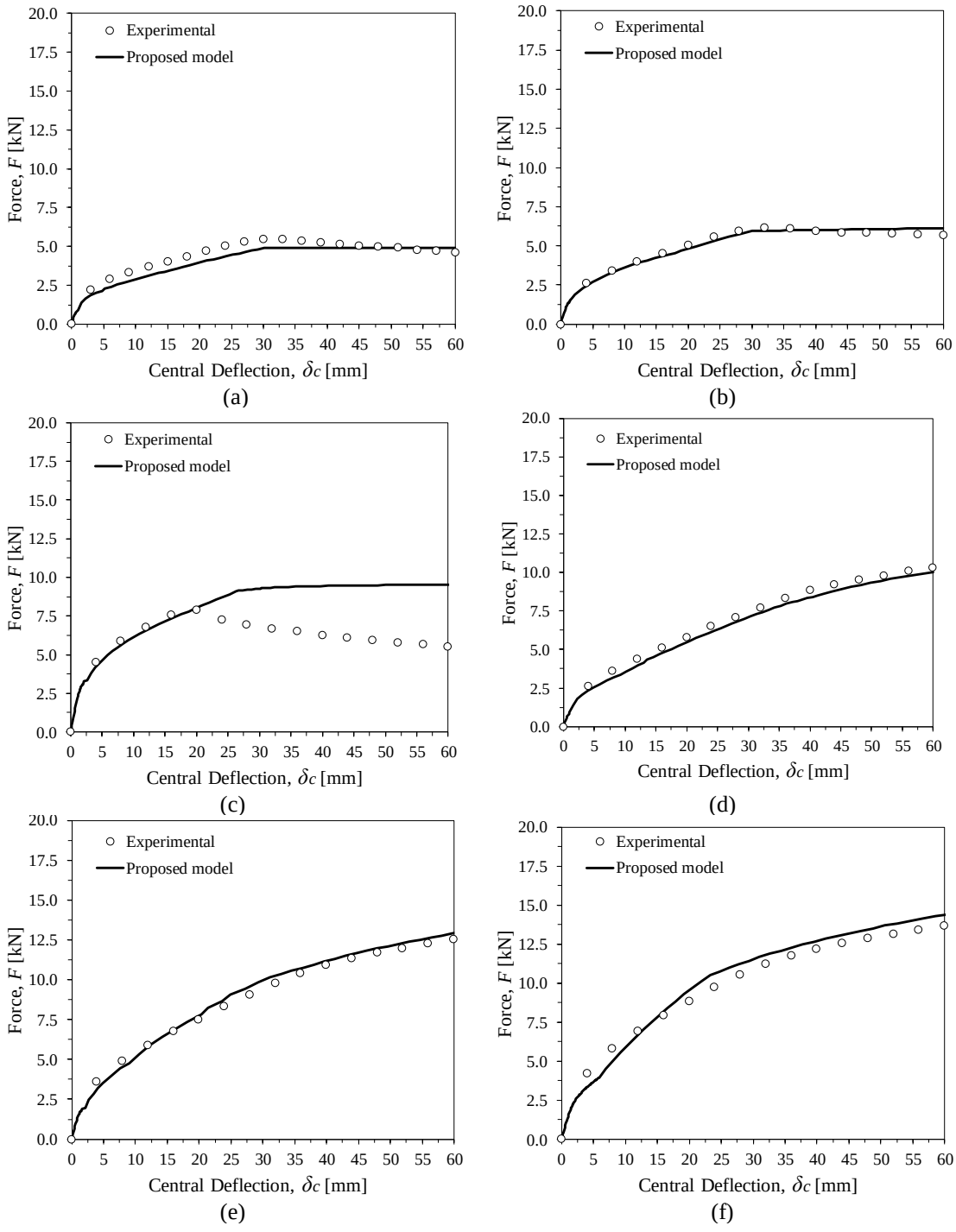

Figure 5.17: Predictive performance of the model for the force-deflection response of (a) B1, (b) B2, (c) B3, (d) B4, (e) B5, (f) B6

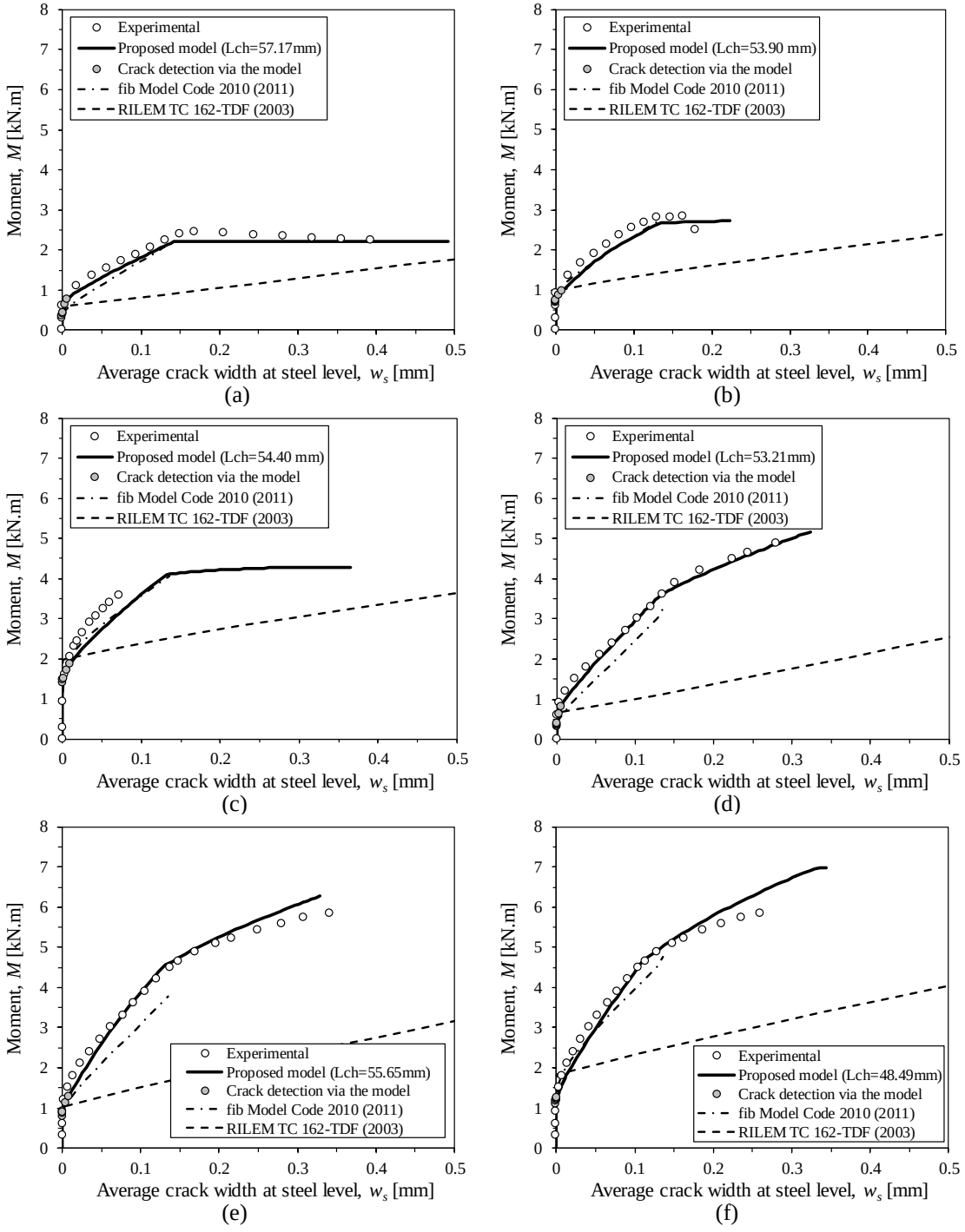

Figure 5.18: Predictive performance of the model for the moment-crack width of (a) B1, (b) B2, (c) B3, (d) B4, (e) B5, (f) B6

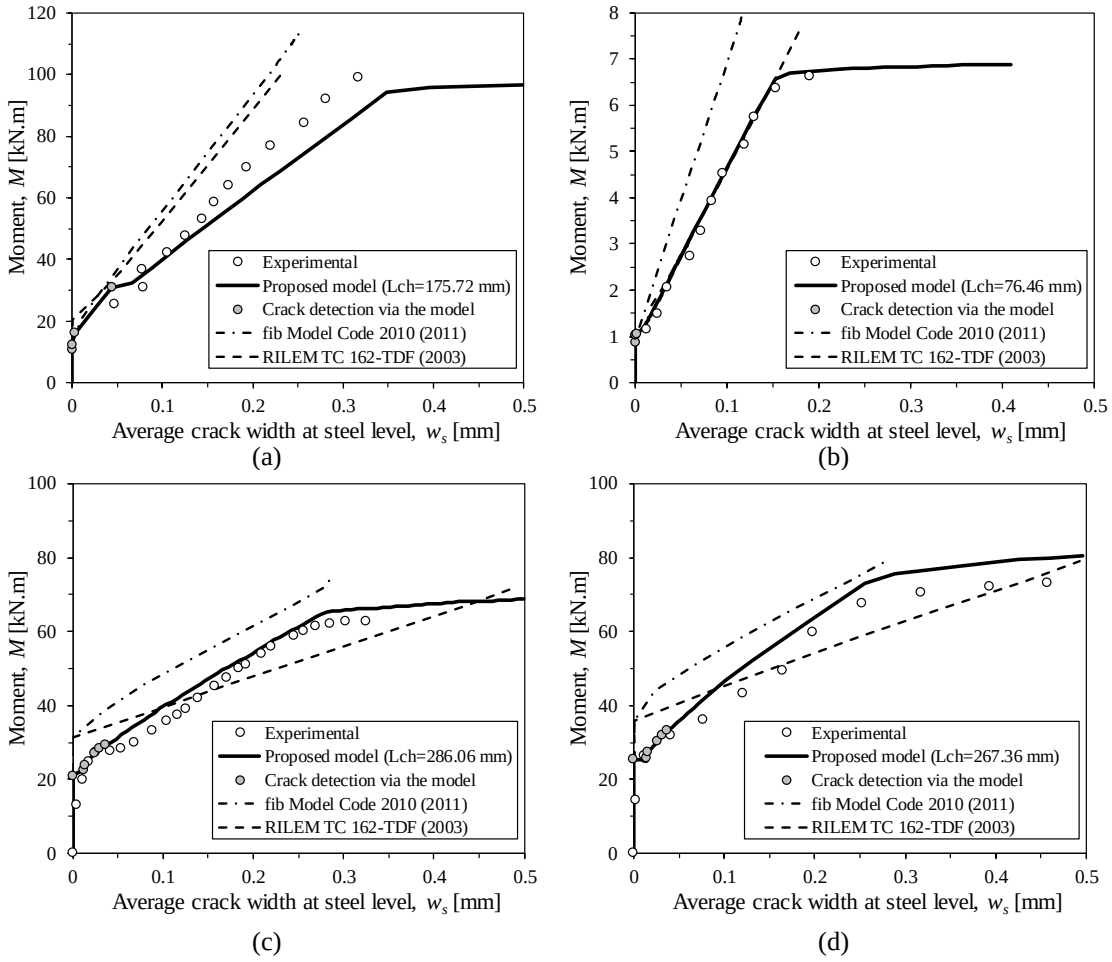

Figure 5.19: Predictive performance of the model for the moment-crack width of (a) B7, (b) B8, (c) B9, (d) B10

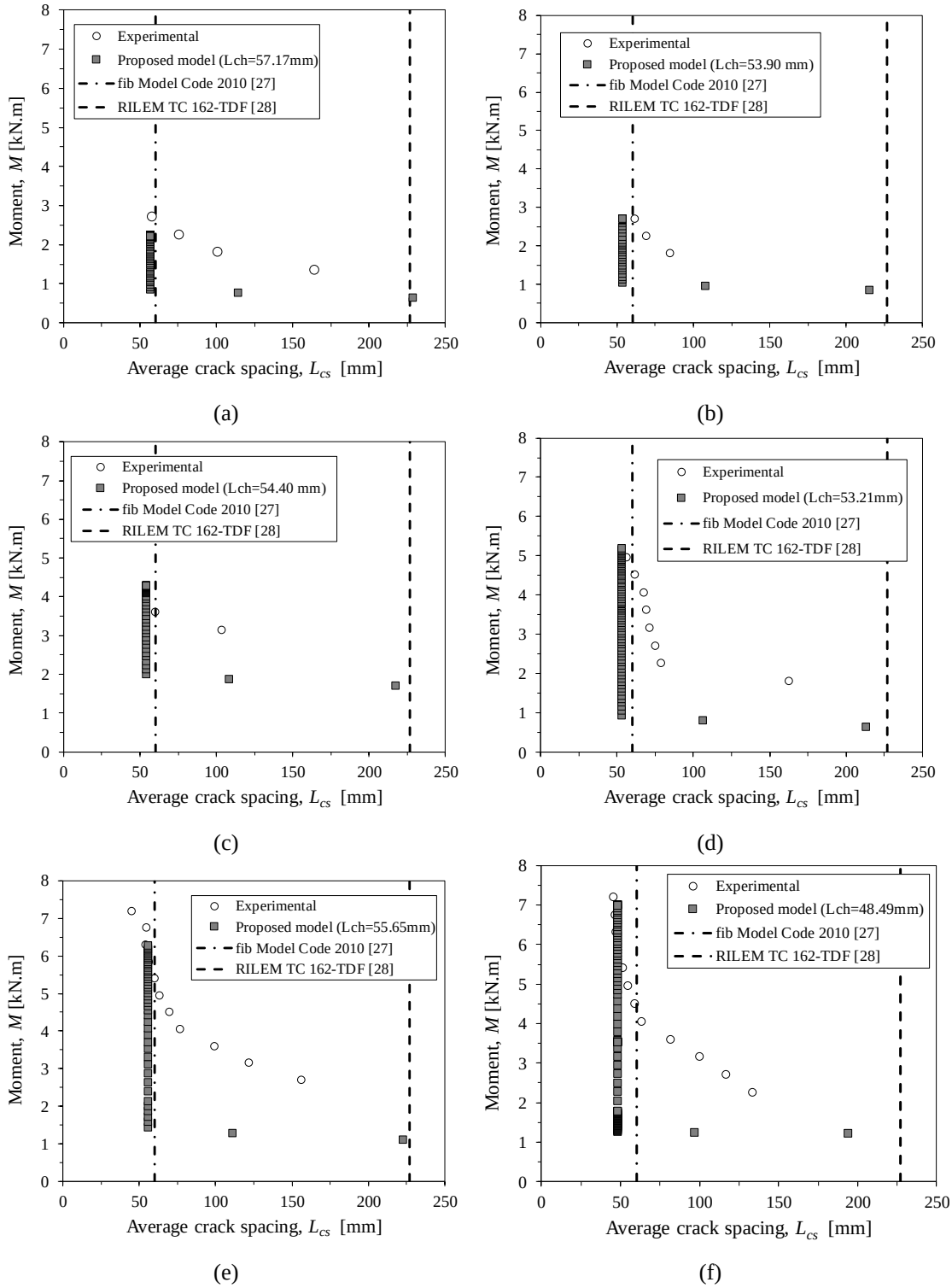

Figure 5.20: Predictive performance of the model for the moment-average crack spacing of (a) B1, (b) B2, (c) B3, (d) B4, (e) B5, and (f) B6

5.5 Predictive performance of available design guidelines

5.5.1 Recommendation of RILEM TC 162-TDF

According to RILEM TC 162-TDF (2003), up to the yield initiation of the steel reinforcement the design value of the crack width (w_d) for R/FRC members subjected principally to flexure or tension is estimated by the following equation:

$$w_d = k_7 \, s_{rm} \, \varepsilon_{sm} \tag{5.96}$$

where k_7 is a coefficient correlating the average crack width to the design value, equal to 1.3 or 1.7 depending on the minimum dimension of the cross-section. In Equation (5.96) s_{rm} is the average final crack spacing (at the cracked stabilised stage) calculated from the following equation:

$$s_{rm} = \left(50 + 0.25 k_3 k_4 \frac{d_b}{\rho_{s,ef}} \right) \left(\frac{50}{l_f / d_f} \right) \tag{5.97}$$

In this equation k_3 is a coefficient to take into account the bond properties of the longitudinal bars, equal to 0.8 and 1.6 for the high bond and plain bars, respectively, while k_4 is a coefficient equal to 0.5 for bending. In Equation (5.97) d_b is the steel bar diameter, l_f / d_f is the fibre aspect ratio, being l_f and d_f the fibre length and diameter, respectively. Furthermore, $\rho_{s,ef}$ is the effective flexural reinforcement ratio determined from the following equation:

$$\rho_{s,ef} = \frac{A_s}{2.5 c_s b} \tag{5.98}$$

where A_s is the cross-sectional area of the longitudinal reinforcement contained within the effective SFRC area in tension ($A_{c,ef} = 2.5 c_s b$). In Equation (5.96) ε_{sm} is the average strain in the reinforcement determined from the following equation:

$$\varepsilon_{sm} = \frac{\sigma_{st}}{E_s}\left[1 - k_{14}k_{15}\left(\frac{\sigma_{sr}}{\sigma_{st}}\right)^2\right] \quad (5.99)$$

where k_{14} is equal to 1.0 and 0.5 for, respectively, high bond and plain bars, while k_{15} is equal to 1.0 and 0.5 for single-short term loading and for sustained and repeated loading, respectively. In Equation (5.99) $\sigma_{st}(=E_s\varepsilon_s)$ is the stress in the steel reinforcement up to the yield initiation, where $\varepsilon_s(=\chi(d-d_{NA}))$ is the strain of the steel reinforcement, being χ and d_{NA}, respectively, the corresponding curvature and the depth of the neutral axes, and d the effective depth of this reinforcement. Furthermore, σ_{sr} is the steel stress at the crack section in the crack formation stage obtained from the following equation:

$$\sigma_{sr} = \frac{(f_{ctm} - f_{Fts,m})}{\rho_{s,eff}}.(1+\gamma_s\rho_{s,eff}) \quad (5.100)$$

being $\gamma_s = E_s / E_c$, f_{ctm} is the average value of the tensile strength and $f_{Fts,m}$ is determined by Equation (5.90). In the application of this approach the following values were adopted: k_7 =1.3; k_3 =0.8; k_4 =0.5; $k_{14} = k_{15}$ =1.0.

5.5.2 Recommendation of *fib* Model Code 2010

According to the *fib* Model Code 2010 (2011) the average crack spacing (s_{rm}) in R/FRC members is estimated by multiplying the length over which slip between concrete and steel occurs ($l_{s,\max}$) by a factor of 1.5. $l_{s,\max}$ is determined from the following equation:

$$l_{s,\max} = k_{11}c_s + \frac{\left(f_{ctm} - f_{Fts,m}\right)}{4\tau_{bm}}\frac{d_b}{\rho_{s,eff}} \quad (5.101)$$

where k_{11} is an empirical coefficient for simulating the influence of the concrete cover thickness that can be assumed equal to 1.0 for the simplicity, and τ_{bm} is the average bond strength between reinforcing bars and surrounding concrete:

$$\tau_{bm} = 1.8 f_{ctm} \tag{5.102}$$

Equation (5.101) is applicable for FRCs when the average residual strength at serviceability limit states $(f_{Fts,m})$ is less than the crack strength of the concrete matrix (f_{ctm}). For the other cases $l_{s,\max} = k_{11} c_s$ is assumed. Considering the *fib* Model Code 2010 (2011) recommendation, the average crack width (w_m) is determined by dividing the design value of crack width, obtained from Equation (5.103), by a factor of 1.7:

$$w_d = \frac{2 l_{s,\max}}{E_s}(\sigma_{st} - k_{12}\sigma_{sr} - k_{13}\varepsilon_{sh}E_s) \tag{5.103}$$

In this equation, σ_{st} and ε_s are the stress and strain of steel reinforcement in the cracked section, and σ_{sr} is determined by Equation (5.100). In the evaluation of the σ_{st} and ε_s the SFRC in tension was considered resisting to a constant value of $f_{Fts,m}$, with a linear stress-strain diagram in the compression zone.

In Equation (5.101) $\rho_{s,eff}$ is the effective reinforcement ratio equal to the maximum of $A_s/(2.5(h-d))$ and $A_s/((h-d_{NA})/3)$, being h the total height of cross-section (see Figure 5.9). Furthermore, in Equation (5.103) k_{12} is additionally an empirical coefficient to assess the mean strain over $l_{s,\max}$, considered equal to 0.6 for short-term loading, and k_{13} is a coefficient for considering the shrinkage contribution, which can be considered equal to zero for the short-term loading, and ε_{sh} is the shrinkage strain.

The predictive performance of the RILEM TC 162-TDF (2003) and *fib* Model Code 2010 (2011) approaches is assessed in terms of moment-average crack width relationship in Figures 5.18 and 5.19, and in the case of moment-crack spacing response in Figure 5.20, respectively, by the prediction of the developed model and ones registered

experimentally. Figure 5.18 shows that when the RILEM TC 162-TDF (2003) was applied to B1 to B6 tested beams, a crack width larger than the one obtained with the proposed model and registered experimentally was estimated. Note that B1 to B6 are the beams made of FRCs whose average residual strength at the serviceability limit states ($f_{Fts,m}$) is greater than the crack strength of the concrete matrix (f_{ctm}). Therefore, the term $f_{ctm} - f_{Fts,m}$ in Equation (5.100) is adopted null, which means σ_{sr}=0. In the case of B7 to B10, the accuracy of the prediction of the RILEM approach is variable. While in the case of B8 the predictive performance of this approach is excellent, however, small values of the width of the crack is predicted by RILEM formulation in the case of B7 series beam considering the test results. In the case of B9 and B10, although RILEM approach has predicted satisfactorily the test results, the evolution of the moment-crack width determined by the RILEM is somewhat different when compared with the test results. These beams are constituted of FRCs for which $f_{Fts,m}$ is smaller than f_{ctm} and accordingly, a non-zero value of term $f_{ctm} - f_{Fts,m}$ is utilised in Equation (5.100). Regarding Figure 5.20, a relatively large average crack spacing is predicted by the RILEM approach for B1 to B6 tested beams.

According to Figure 5.18, the *fib* Model Code 2010 (2011) approach predicted with excellent accuracy the crack width versus applied bending moment response in the case of B1 to B3, where $f_{ctm} - f_{Fts,m}$ equal to zero is used in Equation (5.101), (*i.e.* $l_{s,\max} = k_{11}\, c_s$). However, a relatively larger crack width is determined by the *fib* approach for the hybrid longitudinally reinforced beams (*i.e.* B4 to B6).

As depicted in Figure 5.19, in the case of B7 to B10, a relatively smaller average crack width was obtained with the *fib* Model Code 2010 (2011) approach, where a non-zero value of term $f_{ctm} - f_{Fts,m}$ is utilised. This means that the contribution of the post-cracking of FRC in the *fib* Model Code 2010 (2011) formulation is overestimated. Figure 5.20 demonstrates that the *fib* Model Code 2010 (2011) predicts reliably the average crack spacing for the crack stabilised stage.

5.6 Concluding remarks

In the present chapter, an innovative model was developed based on the moment-rotation response of FRC elements with hybrid flexurally reinforcement (H/FRC). Owing to the layered model approach utilised in the model, a symmetrical cross-section of any shape can be allocated to the R/FRC member. The developed approach can be used for any flexural reinforcing or strengthening scheme, including the use of longitudinal reinforcing steel or FRP bar solely or simultaneously and utilising steel plates or FRP laminated in near-surface mounted (NSM) or externally bonded reinforcement (EBR) strengthening technique.

The bond-slip behaviour between flexural reinforcement and surrounding FRC is mobilised in the model, and the tensile behaviour of FRC is taken into consideration by the stress-crack width relationship, which is the most appropriate constitutive law for evaluating the fracture mechanism of FRC. The computational algorithm adopted in the model is capable of determining the characteristic length of the H/FRC beams, considered equal to the minimum spacing between cracks.

The predictive performance of the proposed model was assessed by simulating experimental tests conducted on R/FRC beams in the experimental program detailed in chapter 3 and the ones provided in the literature. The R/FRC beams comprise a broad variety of geometry, flexural reinforcing scheme, and constituent FRC of various concrete strength class and content of fibres. The model has predicted with excellent accuracy the moment-average crack width and the moment-average crack spacing relationship.

The prediction of the model is compared to the ones obtained by applying the approaches recommended by RILEM TC 162-TDF (2003) and The *fib* Model Code 2010 (2011), which are two pioneer guidelines for mobilising the advantages of adding fibres to concrete for the structural design applications.

It was revealed that the approach recommended by RILEM TC 162-TDF (2003) led to larger crack width in the case of the B1 to B6 beams, for which the average residual strength at serviceability limit states ($f_{Fts,m}$) is greater than the crack strength of the concrete matrix (f_{ctm}), and hence, the term $f_{ctm} - f_{Fts,m}$ is adopted null. This means

the formulation proposed by RILEM TC 162-TDF (2003) may need further improvements to be capable of predicting the crack width of the beams made of deflection-hardening characteristics (Naaman 2008). For the other beams for which $f_{ctm} - f_{Fts,m} > 0$ (*i.e.* B7 to B10), prediction of RILEM TC 162-TDF (2003) approach is acceptable.

In addition, *fib* Model Code 2010 (2011) approach, in general, predicted accurately the crack width of the beams, however, this approach led to a larger crack width in the case of B4 to B6 beams, in which additional FRP bar is used longitudinally with steel reinforcement. On the other word, the contribution of FRP bar to the reduction of the crack width in H/RC beams is not taken into account properly by the *fib* Model Code 2010 (2011) approach.

Furthermore, a relatively large average crack spacing is predicted by the RILEM approach for B1 to B6 tested beams which a reliable crack spacing was predicted by the *fib* Model Code 2010 (2011).

Chapter **6**

Conclusions and Future Developments

6.1 General conclusions

The present work comprises extensive experimental research and analytical/numerical modelling conducted to evaluate the potentiality of a hybrid flexural reinforcement (HFR) reinforcing approach for concrete elements failing in bending. In this approach, FRP bars are placed near the outer surface of the tensile zone and steel bars at an inner level, while the reinforcing mechanism of fibres distributed in fibre reinforced concrete (FRC) is employed to increase the solidity and toughness of the concrete. In such a hybrid reinforcing scheme, the longitudinal reinforcement can be reduced owing to the contribution of fibres. Therefore, the post-cracking characteristics of FRC and the interaction between FRC and embedment reinforcing bar represent the key factors affecting the load carrying capacity and cracking behaviour of the H/FRC flexural

elements. The experimental research of the present work was accomplished at two various levels. At the material level, three series of steel fibre reinforced self-compacting concrete (SFRSCC) designated by C15-f45, C25-f60, and C45-f90 were developed, which are distinguished by the strength class of concrete and content of the used hooked-end steel fibres. The compressive strength of the developed SFRCs was evaluated by the direct compressive test, while the post-cracking response of the SFRCs was characterised through the two approaches; by executing the three-point notched beam bending test (3PNBBT) and deriving the stress-crack width relationship by following the recommendation of *fib* Model Code 2010 (2011), and through the inverse analysis of the force-deflection responses recorded in the 3PNBBT by finite element simulation. It was revealed that the post-cracking response of the SFRCs is improved noticeably by the increase in the volume fraction of fibres. Nevertheless, the approach recommended by *fib* Model Code 2010 (2011) overestimates the stress-crack width response of the SFRCs when compared to the one determined by the inverse analysis.

At the structural level, the force-deflection response and cracking behaviour of the flexural H/FRC beams were evaluated through the four-point bending test. In addition, 18 beams of 2500 mm length and 100 × 150 mm cross-section were cast by the use of three series of developed SFRCs (*i.e.* six samples of each SFRC series). The H/FRC beams were reinforced longitudinally by one steel bar, designated by SR beams, or by the use of steel and GFRP bars, designated by SGR series beam. The tensile behaviour of the used steel and GFRP bar was evaluated by performing the uniaxial tensile test. To pronounce the reinforcing effect of distinct fibres on the structural response of H/FRC beams, relative small ratios of longitudinal reinforcement were utilised. To be specific, the adopted steel reinforcement ratio in SR beams was lower than the balanced reinforcement ratio recommended in the design guideline. In the case of SGR series beam, the adopted reinforcement ratio assures yielding of steel bars before crushing of concrete in compression.

The localisation of crack just after yielding of steel bar was the noticeable observations in the case of SR series beam accompanied by the load deterioration. On the other word, although the contribution of fibres tends to be increased by the reduction of the percentage of the longitudinal reinforcement, localisation of the crack in a cross-

section with the lower amount of fibres and with eventual more porosity and deficiencies may threaten the structural response of the elements. The crack localisation phenomenon right after yield initiation of steel bar was totally remedied by the use of additional FRP longitudinal bar in the case of SGR series beam. However, it was revealed that the influence of the contribution of fibres on the load-carrying capacity of the beams tends to be reduced in the presence of longitudinal GFRP bar.

According to the test results, the increase of 33% and 100% in the content of reinforcing fibres resulted in an increase of 8% and 86% of the load corresponding to the serviceability limit states in the case of SR beams, and 35% and 59% in the case of SGR. The load corresponding to the yield initiation of the steel bar enhanced 11% and 48% in the case of SR series, and 27% and 42% in SGR series beam, respectively, by the increase of 33% and 100% in the volume fraction fibres. Accordingly, it is concluded that the contribution of GFRP bar was more pronounced on the load at yield initiation of SGR beams and less on the load corresponding to the serviceability limit states. This is ascribed to the relatively low modulus of elasticity of the used GFRP bar postpone its effective contribution to larger deflection.

The test results also revealed that the average crack spacing and crack width measured along with the pure bending region of the beams tends to be reduced by the increase in fibres dosage as well as the addition of GFRP bar.

The present work comprises extensive research to advanced modelling of H/FRC flexural beams for evaluating comprehensively the potentiality of such a hybrid reinforcing scheme, by integrating the influence of the key parameters and mechanisms interfering in the structural performance of the H/FRC beams. In this regard, two closed-form solutions were developed based on the smeared crack and discrete crack approaches.

The first model is capable of determining the moment-curvature response of a rectangular cross-section made of FRC reinforced longitudinally by the pre-stressed steel and FRP bars. By adopting a trilinear stress-strain diagram for the tensile behaviour of FRC, this model is capable of simulating both strain-softening and strain-hardening FRC materials, while a bilinear stress-strain behaviour is allocated to FRC in compression. In addition, the tensile behaviour of steel and FRP bars are simulated by a bilinear and linear stress-strain relationship, respectively.

In the adopted approach, the flexural rigidity of the cross-section is derived from the determined moment-curvature response of the cross-section mobilised in the complementary model to predict the force-deflection of the beam by the virtual work method. The excellent predictive performance of the model was assessed by simulating the force-deflection responses registered in experimental programs either the one executed in the present work and the one presented in the literature. The potentiality of the proposed model was additionally, revealed to predict precisely the force-deflection response of reinforced concrete elements flexurally strengthened with pre-stressed FRP systems applied according to the near-surface mounted (NSM) and externally bonded reinforcement (EBR) techniques.

The potentialities of the developed model were employed in a parametric study conducted to evaluate the influence of the key parameters affecting the moment-curvature and force-deflection responses of H/FRC flexural beams. It was observed that the flexural capacity of the cross-section and the load carrying capacity of the beam increase significantly with the increase in the normalised residual strength (μ) and normalised transition strain (α) of FRC. Noticeable influence of μ and α parameters were also observed to the increase in the load at the serviceability limit states and yield initiation of steel bars.

The performed parametric study revealed the increase in the pre-stress level prescribed to the longitudinal reinforcements is pronounced on the load carrying capacity of H/FRC beams, while the deflection at crack initiation is unaffected significantly by the applied pre-stress level. Nevertheless, the deflection amplitude between crack initiation and steel yield initiation decreases with the increase in the pre-stress level may lead to the reduction of the ductility of the beams.

The second numerical/analytical model developed in the present research includes an innovative attitude to predict the cracking behaviour of the H/FRC flexural beams by the moment-rotation approach.

This model considers the bond-slip relationship between the longitudinal reinforcement and surrounding FRC to predict the cracking behaviour of R/FRC elements

failing in bending. In this model, the tensile behaviour of FRC is taken into account in terms of stress-crack width relationship, which is the most appropriate constitutive law for simulation of the FRC fracture mechanism.

The excellent accuracy of the prediction of the model was assessed by simulating experimental tests conducted on R/FRC beams of a vast variety of geometry, flexural reinforcing scheme, and constituent FRC of various concrete strength class and content of fibres.

The prediction of the model is also compared to the ones obtained by employing the approaches recommended by RILEM TC 162-TDF (2003) and the *fib* Model Code 2010 (2011). It was revealed that the approach recommended by RILEM TC 162-TDF (2003) resulted in larger crack width in case the R/FRC beams, for which the average residual strength of the FRC constituent at the serviceability limit states ($f_{Fts,m}$) is greater than the crack strength of the concrete matrix (f_{ctm}). On the other word, the formulation proposed by RILEM TC 162-TDF (2003) may need to further improvement to be capable to predict the crack width of the beams made of deflection-hardening characteristics.

In addition, larger crack width is determined by the approach recommended by *fib* Model Code 2010 (2011) in the case of H/FRC beams, in which the additional FRP bar is used longitudinally with steel reinforcement, which means the contribution of FRP bar to reduction of the crack width in SGR beam is untaken into account properly by the *fib* Model Code 2010 (2011) approach.

6.2 Recommendations for future research

In this research, the structural response of the H/FRC flexural statically determinate beams was evaluated experimentally. The present work in addition comprises the development of two distinct models based on moment-curvature and the moment-rotation approaches to simulate these types of structural elements. The significant influence of the addition of reinforcing fibres on the overall response of the SR/FRC and H/FRC elements were revealed in the executed experiments and the simulation performed by developed models. The following aspects are deserved to be further investigated in future research:

- The durability indexes of the hybrid-reinforcing scheme adopted in the present research should be studied in a comprehensive experimental program.

- In the developed models the contribution of fibres in load bearing mechanism was taken into account in a macro-scale by the employing the post-cracking response of FRC in terms of stress-strain or stress-crack width relationship, which are determined by the mechanical test or through inverse analysis. It is more preferable developing an intermediate chain in modelling which predict the post-cracking response of FRC integrating the pull out response of each individual fibres crossing the crack. In this regard the volume fraction, orientation, and dispersion of fibres, as well as the shape and geometry of fibres are the key parameters.

- Regarding the previous suggestion, the distribution of fibres should be studied precisely. The influence of longitudinal reinforcement on the dispersion of fibres along with the depth of the cross-section should be formulated experimentally. In addition, the influence of the casting methodology and rheology of FRC should be studied on the distribution of fibres along with the beams.

Chapter 7

References

Abdalla H.A. (2002). Evaluation of deflection in concrete members reinforced with fibre reinforced polymer (frp) bars. *Composite Structures*, 56, 63-71.

Abrishami H., and Mitchell D. (1997). Influence of steel fibers on tension stiffening. *Structural Journal*, 94.

ACI-544.2R (1988). Measurement of properties of fibre reinforced concrete. *ACI Materials Journal*, 583-593.

ACI 224R-01 (2001). Control of cracking in concrete structures.

ACI 318-05 (2005). Building code requirements for structural concrete (aci 318-05). Detroit: Farmington Hills, American Concrete Institute.

ACI 440.1R-06 (2007). Guide for the design and construction of concrete reinforced with frp bars. American Concrete Institute, ACI Committee 440

ACI 440R-07 (2007). Report on fibre-reinforced polymer (frp) reinforcement for concrete structures. American Concrete Institute, ACI Committee 440

ACI 544.5R-10 (2010). Report on the physical properties and durability of fiber-reinforced concrete.

ACI Committee 408 (2003). Bond and development of straight reinforcing bars in tension. *Report ACI 408R-03.* Farmington Hills, Michigan.

AFGC-SETRA (2002). *Ultra high performance fibre-reinforced concretes, interim recommendations,* Paris, France, AFGC publication.

Aiello M.A., Leone M., and Pecce M. (2007). Bond performances of frp rebars-reinforced concrete. *Journal of materials in civil engineering,* 19, 205-213.

Aiello M.A., and Ombres L. (2002). Structural performances of concrete beams with hybrid (fiber-reinforced polymer-steel) reinforcements. *Journal of Composites for Construction,* 6, 133-140.

Ali A., J. F.S., and Aurelio M. (2015). Derivation of the σ-w relationship for sfrc from prism bending tests. *Structural Concrete,* 16, 93-105.

Almusallam T.H. (1997). Analytical prediction of flexural behavior of concrete beams reinforced by frp bars. *Journal of Composite Materials,* 31, 640-657.

Alsayed S.H., Al-Salloum Y.A., and Almusallam T.H. (2000). Performance of glass fiber reinforced plastic bars as a reinforcing material for concrete structures. *Composites Part B: Engineering,* 31, 555-567.

Arya C., and Ofori-Darko F.K. (1996). Influence of crack frequency on reinforcement corrosion in concrete. *Cement and Concrete Research,* 26, 345-353.

Arya C., and Wood L.A. (2015). *The relevance of cracking in concrete to reinforcement corrosion,* The Concrete Society.

ASTM-C-1018-97 (1998). *Standard test method for flexural toughness and first-crack strength of fibre-reinforced concrete (using beam with third point loading),* Philadelphia, USA, ASTM.

ASTM A370 (2014). Standard test methods and definitions for mechanical testing of steel products.

Aziz M.A., Paramasivam P., and Lee S.L. (1981). Prospects for natural fibre reinforced concrete in construction *International Journal of Cement Composites and Lightweight Concrete,* 1, 123-132.

Badawi M., and Soudki K. (2009). Flexural strengthening of rc beams with prestressed nsm cfrp rods – experimental and analytical investigation. *Construction and Building Materials,* 23, 3292-3300.

Baena M., Torres L., Turon A., and Barris C. (2009). Experimental study of bond behaviour between concrete and frp bars using a pull-out test. *Composites Part B: Engineering,* 40, 784-797.

Baena M., Torres L., Turon A., and Miàs C. (2013). Analysis of cracking behaviour and tension stiffening in frp reinforced concrete tensile elements. *Composites Part B: Engineering,* 45, 1360-1367.

Bakis C.E., Bank L.C., Brown V.L., Cosenza E., Davalos J.F., Lesko J.J., Machida A., Rizkalla S.H., and Triantafillou T.C. (2002). Fiber-reinforced polymer composites for construction—state-of-the-art review. *Journal of Composites for Construction,* 6, 73-87.

Balaguru P., Gambarova P.G., Rosati G.P., and Schumm C.E. (1996). Bond of reinforcing bars and prestressing tendons in hpfrcc matrices," *High performance fiber reinforced cement composites (hpfrscc).* RILEM, London: E & FN Spon.

Balaguru P.N., and Shah S.P. (1985). Alternative reinforcing materials for less developed countries. *International Journal of Engineering Research and Technology,* 3, 87-105.

Balázs G.L. (1993). Cracking analysis based on slip and bond stresses. *ACI materials journal,* 90, 340-348.

Banthia N., and Trottier J. (1994). Concrete reinforced with deformed steel fibers, part i: Bond-slip mechanisms. *ACI Materials Journal,* 91, 435-446.

Barenblatt G.I. (1959). The formation of equilibrium cracks during brittle fracture. General ideas and hypotheses. Axially-symmetric cracks. *Journal of Applied Mathematics and Mechanics,* 23, 622-636.

Barenblatt G.I. (1962). The mathematical theory of equilibrium cracks in brittle fracture. *In:* Dryden H.L., Von Kármán T., Kuerti G., Van Den Dungen F.H. & Howarth L. (eds.) *Advances in applied mechanics.* Elsevier.

Barragán B.E. (2002). *Failure and toughness of steel fiber reinforced concrete under tension and shear.* Ph.D., Universitat Politécnica de Catalunya.

Barros J., and Figueiras J. (1999a). Flexural behavior of sfrc: Testing and modeling. *Journal of Materials in Civil Engineering,* 11, 331-339.

Barros J.A.O. (1995). *Comportamento do betão reforçado com fibras, análise experimental e simulaçáo numérica.* Ph.D., University of Porto.

Barros J.A.O. (2008). Steel fiber reinforced self-compacting concrete - from the material characterization to the structural analysis. *In:* Barragán B., Pacios A. & Serna P., eds. 1st Spanish Congress on Self-Compacting Concrete, Valencia, Spain. 31–58.

Barros J.A.O. (2009). Nsm post-tensioned cfrp laminates for the flexural strengthening of rc beams. *9th International Symposium on Fiber Reinforced Polymer Reinforcement for Concrete Structures.* Sydney, Australia.

Barros J.A.O., Cunha V.M.C.F., Ribeiro A.F., and Antunes J.A.B. (2005). Post-cracking behaviour of steel fibre reinforced concrete. *Materials and Structures,* 38, 47-56.

Barros J.A.O., and Figueiras J.A. (1999b). Flexural behaviour of steel fibre reinforced concrete: Testing and modelling. *ASCE Materials in Civil Engineering Journal* 11, 331-339.

Barros J.A.O., and Fortes A.S. (2005). Flexural strengthening of concrete beams with cfrp laminates bonded into slits. *Cement and Concrete Composites,* 27, 471-480.

Barros J.A.O., and Foster S.J. (2018). An integrated approach for predicting the shear capacity of fibre reinforced concrete beams. *Engineering Structures,* 174, 346-357.

Barros J.A.O., Gettu R., and Barragan B.E. (2004a). Material nonlinear analysis of steel fibre reinforced concrete beams failing in shear. BEFIB2004, Varenna, Italy. 711-720.

Barros J.A.O., Gettu R., and Barragan B.E. (2004b). Material nonlinear analysis of steel fibre reinforced concrete beams failing in shear. BEFIB2004 conference, Varenna, Lake Como, Italy. 711–720.

Barros J.A.O., Moraes-Neto B.N., Melo G.S.S.A., and Frazão C.M.V. (2015a). Assessment of the effectiveness of steel fibre reinforcement for the punching resistance of flat slabs by experimental research and design approach. *Composites Part B: Engineering,* 78, 8-25.

Barros J.A.O., Pereira E., and Santos S. (2007). Lightweight panels of steel fiber-reinforced self-compacting concrete. *Journal of Materials in Civil Engineering,* 19, 295-304.

Barros J.A.O., Taheri M., and Salehian H. (2015b). A model to simulate the moment–rotation and crack width of frc members reinforced with longitudinal bars. *Engineering Structures,* 100, 43-56.

Barros J.A.O., Taheri M., Salehian H., and Mendes P.J.D. (2012). A design model for fibre reinforced concrete beams pre-stressed with steel and frp bars. *Composite Structures,* 94, 2494-2512.

Barros M.H.F.M., Martins R.A.F., and Ferreira C.C. (2001). Tension stiffening model with increasing damage for reinforced concrete. *Engineering Computations,* 18, 759-785.

Basto C.A.A., and Barros J.A.O. (2008). Numeric simulation of sections submitted to bending. Portugal: Department of Civil Engineering, University of Minho.

Bažant Z. (1984). Size effect in blunt fracture: Concrete, rock, metal. *Journal of Engineering Mechanics,* 110, 518-535.

Bažant Z.P. (1992). Fracture mechanics of concrete structures. *In:* Bažant Z.P., ed. The First International Conference on Fracture Mechanics of Concrete Structures (FraMCoS1), Colorado, USA. Elsevier Applied Science.

Bažant Z.P., and Oh B.H. (1983). Crack band theory for fracture of concrete. *Matériaux et Construction,* 16, 155-177.

Beeby A.W., and Scott R.H. (2004). Insights into the cracking and tension stiffening behaviour of reinforced concrete tension members revealed by computer modelling. *Magazine of Concrete Research,* 56, 179-190.

Benmokrane B., Chaallal O., and Masmoudi R. (1996). Flexural response of concrete beams reinforced with frp reinforcing bar. *ACI Structural Journal,* 91, 46-55.

Bentur A., Diamond S., and Mindess S. (1985). Cracking processes in steel fiber reinforced cement paste. *Cement and Concrete Research,* 15, 331-342.

Bentur A., and Mindess S. (2007). *Fibre reinforced cementitious composites,* Newyork, USA, Taylor & Francis.

Bianco V., Barros J.A., and Monti G. (2009). Bond model of nsm-frp strips in the context of the shear strengthening of rc beams. *Journal of Structural Engineering,* 135, 619-631.

Bischoff P.H. (2003). Tension stiffening and cracking of steel fiber-reinforced concrete. *Journal of Materials in Civil Engineering,* 15, 174-182.

Bischoff P.H. (2005). Reevaluation of deflection prediction for concrete beams reinforced with steel and fiber-reinforce polymer bars. *Journal of Structural Engineering,* 131, 752-767.

Borosnyói A., and Balázs G.L. (2005). Models for flexural cracking in concrete: The state of the art. *Structural Concrete,* 6, 53-62.

Brandt A.M. (1994). *Cement-based composites: Materials, mechanical properties and performance*, Taylor & Francis.

Branson D.E. (1965). Instantaneous and time-dependent deflections of simple and continuous reinforced concrete beams. *HPR.* Alabama Highway Department, Bureau of Public Roads, Ala.

Cairns J., and Plizzari G.A. (2003). Towards a harmonised european bond test. *Materials and Structures,* 36.

CAN/CSA-S806-02 (2007). Design and construction of building components with fibre-reinforced polymers. *In:* Association C.S. (ed.).

Casanova P., and Rossi P. (1997). Analysis and design of sfrc beams. *ACI Structural Journal,* 94, 595-624.

Casanova P., Rossi P., and Schaller l. (1997). Can steel fibers replace transverse reinforcements in reinforced concrete beams? *Materials Journal,* 94, 341-354.

CEB-FIP 1978 (1984). Design manual application of the ceb-fip model code 1978 for concrete structures.

CEB-FIP (1978). Model code for concrete structures. *In:* Recommendations C.-F.I. (ed.) Third edition ed. Paris, France: Comité Euro International du Béton (CEB/FIP).

CEB (1993). Ceb-fip model code 1990: Design code. London. Comité Euro-Internationale du Béton, UK: Thomas Telford.

Charkas H., Rasheedh A., and Melhem H. (2002). Simplified load-deflection calculation of frp strengthened rc beams based on a rigorous approach. *15th ASCE ENGINEERING MECHANICS CONFERENCE,*. New York, USA.

Chen W.F., and Atsuta T. (1976). *Theory of beam columns: In-plane behaviour and design,* New York, USA, McGraw-Hill.

Chiaia B., Fantilli A.P., and Vallini P. (2008). Evaluation of crack width in frc structures and application to tunnel linings. *Materials and Structures,* 42, 339-351.

Ciampi V., Eligehausen R., Bertero V.V., and Popov E.P. (1982). Analytical model for concrete anchorages of reinforcing bars under generalized excitations. University of Califonia, Berkeley, California: Earthquake Engineering Research Center.

CNR-DT 204 (2006). Guidelines for design, construction, and production control of fiber reinforced concrete structures. Rome: National Research Council of Italy.

Conforti A., Minelli F., and Plizzari G.A. (2013). Wide-shallow beams with and without steel fibres: A peculiar behaviour in shear and flexure. *Composites Part B: Engineering,* 51, 282-290.

Cosenza E., Manfredi G., and Realfonzo R. (1997). Behavior and modeling of bond of frp rebars to concrete. *Journal of composites for construction,* 1, 40-51.

Cruz J.S., and Barros J.A.O. (2004). Modeling of bond between near-surface mounted cfrp laminate strips and concrete. *Computers & Structures,* 82, 1513-1521.

Cunha V., Barros J., and Sena-Cruz J. (2010). Pullout behavior of steel fibers in self-compacting concrete. *Journal of Materials in Civil Engineering,* 22, 1-9.

Cunha V.M.C.F. (2010). *Steel fibre reinforced self-compacting concrete: From micro-mechanics to composite behaviour.* Ph.D., University of Minho.

Cunha V.M.C.F., Barros J.A.O., and Sena-Cruz J. (2008). Modelling the influence of age of steel fibre reinforced self-compacting concrete on its compressive behaviour. *Materials and Structures,* 41, 465-478.

Cunha V.M.C.F., Barros J.A.O., and Sena-Cruz J.M. (2009). Tensile behavior of steel fiber reinforced self-compacting concrete. *Fiber-Reinforced Self-Consolidating Concrete.*

Dancygier A.N., and Savir Z. (2006). Flexural behavior of hsfrc with low reinforcement ratios. *Engineering Structures,* 28, 1503-1512.

De Lorenzis L. (2002). *Strengthening of rc structures with near surface mounted frp rods.* PhD, University of Lecce.

Deluce J.R., Lee S.-C., and Vecchio F.J. (2014). Crack model for steel fiber-reinforced concrete members containing conventional reinforcement. *ACI structural journal,* 111, 93-102.

Deluce J.R., and Vecchio F.J. (2013). Cracking behavior of steel fiber-reinforced concrete members containing conventional reinforcement. *ACI STRUCTURAL JOURNAL,* 110, 481-490.

Desnerck P., De Schutter G., and Taerwe L. (2010). A local bond stress-slip model for reinforcing bars in self-compacting concrete. *In:* Oh B.H. (ed.) *Fracture Mechanics of Concrete and Concrete Structures - Assessment, Durability, Monitoring and Retrofitting of Concrete Structures* Seoul, Korea.

di Prisco M., Ferrara L., Colombo M., and Mauri M. (2004). On the identification of sfrc constitutive law in uniaxial tension. *In:* Di Prisco M., Felicetti R. & Plizzari G.A., eds. Sixth RILEM symposium on fibre-reinforced concretes (BEFIB 2004), Varenna. 827–836.

Diamond S., and Huang J. (2001). The itz in concrete – a different view based on image analysis and sem observations. *Cement and Concrete Composites,* 23, 179-188.

DIN 488, Germany Standard Ribbed steel bars (1986).

Dugdale D.S. (1960). Yielding of steel sheets containing slits. *Journal of the Mechanics and Physics of Solids,* 8, 100-104.

El-Mihilmy M.T., and Tedesco J.W. (2000). Deflection of concrete beams strengthened with fiber-reinforced polymer (frp) plates. *ACI Structural Journal,* September/October, 679-688.

Eligehausen R., Popov E.P., and Bertero V.V. (1982). Local bond stress-slip relationships of deformed bars under generalized excitations.

Eligehausen R., Popov E.P., and Bertero V.V. (1983). Local bond stress-slip relationships of deformed bars under generalized excitations. University of California, USA.

EN 1992-1-1 (2004). Eurocode 2: Design of concrete structures { part 1 { 1: General rules and rules for buildings. Brussels: European Committee for Standardization.

EN 14651 (2005). Test method for metallic fibered concrete - measuring the flexural tensile strength (limit of proportionality (lop), residual). *European Committee for Standardization.* Brussels.

Eurocode 2 (1992). Design of concrete structures part 1-1: General rules for buildings. Brussels, Belgium.: European Prestandard.

Fantilli A.P., Mihashi H., and Vallini P. (2009). Multiple cracking and strain hardening in fiber-reinforced concrete under uniaxial tension. *Cement and Concrete Research,* 39, 1217-1229.

Feenstra P.H., and Borst de R. (1995). A constitutive model for reinforced concrete. *Journal of Engineering Mechanics (ASCE),* 121, 587-595.

Fehling E., and Leutbecher T. (2007). Tensile behavior of ultra high performance concrete (uhpfc) reinforced with a combination of steel-fibers and rebars. *3rd international conference on structural mechanics and computations.* Cape Town, South Africa.

fib Bulletin 10 (2000). Bond of reinforcement in concrete, state-of-art report prepared. Lausanne, Switzerland.

fib Bulletin No. 40 (2007). Frp reinforcement in rc structures. CEB-FIP, Task Group 9.3

fib Model Code 2010 (2011). CEB and FIP - Final Draft.

Fischer G., and Li V.C. (2002). Influence of matrix of matrix ductility on tension-stiffening behavior of steel reinforced engineered cementitious composites (ecc). *ACI Structural Journal,,* 99, 104-111.

Georgiadi-Stefanidi K., Mistakidis E., Perdikaris P., and Papatheocharis T. (2011). Numerical simulation of the nonlinear bending response of fibre-reinforced cementitious matrix beams and comparison with experimental results. *Engineering Structures,* 33, 3579-3589.

Gilbert R.I. (2007). Tension stiffening in lightly reinforced concrete slabs. *Journal of Structural Engineering,* 133, 899-903.

Goto Y. (1971). Cracks formed in concrete around deformed tension bars. *ACI Journal Proceedings,* 68, 244-251.

Griffith A.A. (1921). The phenomena of rupture and flow in solids. *Philosophical Transactions of the Royal Society of Londo,* A, 163-198.

Groth P. (2000). *Fibre reinforced concrete - fracture mechanics methods applied on self-compacting concrete and energetically modified binders.* Ph.D. thesis, Lulea University of Technology of Sweden.

Grünewald S. (2004). *Performance-based design of self-compacting fibre reinforced concrete.* Ph.D., Delft University of Technology.

Guinea G.V., Planas J., and Elites M. (1993). Correlation between the softening and size effect curves. JCI International Workshop on Size Effect in Concrete Structures, Sendai, Japan. 211-223.

Hackman L., Farrell M., and Dunham O. (1992). Slurry infiltrated mat concrete - simcon. *ACI Concrete International,* 14, 53-56.

Harajli M., Hamad B., and Karam K. (2002). Bond-slip response of reinforcing bars embedded in plain and fiber concrete. *Journal of Materials in Civil Engineering,* 14, 503-511.

Harajli M.H., Hout M., and Jalkh W. (1995). Local bond stress-slip relationship of reinforcing embedded in fiber reinforced concrete. *ACI Material Journal* 92, 343-354.

Harajli M.H., and Mabsout M.E. (2002). Evaluation of bond strength of steel reinforcing bars in plain and fiber-reinforced concrete. *ACI Structural Journal,* 99, 509-517.

Häussler-Combe U., and Hartig J. (2008). Formulation and numerical implementation of a constitutive law for concrete with strain-based damage and plasticity. *International Journal of Non-Linear Mechanics,* 43, 399-415.

Hillerborg A. (1980). Analysis of fracture by means of the fictitious crack model, particularly for fibre reinforced concrete. *International Journal of Cement Composites and Lightweight Concrete,* 2, 177-184.

Hillerborg A., Modéer M., and Petersson P.E. (1976). Analysis of crack formation and crack growth in concrete by means of fracture mechanics and finite elements. *Cement and Concrete Research,* 6, 773-781.

Hordijk D. (1991). *Local approach to fatigue of concrete.* Ph.D., Delft University of Technology.

Hota S.R., and Naaman A.E. (1997). Bond-stress slip response of reinforcing bars embedded in frc matrices under monotonic and cyclic loading. *ACI Structural Journal,* 94, 525-537.

Hungspreug S. (1981). *Local bond between a steel bar and concrete under high intensity cyclic loading.* PhD, Cornell University, Ithaca, NY.

Irwin G. (1957). Analysis of stresses and strains near the end of a crack traversing a plate. *Journal of Applied Mechanics,* 24, 361-364.

Iyengar S.R.K.T., Raviraj S., and Ravikumar P. (1998). Analysis study of fictitious crack propagation in concrete beams using a bi-linear σ–w relation. *3th International conference on fracture mechanics of concrete and structure (FRAMCOS III).* Japan.

Jones P.A., Austin S.A., and Robins P.J. (2008). Predicting the flexural load–deflection response of steel fibre reinforced concrete from strain, crack-width, fibre pull-out and distribution data. *Materials and Structures,* 41, 449-463.

Jordon R.D., and Frank J.V. (2013). Cracking behavior of steel fiber-reinforced concrete members containing conventional reinforcement. *Structural Journal,* 110.

JSCE-SF4 (1984). Part iii - 2 methods of tests for steel fiber reinforced concrete. *Concrete Library of Japanese Society of Civil Engineers,* 3, 74.

Kang S.-T., Lee Y., Park Y.-D., and Kim J.-K. (2010). Tensile fracture properties of an ultra high performance fiber reinforced concrete (uhpfrc) with steel fiber. *Composite Structures,* 92, 61-71.

Kaufmann W., and Marti P. (1998). Structural concrete : Cracked membrane model. *Journal of Structural Engineering,* 124, 1467-1475.

Kitsutaka Y. (1997). Fracture parameters by polylinear tension-softening analysis. *Journal of Engineering Mechanics,* 123, 444-450.

Kooiman A.G. (2000). *Modelling steel fibre reinforced concrete for structural design.* Ph.D., Delft University of Technology.

Kurihara N., Kunieda M., Kamada T., Uchida Y., and Rokugo K. (2000). Tension softening diagrams and evaluation of properties of steel fiber reinforced concrete. *Engineering Fracture Mechanics,* 65, 235-245.

Lange-Kornbak D., and Karihaloo B.L. (1998). Design of fiber-reinforced dsp mixes for minimum brittleness. *Advanced Cement Based Materials,* 7, 89-101.

Lappa L. (2007). *High strength fibre reinforced concrete: Static and fatigue behavior in bending.* Ph.D. thesis, Delft University of Technology.

Lee J.Y., Kim T.Y., Kim T.J., Yi C.K., Park J.S., You Y.C., and Park Y.H. (2008). Interfacial bond strength of glass fiber reinforced polymer bars in high-strength concrete. *Composites Part B: Engineering,* 39, 258-270.

Lee S.-C., Cho J.-Y., and Vecchio F.J. (2013). Tension-stiffening model for steel fiber-reinforced concrete containing conventional reinforcement. *ACI Structural Journal,* July-August 2013.

Leung H.Y., and Balendran R.V. (2003). Flexural behaviour of concrete beams internally reinforced with gfrp rods and steel rebars. *Journal of Structural Survey* 21, 146-157.

Li V., and Leung C. (1992). Steady-state and multiple cracking of short random fiber composites. *Journal of Engineering Mechanics,* 118, 2246-2264.

Li V.C. (1992). Postcrack scaling relations for fiber reinforced cementitious composites. *Journal of Materials in Civil Engineering,* 4, 41-57.

Li V.C., and Stang H. (1997). Interface property characterization and strengthening mechanisms in fiber reinforced cement based composites. *Advanced Cement Based Materials,* 6, 1-20.

Li V.C., Stang H., and Krenchel H. (1993). Micromechanics of crack bridging in fibre-reinforced concrete. *Materials and Structures,* 26, 486-494.

Li Z. (2011). *Advanced concrete technology,* Hoboken, New Jersey, United States, JOHN WILEY & SONS, INC.

Lim T.Y., Paramasivam P., and Lee S.L. (1987). Analytical model for tensile behavior of steel-fiber concrete. *ACI Materials Journal,* 84, 286–551.

Lin X., and Zhang Y.X. (2014). Evaluation of bond stress-slip models for frp reinforcing bars in concrete. *Composite Structures,* 107, 131-141.

Löfgren I., Stang H., and Olesen J.F. (2008). The wst method, a fracture mechanics test method for frc. *Materials and Structures,* 41, 197-211.

Lok T.S., and Xiao J.R. (1998). Tensile behaviour and moment–curvature relationship of steel fibre reinforced concrete. *Magazine of Concrete Research,* 50, 359–368.

Lundgren K. (2005). Bond between ribbed bars and concrete. Part 1: Modified model. *Magazine of Concrete Research,* 57, 371–382.

Lundgren K., Robuschi S., and Zandi K. (2019). Methodology for testing rebar-concrete bond in specimens from decommissioned structures. *International Journal of Concrete Structures and Materials*.

Lutz L.A., and Gergely P. (1967). Mechanics of bond and slip of deformed bars in concrete. *ACI Journal,* 711–721.

Maidl B. (1995). *Steel fibre reinforced concrete*, Ernst & Sohn.

Malvar L.J., and Warren G.E. (1992). Bond of reinforcement under controlled confinement. *ACI Materials Journal,* 89, 593–601.

Markovic I. (2006). *High-performance hybrid-fibre concrete: Development and utilisation.* Ph.D., Delft University of Technology.

Markovic I., Walraven J.C., and van Mier J.G.M. (2004). Tensile response of hybrid-fibre concrete. *Proceedings of the 6th RILEM Symposium on fibre-reinforced concretes (BEFIB2004).* Varenna, Italy.

Martin H. (1973). On the interrelation among surface roughness, bond and bar stiffness in the reinforcement subject to short-term loading (in german). *Deutscher Ausschuss Stahlbeto,* 228, 1-50.

Masmoudi R., Theriault M., and Benmokrane B. (1998). Flexural behavior of concrete beams reinforced with deformed fiber reinforced plastic reinforcing rods. *Structural Journal,* 95.

Massicotte B. (2004). Implementing sfrc design into north american codes: Application to a building floor. *Invited paper to the International workshop on the advanced in fibre reinforced concrete.* Bergamo, Italy.

Mazaheripour H. (2015). *Structural behavior of hybrid gfrp and steel reinforced frc prestressed beams.* Ph.D., University of Minho.

Mazaheripour H., Barros J.A.O., and Sena-Cruz J. (2016a). Tension-stiffening model for frc reinforced by hybrid frp and steel bars. *Composites Part B: Engineering,* 88, 162-181.

Mazaheripour H., Barros J.A.O., Soltanzadeh F., and Sena-Cruz J. (2016b). Deflection and cracking behavior of sfrscc beams reinforced with hybrid prestressed gfrp and steel reinforcements. *Engineering Structures,* 125, 546-565.

Meda A., Minelli F., Plizzari G.A., and Riva P. (2005). Shear behaviour of steel fibre reinforced concrete beams. *Materials and Structures,* 38, 343-351.

Mirza S.M., and Houde J. (1979). Study of bond stress-slip relationships in reinforced concrete, . *ACI Journal,* 76, 19-46.

Moffatt K. (2001). *Analyse de dalles de pont avec armature réduite et béton de fibres metalliques.* MSc, École Polytechnique de Montréal, Montréal,.

Montaignac R., Massicotte B., and Charron J.-P. (2012). Design of sfrc structural elements: Flexural behaviour prediction. *Materials and Structures,* 45, 623-636.

Moraes-Neto B.N., Barros J.A.O., and Melo G.S.S.A. (2013). A model for the prediction of the punching resistance of steel fibre reinforced concrete slabs centrically loaded. *Construction and Building Materials,* 46, 211-223.

Mousa S., Mohamed H.M., Benmokrane B., and Ferrier E. (2018). Flexural behavior of full-scale circular concrete members reinforced with basalt frp bars and spirals: Tests and theoretical studies. *Composite Structures,* 203, 217-232.

Murray A., Gilbert R.I., and Castel A. (2018). Spacing of cracks in reinforced concrete based on a variable transfer length model. *Journal of Structural Engineering,* 144, 04018090.

Naaman A. (1992). Sifcon: Tailored properties for structural performance. *In:* Reinhardt H.W. & Naaman A. (eds.) *Performance fiber reinforced cementitious composites.* London: E & FN Spon.

Naaman A., Namur G., Alwan J., and Najm H. (1991). Fiber pullout and bond slip. I: Analytical study. *Journal of Structural Engineering,* 117, 2769-2790.

Naaman A.E. (2000). Fiber reinforcement for concrete: Looking back, looking ahead. *In:* Rossi P. & Chanvillard G., eds. Proceedings of fifth RILEM Symposium on Fiber Reinforced Concretes (BEFIB2000). France: Rilem Publications, S.A.R.L., 65-86.

Naaman A.E. (2003). *Strain hardening and deflection hardening fiber reinforced cement composites*, RILEM Publications.

Naaman A.E. (2008). High performance fiber reinforced cement composites *In:* Shi C. & Mo Y.L. (eds.) *High-performance construction materials - science and applications.* World Scientific Publishing Co. Pte. Ltd.

Naaman A.E., and Najm H. (1991). Bond-slip mechanisms of steel fibers in concrete. *ACI Materials Journal,* 88, 135-145.

Naaman A.E., and Reinhard H.W. (2005). Proposed classification of hpfrc composites based on their tensile response. *In:* Banthia N., Uomoto A.B.T. & Shah S., eds. Performance, Innovations and Structural Implications (ConMat'05) and Mindess Symposium, University of British Columbia, Vancouver, Canada.

Naaman A.E., and Reinhardt H.W. (2006). Proposed classification of hpfrc composites based on their tensile response. *Materials and Structures,* 39, 547-555.

Naaman A.E., and Shah S.P. (1976). Pull-out mechanism in steel fiber-reinforced concrete. *ACI Journal, Structural Division, ASCE,* 102, 1537-1548.

Nanakorn P., and Horii H. (1996). Back analysis of tension-softening relationship of concrete. *Doboku Gakkai Ronbunshu,* 1996, 265-275.

Nilson A.H. (1968). Nonlinear analysis of reinforced concrete by the finite element method. *ACI Journal,* 65, 757-766.

Noghabai K. (2000). Behavior of tie elements of plain and fibrous concrete and varying cross sections. *ACI Structural Journal,* 97, 277-285.

Nordin H., and Täljsten B. (2006). Concrete beams strengthened with prestressed near surface mounted cfrp. *Journal of Composites for Construction,* 10, 60-68.

Okamura H. (1997). Ferguson lecture for 1996: Self-compacting high-performance concrete. *Concrete International Journal, ACI,* 19, 50-54.

Okamura H., and Ouchi M. (2003). Self-compacting concrete. *Journal of Advanced Concrete Technology,* 1, 5-15.

Olesen J.F. (2001). Cracks in reinforced frc beams subject to bending and axial load. *In:* Borst R.d., Mazars J., Pijaudier-Cabot G. & Van Mier J.G.M., eds. Fracture Mechanics of Concrete Structures, Cachanm France. Swats & Zaltlinger, Usse.

Oliveira F.L. (2010). *Design-oriented constitutive model for steel fibre reinforced concrete.* Ph.D., Universitat Politécnica de Catalunya.

Oliveira Júnior L., Lima Araújo D., Dias Toledo Filho R., Moraes Rego Fairbairn E., and Souza de Andrade M. (2016). Tension stiffening of steel-fiber-reinforced concrete *Acta Scientiarum. Technology,* 38, 456-463

Ortiz Navas F., Navarro-Gregori J., Leiva Herdocia G., Serna P., and Cuenca E. (2018). An experimental study on the shear behaviour of reinforced concrete beams with macro-synthetic fibres. *Construction and Building Materials,* 169, 888-899.

Park R., and Paulay T. (1975). *Reinforced concrete structures,* New York, USA, Wiley.

Pereira E.B., Fischer G., and Barros J.A.O. (2012). Direct assessment of tensile stress-crack opening behavior of strain hardening cementitious composites (shcc). *Cement and Concrete Research,* 42, 834-846.

Pfeiffer U., and Quast U. (2003). Nichtlineares berechnen stabförmiger bauteile. *Beton- und Stahlbetonbau,* 98, 529–538.

Pimentel M., Brüwhiler E., and Figueiras J. (2010). Extended cracked membrane model for the analysis of rc panels. *Engineering Structures,* 32, 1964-1975.

Piyasena R. (2002). *Crack spacing, crack width and tension stiffening effect in reinfroced concrete beams andone-way slabs.* Ph.D., Griffith University.

Prakhya G.K.V., and Morley C.T. (1990). Tension-stiffening and moment-curvature relations of reinforced concrete elements. *ACI Structural Journal* 87, 597-605.

Raphael J.M. (1984). Tensile strength. *Concrete International,* 81, 158–165.

Rashid Y.R. (1968). Ultimate strength analysis of prestressed concrete pressure vessels. *Nuclear Engineering and Design,* 7, 334-344.

Redaelli D., and Muttoni A. (2007). Tensile behaviour of reinforced ultra-high performance fiber reinforced concrete element. *fib symposium: concrete structures: stimulators of development.* . Croatia, Dubrovnik.

Rehm G. (1961). Ueber die grundlagen des verbundes zwischen stahl und beton (about the fundaments of bond between steel and concrete). *Deutscher Ausschuss fUr Stahlbeton.* Berlin.

Ribeiro F., Sena-Cruz J., Branco F.G., and Júlio E. (2018). Hybrid effect and pseudo-ductile behaviour of unidirectional interlayer hybrid frp composites for civil engineering applications. *Construction and Building Materials,* 171, 871-890.

RILEM TC 148-SSC (2000). Strain softening of concrete-test methods for compressive softening, test method for measurement of the strain-softening behaviour of concrete under uniaxial compression. *Materials and Structures,* 33, 347-351.

RILEM TC 162-TDF (2001). Test and desgin methods for steel fibre reinforced concrete, uniaxial tension test for steel fibre reinforced concrete. *Materials and Structures,* 34, 3-6.

RILEM TC 162-TDF (2002). Design of steel fibre reinforced concrete using the σ-w method: Principles and applications. *Materials and Structures,* 35, 262-278.

RILEM TC 162-TDF (2003). Test and design methods for steel fibre reinforced concrete, σ-ε design method - final recommendation. *Materials and Structures,* 36, 560-567.

RILEM TC 188-CSC (2006). Final report of rilem tc 188-csc: Casting of self-compacting concrete. *Materials and Structures,* 39, 937-954.

Romualdi J.P., and Batson G.B. (1963). Mechanics of crack arrest in concrete with closely spaced reinforcement. *Journal of the Engineering Mechanics Division, EM3. Proceedings of the American Society of Civil Engineers,* 89, 147-168.

Romualdi J.P., and Mandel J.A. (1964). Tensile strength of concrete affected by uniformly distributed and closely spaced short lengths of wire reinforcement. *Journal Proceedings,* 61.

Rostásy F.S., and Hartwich K. (1988). Bond of deformed reinforcing bar embedded in steel fiber reinforced concrete. *International Journal of Cement Composites and Lightweight Concrete,* 10, 151-158.

Salehian H. (2015). *Evaluation of the performance of steel fibre reinforced self-compacting concrete in elevated slab systems; from the material to the structure.* Ph.D., University of Minho.

Salehian H., and Barros J.A.O. (2015). Assessment of the performance of steel fibre reinforced self-compacting concrete in elevated slabs. *Cement and Concrete Composites,* 55, 268-280.

Salehian H., and Barros J.A.O. (2017). Prediction of the load carrying capacity of elevated steel fibre reinforced concrete slabs. *Composite Structures,* 170, 169-191.

Saliger R. (1936). High-grade steel in reinforced concrete. *Second Congress of the International Association for Bridge and Structural Engineering (IABSE).* Berlin, Germany

Santos P.F.S., Barros J.A.O., and Lourenço L.A.P. (2008). Steel fibres for the shear resistance of high strength concrete beams. *7th RILEM International Symposium on Fibre Reinforced Concrete Design and Applications (BEFIB 2008)* [Online]. [Accessed 17-19 September].

Schiessl P., and Raupach M. (1997). Laboratory studies and calculations on the influence of crack width on chloride-induced corrosion of steel in concrete. *ACI Materials Journal,* 97.

Scrivener K.L., and Kirkpatrick R.J. (2008). Innovation in use and research on cementitious material. *Cement and Concrete Research,* 38, 128-136.

Shah S.P., and Rangan B.V. (1971). Fibre reinforced concrete properties. *ACI Journal Proceedings,* 68, 126-134.

Shah S.P., Swartz S.E., and Ouyang C. (1995). *Fracture mechanics of concrete: Applications of fracture mechanics to concrete, rock and other quasi-brittle materials,* New York, USA, John Wiley & Sons Inc.

Soltanzadeh F., Behbahani A.E., Mazaheripour H., and Barros J.A.O. (2016a). Shear resistance of sfrscc short-span beams without transversal reinforcements. *Composite Structures,* 139, 42-61.

Soltanzadeh F., Edalat-Behbahani A., Barros J.A.O., and Mazaheripour H. (2016b). Effect of fiber dosage and prestress level on shear behavior of hybrid gfrp-steel reinforced concrete i-shape beams without stirrups. *Composites Part B: Engineering,* 102, 57-77.

Soranakom C. (2008). *Multi scale modeling of fibre and fabric reinforced cement based composites.* Ph.D., Arizona State University.

Soranakom C., and Mobasher B. (2008). Correlation of tensile and flexural responses of strain softening and strain hardening cement composites. *Cement and Concrete Composites,* 30, 465-477.

Stähli P., Custer R., and van Mier J.M. (2008). On flow properties, fibre distribution, fibre orientation and flexural behaviour of frc. *Materials and Structures,* 41, 189-196.

Stang H., and Aarre T. (1992). Evaluation of crack width in frc with conventional reinforcement. *Cement and Concrete Composites,* 14, 143-154.

Stang H., and Olesen J.F. (1998). On interpretation of bending frc-materials *Fracture Mechanics of Concrete Structures,* Proceedings FRAMCOS-3 (D-79104 Freiburg, Germany) 511-520).

Strack M. (2008). Modelling of crack opening of sfrc under tension and bending. *In:* Gettu R., ed. 7th International Rilem symposium on FRC: design and application (BEFIB 2008). RILEM Publications SARL, 323–332.

Stroeven P., and Hu J. (2006). Effectiveness near boundaries of fibre reinforcement in concrete. *Materials and Structures,* 39, 1001-1013.

Susetyo J., Gauvreau P., and Vecchio F.J. (2011). Effectiveness of steel fiber as minimum shear reinforcement. *Structural Journal,* 108.

Taerwe L., and Gysel A. (1996). Influence of steel fibers on design stress-strain curve for high-strength concrete. *Journal of Engineering Mechanics,* 122, 695-704.

Taheri M., and Barros J.A.O. (2012). An analytical model to simulate tension stiffening mechanism in moment-rotation response of frc flexural members with tensile longitudinal reinforcement. Guimaraes, Portugal: University of Minho.

Taheri M., Barros J.A.O., and Salehian H. (2011). A design model for strain-softening and strain-hardening fiber reinforced elements reinforced longitudinally with steel and frp bars. *Composites Part B: Engineering,* 42, 1630-1640.

Taheri M., Barros J.A.O., and Salehian H. (2012). Parametric study of the use of strain softening/hardening frc for rc elements failing in bending. *Journal of Materials in Civil Engineering* 24, 259-274.

Tan K.-H., Paramasivam P., and Tan K.-C. (1995). Cracking characteristics of reinforced steel fiber concrete beams under short- and long-term loadings. *Advanced Cement Based Materials,* 2, 127-137.

Tepfers R.A. (1973). *Theory of bond applied to overlapped tensile reinforcement splices for deformed bars.* PhD, Chalmers University of Technology.

Tian Y., and Yuan Y. (2007). Deflection prediction of concrete beams reinforced with gfrp and steel rods. *The 8th International Symposium on Fiber Reinforced Polymer Reinforcement for Concrete Structures (FRPRCS-8).* Patras, Greece.

Tiejiong L., and Theodore L.K. (2019). Numerical assessment of the nonlinear behavior of continuous prestressed steel-concrete composite beams. *Engineering Structures,* 190, 116-127.

Toutanji H.A., and Saafi M. (2009). Flexural behavior of concrete beams reinforced with glass fiber-reinforced polymer (gfrp) bars. *ACI Structural Journal,* 97, 712-719.

UNI 11188 (2004). Design, production and control of steel fibre reinforced structural elements. *Italian Board of Standardization.* Milan, Italy.

Van Mier J.G.M. (1997). *Fracture processes of concrete,* CRC Press.

Van Mier J.G.M., and Van Vliet M.R.A. (2002). Uniaxial tension test for the determination of fracture parameters of concrete: State of the art. *Engineering Fracture Mechanics,* 69, 235-247.

Vandewalle, Nemegeer, Balazs, Barr, Barros, Bartos, Banthia, Criswell, Denarié, di Prisco, Falkner, Gettu, Gopalaratnam, Groth, Häusler, Kooiman, Kovler, Massicotte, Mindess, Reinhardt, Rossi, Schaerlaekens, Schumacher, Schnütgen, Shah, Skarendahl, Stang, Stroeven, Swamy, Tatnall, Teutsch, and Walraven (2003). Rilem tc 162-tdf: Test and design methods for steel fibre reinforced concrete, σ-ε design method - final recommendation. *Materials and Structures,* 36, 560-567.

Vandewalle L. (2000). Cracking behaviour of concrete beams reinforced with a combination of ordinary reinforcement and steel fibers. *Materials and Structures,* 33, 164-170.

Ventura-Gouveia A., Barros J.A.O., and Azevedo A.F.M. (2011). Crack constitutive model for the prediction of punching failure modes of fiber reinforced concrete laminar structures. *Computers & Concrete* 8, 735-755.

Vipulanandan C., and Paul E. (1990). Performance of epoxy and polyester polymer concrete. *ACI Materials Journal,* 87, 241-251.

Wang H., and Belarbi A. (2013). Flexural durability of frp bars embedded in fiber-reinforced-concrete. *Construction and Building Materials,* 44, 541-550.

Weerheijm J. (2013). *Understanding the tensile properties of concrete,* Woodhead Publishing Limited.

Wei S., Mandel J.A., and Said S. (1986). Study of the interface strength in steel fiber-reinforced cement-based composites. *Journal Proceedings,* 83.

Xue W., Tan Y., and Zeng L. (2010). Flexural response predictions of reinforced concrete beams strengthened with prestressed cfrp plates. *Composite Structures,* 92, 612-622.

Yang I.H., Joh C., and Kim B.-S. (2010). Structural behavior of ultra high performance concrete beams subjected to bending. *Engineering Structures,* 32, 3478-3487.

Yang Y., Walraven J., and den Uijl J. (2009). Combined effect of fibers and steel rebars in high performance concrete. 54, 205–224.

Zhang D., and Wu K. (1999). Fracture process zone of notched three-point-bending concrete beams. *Cement and Concrete Research,* 29, 1887-1892.

Appendix A

Crack evolution in the SFRSCC beams reinforced by a steel bar

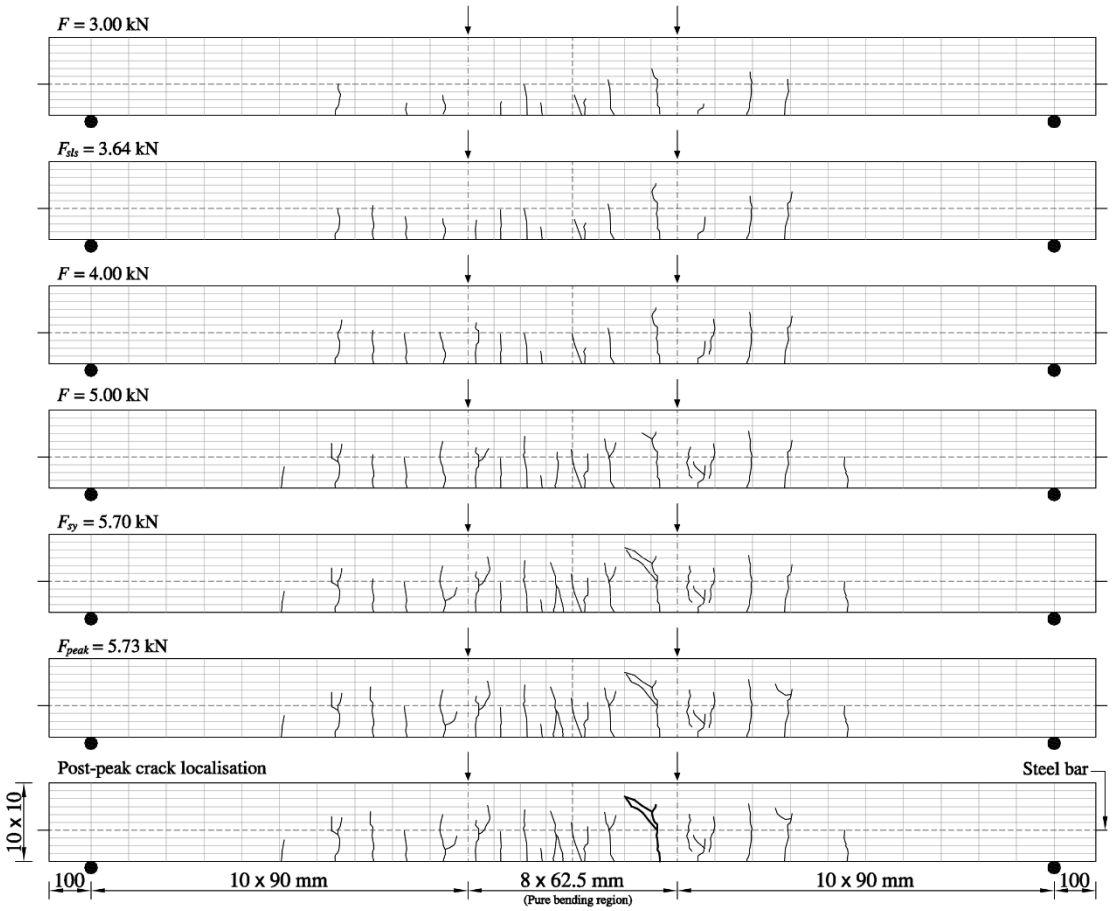

Figure A.1: Crack evolution in SR/FRC1545-1

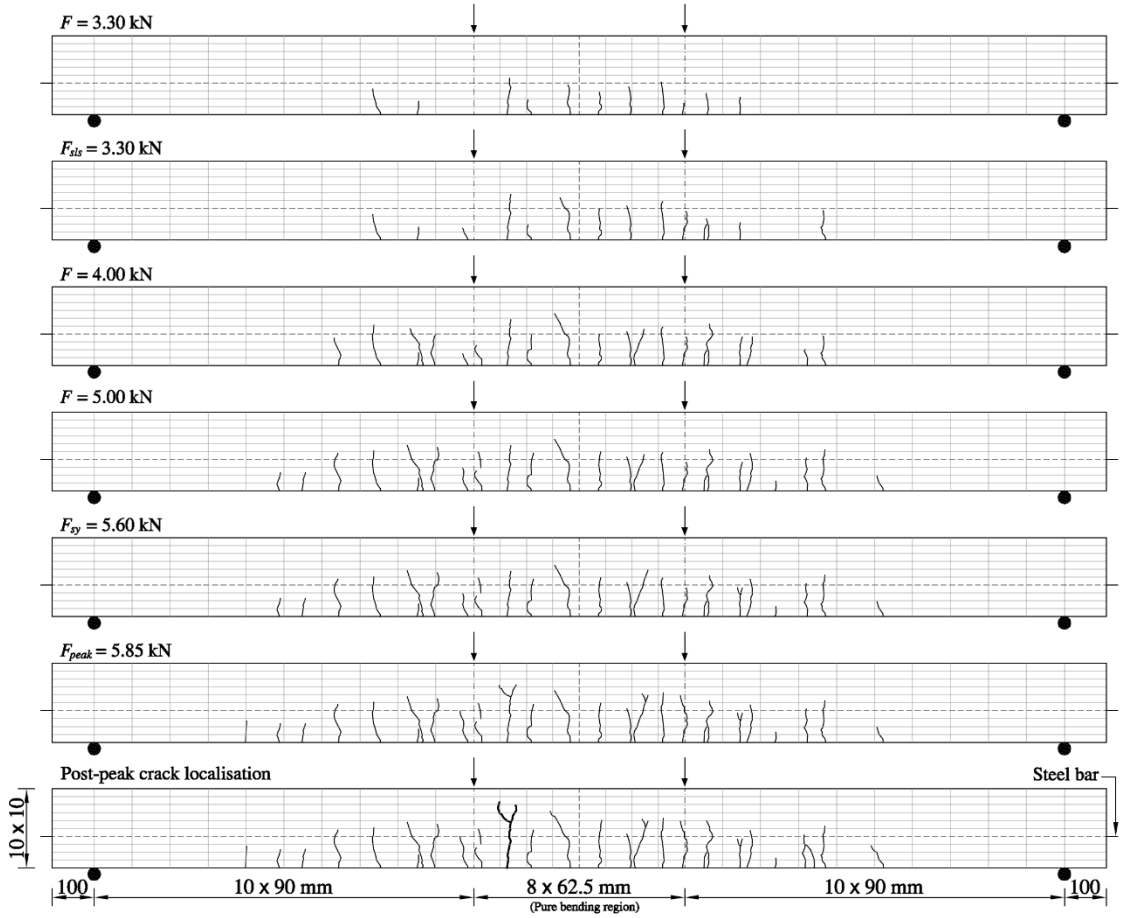

Figure A.2: Crack evolution in SR/FRC1545-2

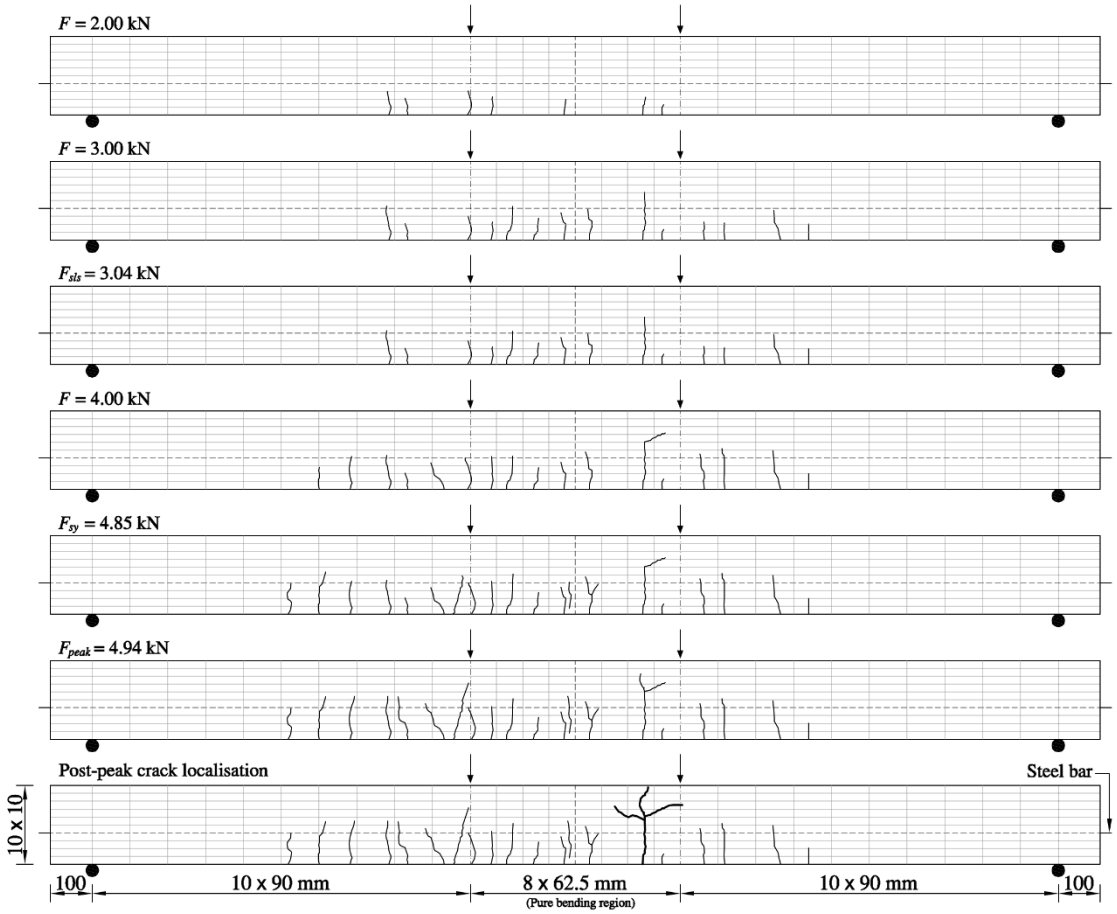

Figure A.3: Crack evolution in SR/FRC1545-3

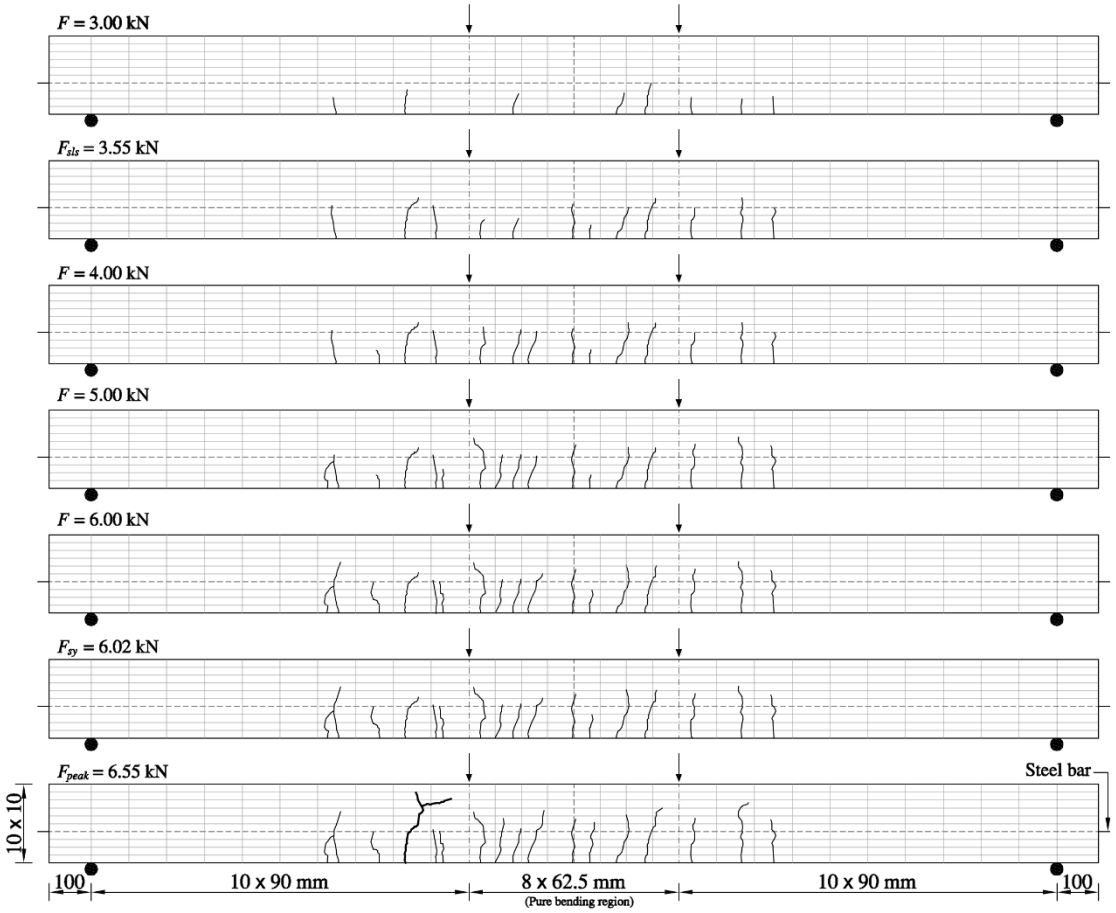

Figure A.4: Crack evolution in SR/FRC2560-1

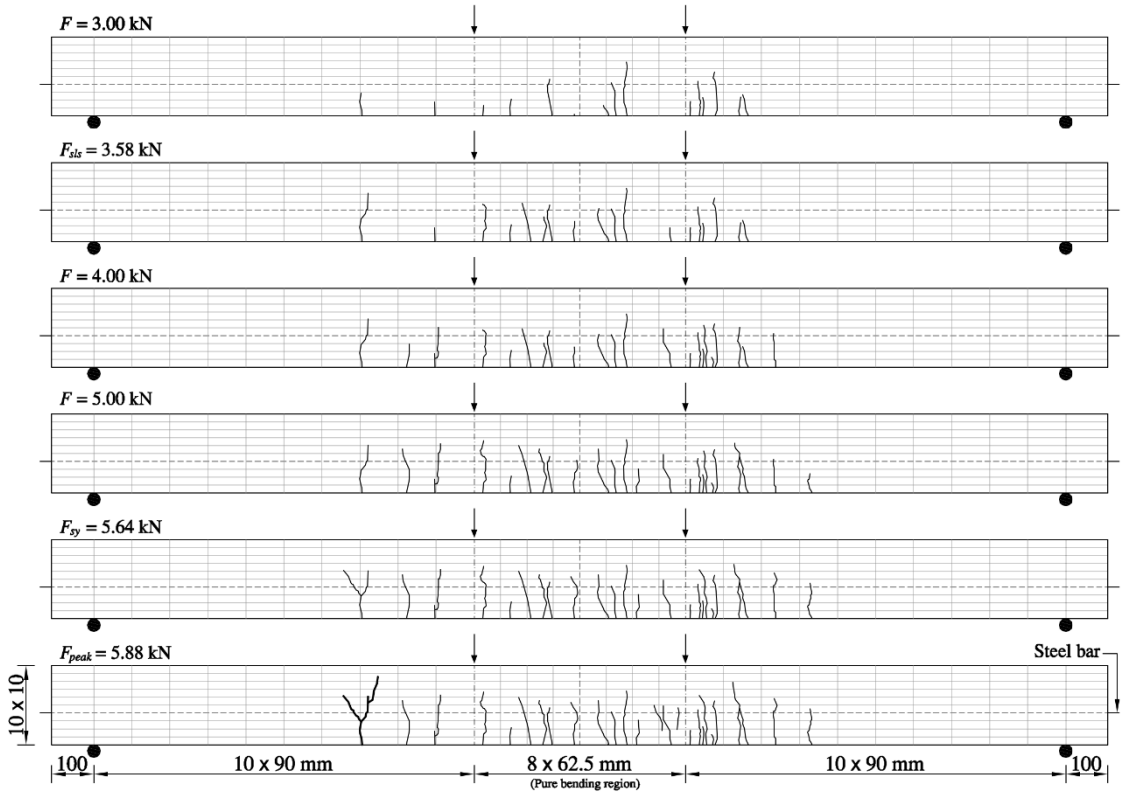

Figure A.5: Crack evolution in SR/FRC2560-2

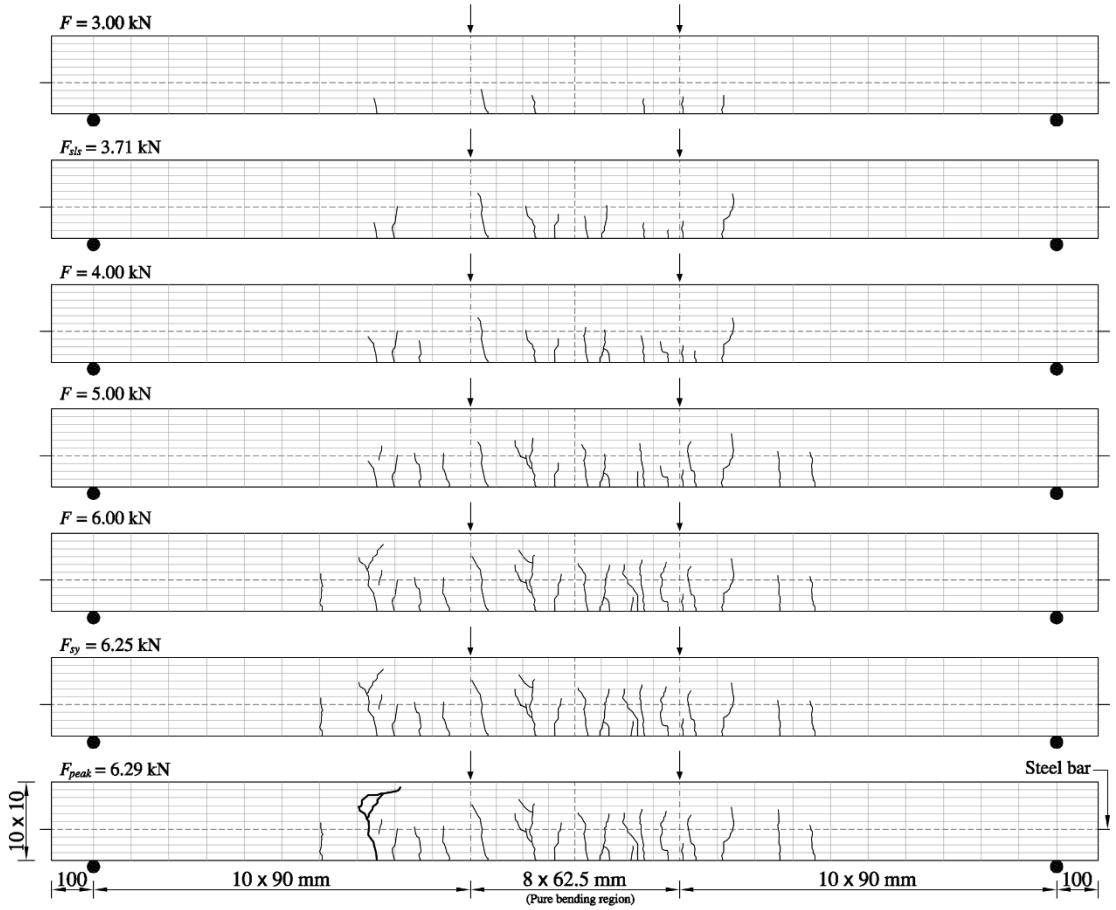

Figure A.6: Crack evolution in SR/FRC2560-3

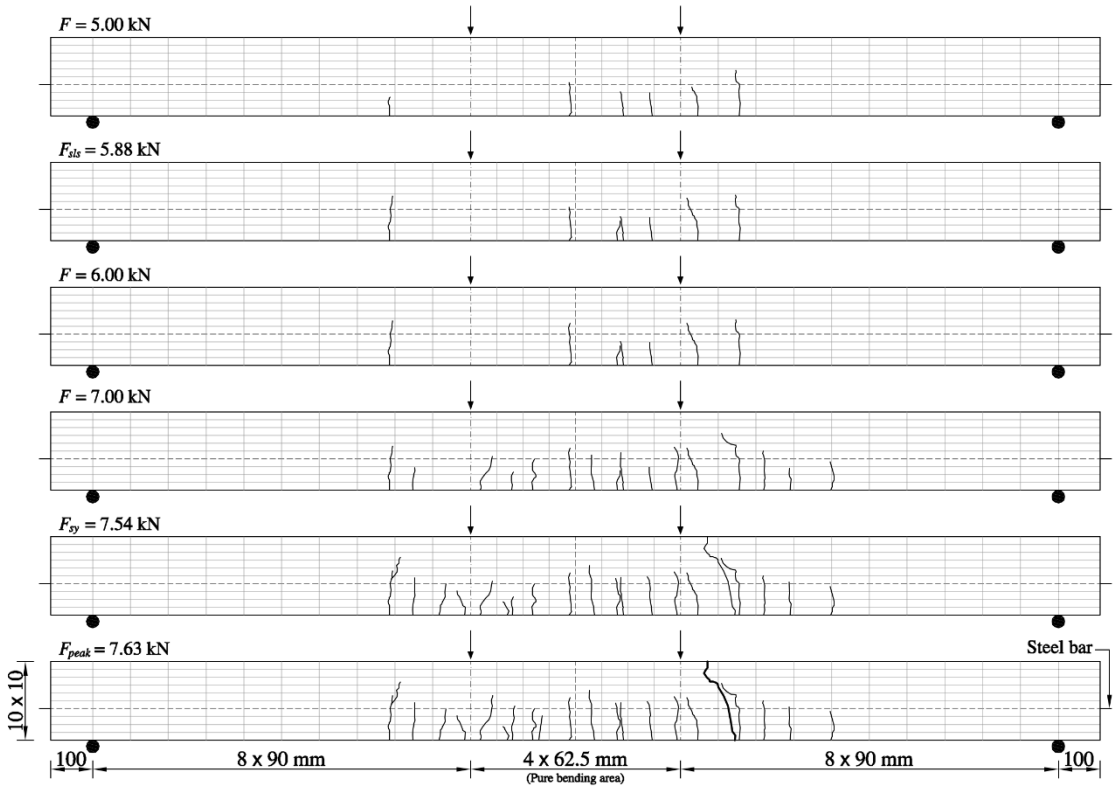

Figure A.7: Crack evolution in SR/FRC4590-1

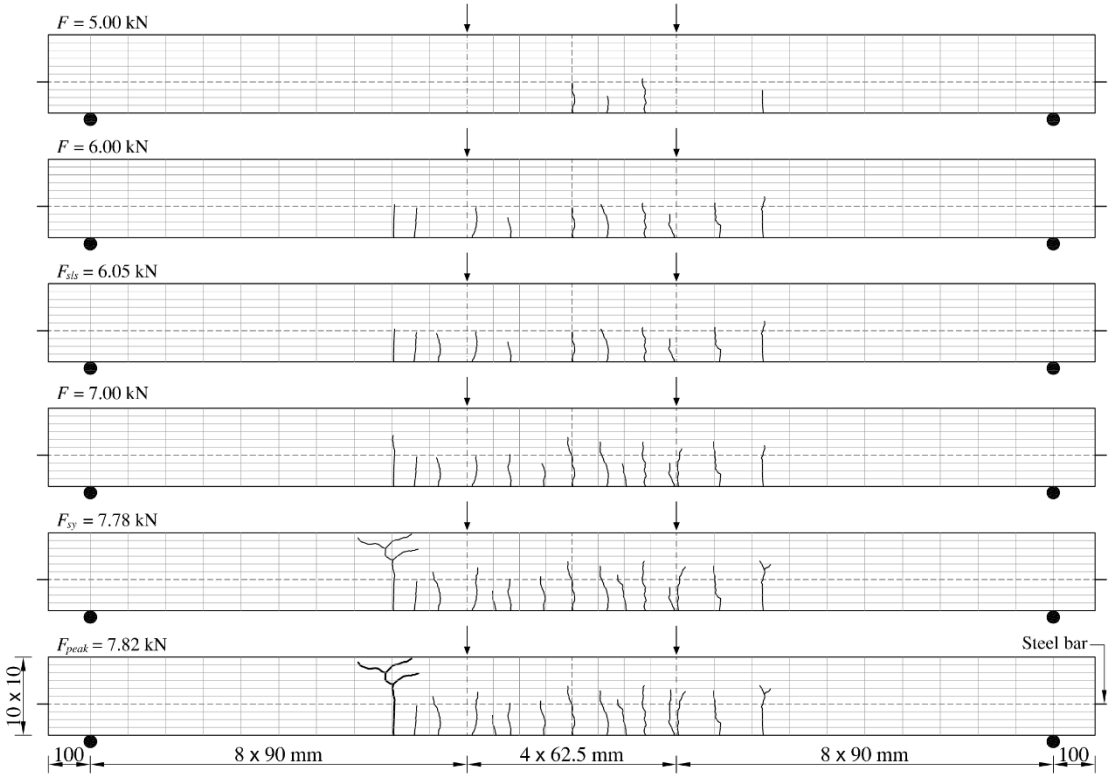

Figure A.8: Crack evolution in SR/FRC4590-2

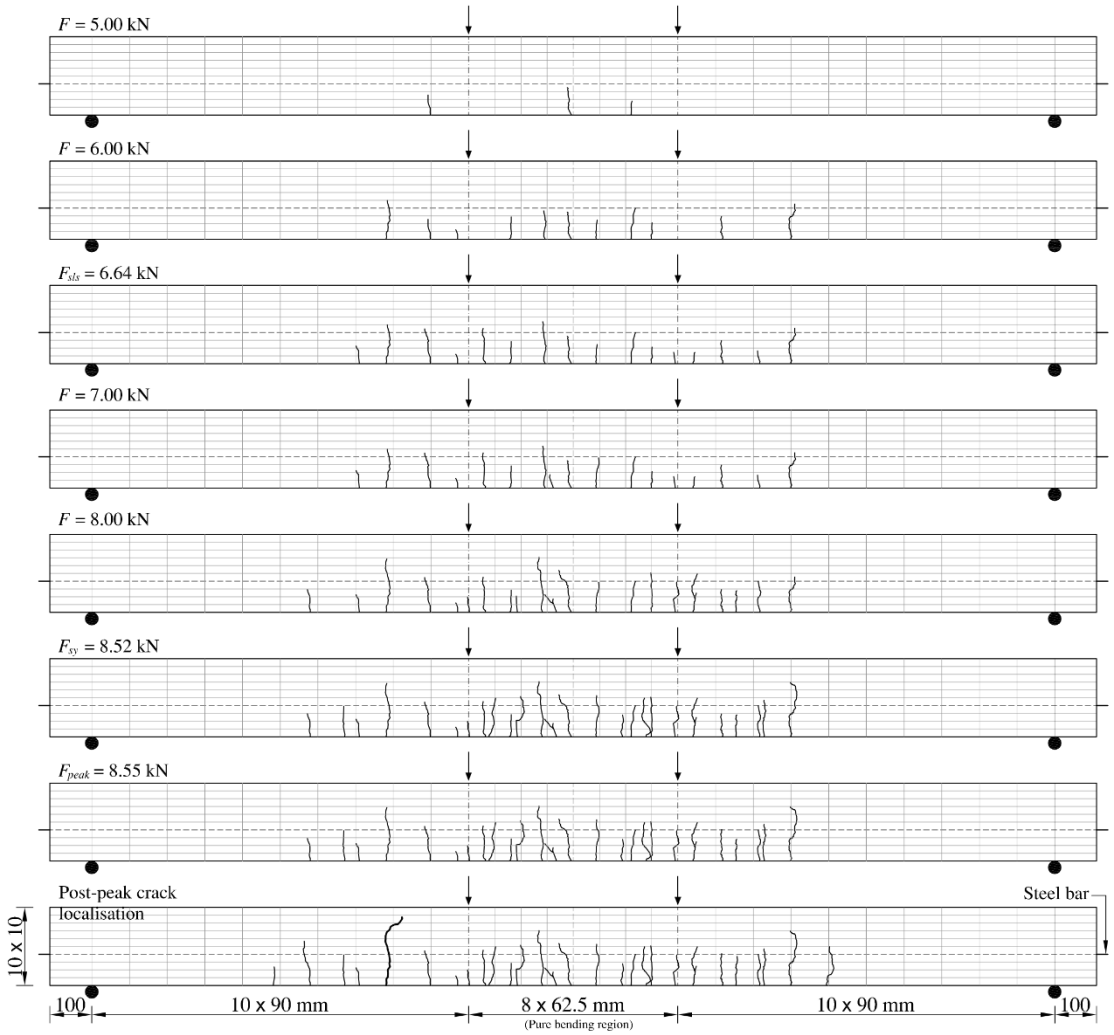

Figure A.9: Crack evolution in SR/FRC4590-3

Appendix B

Crack evolution in tested SFRSCC beams reinforced by steel and GFRP bars

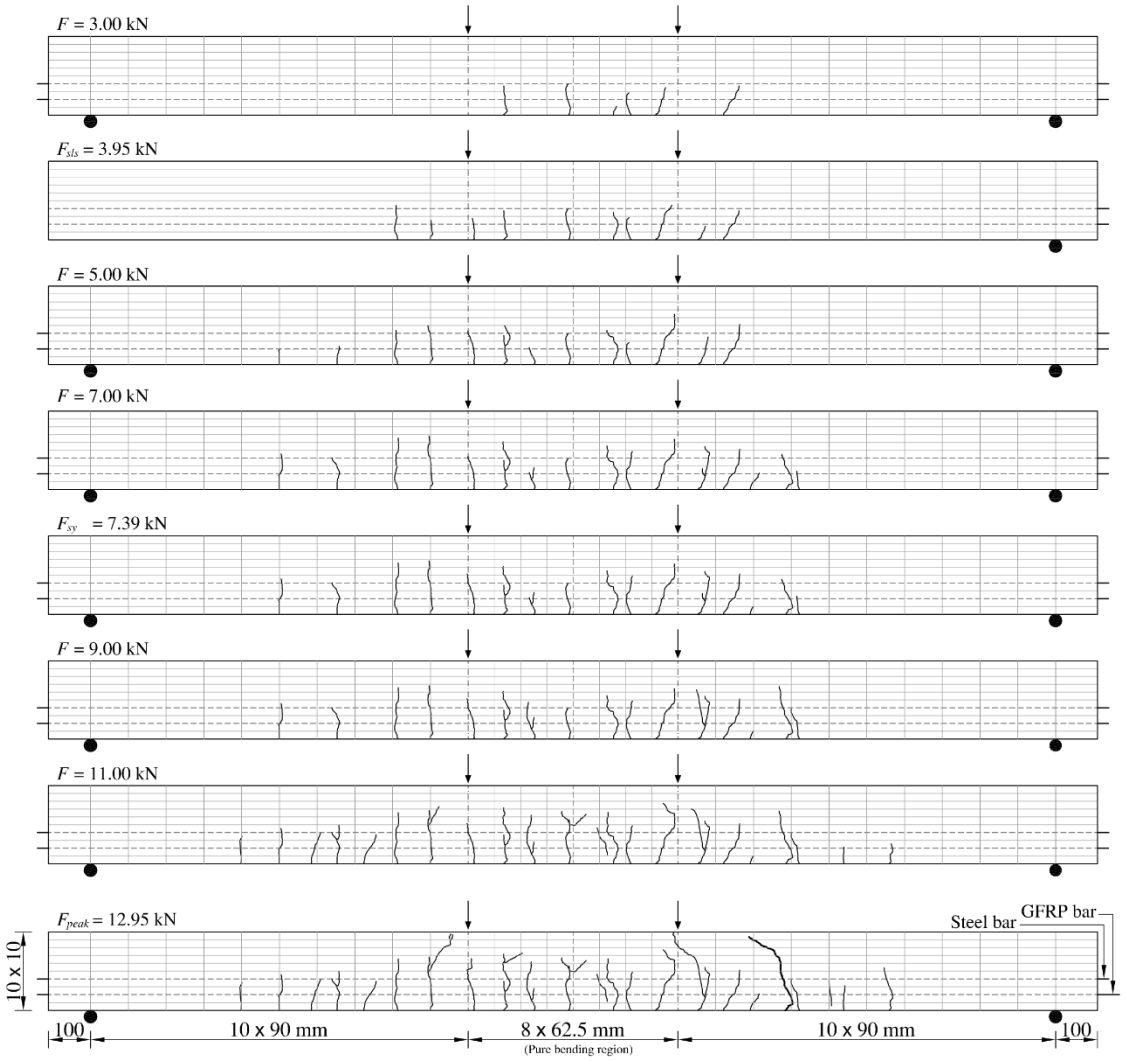

Figure B.1: Crack evolution in SGR/FRC1545-1

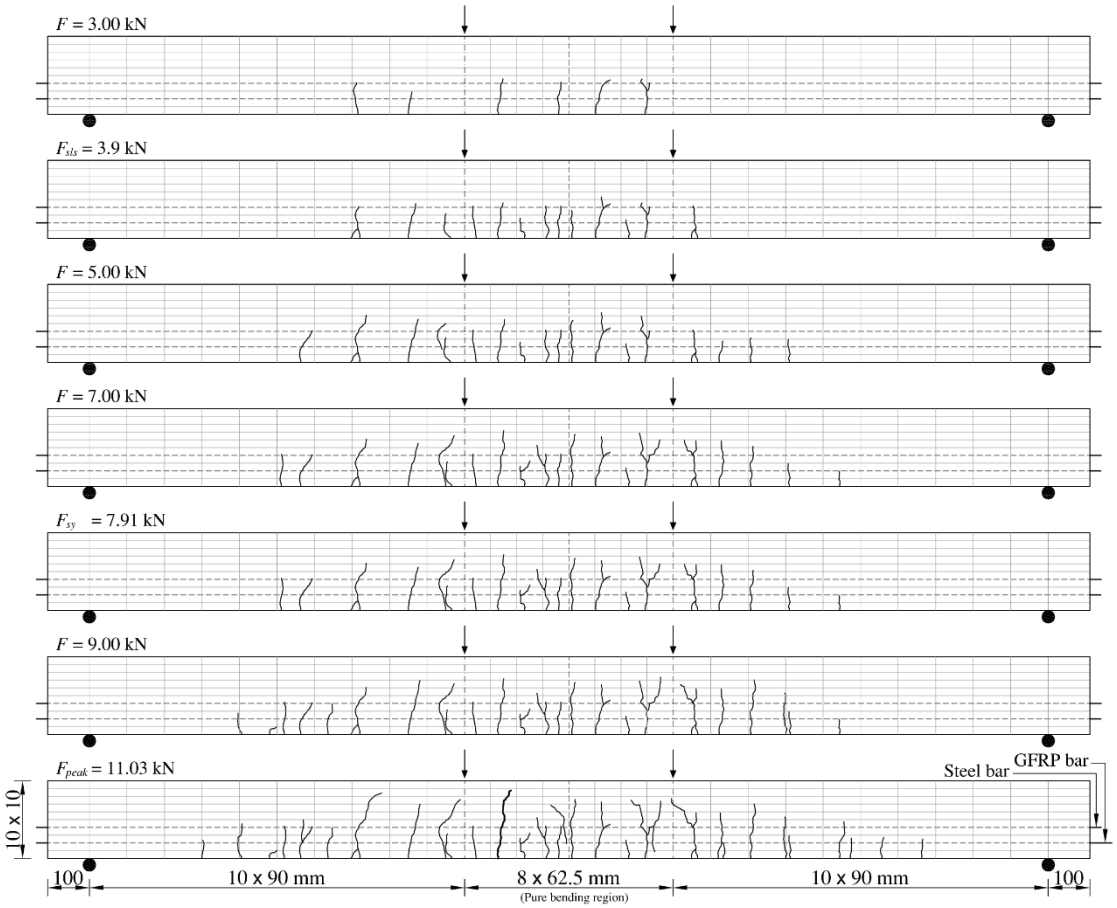

Figure B.2: Crack evolution in SGR/FRC1545-2

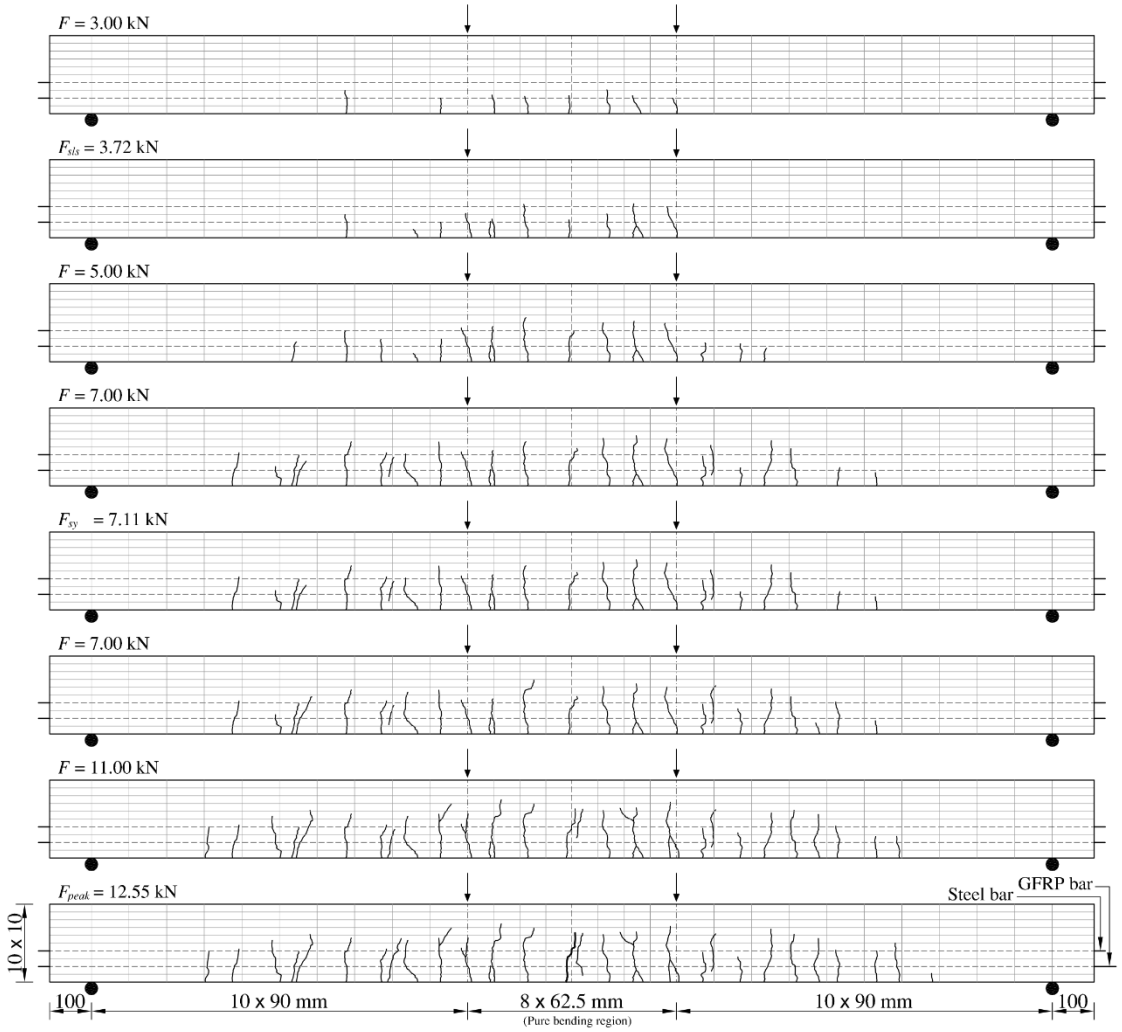

Figure B.3: Crack evolution in SGR/FRC1545-3

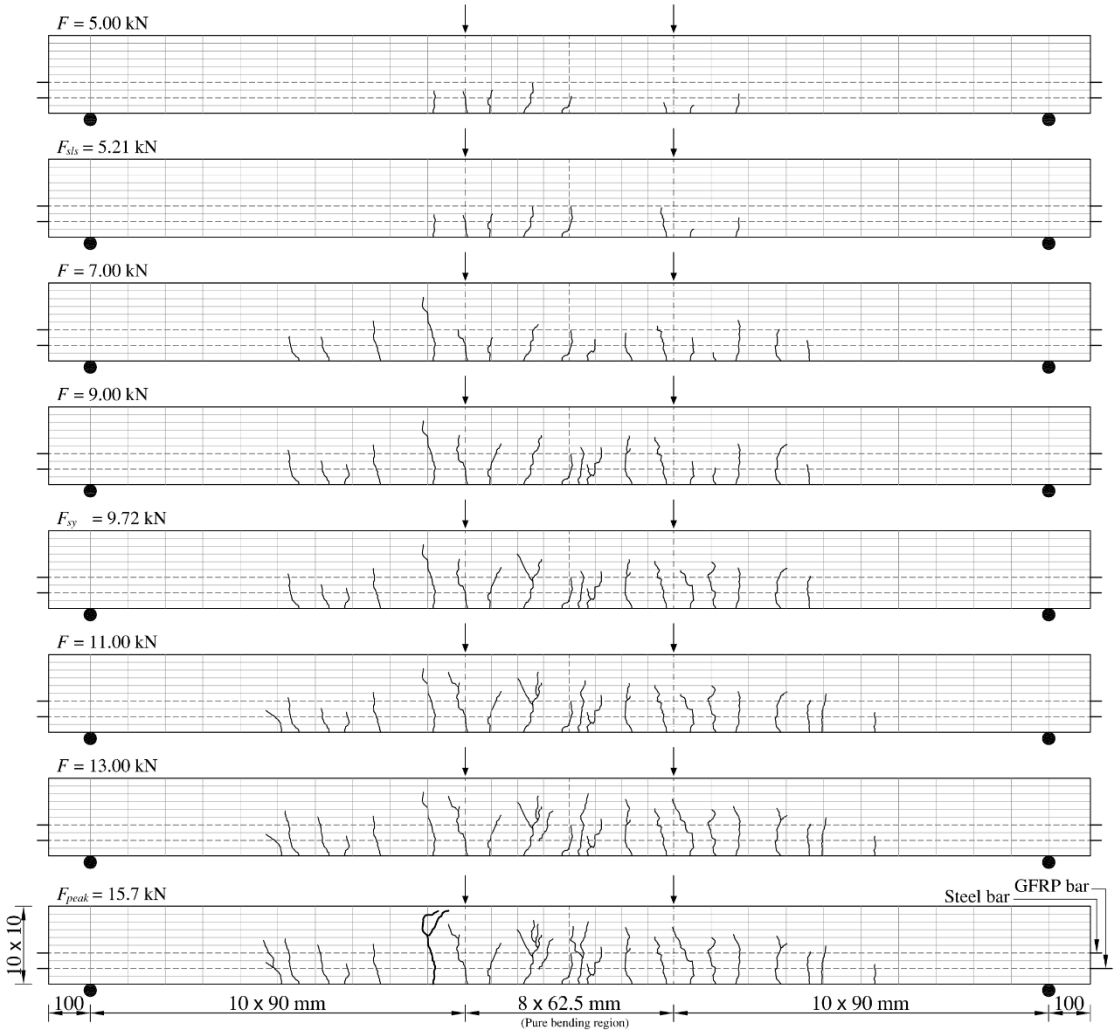

Figure B.4: Crack evolution in SGR/FRC2560-1

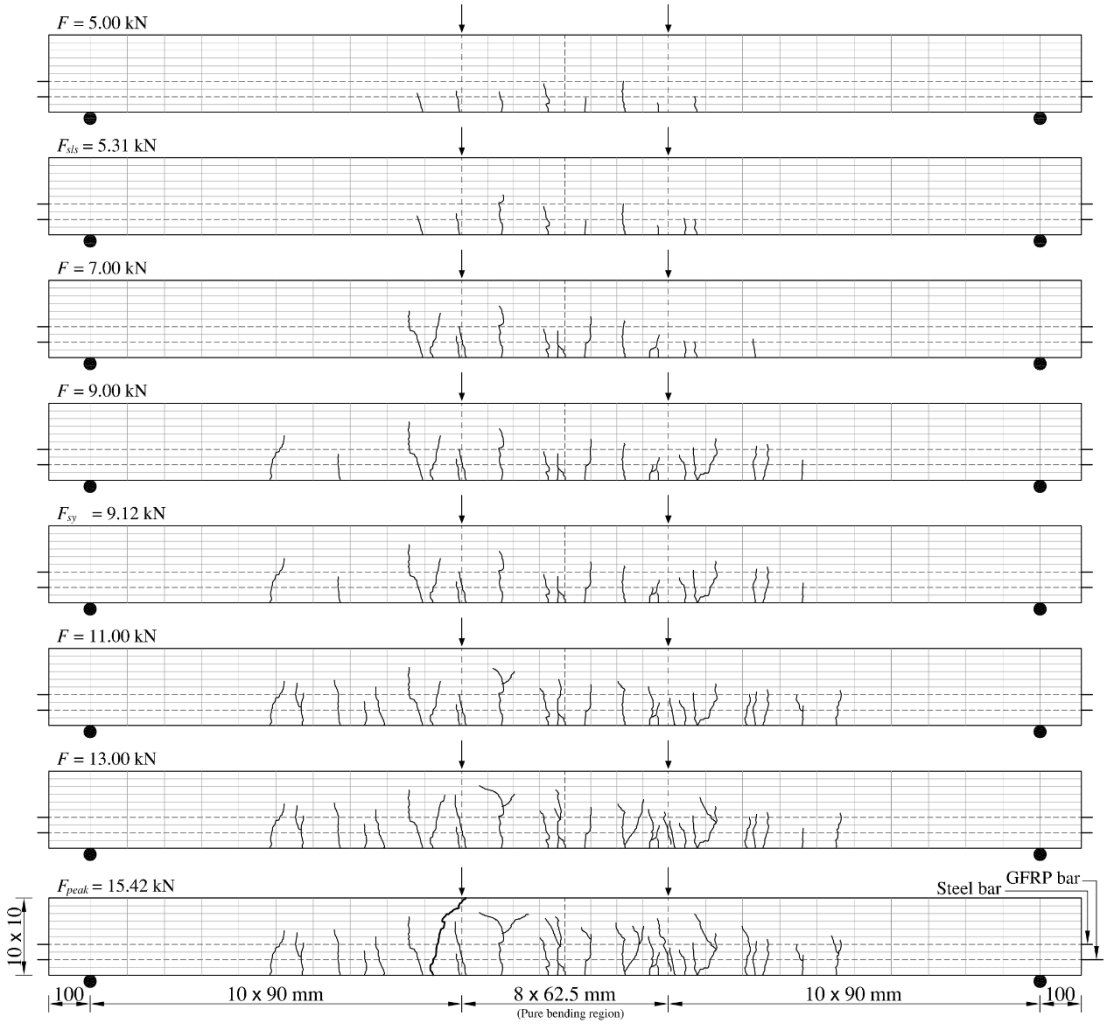

Figure B.5: Crack evolution in SGR/FRC2560-2

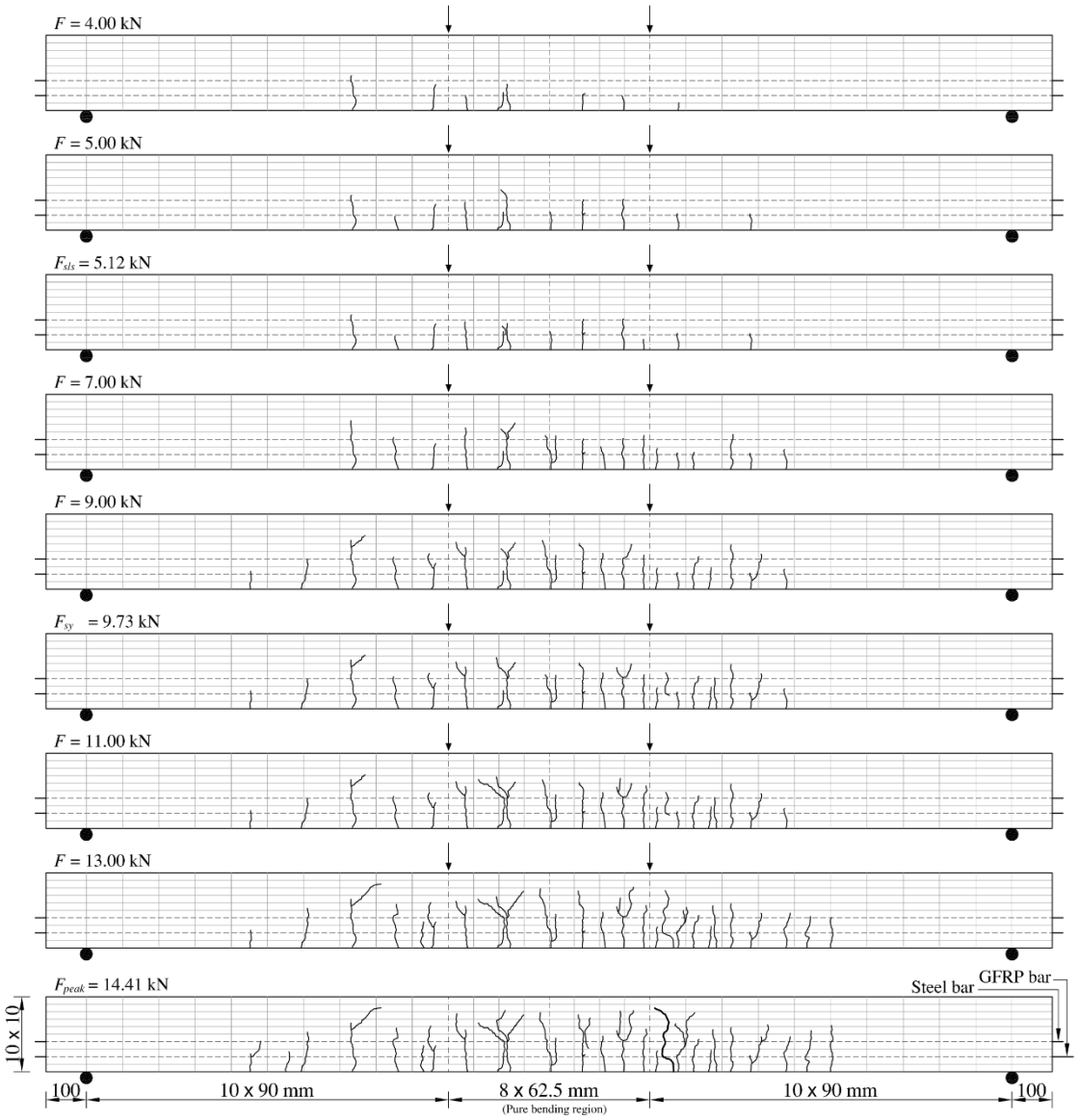

Figure B.6: Crack evolution in SGR/FRC2560-3

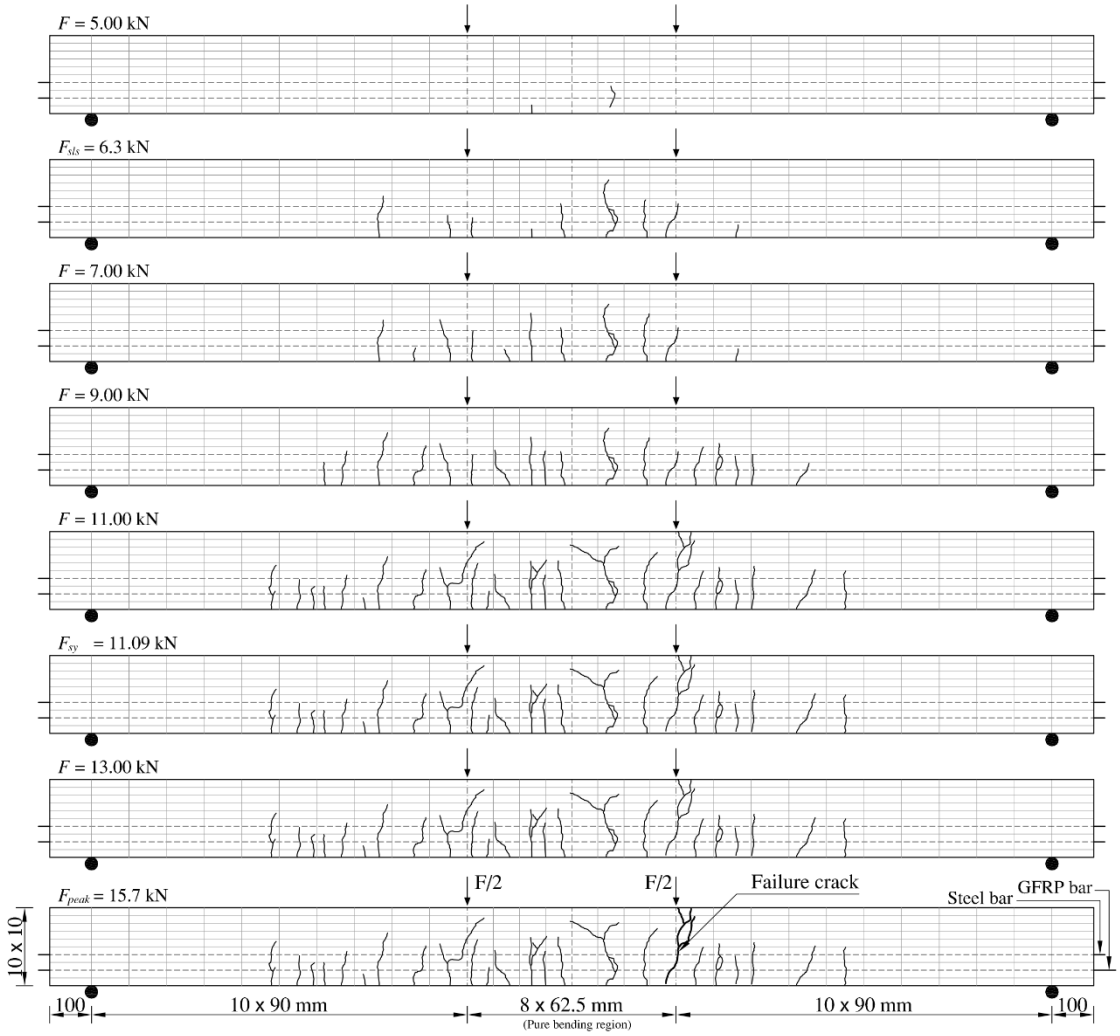

Figure B.7: Crack evolution in SGR/FRC4590-1

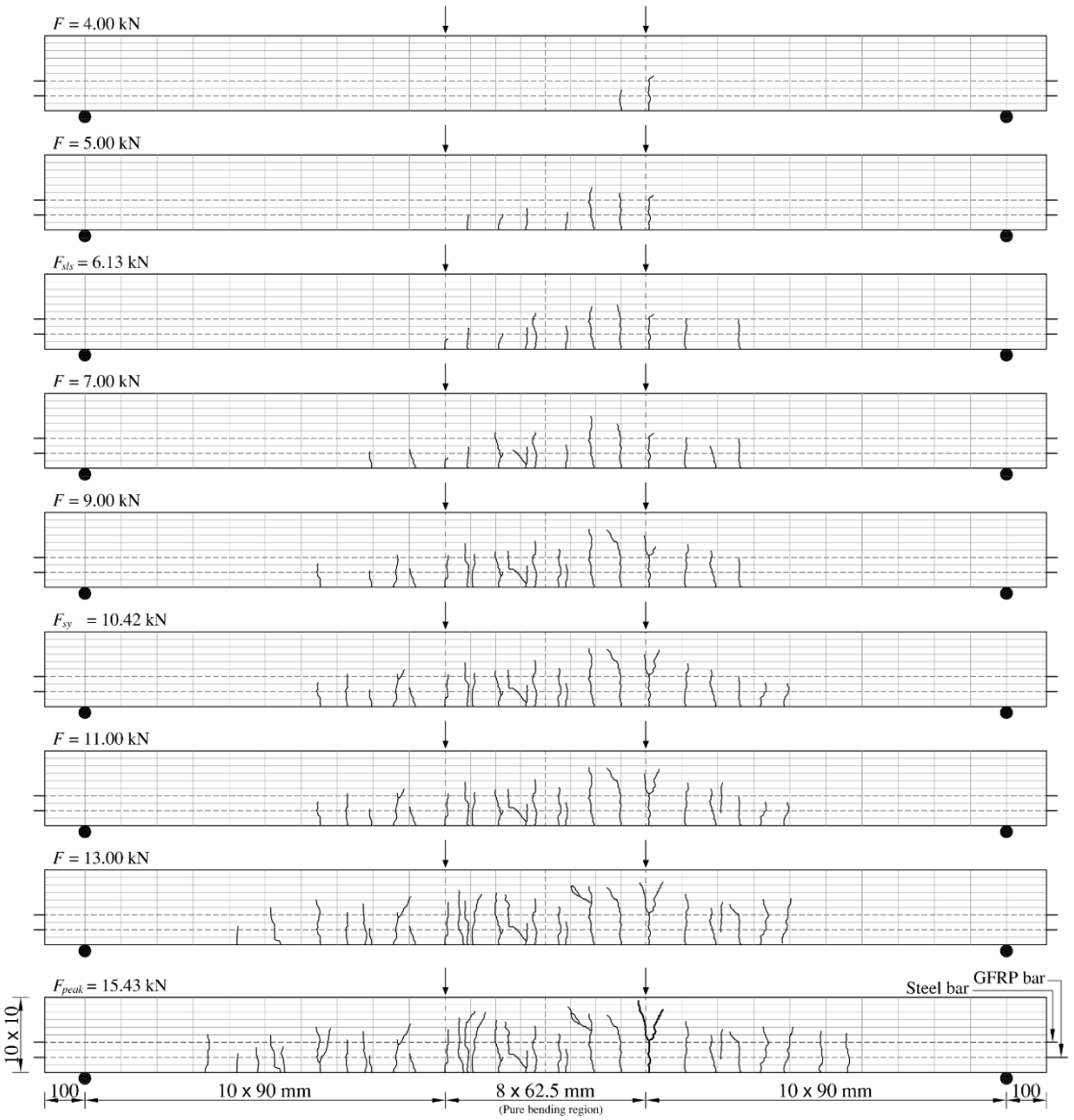

Figure B.8: Crack evolution in SGR/FRC4590-2

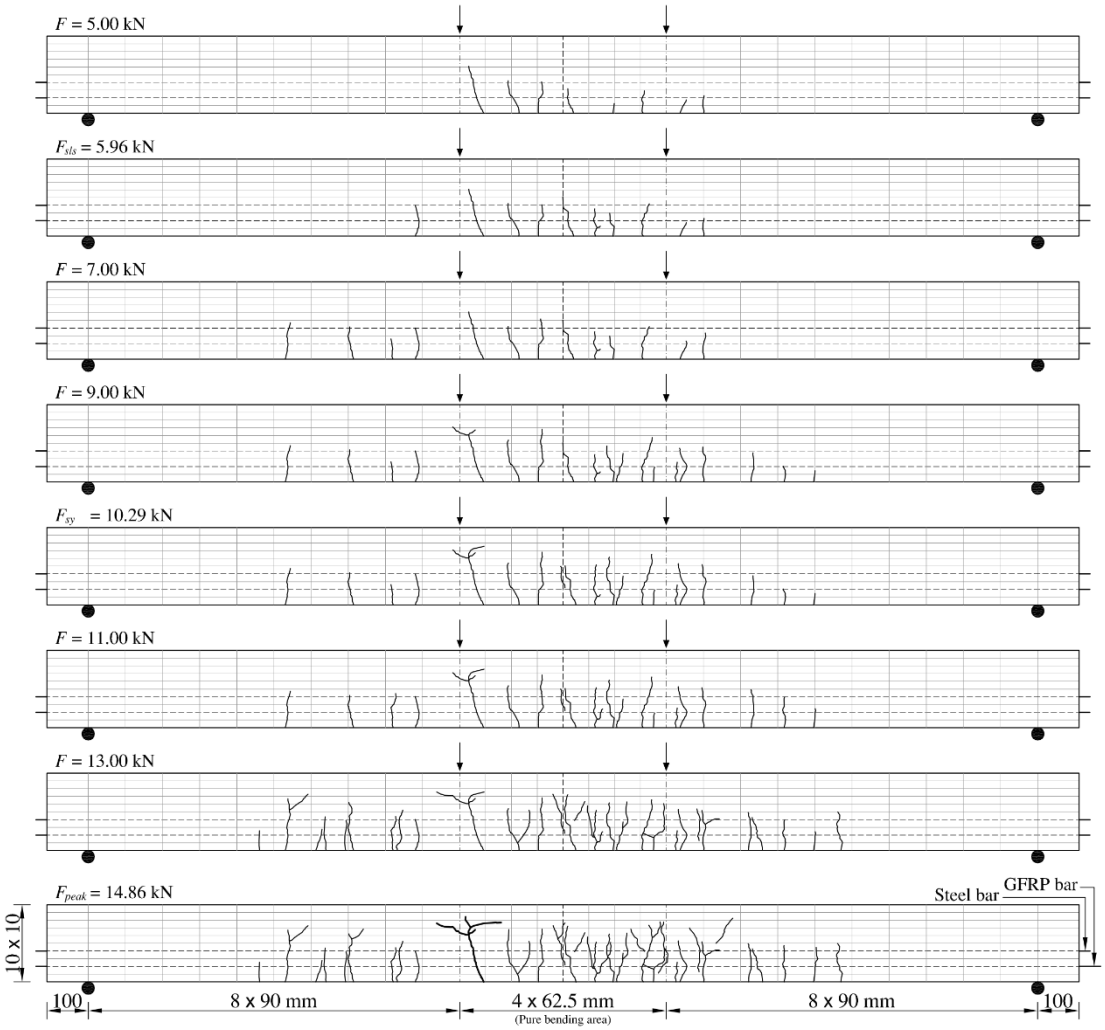

Figure B.9: Crack evolution in SGR/FRC4590-3

Appendix **C**

Deduction of the normalised height of compression and tension zones

Stage 1.1.1.1

$$h_{cc1} = kh \rightarrow \frac{h_{cc1}}{h} = k$$

$$h_{ct1} = h - kh = h(1-k) \rightarrow \frac{h_{t1}}{h} = (1-k)$$

$$h_s = h - kh - \Delta_s h = h(1-k-\Delta_s) \rightarrow \frac{h_s}{h} = (1-k-\Delta_s)$$

$$h_F = h - kh - \Delta_F h = h(1-k-\Delta_F) \rightarrow \frac{h_F}{h} = (1-k-\Delta_F)$$

Stage 2.1.1.1

$$h_{cc1} = kh \rightarrow \frac{h_{cc1}}{h} = k$$

$$\frac{h_{ct1}}{h-kh} = \frac{\varepsilon_{cr}}{\beta\varepsilon_{cr}} \rightarrow \frac{h_{ct1}}{h(1-k)} = \frac{1}{\beta} \rightarrow \frac{h_{ct1}}{h} = \frac{(1-k)}{\beta}$$

$$h_{ct2} = h - h_{cc1} - h_{ct1} \rightarrow \frac{h_{ct2}}{h} = \frac{(1-k)(\beta-1)}{\beta}$$

$$h_s = h - kh - \Delta_s h = h(1-k-\Delta_s) \rightarrow \frac{h_s}{h} = (1-k-\Delta_s)$$

$$h_F = h - kh - \Delta_F h = h(1-k-\Delta_F) \rightarrow \frac{h_F}{h} = (1-k-\Delta_F)$$

Stage 2.1.2.1

$$h_{cc1} = kh \rightarrow \frac{h_{cc1}}{h} = k$$

$$\frac{h_{ct1}}{h-kh}=\frac{\varepsilon_{cr}}{\beta\varepsilon_{cr}} \rightarrow \frac{h_{ct1}}{h(1-k)}=\frac{1}{\beta}\rightarrow \frac{h_{ct1}}{h}=\frac{(1-k)}{\beta}$$

$$h_{ct2}=h-h_{cc1}-h_{ct1}\rightarrow \frac{h_{ct2}}{h}=\frac{(1-k)(\beta-1)}{\beta}$$

$$h_s=h-kh-\Delta_s h=h(1-k-\Delta_s) \rightarrow \frac{h_s}{h}=(1-k-\Delta_s)$$

$$h_F=h-kh-\Delta_F h=h(1-k-\Delta_F) \rightarrow \frac{h_F}{h}=(1-k-\Delta_F)$$

Stage 2.2.1.1

$$\frac{h_{cc1}}{kh}=\frac{\varepsilon_{cy}}{\lambda\varepsilon_{cr}}=\frac{\omega\varepsilon_{cr}}{\frac{k}{1-k}\beta\varepsilon_{cr}}\rightarrow \frac{h_{cc1}}{h}=\frac{\omega(1-k)}{\beta}$$

$$h_{cc2}=kd-h_{cc1}=kh-\frac{\omega(1-k)}{\beta}h\rightarrow \frac{h_{cc2}}{h}=\frac{k\beta-\omega(1-k)}{\beta}$$

$$\frac{h_{ct1}}{h-kh}=\frac{\varepsilon_{cr}}{\beta\varepsilon_{cr}} \rightarrow \frac{h_{ct1}}{h(1-k)}=\frac{1}{\beta}\rightarrow \frac{h_{ct1}}{h}=\frac{(1-k)}{\beta}$$

$$h_{ct2}=h-h_{cc2}-h_{cc1}-h_{ct1}\rightarrow \frac{h_{ct2}}{h}=\frac{(1-k)(\beta-1)}{\beta}$$

$$h_s=h-kh-\Delta_s h=h(1-k-\Delta_s) \rightarrow \frac{h_s}{h}=(1-k-\Delta_s)$$

$$h_F=h-kh-\Delta_F h=h(1-k-\Delta_F) \rightarrow \frac{h_F}{h}=(1-k-\Delta_F)$$

Stage 2.2.2.1

$$\frac{h_{cc1}}{kh}=\frac{\varepsilon_{cy}}{\lambda\varepsilon_{cr}}=\frac{\omega\varepsilon_{cr}}{\frac{k}{1-k}\beta\varepsilon_{cr}}\rightarrow \frac{h_{cc1}}{h}=\frac{\omega(1-k)}{\beta}$$

$$h_{cc2}=kh-h_{cc1}=kh-\frac{\omega(1-k)}{\beta}h\rightarrow \frac{h_{cc2}}{h}=\frac{k\beta-\omega(1-k)}{\beta}$$

$$\frac{h_{ct1}}{h-kh}=\frac{\varepsilon_{cr}}{\beta\varepsilon_{cr}} \rightarrow \frac{h_{ct1}}{h(1-k)}=\frac{1}{\beta}\rightarrow \frac{h_{ct1}}{h}=\frac{(1-k)}{\beta}$$

$$h_{ct2}=h-h_{cc2}-h_{cc1}-h_{ct1}\rightarrow \frac{h_{ct2}}{h}=\frac{(1-k)(\beta-1)}{\beta}$$

$$h_s=h-kh-\Delta_s h=h(1-k-\Delta_s) \rightarrow \frac{h_s}{h}=(1-k-\Delta_s)$$

$$h_F=h-kh-\Delta_F h=h(1-k-\Delta_F) \rightarrow \frac{h_F}{h}=(1-k-\Delta_F)$$

Stage 3.1.1.1

$$h_{cc1} = kh \rightarrow \frac{h_{cc1}}{h} = k$$

$$\frac{h_{ct1}}{h-kh} = \frac{\varepsilon_{cr}}{\beta\varepsilon_{cr}} \rightarrow \frac{h_{ct1}}{h(1-k)} = \frac{1}{\beta} \rightarrow \frac{h_{ct1}}{h} = \frac{(1-k)}{\beta}$$

$$\frac{h_{ct1}}{h_{ct1}+h_{ct2}} = \frac{\varepsilon_{cr}}{\varepsilon_{trn}} \rightarrow \frac{\varepsilon_{cr}}{\alpha\varepsilon_{cr}} = \frac{\frac{(1-k)}{\beta}h}{\frac{(1-k)}{\beta}h + h_{ct2}} \rightarrow \frac{h_{ct2}}{h} = \frac{(1-k)(\alpha-1)}{\beta}$$

$$h_{ct3} = h-kh-h_{ct1}-h_{ct2} = h-kh-\frac{(1-k)}{\beta}h-\frac{(1-k)(\alpha-1)}{\beta}h \rightarrow \frac{h_{ct3}}{h} = \frac{(1-k)(\beta-\alpha)}{\beta}$$

$$h_s = h-kh-\Delta_s h = h(1-k-\Delta_s) \rightarrow \frac{h_s}{h} = (1-k-\Delta_s)$$

$$h_F = h-kh-\Delta_F h = h(1-k-\Delta_F) \rightarrow \frac{h_F}{h} = (1-k-\Delta_F)$$

Stage 3.1.2.1

$$h_{cc1} = kh \rightarrow \frac{h_{cc1}}{h} = k$$

$$\frac{h_{ct1}}{h-kh} = \frac{\varepsilon_{cr}}{\beta\varepsilon_{cr}} \rightarrow \frac{h_{ct1}}{h(1-k)} = \frac{1}{\beta} \rightarrow \frac{h_{ct1}}{h} = \frac{(1-k)}{\beta}$$

$$\frac{h_{ct1}}{h_{ct1}+h_{ct2}} = \frac{\varepsilon_{cr}}{\varepsilon_{trn}} \rightarrow \frac{\varepsilon_{cr}}{\alpha\varepsilon_{cr}} = \frac{\frac{(1-k)}{\beta}h}{\frac{(1-k)}{\beta}h + h_{ct2}} \rightarrow \frac{h_{ct2}}{h} = \frac{(1-k)(\alpha-1)}{\beta}$$

$$h_{ct3} = h-kh-h_{ct1}-h_{ct2} = h-kh-\frac{(1-k)}{\beta}h-\frac{(1-k)(\alpha-1)}{\beta}h \rightarrow \frac{h_{ct3}}{h} = \frac{(1-k)(\beta-\alpha)}{\beta}$$

$$h_s = h-kh-\Delta_s h = h(1-k-\Delta_s) \rightarrow \frac{h_s}{h} = (1-k-\Delta_s)$$

$$h_F = h-kh-\Delta_F h = h(1-k-\Delta_F) \rightarrow \frac{h_F}{h} = (1-k-\Delta_F)$$

Stage 3.2.1.1

$$\frac{h_{cc1}}{kh} = \frac{\varepsilon_{cy}}{\lambda\varepsilon_{cr}} = \frac{\omega\varepsilon_{cr}}{\frac{k}{1-k}\beta\varepsilon_{cr}} \rightarrow \frac{h_{cc1}}{h} = \frac{\omega(1-k)}{\beta}$$

$$h_{cc2} = kh - h_{cc1} = kh - \frac{\omega(1-k)}{\beta}h \rightarrow \frac{h_{cc2}}{h} = \frac{k\beta - \omega(1-k)}{\beta}$$

$$\frac{h_{ct1}}{h-kh} = \frac{\varepsilon_{cr}}{\beta\varepsilon_{cr}} \rightarrow \frac{h_{ct1}}{h(1-k)} = \frac{1}{\beta} \rightarrow \frac{h_{ct1}}{h} = \frac{(1-k)}{\beta}$$

$$\frac{h_{ct1}}{h_{ct1}+h_{ct2}} = \frac{\varepsilon_{cr}}{\varepsilon_{trn}} \rightarrow \frac{\varepsilon_{cr}}{\alpha\varepsilon_{cr}} = \frac{\frac{(1-k)}{\beta}h}{\frac{(1-k)}{\beta}h + h_{ct2}} \rightarrow \frac{h_{ct2}}{h} = \frac{(1-k)(\alpha-1)}{\beta}$$

$$h_{ct3} = h - kd - h_{ct1} - h_{ct2} = h - kh - \frac{(1-k)}{\beta}h - \frac{(1-k)(\alpha-1)}{\beta}h \rightarrow \frac{h_{ct3}}{h} = \frac{(1-k)(\beta-\alpha)}{\beta}$$

$$h_s = h - kh - \Delta_s h = h(1-k-\Delta_s) \quad \rightarrow \quad \frac{h_s}{h} = (1-k-\Delta_s)$$

$$h_F = h - kh - \Delta_F h = h(1-k-\Delta_F) \quad \rightarrow \quad \frac{h_F}{h} = (1-k-\Delta_F)$$

Stage 3.2.1.1

$$\frac{h_{cc1}}{kh} = \frac{\varepsilon_{cy}}{\lambda\varepsilon_{cr}} = \frac{\omega\varepsilon_{cr}}{\frac{k}{1-k}\beta\varepsilon_{cr}} \rightarrow \frac{h_{cc1}}{h} = \frac{\omega(1-k)}{\beta}$$

$$h_{cc2} = kd - h_{cc1} = kh - \frac{\omega(1-k)}{\beta}h \rightarrow \frac{h_{cc2}}{h} = \frac{k\beta - \omega(1-k)}{\beta}$$

$$\frac{h_{ct1}}{h-kh} = \frac{\varepsilon_{cr}}{\beta\varepsilon_{cr}} \rightarrow \frac{h_{ct1}}{h(1-k)} = \frac{1}{\beta} \rightarrow \frac{h_{ct1}}{h} = \frac{(1-k)}{\beta}$$

$$\frac{h_{ct1}}{h_{ct1}+h_{ct2}} = \frac{\varepsilon_{cr}}{\varepsilon_{trn}} \rightarrow \frac{\varepsilon_{cr}}{\alpha\varepsilon_{cr}} = \frac{\frac{(1-k)}{\beta}h}{\frac{(1-k)}{\beta}h + h_{ct2}} \rightarrow \frac{h_{ct2}}{h} = \frac{(1-k)(\alpha-1)}{\beta}$$

$$h_{ct3} = h - kd - h_{ct1} - h_{ct2} = h - kh - \frac{(1-k)}{\beta}h - \frac{(1-k)(\alpha-1)}{\beta}h \rightarrow \frac{h_{ct3}}{h} = \frac{(1-k)(\beta-\alpha)}{\beta}$$

$$h_s = h - kh - \Delta_s h = h(1-k-\Delta_s) \quad \rightarrow \quad \frac{h_s}{h} = (1-k-\Delta_s)$$

$$h_F = h - kh - \Delta_F h = h(1-k-\Delta_F) \quad \rightarrow \quad \frac{h_F}{h} = (1-k-\Delta_F)$$

Appendix **D**

Deduction of the normalised stresses

Stage 1.1.1.1

$$\sigma_{cc1} = \gamma E_c \lambda \varepsilon_{cr} = \gamma E_c \left(\frac{k}{1-k} \right) \beta \varepsilon_{cr} \rightarrow \frac{\sigma_{cc1}}{E_c \varepsilon_{cr}} = \frac{\gamma \beta k}{1-k}$$

$$\sigma_{ct1} = E_c \beta \varepsilon_{cr} \rightarrow \frac{\sigma_{ct1}}{E_c \varepsilon_{cr}} = \beta$$

$$\sigma_s = \gamma_s E_c \psi \varepsilon_{cr} = \gamma_s E_c \frac{\left(1-k-\Delta_s\right)}{1-k} \beta \varepsilon_{cr} \rightarrow \frac{\sigma_s}{E_c \varepsilon_{cr}} = \frac{\gamma_s \beta \left(1-k-\Delta_s\right)}{1-k}$$

$$\sigma_F = \gamma_F E_c \nu_F \varepsilon_{cr} = \gamma_F E_c \frac{\left(1-k-\Delta_F\right)}{1-k} \beta \varepsilon_{cr} \rightarrow \frac{\sigma_F}{E_c \varepsilon_{cr}} = \frac{\gamma_F \beta \left(1-k-\Delta_F\right)}{1-k}$$

Stage 2.1.1.1

$$\sigma_{cc1} = \gamma E_c \lambda \varepsilon_{cr} = \gamma E_c \left(\frac{k}{1-k} \right) \beta \varepsilon_{cr} \rightarrow \frac{\sigma_{cc1}}{E_c \varepsilon_{cr}} = \frac{\gamma \beta k}{1-k}$$

$$\sigma_{ct1} = \sigma_{cr} = E_c \varepsilon_{cr} \rightarrow \frac{\sigma_{ct1}}{E_c \varepsilon_{cr}} = 1$$

$$\sigma_{ct2} = E_c \varepsilon_{cr} + \eta E_c \left(\varepsilon_t - \varepsilon_{cr} \right) = E_c \varepsilon_{cr} + \eta E_c (\beta \varepsilon_{cr} - \varepsilon_{cr}) \rightarrow \frac{\sigma_{ct2}}{E_c \varepsilon_{cr}} = 1 + \eta \left(\beta - 1 \right)$$

$$\sigma_s = \gamma_s E_c \psi \varepsilon_{cr} = \gamma_s E_c \frac{\left(1-k-\Delta_s\right)}{1-k} \beta \varepsilon_{cr} \rightarrow \frac{\sigma_s}{E_c \varepsilon_{cr}} = \frac{\gamma_s \beta \left(1-k-\Delta_s\right)}{1-k}$$

$$\sigma_F = \gamma_F E_c \nu_F \varepsilon_{cr} = \gamma_F E_c \frac{\left(1-k-\Delta_F\right)}{1-k}\beta\varepsilon_{cr} \rightarrow \frac{\sigma_F}{E_c\varepsilon_{cr}} = \frac{\gamma_F\beta\left(1-k-\Delta_F\right)}{1-k}$$

Stage 2.1.2.1

$$\sigma_{cc1} = \gamma E_c \lambda \varepsilon_{cr} = \gamma E_c \left(\frac{k}{1-k}\right)\beta\varepsilon_{cr} \rightarrow \frac{\sigma_{cc1}}{E_c\varepsilon_{cr}} = \frac{\gamma\beta k}{1-k}$$

$$\sigma_{ct1} = \sigma_{cr} = E_c\varepsilon_{cr} \rightarrow \frac{\sigma_{ct1}}{E_c\varepsilon_{cr}} = 1$$

$$\sigma_{ct2} = E_c\varepsilon_{cr} + \eta E_c\left(\varepsilon_t - \varepsilon_{cr}\right) = E_c\varepsilon_{cr} + \eta E_c(\beta\varepsilon_{cr} - \varepsilon_{cr}) \rightarrow \frac{\sigma_{ct2}}{E_c\varepsilon_{cr}} = 1+\eta\left(\beta-1\right)$$

$$\sigma_s = \gamma_s E_c \zeta \varepsilon_{cr} \rightarrow \frac{\sigma_s}{E_c\varepsilon_{cr}} = \zeta\gamma_s$$

$$\sigma_F = \gamma_F E_c \nu_F \varepsilon_{cr} = \gamma_F E_c \frac{\left(1-k-\Delta_F\right)}{1-k}\beta\varepsilon_{cr} \rightarrow \frac{\sigma_F}{E_c\varepsilon_{cr}} = \frac{\gamma_F\beta\left(1-k-\Delta_F\right)}{1-k}$$

Stage 2.2.1.1

$$\sigma_{cc2} = \omega\varepsilon_{cr}\gamma E_c \rightarrow \frac{\sigma_{cc,top}}{E_c\varepsilon_{cr}} = \omega\gamma$$

$$\sigma_{cc1} = \omega\varepsilon_{cr}\gamma E_c \rightarrow \frac{\sigma_{cc1}}{E_c\,\varepsilon_{cr}} = \omega\gamma$$

$$\sigma_{ct1} = f_{cr} = E_c\,\varepsilon_{cr} \rightarrow \frac{\sigma_{ct1}}{E_c\,\varepsilon_{cr}} = 1$$

$$\sigma_{ct2} = E_c\,\varepsilon_{cr} + \eta E_c\left(\varepsilon_t - \varepsilon_{cr}\right) = E_c\,\varepsilon_{cr} + \eta E_c\,(\beta\varepsilon_{cr} - \varepsilon_{cr}) \rightarrow \frac{\sigma_{ct2}}{E_c\,\varepsilon_{cr}} = 1+\eta\left(\beta-1\right)$$

$$\sigma_s = \gamma_s E_c \psi \varepsilon_{cr} = \gamma_s E_c \frac{\left(1-k-\Delta_s\right)}{1-k}\beta\varepsilon_{cr} \rightarrow \frac{\sigma_s}{E_c\varepsilon_{cr}} = \frac{\gamma_s\beta\left(1-k-\Delta_s\right)}{1-k}$$

$$\sigma_F = \gamma_F E_c \nu_F \varepsilon_{cr} = \gamma_F E_c \frac{\left(1-k-\Delta_F\right)}{1-k}\beta\varepsilon_{cr} \rightarrow \frac{\sigma_F}{E_c\varepsilon_{cr}} = \frac{\gamma_F\beta\left(1-k-\Delta_F\right)}{1-k}$$

Stage 2.2.2.1

$$\sigma_{cc2} = \omega\varepsilon_{cr}\gamma E_c \rightarrow \frac{\sigma_{cc2}}{E_c\,\varepsilon_{cr}} = \omega\gamma$$

$$\sigma_{cc1} = \omega\varepsilon_{cr}\gamma E_c \rightarrow \frac{\sigma_{cc1}}{E_c\,\varepsilon_{cr}} = \omega\gamma$$

$$\sigma_{ct1} = f_{cr} = E_c\,\varepsilon_{cr} \rightarrow \frac{\sigma_{ct1}}{E_c\,\varepsilon_{cr}} = 1$$

$$\sigma_{ct2} = E_c\,\varepsilon_{cr} + \eta E_c\left(\varepsilon_t - \varepsilon_{cr}\right) = E_c\,\varepsilon_{cr} + \eta E_c\ (\beta\varepsilon_{cr} - \varepsilon_{cr}) \rightarrow \frac{\sigma_{ct2}}{E_c\,\varepsilon_{cr}} = 1 + \eta\left(\beta - 1\right)$$

$$\sigma_s = \gamma_s E_c \zeta\varepsilon_{cr} \quad \rightarrow \frac{\sigma_s}{E_c\varepsilon_{cr}} = \zeta\gamma_s$$

$$\sigma_F = \gamma_F E_c \nu_F \varepsilon_{cr} = \gamma_F E_c \frac{\left(1 - k - \Delta_F\right)}{1 - k}\beta\varepsilon_{cr} \rightarrow \frac{\sigma_F}{E_c\varepsilon_{cr}} = \frac{\gamma_F\beta\left(1 - k - \Delta_F\right)}{1 - k}$$

Stage 3.1.1.1

$$\sigma_{cc1} = \gamma E_c\,\lambda\varepsilon_{cr} = \gamma E_c\left(\frac{k}{1-k}\right)\beta\varepsilon_{cr} \rightarrow \frac{\sigma_{cc1}}{E_c\,\varepsilon_{cr}} = \frac{\gamma\beta k}{1-k}$$

$$\sigma_{ct1} = \sigma_{cr} = \ E_c\,\varepsilon_{cr} \rightarrow \frac{\sigma_{ct1}}{E_c\,\varepsilon_{cr}} = 1$$

$$\sigma_{ct2} = E_c\,\varepsilon_{cr} + \eta E_c\left(\varepsilon_{trn} - \varepsilon_{cr}\right) = E_c\,\varepsilon_{cr} + \eta E_c\ (\alpha\varepsilon_{cr} - \ \varepsilon_{cr}) \rightarrow \frac{\sigma_{ct2}}{E_c\,\varepsilon_{cr}} = 1 + \eta\left(\alpha - 1\right)$$

$$\sigma_{ct3} = \sigma_{cst} = \mu E_c\,\varepsilon_{cr} \rightarrow \frac{\sigma_{ct3}}{E_c\,\varepsilon_{cr}} = \mu$$

$$\sigma_s = \gamma_s E_c \psi\varepsilon_{cr} = \gamma_s E_c \frac{\left(1 - k - \Delta_s\right)}{1 - k}\beta\varepsilon_{cr} \rightarrow \frac{\sigma_s}{E_c\varepsilon_{cr}} = \frac{\gamma_s\beta\left(1 - k - \Delta_s\right)}{1 - k}$$

$$\sigma_F = \gamma_F E_c \nu_F \varepsilon_{cr} = \gamma_F E_c \frac{\left(1 - k - \Delta_F\right)}{1 - k}\beta\varepsilon_{cr} \rightarrow \frac{\sigma_F}{E_c\varepsilon_{cr}} = \frac{\gamma_F\beta\left(1 - k - \Delta_F\right)}{1 - k}$$

Stage 3.1.2.1

$$\sigma_{cc1} = \gamma E_c \lambda \varepsilon_{cr} = \gamma E_c \left(\frac{k}{1-k} \right) \beta \varepsilon_{cr} \rightarrow \frac{\sigma_{cc1}}{E_c \varepsilon_{cr}} = \frac{\gamma \beta k}{1-k}$$

$$\sigma_{ct1} = \sigma_{cr} = E_c \varepsilon_{cr} \rightarrow \frac{\sigma_{ct1}}{E_c \varepsilon_{cr}} = 1$$

$$\sigma_{ct2} = E_c \varepsilon_{cr} + \eta E_c \left(\varepsilon_{trn} - \varepsilon_{cr} \right) = E_c \varepsilon_{cr} + \eta E_c \left(\alpha \varepsilon_{cr} - \varepsilon_{cr} \right) \rightarrow \frac{\sigma_{ct2}}{E_c \varepsilon_{cr}} = 1 + \eta \left(\alpha - 1 \right)$$

$$\sigma_{ct3} = \sigma_{cst} = \mu E_c \varepsilon_{cr} \rightarrow \frac{\sigma_{ct3}}{E_c \varepsilon_{cr}} = \mu$$

$$\sigma_s = \gamma_s E_c \zeta \varepsilon_{cr} \rightarrow \frac{\sigma_s}{E_c \varepsilon_{cr}} = \zeta \gamma_s$$

$$\sigma_F = \gamma_F E_c \nu_F \varepsilon_{cr} = \gamma_F E_c \frac{\left(1-k-\Delta_F \right)}{1-k} \beta \varepsilon_{cr} \rightarrow \frac{\sigma_F}{E_c \varepsilon_{cr}} = \frac{\gamma_F \beta \left(1-k-\Delta_F \right)}{1-k}$$

Stage 3.2.1.1

$$\sigma_{cc2} = \omega \varepsilon_{cr} \gamma E_c \rightarrow \frac{\sigma_{cc2}}{E_c \varepsilon_{cr}} = \omega \gamma$$

$$\sigma_{cc1} = \omega \varepsilon_{cr} \gamma E_c \rightarrow \frac{\sigma_{cc1}}{E_c \varepsilon_{cr}} = \omega \gamma$$

$$\sigma_{ct1} = \sigma_{cr} = E_c \varepsilon_{cr} \rightarrow \frac{\sigma_{ct1}}{E_c \varepsilon_{cr}} = 1$$

$$\sigma_{ct2} = E_c \varepsilon_{cr} + \eta E_c \left(\varepsilon_{trn} - \varepsilon_{cr} \right) = E_c \varepsilon_{cr} + \eta E_c \left(\alpha \varepsilon_{cr} - \varepsilon_{cr} \right) \rightarrow \frac{\sigma_{ct2}}{E_c \varepsilon_{cr}} = 1 + \eta \left(\alpha - 1 \right)$$

$$\sigma_{ct3} = \sigma_{cst} = \mu E_c \varepsilon_{cr} \rightarrow \frac{\sigma_{ct3}}{E_c \varepsilon_{cr}} = \mu$$

$$\sigma_s = \gamma_s E_c \psi \varepsilon_{cr} = \gamma_s E_c \frac{(1-k-\Delta_s)}{1-k} \beta \varepsilon_{cr} \rightarrow \frac{\sigma_s}{E_c \varepsilon_{cr}} = \frac{\gamma_s \beta (1-k-\Delta_s)}{1-k}$$

$$\sigma_F = \gamma_F E_c \nu_F \varepsilon_{cr} = \gamma_F E_c \frac{(1-k-\Delta_F)}{1-k} \beta \varepsilon_{cr} \rightarrow \frac{\sigma_F}{E_c \varepsilon_{cr}} = \frac{\gamma_F \beta (1-k-\Delta_F)}{1-k}$$

Stage 3.2.2.1

$$\sigma_{cc2} = \omega \varepsilon_{cr} \gamma E_c \rightarrow \frac{\sigma_{cc2}}{E_c \varepsilon_{cr}} = \omega \gamma$$

$$\sigma_{cc1} = \omega \varepsilon_{cr} \gamma E_c \rightarrow \frac{\sigma_{cc1}}{E_c \varepsilon_{cr}} = \omega \gamma$$

$$\sigma_{ct1} = \sigma_{cr} = E_c \varepsilon_{cr} \rightarrow \frac{\sigma_{ct1}}{E_c \varepsilon_{cr}} = 1$$

$$\sigma_{ct2} = E_c \varepsilon_{cr} + \eta E_c (\varepsilon_{trn} - \varepsilon_{cr}) = E_c \varepsilon_{cr} + \eta E_c (\alpha \varepsilon_{cr} - \varepsilon_{cr}) \rightarrow \frac{\sigma_{ct2}}{E_c \varepsilon_{cr}} = 1 + \eta (\alpha - 1)$$

$$\sigma_{ct3} = \sigma_{cst} = \mu E_c \varepsilon_{cr} \rightarrow \frac{\sigma_{ct3}}{E_c \varepsilon_{cr}} = \mu$$

$$\sigma_s = \gamma_s E_c \zeta \varepsilon_{cr} \rightarrow \frac{\sigma_s}{E_c \varepsilon_{cr}} = \zeta \gamma_s$$

$$\sigma_F = \gamma_F E_c \nu_F \varepsilon_{cr} = \gamma_F E_c \frac{(1-k-\Delta_F)}{1-k} \beta \varepsilon_{cr} \rightarrow \frac{\sigma_F}{E_c \varepsilon_{cr}} = \frac{\gamma_F \beta (1-k-\Delta_F)}{1-k}$$

Appendix **E**

Deduction of the normalised forces

Stage 1.1.1.1

$$F_{cc1} = \sigma_{cc1} \times h_{cc1} \times \frac{b}{2} = \frac{\gamma\beta k}{1-k} E_c \varepsilon_{cr} \times kh \times \frac{b}{2} \rightarrow \frac{F_{cc1}}{bhE_c\varepsilon_{cr}} = \frac{\gamma\beta k^2}{2(1-k)}$$

$$F_{ct1} = \sigma_{ct1} \times h_{ct1} \times \frac{b}{2} = \beta E \varepsilon_{cr} \times (1-k)h \times \frac{b}{2} \rightarrow \frac{F_{ct1}}{bhE_c\varepsilon_{cr}} = \frac{\beta(1-k)}{2}$$

$$F_s = \sigma_s \times \rho_s b d_s = \gamma_s E_c \frac{(1-k-\Delta_s)}{1-k} \beta\varepsilon_{cr} \times \rho_s b d_s \times \frac{h}{h} \rightarrow \frac{F_s}{bhE_c\varepsilon_{cr}} = \frac{\gamma_s\beta\rho_s d_s (1-k-\Delta_s)}{(1-k)h}$$

$$F_F = \sigma_F \times \rho_F b d_F = \gamma_F E_c \frac{(1-k-\Delta_F)}{1-k} \beta\varepsilon_{cr} \times \rho_F b d_F \times \frac{h}{h} \rightarrow \frac{F_F}{bhE_c\varepsilon_{cr}} = \frac{\gamma_F\beta\rho_F d_F (1-k-\Delta_F)}{(1-k)h}$$

Stage 2.1.1.1

$$F_{cc1} = \sigma_{cc1} \times h_{cc1} \times \frac{b}{2} = \frac{\gamma\beta k}{1-k} E_c \varepsilon_{cr} \times kh \times \frac{b}{2} \rightarrow \frac{F_{cc1}}{bhE_c\varepsilon_{cr}} = \frac{\gamma\beta k^2}{2(1-k)}$$

$$F_{ct1} = \sigma_{ct1} \times h_{ct1} \times \frac{b}{2} = E_c \varepsilon_{cr} \times \frac{1-k}{\beta} h \times \frac{b}{2} \rightarrow \frac{F_{ct1}}{bhE_c\varepsilon_{cr}} = \frac{1-k}{2\beta}$$

$$F_{ct2} = (\sigma_{ct1} + \sigma_{ct2}) h_{ct2} \times \frac{b}{2} = \left(1+1+\eta(\beta-1)\right) E_c \varepsilon_{cr} \times \frac{(1-k)(\beta-1)}{\beta} h \times \frac{b}{2}$$

$$\rightarrow \frac{F_{ct2}}{bhE_c\varepsilon_{cr}} = \frac{(1-k)(\beta-1)(\eta\beta-\eta+2)}{2\beta}$$

$$F_s = \sigma_s \times \rho_s b d_s = \gamma_s E_c \frac{(1-k-\Delta_s)}{1-k} \beta \varepsilon_{cr} \times \rho_s b d_s \times \frac{h}{h} \rightarrow \frac{F_s}{bhE_c\varepsilon_{cr}} = \frac{\gamma_s \beta \rho_s d_s (1-k-\Delta_s)}{(1-k)h}$$

$$F_F = \sigma_F \times \rho_F b d_F = \gamma_F E_c \frac{(1-k-\Delta_F)}{1-k} \beta \varepsilon_{cr} \times \rho_F b d_F \times \frac{h}{h} \rightarrow \frac{F_F}{bhE_c\varepsilon_{cr}} = \frac{\gamma_F \beta \rho_F d_F (1-k-\Delta_F)}{(1-k)h}$$

Stage 2.1.2.1

$$F_{cc1} = \sigma_{cc1} \times h_{cc1} \times \frac{b}{2} = \frac{\gamma\beta k}{1-k} E_c \varepsilon_{cr} \times kh \times \frac{b}{2} \rightarrow \frac{F_{cc1}}{bhE_c\varepsilon_{cr}} = \frac{\gamma\beta k^2}{2(1-k)}$$

$$F_{ct1} = \sigma_{ct1} \times h_{ct1} \times \frac{b}{2} = E_c \varepsilon_{cr} \times \frac{1-k}{\beta} h \times \frac{b}{2} \rightarrow \frac{F_{ct1}}{bhE_c\varepsilon_{cr}} = \frac{1-k}{2\beta}$$

$$F_{ct2} = (\sigma_{ct1} + \sigma_{ct2}) h_{t2} \times \frac{b}{2} = \left(1+1+\eta(\beta-1)\right) E_c \varepsilon_{cr} \times \frac{(1-k)(\beta-1)}{\beta} h \times \frac{b}{2}$$

$$\rightarrow \frac{F_{ct2}}{bhE_c\varepsilon_{cr}} = \frac{(1-k)(\beta-1)(\eta\beta-\eta+2)}{2\beta}$$

$$F_s = \sigma_{sy} \times \rho_s b d_s = \gamma_s E_c \zeta \varepsilon_{cr} \times \rho_s b d_s \times \frac{h}{h} \rightarrow \frac{F_s}{bhE_c\varepsilon_{cr}} = \frac{\zeta\gamma_s\rho_s d_s}{h}$$

$$F_F = \sigma_F \times \rho_F b d_F = \gamma_F E_c \frac{(1-k-\Delta_F)}{1-k} \beta \varepsilon_{cr} \times \rho_F b d_F \times \frac{h}{h} \rightarrow \frac{F_F}{bhE_c\varepsilon_{cr}} = \frac{\gamma_F \beta \rho_F d_F (1-k-\Delta_F)}{(1-k)h}$$

Stage 2.2.1.1

$$F_{cc1} = \sigma_{cc1} \times h_{cc1} \times \frac{b}{2} = \omega\gamma E_c \varepsilon_{cr} \times \frac{\omega(1-k)}{\beta} h \times \frac{b}{2} \rightarrow \frac{F_{cc1}}{bhE_c\varepsilon_{cr}} = \frac{\omega^2\gamma(1-k)}{2\beta}$$

$$F_{cc2} = \sigma_{cc2} \times h_{cc2} \times b = \omega\gamma E_c \varepsilon_{cr} \times \frac{k\beta - \omega(1-k)}{\beta} bh \rightarrow \frac{F_{cc2}}{bhE_c\varepsilon_{cr}} = \frac{\omega\gamma}{\beta}(\beta k + \omega k - \omega)$$

$$F_{ct1} = \sigma_{ct1} \times h_{ct1} \times \frac{b}{2} = E_c \varepsilon_{cr} \times \frac{1-k}{\beta} h \times \frac{b}{2} \rightarrow \frac{F_{ct1}}{bhE_c\varepsilon_{cr}} = \frac{1-k}{2\beta}$$

$$F_{ct2} = (\sigma_{ct1} + \sigma_{ct2}) h_{ct2} \times \frac{b}{2} = \left(1+1+\eta(\beta-1)\right) E_c \varepsilon_{cr} \times \frac{(1-k)(\beta-1)}{\beta} h \times \frac{b}{2}$$

$$\rightarrow \frac{F_{ct2}}{bhE_c\varepsilon_{cr}} = \frac{(1-k)(\beta-1)(\eta\beta-\eta+2)}{2\beta}$$

$$F_s = \sigma_s \times \rho_s b d_s = \gamma_s E_c \frac{(1-k-\Delta_s)}{1-k}\beta\varepsilon_{cr} \times \rho_s b d_s \times \frac{h}{h} \rightarrow \frac{F_s}{bhE_c\varepsilon_{cr}} = \frac{\gamma_s\beta\rho_s d_s(1-k-\Delta_s)}{(1-k)h}$$

$$F_F = \sigma_F \times \rho_F b d_F = \gamma_F E_c \frac{(1-k-\Delta_F)}{1-k}\beta\varepsilon_{cr} \times \rho_F b d_F \times \frac{h}{h} \rightarrow \frac{F_F}{bhE_c\varepsilon_{cr}} = \frac{\gamma_F\beta\rho_F d_F(1-k-\Delta_F)}{(1-k)h}$$

Stage 2.2.2.1

$$F_{cc1} = \sigma_{cc1} \times h_{cc1} \times \frac{b}{2} = \omega\gamma E_c\varepsilon_{cr} \times \frac{\omega(1-k)}{\beta}h \times \frac{b}{2} \rightarrow \frac{F_{cc1}}{bhE_c\varepsilon_{cr}} = \frac{\omega^2\gamma(1-k)}{2\beta}$$

$$F_{cc2} = \sigma_{cc2} \times h_{cc2} \times b = \omega\gamma E_c\varepsilon_{cr} \times \frac{k\beta-\omega(1-k)}{\beta}bh \rightarrow \frac{F_{cc2}}{bhE_c\varepsilon_{cr}} = \frac{\omega\gamma}{\beta}(\beta k+\omega k-\omega)$$

$$F_{ct1} = \sigma_{ct1} \times h_{ct1} \times \frac{b}{2} = E_c\varepsilon_{cr} \times \frac{1-k}{\beta}h \times \frac{b}{2} \rightarrow \frac{F_{ct1}}{bhE_c\varepsilon_{cr}} = \frac{1-k}{2\beta}$$

$$F_{ct2} = (\sigma_{ct1}+\sigma_{ct2})h_{t2} \times \frac{b}{2} = \left(1+1+\eta(\beta-1)\right)E_c\varepsilon_{cr} \times \frac{(1-k)(\beta-1)}{\beta}h \times \frac{b}{2}$$

$$\rightarrow \frac{F_{ct2}}{bhE_c\varepsilon_{cr}} = \frac{(1-k)(\beta-1)(\eta\beta-\eta+2)}{2\beta}$$

$$F_s = \sigma_{sy} \times \rho_s b d_s = \gamma_s E_c\zeta\varepsilon_{cr} \times \rho_s b d_s \times \frac{h}{h} \rightarrow \frac{F_s}{bhE_c\varepsilon_{cr}} = \frac{\zeta\gamma_s\rho_s d_s}{h}$$

$$F_F = \sigma_F \times \rho_F b d_F = \gamma_F E_c \frac{(1-k-\Delta_F)}{1-k}\beta\varepsilon_{cr} \times \rho_F b d_F \times \frac{h}{h} \rightarrow \frac{F_F}{bhE_c\varepsilon_{cr}} = \frac{\gamma_F\beta\rho_F d_F(1-k-\Delta_F)}{(1-k)h}$$

Stage 3.1.1.1

$$F_{cc1} = \sigma_{cc1} \times h_{cc1} \times \frac{b}{2} = \frac{\gamma\beta k}{1-k}E_c\varepsilon_{cr} \times kh \times \frac{b}{2} \rightarrow \frac{F_{cc1}}{bhE_c\varepsilon_{cr}} = \frac{\gamma\beta k^2}{2(1-k)}$$

$$F_{ct1} = \sigma_{ct1} \times h_{ct1} \times \frac{b}{2} = E_c\varepsilon_{cr} \times \frac{1-k}{\beta}h \times \frac{b}{2} \rightarrow \frac{F_{ct1}}{bhE_c\varepsilon_{cr}} = \frac{1-k}{2\beta}$$

$$F_{ct2}=(\sigma_{ct1}+\sigma_{ct2})h_{ct2}\times\frac{b}{2}=\left(1+1+\eta\left(\alpha-1\right)\right)E_c\varepsilon_{cr}\times\frac{\left(1-k\right)\left(\alpha-1\right)}{\beta}h\times\frac{b}{2}$$

$$\rightarrow\frac{F_{ct2}}{bhE_c\varepsilon_{cr}}=\frac{\left(1-k\right)\left(\alpha-1\right)\left(\eta\alpha-\eta+2\right)}{2\beta}$$

$$F_{ct3}=\sigma_{ct3}\times h_{ct3}\times b=\mu E_c\varepsilon_{cr}\times\frac{\left(1-k\right)\left(\beta-\alpha\right)}{\beta}h\times b\rightarrow\frac{F_{ct3}}{bhE_c\varepsilon_{cr}}=\frac{\left(1-k\right)\left(\beta-\alpha\right)\mu}{\beta}$$

$$F_s=\sigma_s\times\rho_s bd_s=\gamma_s E_c\frac{\left(1-k-\Delta_s\right)}{1-k}\beta\varepsilon_{cr}\times\rho_s bd_s\times\frac{h}{h}\rightarrow\frac{F_s}{bhE_c\varepsilon_{cr}}=\frac{\gamma_s\beta\rho_s d_s\left(1-k-\Delta_s\right)}{\left(1-k\right)h}$$

$$F_F=\sigma_F\times\rho_F bd_F=\gamma_F E_c\frac{\left(1-k-\Delta_F\right)}{1-k}\beta\varepsilon_{cr}\times\rho_F bd_F\times\frac{h}{h}\rightarrow\frac{F_F}{bhE_c\varepsilon_{cr}}=\frac{\gamma_F\beta\rho_F d_F\left(1-k-\Delta_F\right)}{\left(1-k\right)h}$$

Stage 3.1.2.1

$$F_{cc1}=\sigma_{cc1}\times h_{cc1}\times\frac{b}{2}=\frac{\gamma\beta k}{1-k}E_c\varepsilon_{cr}\times kh\times\frac{b}{2}\rightarrow\frac{F_{cc1}}{bhE_c\varepsilon_{cr}}=\frac{\gamma\beta k^2}{2\left(1-k\right)}$$

$$F_{ct1}=\sigma_{ct1}\times h_{ct1}\times\frac{b}{2}=E_c\varepsilon_{cr}\times\frac{1-k}{\beta}h\times\frac{b}{2}\rightarrow\frac{F_{ct1}}{bhE_c\varepsilon_{cr}}=\frac{1-k}{2\beta}$$

$$F_{ct2}=(\sigma_{ct1}+\sigma_{ct2})h_{ct2}\times\frac{b}{2}=\left(1+1+\eta\left(\alpha-1\right)\right)E_c\varepsilon_{cr}\times\frac{\left(1-k\right)\left(\alpha-1\right)}{\beta}h\times\frac{b}{2}$$

$$\rightarrow\frac{F_{ct2}}{bhE_c\varepsilon_{cr}}=\frac{\left(1-k\right)\left(\alpha-1\right)\left(\eta\alpha-\eta+2\right)}{2\beta}$$

$$F_{ct3}=\sigma_{ct3}\times h_{ct3}\times b=\mu E_c\varepsilon_{cr}\times\frac{\left(1-k\right)\left(\beta-\alpha\right)}{\beta}h\times b\rightarrow\frac{F_{ct3}}{bhE_c\varepsilon_{cr}}=\frac{\left(1-k\right)\left(\beta-\alpha\right)\mu}{\beta}$$

$$F_s=\sigma_{sy}\times\rho_s bd_s=\gamma_s E_c\zeta\varepsilon_{cr}\times\rho_s bd_s\times\frac{h}{h}\rightarrow\frac{F_s}{bhE_c\varepsilon_{cr}}=\frac{\zeta\gamma_s\rho_s d_s}{h}$$

$$F_F=\sigma_F\times\rho_F bd_F=\gamma_F E_c\frac{\left(1-k-\Delta_F\right)}{1-k}\beta\varepsilon_{cr}\times\rho_F bd_F\times\frac{h}{h}\rightarrow\frac{F_F}{bhE_c\varepsilon_{cr}}=\frac{\gamma_F\beta\rho_F d_F\left(1-k-\Delta_F\right)}{\left(1-k\right)h}$$

Stage 3.2.1.1

$$F_{cc1}=\sigma_{cc1}\times h_{cc1}\times\frac{b}{2}=\omega\gamma E_c\varepsilon_{cr}\times\frac{\omega(1-k)}{\beta}h\times\frac{b}{2}\rightarrow\frac{F_{cc1}}{bhE_c\varepsilon_{cr}}=\frac{\omega^2\gamma(1-k)}{2\beta}$$

$$F_{cc2}=\sigma_{cc2}\times h_{cc2}\times b=\omega\gamma E_c\varepsilon_{cr}\times\frac{k\beta-\omega(1-k)}{\beta}bh\rightarrow\frac{F_{cc2}}{bhE_c\varepsilon_{cr}}=\frac{\omega\gamma}{\beta}(\beta k+\omega k-\omega)$$

$$F_{ct1}=\sigma_{ct1}\times h_{ct1}\times\frac{b}{2}=E_c\varepsilon_{cr}\times\frac{1-k}{\beta}h\times\frac{b}{2}\rightarrow\frac{F_{ct1}}{bhE_c\varepsilon_{cr}}=\frac{1-k}{2\beta}$$

$$F_{ct2}=(\sigma_{ct1}+\sigma_{ct2})h_{ct2}\times\frac{b}{2}=\left(1+1+\eta(\alpha-1)\right)E_c\varepsilon_{cr}\times\frac{(1-k)(\alpha-1)}{\beta}h\times\frac{b}{2}$$

$$\rightarrow\frac{F_{ct2}}{bhE_c\varepsilon_{cr}}=\frac{(1-k)(\alpha-1)(\eta\alpha-\eta+2)}{2\beta}$$

$$F_{ct3}=\sigma_{ct3}\times h_{ct3}\times b=\mu E_c\varepsilon_{cr}\times\frac{(1-k)(\beta-\alpha)}{\beta}h\times b\rightarrow\frac{F_{ct3}}{bhE_c\varepsilon_{cr}}=\frac{(1-k)(\beta-\alpha)\mu}{\beta}$$

$$F_s=\sigma_s\times\rho_s bd_s=\gamma_s E_c\frac{(1-k-\Delta_s)}{1-k}\beta\varepsilon_{cr}\times\rho_s bd_s\times\frac{h}{h}\rightarrow\frac{F_s}{bhE_c\varepsilon_{cr}}=\frac{\gamma_s\beta\rho_s d_s(1-k-\Delta_s)}{(1-k)h}$$

$$F_F=\sigma_F\times\rho_F bd_F=\gamma_F E_c\frac{(1-k-\Delta_F)}{1-k}\beta\varepsilon_{cr}\times\rho_F bd_F\times\frac{h}{h}\rightarrow\frac{F_F}{bhE_c\varepsilon_{cr}}=\frac{\gamma_F\beta\rho_F d_F(1-k-\Delta_F)}{(1-k)h}$$

Stage 3.2.2.1

$$F_{cc1}=\sigma_{cc1}\times h_{cc1}\times\frac{b}{2}=\omega\gamma E_c\varepsilon_{cr}\times\frac{\omega(1-k)}{\beta}h\times\frac{b}{2}\rightarrow\frac{F_{cc1}}{bhE_c\varepsilon_{cr}}=\frac{\omega^2\gamma(1-k)}{2\beta}$$

$$F_{cc2}=\sigma_{cc2}\times h_{cc2}\times b=\omega\gamma E_c\varepsilon_{cr}\times\frac{k\beta-\omega(1-k)}{\beta}bh\rightarrow\frac{F_{cc2}}{bhE_c\varepsilon_{cr}}=\frac{\omega\gamma}{\beta}(\beta k+\omega k-\omega)$$

$$F_{ct1}=\sigma_{ct1}\times h_{ct1}\times\frac{b}{2}=E_c\varepsilon_{cr}\times\frac{1-k}{\beta}h\times\frac{b}{2}\rightarrow\frac{F_{ct1}}{bhE_c\varepsilon_{cr}}=\frac{1-k}{2\beta}$$

$$F_{ct2}=(\sigma_{ct1}+\sigma_{ct2})h_{ct2}\times\frac{b}{2}=\left(1+1+\eta(\alpha-1)\right)E_c\varepsilon_{cr}\times\frac{(1-k)(\alpha-1)}{\beta}h\times\frac{b}{2}$$

$$\rightarrow\frac{F_{ct2}}{bhE_c\varepsilon_{cr}}=\frac{(1-k)(\alpha-1)(\eta\alpha-\eta+2)}{2\beta}$$

$$F_{ct3}=\sigma_{ct3}\times h_{ct3}\times b=\mu E_c\varepsilon_{cr}\times\frac{(1-k)(\beta-\alpha)}{\beta}h\times b\rightarrow\frac{F_{ct3}}{bhE_c\varepsilon_{cr}}=\frac{(1-k)(\beta-\alpha)\mu}{\beta}$$

$$F_s=\sigma_{sy}\times\rho_s bd_s=\gamma_s E_c\zeta\varepsilon_{cr}\times\rho_s bd_s\times\frac{h}{h}\rightarrow\frac{F_s}{bhE_c\varepsilon_{cr}}=\frac{\zeta\gamma_s\rho_s d_s}{h}$$

$$F_F=\sigma_F\times\rho_F bd_F=\gamma_F E_c\frac{(1-k-\Delta_F)}{1-k}\beta\varepsilon_{cr}\times\rho_F bd_F\times\frac{h}{h}\rightarrow\frac{F_F}{bhE_c\varepsilon_{cr}}=\frac{\gamma_F\beta\rho_F d_F(1-k-\Delta_F)}{(1-k)h}$$

Appendix **F**

Deduction of the normalised arm of the forces with respect to the neutral axis

Stage 1.1.1.1

$$y_{cc1} = \frac{2}{3} h_{cc1} = \frac{2}{3} kh \rightarrow \frac{y_{cc1}}{h} = \frac{2}{3} k$$

$$y_{ct1} = \frac{2}{3} h_{ct1} = \frac{2}{3} h(1-k) \rightarrow \frac{y_{ct1}}{h} = \frac{2}{3}(1-k)$$

$$y_s = h_s = h(1-k-\Delta_s) \rightarrow \frac{y_s}{h} = (1-k-\Delta_s)$$

$$y_F = h_F = h(1-k-\Delta_F) \rightarrow \frac{y_F}{h} = (1-k-\Delta_F)$$

Stage 2.1.1.1

$$y_{cc1} = \frac{2}{3} h_{cc1} = \frac{2}{3} kh \rightarrow \frac{y_{cc1}}{h} = \frac{2}{3} k$$

$$y_{ct1} = \frac{2}{3} h_{ct1} \rightarrow \frac{y_{ct1}}{h} = \frac{2}{3} \frac{(1-k)}{\beta}$$

$$y_{ct2} = h_{ct1} + y'_{ct2}$$

$$y'_{ct2} = \frac{\frac{h_{ct2}^2}{6}(\sigma_{ct1} - \sigma_{ct2}) + \sigma_{ct2} \frac{h_{ct2}^2}{2}}{\frac{1}{2}(\sigma_{ct1} + \sigma_{ct2}) h_{ct2}} \rightarrow \frac{y_{ct2}}{h} = \frac{2\eta\beta^2 - \eta\beta - \eta + 3\beta + 3}{3\beta(\eta\beta - \eta + 2)}(1-k)$$

$$y_s = h_s = h(1-k-\Delta_s) \rightarrow \frac{y_s}{h} = (1-k-\Delta_s)$$

$$y_F = h_F = h\left(1-k-\Delta_F\right) \rightarrow \frac{y_F}{h} = \left(1-k-\Delta_F\right)$$

Stage 2.1.2.1

$$y_{cc1} = \frac{2}{3}h_{cc1} = \frac{2}{3}kh \rightarrow \frac{y_{cc1}}{h} = \frac{2}{3}k$$

$$y_{ct1} = \frac{2}{3}h_{ct1} = \frac{2}{3}\frac{\left(1-k\right)}{\beta}h \rightarrow \frac{y_{ct1}}{h} = \frac{2}{3}\frac{\left(1-k\right)}{\beta}$$

$$y_{ct2} = h_{ct1} + y'_{ct2}$$

$$y'_{ct2} = \frac{\frac{h_{ct2}^2}{6}\left(\sigma_{ct1}-\sigma_{ct2}\right)+\sigma_{ct2}\frac{h_{ct2}^2}{2}}{\frac{1}{2}\left(\sigma_{ct1}+\sigma_{ct2}\right)h_{ct2}} \rightarrow \frac{y_{ct2}}{h} = \frac{2\eta\beta^2-\eta\beta-\eta+3\beta+3}{3\beta\left(\eta\beta-\eta+2\right)}\left(1-k\right)$$

$$y_s = h_s = h\left(1-k-\Delta_s\right) \rightarrow \frac{y_s}{h} = \left(1-k-\Delta_s\right)$$

$$y_F = h_F = h\left(1-k-\Delta_F\right) \rightarrow \frac{y_F}{h} = \left(1-k-\Delta_F\right)$$

Stage 2.2.1.1

$$y_{cc1} = \frac{2}{3}h_{cc1} \rightarrow \frac{y_{cc1}}{h} = \frac{2}{3}\frac{\omega\left(1-k\right)}{\beta}$$

$$y_{cc2} = h_{cc1} + \frac{h_{cc2}}{2} = \frac{\omega\left(1-k\right)}{\beta}h + \frac{k\beta-\omega\left(1-k\right)}{2\beta}h \rightarrow \frac{y_{cc2}}{h} = \frac{k\beta+\omega\left(1-k\right)}{2\beta}$$

$$y_{ct1} = \frac{2}{3}h_{ct1} = \frac{2}{3}\frac{\left(1-k\right)}{\beta}h \rightarrow \frac{y_{ct1}}{h} = \frac{2}{3}\frac{\left(1-k\right)}{\beta}$$

$$y_{ct2} = h_{ct1} + y'_{ct2}$$

$$y'_{ct2} = \frac{\frac{h_{ct2}^2}{6}\left(\sigma_{ct1}-\sigma_{ct2}\right)+\sigma_{ct2}\frac{h_{ct2}^2}{2}}{\frac{1}{2}\left(\sigma_{ct1}+\sigma_{ct2}\right)h_{ct2}} \rightarrow \frac{y_{ct2}}{h} = \frac{2\eta\beta^2-\eta\beta-\eta+3\beta+3}{3\beta\left(\eta\beta-\eta+2\right)}\left(1-k\right)$$

$$y_s = h_s = h\left(1-k-\Delta_s\right) \rightarrow \frac{y_s}{h} = \left(1-k-\Delta_s\right)$$

$$y_F = h_F = h\left(1-k-\Delta_F\right) \rightarrow \frac{y_F}{h} = \left(1-k-\Delta_F\right)$$

Stage 2.2.2.1

$$y_{cc1} = \frac{2}{3}h_{cc1} \rightarrow \frac{y_{cc1}}{d} = \frac{2}{3}\frac{\omega\left(1-k\right)}{\beta}$$

$$y_{cc2} = h_{cc1} + \frac{h_{cc2}}{2} = \frac{\omega\left(1-k\right)}{\beta}d + \frac{k\beta-\omega\left(1-k\right)}{2\beta}d \rightarrow \frac{y_{cc2}}{d} = \frac{k\beta+\omega\left(1-k\right)}{2\beta}$$

$$y_{ct1} = \frac{2}{3}h_{ct1} = \frac{2}{3}\frac{\left(1-k\right)}{\beta}d \rightarrow \frac{y_{ct1}}{d} = \frac{2}{3}\frac{\left(1-k\right)}{\beta}$$

$$y_{ct2} = h_{ct1} + y'_{ct2}$$

$$y'_{ct2} = \frac{\frac{h_{ct2}^2}{6}\left(\sigma_{ct1}-\sigma_{ct2}\right)+\sigma_{ct2}\frac{h_{ct2}^2}{2}}{\frac{1}{2}\left(\sigma_{ct1}+\sigma_{ct2}\right)h_{ct2}} \rightarrow \frac{y_{ct2}}{h} = \frac{2\eta\beta^2-\eta\beta-\eta+3\beta+3}{3\beta\left(\eta\beta-\eta+2\right)}\left(1-k\right)$$

$$y_s = h_s = h\left(1-k-\Delta_s\right) \rightarrow \frac{y_s}{h} = \left(1-k-\Delta_s\right)$$

$$y_F = h_F = h\left(1-k-\Delta_F\right) \rightarrow \frac{y_F}{h} = \left(1-k-\Delta_F\right)$$

Stage 3.1.1.1

$$y_{cc1} = \frac{2}{3}h_{cc1} = \frac{2}{3}kh \rightarrow \frac{y_{cc1}}{h} = \frac{2}{3}k$$

$$y_{ct1} = \frac{2}{3}h_{ct1} = \frac{2}{3}\frac{\left(1-k\right)}{\beta}h \rightarrow \frac{y_{ct1}}{h} = \frac{2}{3}\frac{\left(1-k\right)}{\beta}$$

$$y_{ct2} = h_{ct1} + y'_{ct2}$$

$$y'_{ct2} = \frac{\frac{h_{ct2}^2}{6}\left(\sigma_{ct1}-\sigma_{ct2}\right)+\sigma_{ct2}\frac{h_{ct2}^2}{2}}{\frac{1}{2}\left(\sigma_{ct1}+\sigma_{ct2}\right)h_{ct2}} \rightarrow \frac{y_{ct2}}{h} = \frac{2\eta\alpha^2-\eta\alpha-\eta+3\alpha+3}{3\beta\left(\eta\alpha-\eta+2\right)}\left(1-k\right)$$

$$y_{ct3} = h_{ct1} + h_{ct2} + \frac{h_{ct3}}{2} \rightarrow \frac{y_{ct3}}{h} = \frac{\left(\alpha+\beta\right)}{2\beta}\left(1-k\right)$$

$$y_s = h_s = h\left(1-k-\Delta_s\right) \rightarrow \frac{y_s}{h} = \left(1-k-\Delta_s\right)$$

$$y_F = h_F = h\left(1-k-\Delta_F\right) \rightarrow \frac{y_F}{h} = \left(1-k-\Delta_F\right)$$

Stage 3.1.2.1

$$y_{cc1} = \frac{2}{3}h_{cc1} = \frac{2}{3}kh \rightarrow \frac{y_{cc1}}{h} = \frac{2}{3}k$$

$$y_{ct1} = \frac{2}{3}h_{ct1} = \frac{2}{3}\frac{\left(1-k\right)}{\beta}h \rightarrow \frac{y_{ct1}}{h} = \frac{2}{3}\frac{\left(1-k\right)}{\beta}$$

$$y_{ct2} = h_{ct1} + y'_{ct2}$$

$$y'_{ct2} = \frac{\frac{h_{ct2}^2}{6}\left(\sigma_{ct1}-\sigma_{ct2}\right)+\sigma_{ct2}\frac{h_{ct2}^2}{2}}{\frac{1}{2}\left(\sigma_{ct1}+\sigma_{ct2}\right)h_{ct2}} \rightarrow \frac{y_{ct2}}{h} = \frac{2\eta\alpha^2-\eta\alpha-\eta+3\alpha+3}{3\beta\left(\eta\alpha-\eta+2\right)}\left(1-k\right)$$

$$y_{ct3} = h_{ct1} + h_{ct2} + \frac{h_{ct3}}{2} \rightarrow \frac{y_{ct3}}{h} = \frac{\left(\alpha+\beta\right)}{2\beta}\left(1-k\right)$$

$$y_s = h_s = h\left(1-k-\Delta_s\right) \rightarrow \frac{y_s}{h} = \left(1-k-\Delta_s\right)$$

$$y_F = h_F = h\left(1-k-\Delta_F\right) \rightarrow \frac{y_F}{h} = \left(1-k-\Delta_F\right)$$

Stage 3.2.1.1

$$y_{cc1} = \frac{2}{3}h_{cc1} \rightarrow \frac{y_{cc1}}{d} = \frac{2}{3}\frac{\omega\left(1-k\right)}{\beta}$$

$$y_{cc2} = h_{cc1} + \frac{h_{cc2}}{2} = \frac{\omega\left(1-k\right)}{\beta}d + \frac{k\beta-\omega\left(1-k\right)}{2\beta}d \rightarrow \frac{y_{cc2}}{d} = \frac{k\beta+\omega\left(1-k\right)}{2\beta}$$

$$y_{ct1} = \frac{2}{3}h_{ct1} = \frac{2}{3}\frac{\left(1-k\right)}{\beta}h \rightarrow \frac{y_{ct1}}{h} = \frac{2}{3}\frac{\left(1-k\right)}{\beta}$$

$$y_{ct2} = h_{ct1} + y'_{ct2}$$

$$y'_{ct2} = \frac{\frac{h_{ct2}^2}{6}\left(\sigma_{ct1} - \sigma_{ct2}\right) + \sigma_{ct2}\frac{h_{ct2}^2}{2}}{\frac{1}{2}\left(\sigma_{ct1} + \sigma_{ct2}\right)h_{ct2}} \rightarrow \frac{y_{ct2}}{h} = \frac{2\eta\alpha^2 - \eta\alpha - \eta + 3\alpha + 3}{3\beta\left(\eta\alpha - \eta + 2\right)}\left(1-k\right)$$

$$y_{ct3} = h_{ct1} + h_{ct2} + \frac{h_{ct3}}{2} \rightarrow \frac{y_{ct3}}{h} = \frac{\left(\alpha+\beta\right)}{2\beta}\left(1-k\right)$$

$$y_s = h_s = h\left(1-k-\Delta_s\right) \rightarrow \frac{y_s}{h} = \left(1-k-\Delta_s\right)$$

$$y_F = h_F = h\left(1-k-\Delta_F\right) \rightarrow \frac{y_F}{h} = \left(1-k-\Delta_F\right)$$

Stage 3.2.2.1

$$y_{cc1} = \frac{2}{3}h_{cc1} \rightarrow \frac{y_{cc1}}{d} = \frac{2}{3}\frac{\omega\left(1-k\right)}{\beta}$$

$$y_{cc2} = h_{cc1} + \frac{h_{cc2}}{2} = \frac{\omega\left(1-k\right)}{\beta}d + \frac{k\beta - \omega\left(1-k\right)}{2\beta}d \rightarrow \frac{y_{cc2}}{d} = \frac{k\beta + \omega\left(1-k\right)}{2\beta}$$

$$y_{ct1} = \frac{2}{3}h_{ct1} = \frac{2}{3}\frac{\left(1-k\right)}{\beta}h \rightarrow \frac{y_{ct1}}{h} = \frac{2}{3}\frac{\left(1-k\right)}{\beta}$$

$$y_{ct2} = h_{ct1} + y'_{ct2}$$

$$y'_{ct2} = \frac{\frac{h_{ct2}^2}{6}\left(\sigma_{ct1} - \sigma_{ct2}\right) + \sigma_{ct2}\frac{h_{ct2}^2}{2}}{\frac{1}{2}\left(\sigma_{ct1} + \sigma_{ct2}\right)h_{ct2}} \rightarrow \frac{y_{ct2}}{h} = \frac{2\eta\alpha^2 - \eta\alpha - \eta + 3\alpha + 3}{3\beta\left(\eta\alpha - \eta + 2\right)}\left(1-k\right)$$

$$y_{ct3} = h_{ct1} + h_{ct2} + \frac{h_{ct3}}{2} \rightarrow \frac{y_{ct3}}{h} = \frac{\left(\alpha+\beta\right)}{2\beta}\left(1-k\right)$$

$$y_s = h_s = h\left(1-k-\Delta_s\right) \rightarrow \frac{y_s}{h} = \left(1-k-\Delta_s\right)$$

$$y_F = h_F = h\left(1-k-\Delta_F\right) \rightarrow \frac{y_F}{h} = \left(1-k-\Delta_F\right)$$

Appendix **G**

Deduction of the depth of the neutral axis parameter

Stage 1.1.1.1

$$\sum F = 0 \rightarrow -F_{cc1} + F_{ct1} + F_s + F_F + F_s^{pr} + F_F^{pr} = 0$$

$$\rightarrow -\frac{\gamma\beta k^2}{2(1-k)} + \frac{\beta(1-k)}{2} + \frac{\gamma_s\beta\rho_s d_s(1-k-\Delta_s)}{(1-k)h} + \frac{\gamma_F\beta\rho_F d_F(1-k-\Delta_F)}{(1-k)h} + F_s^{pr} + F_F^{pr} = 0$$

$$\rightarrow k_1 = \begin{cases} \dfrac{2B_s d_s/h(1-\Delta_s) + 2B_F d_F/h(1-\Delta_F) + 1 + (2F_{pr}/\beta)}{2\sqrt{D_{1111}}} & for\ \gamma = 1 \\ \dfrac{-(1 + B_s d_s/h + B_F d_F/h + (F_{pr}/\beta)) + \sqrt{D_{1111}}}{(\gamma - 1)} & for\ \gamma \neq 1 \end{cases}$$

$$D_{1111} = (B_s d_s/h + B_F d_F/h + 1 + (1/\beta)F_{pr})^2 - (1-\gamma)(1 + 2B_s d_s/h(1-\Delta_s) + 2B_F d_F/h(1-\Delta_f) + (2/\beta)F_{pr})$$

$$B_s = \gamma_s\rho_s,\ B_F = \gamma_F\rho_F,\ F_{pr} = F_s^{pr} + F_F^{pr}$$

Stage 2.1.1.1

$$\sum F = 0 \rightarrow -F_{cc1} + F_{ct1} + F_{ct2} + F_s + F_F + F_s^{pr} + F_F^{pr} = 0$$

$$\rightarrow -\frac{\gamma\beta k_{2111}^2}{2(1-k_{2111})} + \frac{(1-k_{2111})}{2\beta} + \frac{(1-k_{2111})(\beta-1)(\eta\beta-\eta+2)}{2\beta} + \frac{\gamma_s\beta\rho_s d_s(1-k_{2111}-\Delta_s)}{(1-k_{2111})h} + \frac{\gamma_F\beta\rho_F d_F(1-k_{2111}-\Delta_F)}{(1-k_{2111})h} + F_s^{pr} + F_F^{pr} = 0$$

$$\rightarrow k_{2111} = \frac{D_{2111} + \beta\left(\beta\left(B_s d_s / h + B_F d_F / h\right) + F_{pr}\right)}{D_{2111} - \beta^2\gamma} - \left(\frac{1}{D_{2111} - \beta^2\gamma}\right)\left[\left(D_{2111} + \beta\left(\beta\left(B_s d_s / h + B_F d_F / h\right) + F_{pr}\right)\right)^2 - \left(D_{2111} - \beta^2\gamma\right)\left(D_{2111} + 2\beta\left(\beta\left(B_s d_s / h(1-\Delta_s) + B_F d_F / h(1-\Delta_f)\right) + F_{pr}\right)\right)\right]^{0.5}$$

$$D_{2111} = \eta(\beta-1)^2 + 2\beta - 1,\ B_s = \gamma_s\rho_s,\ B_F = \gamma_F\rho_F,\ F_{pr} = F_s^{pr} + F_F^{pr}$$

Stage 2.1.2.1

$$\sum F = 0 \rightarrow -F_{cc1} + F_{ct1} + F_{ct2} + F_{sy} + F_F + F_F^{pr} = 0$$

$$\rightarrow -\frac{\gamma\beta k_{2121}^2}{2(1-k_{2121})} + \frac{(1-k_{2121})}{2\beta} + \frac{(1-k_{2121})(\beta-1)(\eta\beta-\eta+2)}{2\beta} + \frac{\zeta\gamma_s\rho_s d_s}{h} + \frac{\gamma_F\beta\rho_F d_F(1-k_{2121}-\Delta_F)}{(1-k_{2121})h} + F_F^{pr} = 0$$

$$\rightarrow k_{2121} = \frac{D_{2121} + \beta\left(\zeta B_s d_s / h + \beta B_F d_F / h + F_F^{pr}\right)}{D_{2121} - \beta^2\gamma} - \left(\frac{1}{D_{2121} - \beta^2\gamma}\right)\left[\left(D_{2121} + \beta\left(\zeta B_s d_s / h + \beta B_F d_F / h + F_F^{pr}\right)\right)^2 - \left(D_{2121} - \beta^2\gamma\right)\left(D_{2121} + 2\beta\left(\zeta B_s d_s / h + \beta B_F d_F / h(1-\Delta_F) + F_F^{pr}\right)\right)\right]^{0.5}$$

$$D_{2121} = \eta(\beta-1)^2 + 2\beta - 1,\ B_s = \gamma_s\rho_s,\ B_F = \gamma_F\rho_F$$

Stage 2.2.1.1

$$\sum F = 0 \rightarrow -F_{cc1} - F_{cc2} + F_{ct1} + F_{ct2} + F_s + F_F + F_s^{pr} + F_F^{pr} = 0$$

$$\rightarrow -\frac{\omega^2\gamma\left(1-k_{2211}\right)}{2\beta} - \frac{\omega\gamma\left(\beta k_{2211} + \omega k_{2211} - \omega\right)}{\beta} + \frac{\left(1-k_{2211}\right)}{2\beta}$$
$$+\frac{\left(1-k_{2211}\right)\left(\beta-1\right)\left(\eta\beta-\eta+2\right)}{2\beta} + \frac{\gamma_s\beta\rho_s d_s\left(1-k_{2211}-\Delta_s\right)}{\left(1-k_{2211}\right)h}$$
$$+\frac{\gamma_F\beta\rho_F d_F\left(1-k_{2211}-\Delta_F\right)}{\left(1-k_{2211}\right)h} + F_s^{pr} + F_F^{pr} = 0$$

$$\rightarrow k_{2211} = \frac{D_{2211} + \beta\left(\omega\gamma + \beta\left(B_s d_s / h + B_F d_F / h\right) + F_{pr}\right)}{D_{2211} + 2\omega\gamma\beta}$$
$$-\left(\frac{1}{D_{2211} + 2\omega\gamma\beta}\right)\left[\left(D_{2211} + \beta\left(\omega\gamma + \beta\left(B_s d_s / h + B_F d_F / h\right) + F_{pr}\right)\right)^2\right.$$
$$\left.-\left(D_{2211} + 2\omega\gamma\beta\right)\left(D_{2211} + 2\beta\left(\beta B_s d_s / h\left(1-\Delta_s\right) + \beta B_F d_F / h\left(1-\Delta_F\right) + F_{pr}\right)\right)\right]^{0.5}$$

$D_{2211} = \eta\left(\beta-1\right)^2 + 2\beta - 1 + \omega^2\gamma$, $B_s = \gamma_s\rho_s$, $B_F = \gamma_F\rho_F$, $F_{pr} = F_s^{pr} + F_F^{pr}$

Stage 2.2.2.1

$$\sum F = 0 \rightarrow -F_{cc1} - F_{cc2} + F_{ct1} + F_{ct2} + F_{sy} + F_F + F_F^{pr} = 0$$

$$\rightarrow -\frac{\omega^2\gamma\left(1-k_{2221}\right)}{2\beta} - \frac{\omega\gamma\left(\beta k_{2221} + \omega k_{2221} - \omega\right)}{\beta} + \frac{\left(1-k_{2221}\right)}{2\beta}$$
$$+\frac{\left(1-k_{2221}\right)\left(\beta-1\right)\left(\eta\beta-\eta+2\right)}{2\beta} + \frac{\zeta\gamma_s\rho_s d_s}{h}$$
$$+\frac{\gamma_F\beta\rho_F d_F\left(1-k-\Delta_F\right)}{\left(1-k\right)h} + F_F^{pr} = 0$$

$$\rightarrow k_{2221}=\frac{D_{2221}+\beta\left(\beta B_F d_F/h+\zeta B_s d_s/h+\omega\gamma+F_F^{pr}\right)}{D_{2221}+2\omega\gamma\beta}$$
$$-\left(\frac{1}{D_{2221}+2\omega\gamma\beta}\right)\left[\left(D_{2221}+\beta\left(\beta B_F d_F/h+\zeta B_s d_s/h+\omega\gamma+F_F^{pr}\right)\right)^2\right.$$
$$\left.-\left(D_{2221}+2\omega\gamma\beta\right)\left(D_{2221}+2\beta\left(\zeta B_s d_s/h+\beta B_F d_F/h\left(1-\Delta_F\right)+F_F^{pr}\right)\right)\right]^{0.5}$$

$$D_{2221}=\eta\left(\beta-1\right)^2+2\beta-1+\omega^2\gamma\ ,\ B_s=\gamma_s\rho_s,\ B_F=\gamma_F\rho_F$$

Stage 3.1.1.1

$$\sum F=0\rightarrow -F_{cc1}+F_{ct1}+F_{ct2}+F_{ct3}+F_s+F_F+F_s^{pr}+F_F^{pr}=0$$

$$\rightarrow -\frac{\gamma\beta k_{3111}^2}{2\left(1-k_{3111}\right)}+\frac{\left(1-k_{3111}\right)}{2\beta}+\frac{\left(1-k_{3111}\right)\left(\alpha-1\right)\left(\eta\alpha-\eta+2\right)}{2\beta}$$
$$+\frac{\left(1-k_{3111}\right)\left(\beta-\alpha\right)\mu}{\beta}+\frac{\gamma_s\beta\rho_s d_s\left(1-k_{3111}-\Delta_s\right)}{\left(1-k_{3111}\right)h}$$
$$+\frac{\gamma_F\beta\rho_F d_F\left(1-k_{3111}-\Delta_F\right)}{\left(1-k_{3111}\right)h}+F_s^{pr}+F_F^{pr}=0$$

$$\rightarrow k_{3111}=\frac{D_{3111}+\beta\left(\beta\left(B_s d_s/h+B_F d_F/h\right)+F_{pr}\right)}{D_{3111}-\beta^2\gamma}$$
$$-\left(\frac{1}{D_{3111}-\beta^2\gamma}\right)\left[\left(D_{3111}+\beta\left(\beta\left(B_s d_s/h+B_F d_F/h\right)+F_{pr}\right)\right)^2\right.$$
$$\left.-\left(D_{3111}-\beta^2\gamma\right)\left(D_{3111}+2\beta\left(\beta\left(B_s d_s/h\left(1-\Delta_s\right)+B_F d_F/h\left(1-\Delta_F\right)\right)+F_{pr}\right)\right)\right]^{0.5}$$

$$D_{3111}=\eta\left(\alpha-1\right)^2+2\left(\alpha\left(1-\mu\right)+\mu\beta\right)-1,\ B_s=\gamma_s\rho_s,\ B_F=\gamma_F\rho_F,\ F_{pr}=F_s^{pr}+F_F^{pr}$$

Stage 3.1.2.1

$$\sum F = 0 \rightarrow -F_{cc1} + F_{ct1} + F_{ct2} + F_{ct3} + F_{sy} + F_F + F_F^{pr} = 0$$

$$\rightarrow -\frac{\gamma\beta k_{3121}^2}{2(1-k_{3121})} + \frac{(1-k_{3121})}{2\beta} + \frac{(1-k_{3121})(\alpha-1)(\eta\alpha-\eta+2)}{2\beta} + \frac{(1-k_{3121})(\beta-\alpha)\mu}{\beta} + \frac{\zeta\gamma_s\rho_s d_s}{h} + \frac{\gamma_F\beta\rho_F d_F(1-k_{3121}-\Delta_F)}{(1-k_{3121})h} + F_F^{pr} = 0$$

$$\rightarrow k_{3121} = \frac{D_{3121} + \beta\left(\beta B_F d_F / h + \zeta B_s d_s / h + F_F^{pr}\right)}{D_{3121} - \beta^2\gamma} - \left(\frac{1}{D_{3121} - \beta^2\gamma}\right)\left[\left(D_{3121} + \beta\left(\beta B_F d_F / h + \zeta B_s d_s / h + F_F^{pr}\right)\right)^2 - \left(D_{3121} - \beta^2\gamma\right)\left(D_{3121} + 2\beta\left(\zeta B_s d_s / h + \beta B_F d_F / h(1-\Delta_F) + F_F^{pr}\right)\right)\right]^{0.5}$$

$$D_{3121} = \eta(\alpha-1)^2 + 2\left(\alpha(1-\mu) + \mu\beta\right) - 1,\ B_s = \gamma_s\rho_s,\ B_F = \gamma_F\rho_F$$

Stage 3.2.1.1

$$\sum F = 0 \rightarrow -F_{cc1} - F_{cc2} + F_{ct1} + F_{ct2} + F_{ct3} + F_s + F_F + F_s^{pr} + F_F^{pr} = 0$$

$$\rightarrow -\frac{\omega^2\gamma(1-k_{3211})}{2\beta} - \frac{\omega\gamma\left(\beta k_{3211} + \omega k_{3211} - \omega\right)}{\beta} + \frac{(1-k_{3211})}{2\beta} + \frac{(1-k_{3211})(\alpha-1)(\eta\alpha-\eta+2)}{2\beta} + \frac{(1-k_{3211})(\beta-\alpha)\mu}{\beta} + \frac{\gamma_s\beta\rho_s d_s(1-k_{3211}-\Delta_s)}{(1-k_{3211})h} + \frac{\gamma_F\beta\rho_F d_F(1-k_{3211}-\Delta_F)}{(1-k_{3211})h} + F_s^{pr} + F_F^{pr} = 0$$

$$\rightarrow k_{3211} = \frac{D_{3211} + \beta\left(\beta\left(B_s d_s / h + B_F d_F / h\right) + \omega\gamma + F_{pr}\right)}{D_{3211} + 2\omega\gamma\beta} - \left(\frac{1}{D_{3211} + 2\omega\gamma\beta}\right)\left[\left(D_{3211} + \beta\left(\beta\left(B_s d_s / h + B_F d_F / h\right) + \omega\gamma + F_{pr}\right)\right)^2 - \left(D_{3211} + 2\omega\gamma\beta\right)\left(D_{3211} + 2\beta\left(\beta\left(B_s d_s / h(1-\Delta_s) + B_F d_F / h(1-\Delta_F)\right) + F_{pr}\right)\right)\right]^{0.5}$$

$$D_{3211} = \eta(\alpha-1)^2 + 2\left(\alpha(1-\mu) + \mu\beta\right) + \omega^2\gamma - 1,\ B_s = \gamma_s\rho_s,\ B_F = \gamma_F\rho_F,\ F_{pr} = F_s^{pr} + F_F^{pr}$$

Stage 3.2.2.1

$$\sum F = 0 \rightarrow -F_{cc1} - F_{cc2} + F_{ct1} + F_{ct2} + F_{ct3} + F_{sy} + F_F + F_F^{pr} = 0$$

$$\rightarrow -\frac{\omega^2\gamma\left(1-k_{3221}\right)}{2\beta} - \frac{\omega\gamma\left(\beta k_{3221} + \omega k_{3221} - \omega\right)}{\beta} + \frac{\left(1-k_{3221}\right)}{2\beta}$$
$$+ \frac{\left(1-k_{3221}\right)\left(\alpha-1\right)\left(\eta\alpha-\eta+2\right)}{2\beta} + \frac{\left(1-k_{3221}\right)\left(\beta-\alpha\right)\mu}{\beta}$$
$$+ \frac{\zeta\gamma_s\rho_s d_s}{h} + \frac{\gamma_F\beta\rho_F d_F\left(1-k_{3221}-\Delta_F\right)}{\left(1-k_{3221}\right)h}$$
$$+ F_F^{pr} = 0$$

$$\rightarrow k_{3221} = \frac{D_{3221} + \beta\left(\zeta B_s d_s / h + \omega\gamma + F_F^{pr}\right) + \beta^2 B_F d_F / h}{D_{3221} + 2\omega\gamma\beta}$$
$$-\left(\frac{1}{D_{3221} + 2\omega\gamma\beta}\right)\left[\left(D_{3221} + \beta\left(\zeta B_s d_s / h + \omega\gamma + F_F^{pr}\right) + \beta^2 B_F d_F / h\right)^2\right.$$
$$\left.-\left(D_{3221} + 2\omega\gamma\beta\right)\left(D_{3221} + 2\beta\left(\zeta B_s d_s / h + \beta B_F d_F / h\left(1-\Delta_F\right) + F_F^{pr}\right)\right)\right]^{0.5}$$

$$D_{3221} = \eta\left(\alpha-1\right)^2 + 2\left(\alpha\left(1-\mu\right) + \mu\beta\right) + \omega^2\gamma - 1$$

$$B_s = \gamma_s\rho_s,\ B_F = \gamma_F\rho_F$$

Appendix **H**

Deduction of the normalised bending moment and corresponding curvature

Stage 1.1.1.1

$$M_{1111} = F_{cc1}y_{cc1} + F_{ct1}y_{ct1} + F_s y_s + F_F y_F + F_s^{pr}(1-k_{1111}-\Delta_s) + F_F^{pr}(1-k_{1111}-\Delta_F)$$

$$= \frac{\gamma\beta k^2}{2(1-k_{1111})} bhE_c\varepsilon_{cr} \times \frac{2}{3}k_{1111}h + \frac{\beta(1-k_{1111})}{2} bhE_c\varepsilon_{cr} \times \frac{2(1-k_{1111})}{3}\ h$$

$$+ \frac{\gamma_s\beta\rho_s d_s(1-k_{1111}-\Delta_s)}{(1-k_{1111})h} bhE_c\varepsilon_{cr}(1-k_{1111}-\Delta_s)h$$

$$+ \frac{\gamma_F\beta\rho_F d_F(1-k-\Delta_F)}{(1-k_{1111})h} bhE_c\varepsilon_{cr}(1-k_{1111}-\Delta_F)h$$

$$+ F_s^{pr}(1-k_{1111}-\Delta_s) + F_F^{pr}(1-k_{1111}-\Delta_F)$$

$$M'_{1111} = \frac{M_{1111}}{M_{cr}} = \frac{M_{1111}}{E_c\varepsilon_{cr}bh^2/6}$$

$$= \frac{2\left[\beta\gamma k^3 h + \beta h(1-k_{1111})^3 + 3B_s\beta d_s(1-k_{1111}-\Delta_s)^2\right]}{(1-k_{1111})h}$$

$$= \frac{6B_F\beta d_F(1-k_{1111}-\Delta_F)^2}{(1-k_{1111})h} + (M'_{pr})_{1111}$$

$$\left(M'_{pr}\right)_{1111} = \frac{6}{bhE_c\varepsilon_{cr}}\left(F_s^{pr}(1-k_{1111}-\Delta_s) + F_F^{pr}(1-k_{1111}-\Delta_F)\right)$$

Stage 2.1.1.1

$$M_{2111} = F_{cc1}y_{cc1} + F_{ct1}y_{ct1} + F_{ct2}y_{ct2} + F_s y_s + F_F y_F + F_s^{pr}(1-k_{2111}-\Delta_s) + F_F^{pr}(1-k_{2111}-\Delta_F)$$
$$= \frac{\gamma\beta k^2}{2(1-k_{2111})} bhE_c\varepsilon_{cr} \times \frac{2}{3}k_{2111}h + \frac{(1-k_{2111})}{2\beta} bhE_c\varepsilon_{cr} \times \frac{2(1-k_{2111})}{3\beta} h$$
$$+ \frac{(1-k_{2111})(\beta-1)(\eta\beta-\eta+2)}{2\beta} bhE_c\varepsilon_{cr} \times \frac{2\eta\beta^2-\eta\beta-\eta+3\beta+3}{3\beta(\eta\beta-\eta+2)}(1-k_{2111})h$$
$$+ \frac{\gamma_s\beta\rho_s d_s(1-k_{2111}-\Delta_s)}{(1-k_{2111})h} bhE_c\varepsilon_{cr}(1-k_{2111}-\Delta_s)h$$
$$+ \frac{\gamma_F\beta\rho_F d_F(1-k_{2111}-\Delta_F)}{(1-k_{2111})h} bhE_c\varepsilon_{cr}(1-k_{2111}-\Delta_F)h$$
$$++ F_s^{pr}(1-k_{2111}-\Delta_s) + F_F^{pr}(1-k_{2111}-\Delta_F)$$

$$M'_{2111} = \frac{M_{2111}}{M_{cr}} = \frac{M_{2111}}{E_c\varepsilon_{cr}bh^2/6}$$
$$= \frac{\left[2\beta^3\gamma k_{2111}^3 h + 2h(1-k_{2111})^3 + h(1-k_{2111})^3(\beta-1)C_{2111}\right]}{\beta^2(1-k_{2111})h}$$
$$+ \frac{\left[6B_s\beta^3 d_s(1-k_{2111}-\Delta_s)^2 + 6B_F\beta^3 d_F(1-k_{2111}-\Delta_F)^2\right]}{\beta^2(1-k_{2111})h} + (M'_{pr})_{2111}$$

$$\left(M'_{pr}\right)_{2111} = \frac{6}{bhE_c\varepsilon_{cr}}\left(F_s^{pr}(1-k_{2111}-\Delta_s) + F_F^{pr}(1-k_{2111}-\Delta_F)\right)$$

Stage 2.1.2.1

$$M_{2121} = F_{cc1}y_{cc1} + F_{ct1}y_{ct1} + F_{ct2}y_{ct2} + F_s y_s + F_F y_F + F_s^{pr}(1-k_{2121}-\Delta_s) + F_F^{pr}(1-k_{2121}-\Delta_F)$$
$$= \frac{\gamma\beta k_{2121}^2}{2(1-k_{2121})} bhE_c\varepsilon_{cr} \times \frac{2}{3}k_{2121}h + \frac{(1-k_{2121})}{2\beta} bhE_c\varepsilon_{cr} \times \frac{2(1-k_{2121})}{3\beta} h$$
$$+ \frac{(1-k_{2121})(\beta-1)(\eta\beta-\eta+2)}{2\beta} bhE_c\varepsilon_{cr} \times \frac{2\eta\beta^2-\eta\beta-\eta+3\beta+3}{3\beta(\eta\beta-\eta+2)}(1-k_{2121})h$$
$$+ \frac{\zeta\gamma_s\rho_s d_s}{h} bhE_c\varepsilon_{cr}(1-k_{2121}-\Delta_s)h + \frac{\gamma_F\beta\rho_F d_F(1-k_{2121}-\Delta_F)}{(1-k_{2121})h} bhE_c\varepsilon_{cr}(1-k_{2121}-\Delta_F)h$$
$$+ F_s^{pr}(1-k_{2121}-\Delta_s) + F_F^{pr}(1-k_{2121}-\Delta_F)$$

$$M'_{2121} = \frac{M_{2121}}{M_{cr}} = \frac{M_{2111}}{E_c \varepsilon_{cr} b h^2 / 6}$$
$$= \frac{\left[2\beta^3 \gamma k^3 h + 2h(1-k_{2121})^3 + h(1-k_{2121})^3(\beta-1)C_{2121}\right]}{\beta^2(1-k_{2121})h}$$
$$+ \frac{\left[6B_s\beta^2\xi d_s(1-k_{2121})(1-k_{2121}-\Delta_s) + 6B_F\beta^3 d_F(1-k_{2121}-\Delta_F)^2\right]}{\beta^2(1-k_{2121})h} + (M'_{pr})_{2121}$$

$$\left(M'_{pr}\right)_{2121} = \frac{6}{bhE_c\varepsilon_{cr}}\left(F_s^{pr}(1-k_{2121}-\Delta_s) + F_F^{pr}(1-k_{2121}-\Delta_F)\right)$$

Stage 2.2.1.1

$$M_{2211} = F_{cc1}y_{cc1} + F_{cc2}y_{cc2} + F_{ct1}y_{ct1} + F_{ct2}y_{ct2} + F_s y_s + F_f y_f + F_s^{pr}(1-k_{2211}-\Delta_s)$$
$$+ F_F^{pr}(1-k_{2211}-\Delta_F)$$
$$= \frac{\omega^2\gamma\left(1-k_{2211}\right)}{2\beta} bhE_c\varepsilon_{cr} \times \frac{2\omega\left(1-k_{2211}\right)}{3\beta} h$$
$$+ \frac{\omega\gamma\left(\beta k_{2211} + \omega k_{2211} - \omega\right)}{\beta} bhE_c\varepsilon_{cr} \times \frac{k_{2211}\beta + \omega\left(1-k_{2211}\right)}{2\beta} h$$
$$+ \frac{\left(1-k_{2211}\right)}{2\beta} bhE_c\varepsilon_{cr} \times \frac{2\left(1-k_{2211}\right)}{3\beta} h$$
$$+ \frac{\left(1-k_{2211}\right)\left(\beta-1\right)\left(\eta\beta-\eta+2\right)}{2\beta} bhE_c\varepsilon_{cr} \times \frac{2\eta\beta^2-\eta\beta-\eta+3\beta+3}{3\beta\left(\eta\beta-\eta+2\right)}\left(1-k_{2211}\right)h$$
$$+ \frac{\gamma_s\beta\rho_s d_s\left(1-k_{2211}-\Delta_s\right)}{\left(1-k_{2211}\right)h} bhE_c\varepsilon_{cr} \times (1-k_{2211}-\Delta_s)h$$
$$+ \frac{\gamma_F\beta\rho_F d_F\left(1-k_{2211}-\Delta_F\right)}{\left(1-k_{2211}\right)h} bhE_c\varepsilon_{cr} \times (1-k_{2211}-\Delta_F)h$$
$$+ F_s^{pr}(1-k_{2211}-\Delta_s) + F_F^{pr}(1-k_{2211}-\Delta_F)$$

$$M'_{2211} = \frac{M_{2211}}{M_{cr}} = \frac{M_{2211}}{E_c \varepsilon_{cr} b h^2 / 6}$$
$$= \frac{\left[3h\omega\gamma(\beta k_{2211} + \omega k_{2211} - \omega)(k_{2211}\beta + \omega(1-k_{2211}))(1-k_{2211})\right]}{\beta^2(1-k_{2211})h}$$
$$= \frac{\left[2h\omega^3\gamma(1-k_{2211})^3 + 2h(1-k_{2211})^3\right]}{\beta^2(1-k_{2211})h} + \frac{\left[h(1-k_{2211})^3(\beta-1)C_{2211}\right]}{\beta^2(1-k_{2211})h}$$
$$+ \frac{\left[6B_s\beta^3 d_s(1-k_{2211}-\Delta_s)^2 + 6B_F\beta^3 d_F(1-k_{2211}-\Delta_F)^2\right]}{\beta^2(1-k_{2211})h}$$
$$+ (M'_{pr})_{2211}$$

$$\left(M'_{pr}\right)_{2211} = \frac{6}{bhE_c\varepsilon_{cr}}\left(F_s^{pr}(1-k_{2211}-\Delta_s) + F_F^{pr}(1-k_{2211}-\Delta_F)\right)$$

Stage 2.2.2.1

$$M_{2221} = F_{cc1}y_{cc1} + F_{cc2}y_{cc2} + F_{ct1}y_{ct1} + F_{ct2}y_{ct2} + F_s y_s + F_F y_F + F_s^{pr}(1-k_{2221}-\Delta_s) + F_F^{pr}(1-k_{2221}-\Delta_F)$$

$$= \frac{\omega^2\gamma(1-k_{2221})}{2\beta} bhE_c\varepsilon_{cr} \times \frac{2\omega(1-k_{2221})}{3\beta}h + \frac{\omega\gamma(\beta k + \omega k - \omega)}{\beta} bhE_c\varepsilon_{cr} \times \frac{k\beta + \omega(1-k)}{2\beta}h$$
$$+ \frac{(1-k)}{2\beta} bhE_c\varepsilon_{cr} \times \frac{2(1-k)}{3\beta}h + \frac{(1-k)(\beta-1)(\eta\beta-\eta+2)}{2\beta} bhE_c\varepsilon_{cr} \times \frac{2\eta\beta^2-\eta\beta-\eta+3\beta+3}{3\beta(\eta\beta-\eta+2)}(1-k)h$$
$$+ \frac{\zeta\gamma_s\rho_s d_s}{h} bhE_c\varepsilon_{cr}(1-k-\Delta_s)h + \frac{\gamma_F\beta\rho_F d_F(1-k-\Delta_F)}{(1-k)h} bhE_c\varepsilon_{cr} \times (1-k-\Delta_F)h$$
$$+ F_s^{pr}(1-k_{2221}-\Delta_s) + F_F^{pr}(1-k_{2221}-\Delta_F)$$

$$M'_{2221} = \frac{M_{2221}}{M_{cr}} = \frac{M_{2221}}{E_c\varepsilon_{cr} b h^2 / 6}$$
$$= \frac{2h\omega^3\gamma(1-k_{2221})^3 + 3h\omega\gamma(\beta k_{2221} + \omega k_{2221} - \omega)(k_{2221}\beta + \omega(1-k_{2221}))(1-k_{2221})}{\beta^2(1-k_{2221})h}$$
$$= \frac{2h(1-k_{2221})^3 + h(1-k_{2221})^3(\beta-1)C_{2221} + 6B_s\beta^2\xi d_s(1-k_{2221})(1-k_{2221}-\Delta_s)}{\beta^2(1-k_{2221})h}$$
$$+ \frac{6B_F\beta^3 d_F(1-k_{2221}-\Delta_F)^2}{\beta^2(1-k_{2221})h} + (M'_{pr})_{2221}$$

$$\left(M'_{pr}\right)_{2211} = \frac{6}{bhE_c\varepsilon_{cr}}\left(F_s^{pr}(1-k_{2221}-\Delta_s) + F_F^{pr}(1-k_{2221}-\Delta_F)\right)$$

Stage 3.1.1.1

$$M_{3111} = F_{cc1}y_{cc1} + F_{ct1}y_{ct1} + F_{ct2}y_{ct2} + F_{ct3}y_{ct3} + F_s y_s + F_F y_F + F_s^{pr}(1-k_{3111}-\Delta_s) + F_F^{pr}(1-k_{3111}-\Delta_F)$$

$$= \frac{\gamma\beta k^2}{2(1-k_{3111})} bhE_c\varepsilon_{cr} \times \frac{2}{3}k_{3111}h + \frac{(1-k_{3111})}{2\beta} bhE_c\varepsilon_{cr} \times \frac{2(1-k_{3111})}{3\beta}\ h$$
$$+ \frac{(1-k_{3111})(\alpha-1)(\eta\alpha-\eta+2)}{2\beta} bhE_c\varepsilon_{cr} \times \frac{2\eta\alpha^2-\eta\alpha-\eta+3\alpha+3}{3\beta(\eta\alpha-\eta+2)}(1-k_{3111})h$$
$$+ \frac{(1-k_{3111})(\beta-\alpha)\mu}{\beta} bhE_c\varepsilon_{cr} \times \frac{(\alpha+\beta)(1-k_{3111})}{2\beta}h$$
$$+ \frac{\gamma_s\beta\rho_s d_s(1-k_{3111}-\Delta_s)}{(1-k_{3111})h} bhE_c\varepsilon_{cr}(1-k_{3111}-\Delta_s)h$$
$$+ \frac{\gamma_F\beta\rho_F d_F(1-k_{3111}-\Delta_F)}{(1-k_{3111})h} bhE_c\varepsilon_{cr}(1-k_{3111}-\Delta_F)h$$
$$+ F_s^{pr}(1-k_{3111}-\Delta_s) + F_F^{pr}(1-k_{3111}-\Delta_F)$$

$$M'_{3111} = \frac{M_{3111}}{M_{cr}} = \frac{M_{3111}}{E_c\varepsilon_{cr}bh^2/6}$$
$$= \frac{2\gamma\beta^3 {k_{3111}}^3 h + 2(1-k_{3111})^3 h + (1-k_{3111})^3(\alpha-1)C_{3111}h}{\beta^2(1-k_{3111})h}$$
$$+ \frac{3(1-k_{3111})^3(\beta-\alpha)(\alpha+\beta)\mu h + 2\gamma\beta^3 {k_{3111}}^3 h + 2(1-k_{3111})^3 h}{\beta^2(1-k_{3111})h}$$
$$+ \frac{(1-k_{3111})^3(\alpha-1)C_{3111}h + 3(1-k_{3111})^3(\beta-\alpha)(\alpha+\beta)\mu h}{\beta^2(1-k_{3111})h}$$
$$+ \frac{6B_s\beta^3 d_s(1-k_{3111}-\Delta_s)^2 + 6B_F\beta^3 d_F(1-k_{3111}-\Delta_F)^2}{\beta^2(1-k_{3111})h} + (M'_{pr})_{3111}$$

$$\left(M'_{pr}\right)_{3111} = \frac{6}{bhE_c\varepsilon_{cr}}\left(F_s^{pr}(1-k_{3111}-\Delta_s) + F_F^{pr}(1-k_{3111}-\Delta_F)\right)$$

Stage 3.1.2.1

$$M_{3121} = F_{cc1}y_{cc1} + F_{ct1}y_{ct1} + F_{ct2}y_{ct2} + F_{ct3}y_{ct3} + F_s y_s + F_F y_F + F_s^{pr}(1-k_{3121}-\Delta_s) + F_F^{pr}(1-k_{3121}-\Delta_F)$$

$$= \frac{\gamma\beta k_{3121}^2}{2(1-k_{3121})} bhE_c\varepsilon_{cr} \times \frac{2}{3}k_{3121}h + \frac{(1-k_{3121})}{2\beta} bhE_c\varepsilon_{cr} \times \frac{2(1-\mathrm{k})k_{3121}}{3\beta}\ h$$
$$+ \frac{(1-k)(\alpha-1)(\eta\alpha-\eta+2)}{2\beta} bhE_c\varepsilon_{cr} \frac{2\eta\alpha^2-\eta\alpha-\eta+3\alpha+3}{3\beta(\eta\alpha-\eta+2)}(1-k_{3121})h$$
$$+ \frac{(1-k_{3121})(\beta-\alpha)\mu}{\beta} bhE_c\varepsilon_{cr} \frac{(\alpha+\beta)(1-k_{3121})}{2\beta}h$$

$$M'_{3121} = \frac{M_{3121}}{M_{cr}} = \frac{M_{3121}}{E_c\varepsilon_{cr}bh^2/6}$$
$$= \frac{2\gamma\beta^3 k_{3121}^3 h + 2(1-k_{3121})^3 h + (1-k_{3121})^3(\alpha-1)C_{3121}h}{\beta^2(1-k_{3121})h}$$
$$+ \frac{3(1-k_{3121})^3(\beta-\alpha)(\alpha+\beta)\mu h + 6B_s\beta^2\xi d_s(1-k_{3121})(1-k_{3121}-\Delta_s)}{\beta^2(1-k_{3121})h}$$
$$+ \frac{6B_F\beta^3 d_F(1-k_{3121}-\Delta_F)^2}{\beta^2(1-k_{3121})h} + (M'_{pr})_{3121}$$

$$+ \frac{\left[6B_s\beta^2\xi d_s(1-k_{3121})(1-k_{3121}-\Delta_s) + 6B_F\beta^3 d_F(1-k_{3121}-\Delta_F)^2\right]}{\beta^2(1-k_{3121})h} + (M'_{pr})_{3121}$$

$$\left(M'_{pr}\right)_{3121} = \frac{6}{bhE_c\varepsilon_{cr}}\left(F_s^{pr}(1-k_{3121}-\Delta_s) + F_F^{pr}(1-k_{3121}-\Delta_F)\right)$$

Stage 3.2.1.1

$$M_{3211} = F_{cc1}y_{cc1} + F_{cc2}y_{cc2} + F_{ct1}y_{ct1} + F_{ct2}y_{ct2} + F_{ct3}y_{ct3} + F_s y_s + F_F y_F + F_s^{pr}(1-k_{3121}-\Delta_s) + F_F^{pr}(1-k_{3121}-\Delta_F)$$

$$= \frac{\omega^2\gamma(1-k_{3121})}{2\beta} bhE_c\varepsilon_{cr} \times \frac{2}{3}\frac{\omega(1-k_{3121})}{\beta}h + \frac{\omega\gamma(\beta k_{3121}+\omega k_{3121}-\omega)}{\beta} bhE_c\varepsilon_{cr}$$
$$\times \frac{k_{3121}\beta+\omega(1-k_{3121})}{2\beta}h + \frac{(1-k)k_{3121}}{2\beta} bhE_c\varepsilon_{cr} \times \frac{2(1-k_{3121})}{3\beta}\ h$$
$$+ \frac{(1-k_{3121})(\alpha-1)(\eta\alpha-\eta+2)}{2\beta} bhE_c\varepsilon_{cr} \times \frac{2\eta\alpha^2-\eta\alpha-\eta+3\alpha+3}{3\beta(\eta\alpha-\eta+2)}(1-k_{3121})k_{3121}h$$
$$+ \frac{(1-k_{3121})(\beta-\alpha)\mu}{\beta} bhE_c\varepsilon_{cr}\frac{(\alpha+\beta)(1-k_{3121})}{2\beta}h$$
$$+ \frac{\gamma_s\beta\rho_s d_s(1-k_{3121}-\Delta_s)}{(1-k_{3121})h} bhE_c\varepsilon_{cr}(1-k_{3121}-\Delta_s)h$$
$$+ \frac{\gamma_F\beta\rho_F d_F(1-k_{3121}-\Delta_F)}{(1-k_{3121})h} bhE_c\varepsilon_{cr}(1-k_{3121}-\Delta_F)h$$
$$+ F_s^{pr}(1-k_{3121}-\Delta_s) + F_F^{pr}(1-k_{3121}-\Delta_F)$$

$$M'_{3211} = \frac{M_{3211}}{M_{cr}} = \frac{M_{3121}}{E_c\varepsilon_{cr}bh^2/6}$$
$$= \frac{2h\omega^3\gamma(1-k_{3211})^3 + 2(1-k_{3211})^3 h}{\beta^2(1-k_{3211})h}$$
$$+ \frac{3h\omega\gamma(\beta k_{3211}+\omega k_{3211}-\omega)(k_{3211}\beta+\omega(1-k_{3211}))(1-k_{3211})}{\beta^2(1-k_{3211})h}$$
$$+ \frac{(1-k_{3211})^3(\alpha-1)C_{3211}h + 3(1-k_{3211})^3(\beta-\alpha)(\alpha+\beta)\mu h}{\beta^2(1-k_{3211})h}$$
$$+ \frac{+6B_s\beta^3 d_s(1-k_{3211}-\Delta_s)^2 + 6B_F\beta^3 d_F(1-k_{3211}-\Delta_F)^2}{\beta^2(1-k_{3211})h} + (M'_{pr})_{3211}$$

$$\left(M'_{pr}\right)_{3211} = \frac{6}{bhE_c\varepsilon_{cr}}\left(F_s^{pr}(1-k_{3211}-\Delta_s) + F_F^{pr}(1-k_{3211}-\Delta_F)\right)$$

Stage 3.2.1.1

$$M_{3221} = F_{cc1}y_{cc1} + F_{cc2}y_{cc2} + F_{ct1}y_{ct1} + F_{ct2}y_{ct2} + F_{ct3}y_{ct3} + F_s y_s + F_F y_F + F_s^{pr}(1-k_{3221}-\Delta_s) + F_F^{pr}(1-k_{3221}-\Delta_F)$$

$$= \frac{\omega^2\gamma(1-k)k_{3221}}{2\beta} bhE_c\varepsilon_{cr} \times \frac{2}{3}\frac{\omega(1-k_{3221})}{\beta}h + \frac{\omega\gamma(\beta k_{3221} + \omega k_{3221} - \omega)}{\beta} bhE_c\varepsilon_{cr}$$
$$\times \frac{k_{3221}\beta + \omega(1-k)k_{3221}}{2\beta}h + \frac{(1-k_{3221})}{2\beta} bhE_c\varepsilon_{cr} \times \frac{2(1-k_{3221})}{3\beta}\ h$$
$$+ \frac{(1-k_{3221})(\alpha-1)(\eta\alpha-\eta+2)}{2\beta} bhE_c\varepsilon_{cr}\frac{2\eta\alpha^2-\eta\alpha-\eta+3\alpha+3}{3\beta(\eta\alpha-\eta+2)}(1-k_{3221})h$$
$$+ \frac{(1-k_{3221})(\beta-\alpha)\mu}{\beta} bhE_c\varepsilon_{cr}\frac{(\alpha+\beta)(1-k)k_{3221}}{2\beta}h + \frac{\zeta\gamma_s\rho_s d_s}{h} bhE_c\varepsilon_{cr}(1-k_{3221}-\Delta_s)h$$
$$+ \frac{\gamma_F\beta\rho_F d_F(1-k_{3221}-\Delta_F)}{(1-k_{3221})h} bhE_c\varepsilon_{cr}(1-k_{3221}-\Delta_F)h + F_s^{pr}(1-k_{3221}-\Delta_s) + F_F^{pr}(1-k_{3221}-\Delta_F)$$

$$M'_{3221} = \frac{M_{3221}}{M_{cr}} = \frac{M_{3221}}{E_c\varepsilon_{cr}bh^2/6}$$
$$= \frac{2h\omega^3\gamma(1-k_{3221})^3 + 2(1-k_{3221})^3 h}{\beta^2(1-k_{3221})h}$$
$$+ \frac{3h\omega\gamma(\beta k_{3221} + \omega k_{3221} - \omega)(k_{3221}\beta + \omega(1-k_{3221}))(1-k_{3221})}{\beta^2(1-k_{3221})h}$$
$$+ \frac{(1-k_{3221})^3(\alpha-1)C_{3221}h + 3(1-k_{3221})^3(\beta-\alpha)(\alpha+\beta)\mu h}{\beta^2(1-k_{3221})h}$$
$$+ \frac{6B_s\beta^2\xi d_s(1-k_{3221})(1-k_{3221}-\Delta_s)}{\beta^2(1-k_{3221})h}$$
$$+ \frac{6B_F\beta^3 d_F(1-k_{3221}-\Delta_F)^2}{\beta^2(1-k_{3221})h} + (M'_{pr})_{3221}$$

$$\left(M'_{pr}\right)_{3221} = \frac{6}{bhE_c\varepsilon_{cr}}\left(F_s^{pr}(1-k_{3221}-\Delta_s) + F_F^{pr}(1-k_{3221}-\Delta_F)\right)$$